

1 **A Novel Liquid Argon Time Projection**
2 **Chamber Detector: The ArgonCube**
3 **Concept**

4 **Inauguraldissertation**
5 der Philosophisch-naturwissenschaftlichen Fakultät
6 der Universität Bern

7 vorgelegt von

8 **Damian Goeldi**

9 von Sennwald SG

10 Leiter der Arbeit

11 **Prof. Dr. A. Ereditato**

12 Albert Einstein Center for Fundamental Physics
13 Laboratory for High Energy Physics
14 Physics Institute

1 **A Novel Liquid Argon Time Projection**
2 **Chamber Detector: The ArgonCube**
3 **Concept**

4 **Inauguraldissertation**

5 der Philosophisch-naturwissenschaftlichen Fakultät⁵
6 der Universität Bern⁶

7 vorgelegt von⁷

8 **Damian Goeldi**

9 von Sennwald SG⁹

10 Leiter der Arbeit

11 **Prof. Dr. A. Ereditato**

12 Albert Einstein Center for Fundamental Physics
13 Laboratory for High Energy Physics
14 Physics Institute

¹ Von der Philosophisch-naturwissenschaftlichen Fakultät angenommen.

Bern, (Prüfungsdatum)

²

Der Dekan:

Prof. Dr. (Initiale Name)

¹ To Bäschu.

² It was always inspiring and great fun conducting research with you.

Abstract

2 Neutrino mixing and oscillations have been extensively studied during the last few
3 decades. Nevertheless, several unanswered questions remain, in particular CP violation
4 in the lepton sector and the ordering of the neutrino masses. A next-generation
5 Deep Underground Neutrino Experiment (DUNE) is being built to answer them
6 via observation of long-baseline neutrino oscillations. Liquid Argon Time Projection
7 Chambers (LArTPCs) were chosen as Far Detectors (FDs). In addition, a LArTPC
8 component in the Near Detector (ND) complex is necessary. Even though, the high-rate
9 ND environment poses significant challenges to traditional LArTPC designs. Their wire
10 charge readout reduces the excellent 3D tracking capabilities of a LArTPC to a number
11 of 2D projections. In addition, LArTPCs are comparatively slow detectors due to the
12 finite charge drift velocity ($\sim 1 \text{ mm } \mu\text{s}^{-1}$). A number of improvements are presented
13 in this thesis. To overcome limitations, a pixelated charge readout for LArTPCs was
14 developed and successfully tested. A software framework was established to reconstruct
15 recorded cosmic muon tracks employing a Kalman filter. Pixelated charge readout
16 systems represent the single largest advancement in the sensitivity of LArTPCs, enabling
17 true 3D tracking, thereby reducing event pile-up and improving background rejection.
18 The large volumes required by the DUNE LArTPCs result in longer drift distances and
19 thus require higher drift voltages. A method was developed to operate LArTPCs at
20 electric fields an order of magnitude higher than before. It was found however that it
21 is reasonable to keep fields below 40 kV cm^{-1} at all points in the detector to guarantee
22 a safe operation. The presented R&D is aimed towards the development of a new
23 fully-modular, pixelated LArTPC concept—ArgonCube. Splitting the detector volume
24 into small self-contained TPC sharing a common LAr bath, reduces the required drift
25 voltages to a handleable level. A pixelated charge readout paired with new electronics

¹ will exploit true 3D tracking to cope with the expected event pile-up. It was found that
² the impact of pile-up on the reconstructed neutrino energy in ArgonCube has a mean
³ between 2 % and 3 %, and is below 0.1 % for more than 50 % of the neutrino events. At
⁴ the time of writing, ArgonCube is the top candidate for the LAr component in the DUNE
⁵ ND complex.

¹ Preface

² preface

³ Chapter 2 will give an overview of the history of neutrino detectors, describe the
⁴ current state of the field and then introduce the most relevant physics. Giunti and Kim
⁵ provide a more detailed history of neutrino physics. [1]

⁶ The work in Chapter 6 was a collaboration with the neutrino group at LBNL. In
⁷ particular, they provided the simulation tool, Argon Box, as well as the raw simulation
⁸ data. The π^0 pile-up study was done by the author with advice from C. Marshall from
⁹ LBNL.

¹ Todo list

2	■ preface	viii
3	■ Check preamble	1
4	■ Replace backslash space after commands by braces	1
5	■ Optimise float placement, short captions for lists of floats	1
6	■ Dean, Date	1
7	■ Add Ref./Reference in front of citations?	1
8	■ Check/redo all plots	1
9	■ test	1
10	■ inline test	1
11	■ remove octant or explain	27
12	■ sauce	32
13	■ LAr specs	48
14	■ check dimensions	78
15	■ sauce	82
16	■ sauce	102
17	■ sauce	102
18	■ better, more recent picture	129
19	■ Is this still valid?	138
20	■ justify!	147

0. Preface

1	■ acknowledgements	173
---	------------------------------	-----

Contents

1	1. Introduction	2
3	2. Neutrinos and their Detection	9
4	2.1. History	9
5	2.2. Neutrino Oscillation	17
6	2.3. DUNE	22
7	2.4. Neutrino Interaction with Matter	27
8	2.5. Final State Detection	33
9	3. The Liquid Argon Time Projection Chamber	43
10	3.1. Liquid Argon as a Detection Medium	44
11	3.2. Electric Field Generation	48
12	3.3. Charge Readout	49
13	3.4. Light Readout	49
14	3.5. Charge Readout Electronics	50
15	3.6. Challenges of Future Detectors	51
16	4. Experimental Studies on High Voltage, Charge Readout, and Light Collection	54
17	4.1. High Voltage	54
18	4.2. Charge Readout	77

Contents

¹	4.3. Charge Readout Electronics	84
²	4.4. Light Collection	101
³	5. A Novel Implementation of the LArTPC Technology	109
⁴	5.1. First Results from the ArgonCube Pixel Demonstrator	109
⁵	5.2. PixLAr	126
⁶	5.3. The ArgonCube Approach	128
⁷	6. Towards the DUNE Near Detector	135
⁸	6.1. ArgonCube in the DUNE Near Detector	135
⁹	6.2. Feasibility Study of a Pixelated LArTPC for the DUNE Near Detector .	142
¹⁰	7. Conclusion	170
¹¹	Acknowledgements	173
¹²	Bibliography	174
¹³	A. DUNE ND Event Pile-up Study Data	189
¹⁴	A.1. 2 MW Beam at 80 GeV Proton Energy	189
¹⁵	A.2. 2 MW Beam at 80 GeV Proton Energy, XZ Projection	201
¹⁶	A.3. 10 MW Beam at 80 GeV Proton Energy	215

List of Figures

2	2.1. Neutrino mass ordering	22
3	2.2. DUNE	23
4	2.3. DUNE neutrino fluxes.	25
5	2.4. Neutrino oscillation probabilities.	26
6	2.5. DUNE δ_{CP} sensitivity	27
7	2.6. Neutrino electron scattering	30
8	2.7. Antineutrino electron scattering	30
9	2.8. Neutrino interaction cross-section	32
10	2.9. Stopping power	34
11	3.1. LAr recombination measurements	46
12	4.1. HV test setup	55
13	4.2. HV test field map	56
14	4.3. HV test schematic	57
15	4.4. HV test high-speed footage	59
16	4.5. HV test current-voltage characteristics	61
17	4.6. HV test streamer image	62
18	4.7. HV test breakdown field versus stressed cathode area	64
19	4.8. HV test field emission and streamer spectra	65
20	4.9. HV test electro-luminescence brightness	72

List of Figures

1	4.10. HV test spark spectrum	73
2	4.11. HV test integrated charge versus breakdown voltage	74
3	4.12. HV test peak current versus maximum breakdown field	75
4	4.13. HV test plateau current versus maximum breakdown field	75
5	4.14. HV test plateau current versus peak current	76
6	4.15. HV test minimum streamer velocity versus maximum breakdown field . .	76
7	4.16. Copper on Kapton readout plane	78
8	4.17. Copper on Kapton test TPC	79
9	4.18. Copper on Kapton test muon event	80
10	4.19. Differential signalling	87
11	4.20. ARGONTUBE readout chain	89
12	4.21. Event from first pixel demonstrator measurement campaign	96
13	4.22. Noise distributions from first pixel demonstrator measurement campaign	97
14	4.23. Event from second pixel demonstrator measurement campaign	98
15	4.24. Noise distributions from second pixel demonstrator measurement campaign	99
16	4.25. Linearity measurement of BNL cryogenic ADC ASICs	100
17	4.26. 10 cm × 10 cm ArCLight prototype	104
18	4.27. ArCLight light collector cross-section	105
19	4.28. Measured ArCLight PDE	107
20	4.29. PixLAr ArCLight response stability	108
21	5.1. Pixel demonstrator readout plane	110
22	5.2. Pixel demonstrator bias circuit	111
23	5.3. Pixel demonstrator charge readout transparency	112
24	5.4. Engineering drawing of pixel demonstrator TPC	113
25	5.5. Pixel demonstrator close-up	114
26	5.6. Unfiltered raw data of typical pixel demonstrator event	121

List of Figures

1	5.7. Filtered data of typical pixel demonstrator event	122
2	5.8. Pulse shapes of typical pixel demonstrator event	123
3	5.9. Reconstructed 3D hits of typical pixel demonstrator event	124
4	5.10. Kalman-fitted track of typical pixel demonstrator event	125
5	5.11. PixLAr half plane with attached ArCLight module	126
6	5.12. PixLAr beam event	127
7	5.13. ArgonCube module schematic	129
8	5.14. ArgonCube module insertion and extraction	131
9	6.1. ArgonCube 2×2 prototype module dimensions	136
10	6.2. ArgonCube 2×2 prototype module engineering drawing	137
11	6.3. ArgonCube DUNE ND hadron containment	140
12	6.4. ArgonCube DUNE ND artistic view	141
13	6.5. Average current collected for one spill as a function of time	143
14	6.6. Pile-up study example event	146
15	6.7. Pile-up study example event zoom	156
16	6.8. Pile-up study missed fractional vs. true photon energy, 2 MW beam . . .	157
17	6.9. Pile-up study mean missed fractional vs. true photon energy, 2 MW beam	157
18	6.10. Pile-up study photon vs. missed energy fraction, 2 MW beam	158
19	6.11. Pile-up study mean missed vs. true photon energy, 2 MW beam	158
20	6.12. Pile-up study mean misidentified vs. true neutrino energy, 2 MW beam . .	159
21	6.13. Pile-up study mean misidentified fractional vs. true neutrino energy, 2 MW beam	160
22	6.14. Pile-up study neutrino vs. misidentified energy fraction, 2 MW beam . . .	161
23	6.15. Pile-up study mean missed fractional vs. true photon energy, 2 MW beam, XZ projection	162

List of Figures

1	6.16. Pile-up study mean misidentified vs. true neutrino energy, 2 MW beam, XZ projection	163
2		
3	6.17. Pile-up study mean misidentified fractional vs. true neutrino energy, 2 MW beam, XZ projection	164
4		
5	6.18. Pile-up study neutrino vs. misidentified energy fraction, 2 MW beam, XZ projection	165
6		
7	6.19. Pile-up study mean missed fractional vs. true photon energy, 10 MW beam	166
8		
9	6.20. Pile-up study mean misidentified vs. true neutrino energy, 10 MW beam .	167
10		
11	6.21. Pile-up study mean misidentified fractional vs. true neutrino energy, 10 MW beam	168
12		
13	6.22. Pile-up study neutrino vs. misidentified energy fraction, 10 MW beam .	169
14		
15	A.1. Pile-up study missed vs. true photon energy, 2 MW beam	189
16		
17	A.2. Pile-up study mean missed vs. true photon energy, 2 MW beam	190
18		
19	A.3. Pile-up study missed fractional vs. true photon energy, 2 MW beam . . .	190
20		
21	A.4. Pile-up study mean missed fractional vs. true photon energy, 2 MW beam	191
22		
23	A.5. Pile-up study photon vs. missed energy fraction, 2 MW beam	191
24		
25	A.6. Pile-up study misidentified vs. true neutrino energy, 2 MW beam	192
26		
27	A.7. Pile-up study misidentified vs. true neutrino energy, no muons, 2 MW beam	193
28		
29	A.8. Pile-up study misidentified vs. true neutrino energy, only neutrals, 2 MW beam	194
30		
31	A.9. Pile-up study mean misidentified vs. true neutrino energy, 2 MW beam .	195
32		
33	A.10. Pile-up study misidentified fractional vs. true neutrino energy, 2 MW beam	196
34		
35	A.11. Pile-up study misidentified fractional vs. true neutrino energy, no muons, 2 MW beam	197
36		
37	A.12. Pile-up study misidentified fractional vs. true neutrino energy, only neutrals, 2 MW beam	198
38		

List of Figures

1	A.13.Pile-up study mean misidentified fractional vs. true neutrino energy, 2 MW beam	199
2	A.14.Pile-up study neutrino vs. misidentified energy fraction, 2 MW beam . . .	200
3	A.15.Pile-up study missed vs. true photon energy, 2 MW beam, XZ projection	201
4	A.16.Pile-up study mean missed vs. true photon energy, 2 MW beam, XZ projection	202
5	A.17.Pile-up study missed fractional vs. true photon energy, 2 MW beam, XZ projection	203
6	A.18.Pile-up study mean missed fractional vs. true photon energy, 2 MW beam, XZ projection	204
7	A.19.Pile-up study photon vs. missed energy fraction, 2 MW beam, XZ projection	205
8	A.20.Pile-up study misidentified vs. true neutrino energy, 2 MW beam, XZ projection	206
9	A.21.Pile-up study misidentified vs. true neutrino energy, no muons, 2 MW beam, XZ projection	207
10	A.22.Pile-up study misidentified vs. true neutrino energy, only neutrals, 2 MW beam, XZ projection	208
11	A.23.Pile-up study mean misidentified vs. true neutrino energy, 2 MW beam, XZ projection	209
12	A.24.Pile-up study misidentified fractional vs. true neutrino energy, 2 MW beam, XZ projection	210
13	A.25.Pile-up study misidentified fractional vs. true neutrino energy, no muons, 2 MW beam, XZ projection	211
14	A.26.Pile-up study misidentified fractional vs. true neutrino energy, only neutrals, 2 MW beam, XZ projection	212

List of Figures

1	A.27.Pile-up study mean misidentified fractional vs. true neutrino energy, 2 MW beam, XZ projection	213
2		
3	A.28.Pile-up study neutrino vs. misidentified energy fraction, 2 MW beam, XZ projection	214
4		
5	A.29.Pile-up study missed vs. true photon energy, 10 MW beam	215
6		
7	A.30.Pile-up study mean missed vs. true photon energy, 10 MW beam	216
8		
9	A.31.Pile-up study missed fractional vs. true photon energy, 10 MW beam . . .	216
10		
11	A.32.Pile-up study mean missed fractional vs. true photon energy, 10 MW beam . .	217
12		
13	A.33.Pile-up study photon vs. missed energy fraction, 10 MW beam	217
14		
15	A.34.Pile-up study misidentified vs. true neutrino energy, 10 MW beam	218
16		
17	A.35.Pile-up study misidentified vs. true neutrino energy, no muons, 10 MW beam	219
18		
19	A.36.Pile-up study misidentified vs. true neutrino energy, only neutrals, 10 MW beam	220
20		
21	A.37.Pile-up study mean misidentified vs. true neutrino energy, 10 MW beam .	221
22		
23	A.38.Pile-up study misidentified fractional vs. true neutrino energy, 10 MW beam .	222
24		
25	A.39.Pile-up study misidentified fractional vs. true neutrino energy, no muons, 10 MW beam	223
26		
27	A.40.Pile-up study misidentified fractional vs. true neutrino energy, only neutrals, 10 MW beam	224
28		
29	A.41.Pile-up study mean misidentified fractional vs. true neutrino energy, 10 MW beam	225
30		
31	A.42.Pile-up study neutrino vs. misidentified energy fraction, 10 MW beam . .	226
32		

List of Tables

2	2.1. Neutrino oscillation parameters	21
3	2.2. DUNE beam parameters and ND rates	24
4	2.3. DUNE ND event rates	28
5	3.1. LAr properties	44
6	4.1. HV test circuit parameters	58
7	4.2. HV test summary	60
8	4.3. HV coating test summary	70
9	5.1. Pixel demonstrator SNR	116
10	6.1. ArgonCube 2×2 prototype and DUNE ND dimensions	139
11	6.2. DUNE ND pile-up simulation parameters	145

¹ Listings

¹ Acronyms

² **1D** 1-Dimensional. 4, 5, 82

³ **2D** 2-Dimensional. vi, 3–5, 43, 49, 52, 80, 152–154, 162–165, 170, 201–214

⁴ **3D** 3-Dimensional. vi, vii, 3–5, 7, 18, 49, 52, 80, 117–119, 124, 133, 147, 155, 171, 172

⁵ **AC** Alternating Current. 94

⁶ **ADC** Analogue-to-Digital Converter. 92–94, 100

⁷ **AGS** Alternating Gradient Synchrotron. 10

⁸ **ARAPUCA** Argon R&D Advanced Program at UniCamp. 103, 104, 106, 127

⁹ **ArCLight** ArgonCube Light readout system. 6, 7, 101, 103–108, 126, 127, 133, 134, 138,
¹⁰ 142, 172

¹¹ **ArgonNeuT** Argon Neutrino Test. 116, 126

¹² **ASIC** Application-Specific Integrated Circuit. 88, 93, 94, 100

¹³ **BNL** Brookhaven National Laboratory. 10, 88, 92–95, 100

¹⁴ **CC** Charged Current. 27, 28, 30–32

¹⁵ **CCD** Charge-Coupled Device. 16

Acronyms

- ¹ **COH** Coherent. 28, 29, 145
- ² **CP** Charge conjugation Parity. vi, 2, 3, 18, 24, 27
- ³ **CRT** Cosmic Ray Tagger. 101, 102, 113
- ⁴ **DAQ** Data Acquisition. 49, 79, 81–83, 90, 103
- ⁵ **DIS** Deep Inelastic Scattering. 28, 29
- ⁶ **DONUT** Direct Observation of the Nu Tau. 16, 17
- ⁷ **DUNE** Deep Underground Neutrino Experiment. vi, vii, 3–8, 17, 22–25, 27, 28, 30, 52,
⁸ 92, 94, 95, 132, 135, 139–145, 149, 155, 170–172
- ⁹ **EM** ElectroMagnetic. 7, 8, 23, 40–42, 44, 88, 142, 145, 146, 148, 149, 154–169, 189–226
- ¹⁰ **FD** Far Detector. vi, 4, 5, 22, 24, 25, 92, 94, 95, 155, 170
- ¹¹ **FEB** Front-End Board. 101, 102
- ¹² **FEM** Finite Element Method. 55
- ¹³ **FIFO** First In First Out. 95
- ¹⁴ **FNAL** Fermi National Accelerator Laboratory. 16, 22, 23, 64, 106, 108, 126, 138, 140
- ¹⁵ **FR4** Flame Retardant 4. 77
- ¹⁶ **GENFIT** Generic track-Fitting toolkit. 119, 171
- ¹⁷ **GPU** Graphics Processing Unit. 16
- ¹⁸ **HV** High Voltage. 5, 6, 11, 48, 51, 52, 54–57, 59, 69, 111, 114, 128, 130, 137, 141
- ¹⁹ **I²C** Inter-Integrated Circuit. 88, 89

Acronyms

- ¹ **IC** Integrated Circuit. 51
- ² **ICARUS** Imaging Cosmic And Rare Underground Signals. 116
- ³ **IMB** Irvine-Michigan-Brookhaven. 13
- ⁴ **KamiokaNDE** Kamioka Nucleon Decay Experiment. 13, 15, 17
- ⁵ **KamLAND** Kamioka Liquid scintillation AntiNeutrino Detector. 17
- ⁶ **LAr** Liquid Argon. vi, vii, 3–7, 17, 25, 43, 44, 47, 48, 50, 52, 54, 59, 62, 64, 65, 69–71,
⁷ 85, 92, 94, 95, 101–103, 105, 106, 112–114, 119, 125, 126, 128–130, 132, 136, 137,
⁸ 140–142, 145–149, 170–172
- ⁹ **LArIAT** Liquid Argon In A Testbeam. 90, 126, 127
- ¹⁰ **LArPix** Liquid Argon Pixel readout ASIC. 92, 94, 95, 142, 147, 155, 171
- ¹¹ **LArTPC** Liquid Argon Time Projection Chamber. vi, 3–8, 22, 25, 33, 45–52, 69, 71, 77,
¹² 80, 83, 84, 92, 94, 95, 101, 106, 109, 126, 128, 130–132, 135, 140, 142, 144, 147, 150,
¹³ 170–172
- ¹⁴ **LBNL** Lawrence Berkeley National Laboratory. viii, 92, 94, 95, 138, 146, 171
- ¹⁵ **LHEP** Laboratory for High Energy Physics at the University of Bern. 5–7, 45, 47, 48,
¹⁶ 54, 63, 64, 77, 82, 88, 101, 103, 113, 114, 116, 126–128, 130, 135–139, 141, 170, 171
- ¹⁷ **MCS** Multiple Coulomb Scattering. 37, 119, 125, 148, 153
- ¹⁸ **MEC** Meson Exchange Current. 31, 32
- ¹⁹ **MicroBooNE** Micro Booster Neutrino Experiment. 54, 88, 94, 101, 113, 147
- ²⁰ **MicroMeGaS** Micro-Mesh Gaseous Structure. 82, 83

Acronyms

- ¹ **MIP** Minimum Ionising Particle. 35, 37, 50, 84, 115–117, 121–123
- ² **MSW** Mikheyev-Smirnov-Wolfenstein. 21, 24, 26, 30
- ³ **MWPC** Multi-Wire Proportional Chamber. 43
- ⁴ **NC** Neutral Current. 27–30, 32
- ⁵ **ND** Near Detector. vi, vii, 4–8, 17, 24, 25, 28, 30, 52, 92–95, 132, 133, 135, 138–142,
⁶ 144, 146, 147, 149, 150, 154, 155, 170–172
- ⁷ **NIM** Nuclear Instrumentation Module. 86, 89
- ⁸ **PAI** PolyAmide-Imide. 112
- ⁹ **PCA** Principal Component Analysis. 118, 119, 124, 125, 171
- ¹⁰ **PCB** Printed Circuit Board. 77, 83, 84, 90, 91, 104, 105, 109–111, 127, 129, 131, 134,
¹¹ 171
- ¹² **PDE** Photon Detection Efficiency. 105–107
- ¹³ **PEEK** PolyEther Ether Ketone. 112
- ¹⁴ **PET-C** Crystalline PolyEthylene Terephthalate. 55, 114
- ¹⁵ **PMNS** Pontecorvo-Maki-Nakagawa-Sakata. 18
- ¹⁶ **PMT** PhotoMultiplier Tube. 6, 10, 11, 13, 14, 49, 50, 79, 101, 105, 106, 133
- ¹⁷ **POT** Protons On Target. 24, 28, 148
- ¹⁸ **PSU** Power Supply Unit. 55–57, 68
- ¹⁹ **QE** Quasi-Elastic. 28, 31, 32

Acronyms

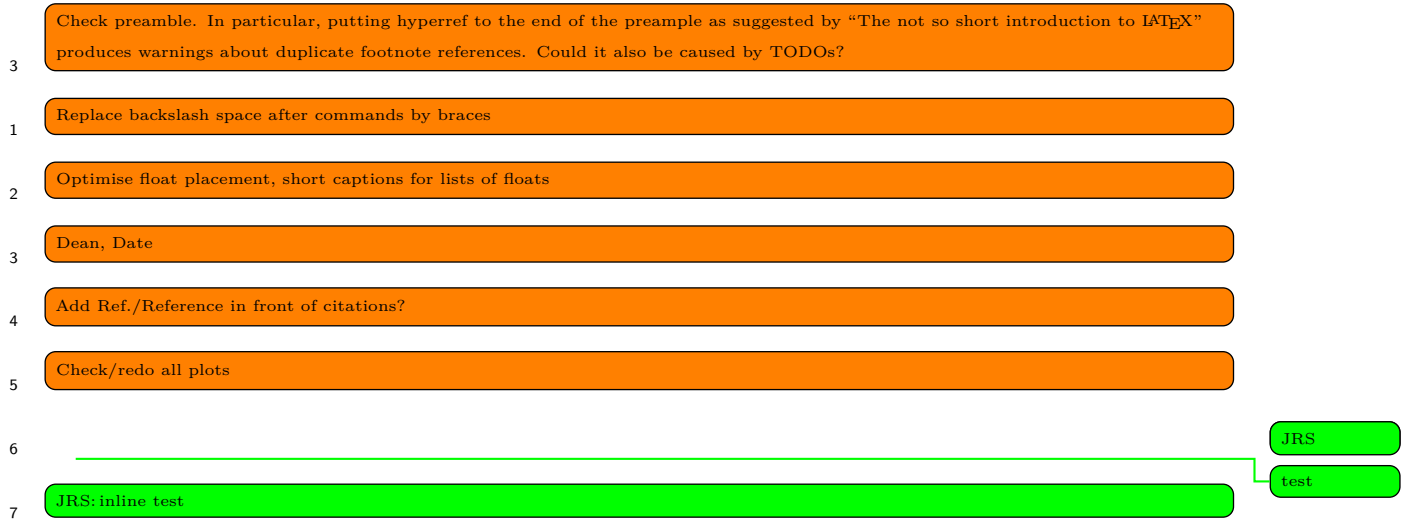
- ¹ **RC** Resistor Capacitor. 115
- ² **RES** Resonant. 28–30, 32, 144
- ³ **RGB** Red Green Blue. 58
- ⁴ **RMS** Root Mean Square. 37
- ⁵ **ROI** Region Of Interest. 81–83, 91, 96–99, 111, 115–118, 121–123, 127
- ⁶ **SBND** Short Baseline Neutrino Detector. 101, 113
- ⁷ **SiPM** Silicon PhotoMultiplier. 6, 101–106, 112–114, 134, 138, 171
- ⁸ **SM** Standard Model. 2
- ⁹ **SNO** Sudbury Neutrino Observatory. 11, 15–17
- ¹⁰ **SNR** Signal-To-Noise Ratio. 79, 84, 115–117, 128, 171
- ¹¹ **SSM** Standard Solar Model. 11, 16
- ¹² **SURF** Sanford Underground Research Facility. 22
- ¹³ **T2K** Tokai To Kamioka. 17
- ¹⁴ **TPB** TetraPhenyl Butadiene. 50, 102, 103, 105, 112, 114
- ¹⁵ **TPC** Time Projection Chamber. vi, 4, 5, 7, 43, 44, 46, 55, 77, 79, 82–84, 92, 95, 101,
- ¹⁶ 102, 111–114, 125–128, 130, 133, 135–139, 143, 144, 147, 171, 172
- ¹⁷ **TTL** Transistor-Transistor-Logic. 58
- ¹⁸ **UV** UltraViolet. 3, 12, 50
- ¹⁹ **VME** VERSAmodule Eurocard. 89

Acronyms

¹ **VUV** Vacuum UltraViolet. 104, 105

² **WLS** WaveLength Shifter. 6, 50, 101–105, 112–114

Acronyms



1. Introduction

¹ The Standard Model (SM) of particle physics has proven to be remarkably precise in its
² predictions over the last decades. However, there are still some missing pieces, namely the
³ intriguing nature of neutrinos. Not only do their mass eigenstates mix with their flavour
⁴ eigenstates but also are their masses smaller than the charged leptons by several orders
⁵ of magnitude. Measuring these effects is not simplified by the fact that the interaction
⁶ rates (cross-section) of neutrinos are extremely small, raising the need for high-intensity
⁷ sources along with extremely massive detectors. This is the reason why it took almost
⁸ 25 years from their proposal to the first measurement of neutrinos. As of today, neutrino
⁹ mixing is well-established and their masses have been proven to be non-zero. The basis
¹⁰ for this was the discovery of neutrino oscillations, a consequence of neutrino flavour
¹¹ mixing paired with non-zero masses. However, there are still several unknowns in today's
¹² neutrino mixing and oscillation model. In particular, the model contains three Charge
¹³ conjugation Parity (CP) violation phases that have yet to be measured. The consequences
¹⁴ of measuring CP violation in neutrino oscillation could be far-reaching. Via certain
¹⁵ cosmological models, it could explain the asymmetry between matter and antimatter in
¹⁶ the universe. Besides, while it is certain that at least two out of the three neutrinos have
¹⁷ non-zero masses, their ordering is still unknown. Its determination will help to integrate
¹⁸ massive neutrinos into the SM where they are currently massless.

¹⁹ Measuring the unknown parameters of the neutrino mixing and oscillation model will
²⁰ require a neutrino interaction sample of unprecedented size. Much of today's knowledge

1. Introduction

21 was gained from neutrinos produced in the Sun and the Earth's atmosphere. However,
1 for future experiments, these and other natural sources are not intense and/or precise
2 enough for the required measurements. Therefore, artificially produced neutrino beams
3 will be employed, paired with huge detectors. Not only are neutrino interactions with
4 matter very rare, they are also quite manifold, giving raise to the need for detectors
5 capable of recording complex event topologies and reconstructing energies precisely.

6 Liquid Argon Time Projection Chambers (LArTPCs) are prime candidates for the
7 aforementioned requirements. They combine a high-density target material with high-
8 precision 3-Dimensional (3D) tracking and calorimetric capabilities. The incoming
9 neutrinos interact with the Liquid Argon (LAr), producing charged secondary particles
10 which in turn ionise argon atoms. By means of an electric field, the produced electron-ion
11 pairs can be separated and drifted towards a 2-Dimensional (2D) charge readout. A
12 small remainder of pairs recombine and produce very prompt (ns) UltraViolet (UV)
13 scintillation light which can be used to determine the propagation time of the charge
14 drifted towards the readout plane. Due to the constant drift velocity of charge in a
15 medium subject to an electric field, the distance from the ionisation location to the
16 readout plane can be precisely determined. Combined with the 2D information from the
17 readout, the full 3D interaction topology can be reconstructed.

18 The Deep Underground Neutrino Experiment (DUNE) is a next generation long-baseline
19 beam neutrino oscillation experiment, placing LArTPCs in an accelerator-produced muon
20 neutrino beam. Neutrino oscillations will be observed over a baseline of 1300 km. Several
21 implications result from the required number of neutrino interactions to be sensitive to
22 CP violation and neutrino mass ordering. As mentioned above, a very intense neutrino
23 beam and a large target mass are necessary. However, this is not enough; at the same
24 time, uncertainties have to be kept low. Statistical uncertainties can be lowered by
25 acquiring more neutrino interactions but this is not true for systematic uncertainties

1. Introduction

which will therefore become the limiting factor. Systematic uncertainties have various sources, some of which can be exploited. Two of the biggest contributors are the neutrino beam and the interaction model of neutrinos with matter. Beam-related uncertainties can be eliminated partially by characterising the neutrino beam at the production location (in addition to replica target experiments). A *Near Detector (ND)* will be placed in front of the beam facility in addition to the *Far Detector (FD)* at the end of the baseline. Many uncertainties cancel out by comparing the neutrino fluxes in the near and FD. To some extent, uncertainties related to the interaction model cancel out as well if the same target material is used in both detectors. Finally, using the same technology in both detectors, cancels even more of the remaining uncertainties. Therefore, the ND complex needs to contain a LArTPC component.

Up until now, LArTPC charge readouts have been realised by means of multiple 1-Dimensional (1D) wire planes—the last of them collecting the charge while the previous ones register the induced voltage pulse by the passing charge—due to technological limitations. Combined with the time of the drifting charge, this results in one 2D image of the event topology per wire plane, effectively reducing the 3D capabilities of the Time Projection Chamber (TPC) to multiple 2D projections. Additionally, LArTPCs are comparatively slow detectors. The minimum drift time of charge in LAr (and thus the readout time) is limited to $\sim 1 \text{ ms m}^{-1}$ by constraints on the maximum cathode voltage. Both the above have not prevented the huge success of LArTPCs up to now. Due to the low interaction cross-section, event rates in current-generation LArTPCs have been low enough to cope with. While this still applies to the DUNE FD, it is certainly not true for the ND. The high-intensity neutrino beam will result in event rates in the ND significantly higher than what contemporary LArTPCs have been exposed to. Even worse, the beam is delivered in very short pulses (spills) of very high intensity. Because these spills are one to two orders of magnitude shorter than a typical LArTPC readout

1. Introduction

cycle, the detector registers several neutrino interactions simultaneously, so-called event pile-up. Combined with the 2D projection readout, this leads to significant difficulties in event reconstruction: disentangling the 3D interaction topologies from the recorded 2D projections.

An obvious solution to this challenge is to regain true 3D information from the TPC by replacing the projective 1D wire planes with a true 2D pixelated charge readout. However, as mentioned above, this is linked to technological challenges. Replacing a two plane wire readout with pixels of the same pitch squares the number of required readout channels. For the LArTPC in the DUNE ND complex with a size of $4\text{ m} \times 5\text{ m} \times 2.5\text{ m}$, this amounts to $\sim 10^6$ cables needing to be routed out of the cryogenic vessel housing the detector. The number of cable feedthroughs can be reduced by digitising charge readout waveforms inside the LAr and using high-speed digital links to aggregate many readout channels on a single cable. However, this is far from trivial. Besides the challenge of adapting existing electronics to the cryogenic temperatures of LAr, heat production has to be kept to a minimum to prevent the LAr from boiling. While such electronics have already been designed for the wire-equipped FDs, the former are not suitable for a pixelated ND due to their power dissipation.

In addition to these readout issues, future large LArTPCs face several other challenges. In particular for the High Voltage (HV) and light readout systems. Earlier studies by the Laboratory for High Energy Physics at the University of Bern (LHEP) showed that the dielectric strength of LAr is much lower than predicted by studies performed in the fifties. [2–4] Again, this could be tolerated in contemporary detectors but will become a serious problem for future experiments. Electronegative impurities present in the LAr result in a finite charge lifetime. This results in a lower limit on the required drift field and therefore cathode voltage. Due to the finite dielectric strength of LAr, the fraction of dead volume required around the cathode scales with detector size unless this

1. Introduction

26 is accounted for by a modified HV system of the detector.

1 In order to get proper timing for the third coordinate, the scintillation light flashes
2 need to be matched to the correct events. This becomes problematic in large monolithic
3 LArTPC in high-pile-up environments.

4 The goal of this work is to establish the key technologies enabling the successful
5 deployment of a LArTPC component in the DUNE ND complex. A introduction to the
6 history and theory of neutrino detection, as well as an overview of DUNE are given in
7 Chapter 2.

8 Chapter 4 contains several studies addressing the challenges met by future LArTPCs.
9 These include a thorough investigation of dielectric breakdowns in LAr, the development
10 of new charge and light readout methods, as well as the evaluation of electronics for
11 pixelated charge readouts.

12 The HV studies include high-speed footage, current-voltage characteristics and
13 spectrometry of the breakdowns. As a result, a hypothesis was developed providing a
14 conclusive explanation of the phenomenon. In addition, a technique was developed to
15 increase the dielectric strength of LAr by an order of magnitude by means of a polymer
16 coating. However, the latter is not suitable for physics experiments as it fails to withstand
17 multiple thermal cycles and loses its protection after a breakdown. A new light readout
18 based on Silicon PhotoMultipliers (SiPMs), ArgonCube Light readout system (ArCLight),
19 developed by LHEP was tested as well. The active area of the SiPMs is drastically
20 increased by coupling them to a light trap formed of a combination of a dichroic filter
21 with a WaveLength Shifter (WLS). This makes it competitive to classical PhotoMultiplier
22 Tubes (PMTs) for large area coverage while requiring a much reduced dead volume.

23 The main contribution to the DUNE ND complex is the demonstration of a pixelated
24 LArTPC. Conventional room-temperature digitisers were combined with analogue
25 multiplexing due to the as yet lacking cryogenic electronics. Several days of cosmic

1. Introduction

26 muon data were collected with a test stand designed and built at LHEP. A software
1 framework was written to reconstruct 3D tracks from the data. Even though the
2 employed pixelated readout yields 3D information on charge deposition in the LArTPC,
3 the necessary analogue multiplexing introduced a certain amount of ambiguity. The latter
4 had to be resolved by the reconstruction algorithm. Finally, the unambiguous positional
5 information was fed to a Kalman filter. This propagates a cosmic muon hypothesis
6 through all the detector measurements taking into account the various involved charge
7 deposition mechanisms in LAr. The end result is a completely reconstructed particle
8 track through the detector. The combination of all the R&D presented in this thesis
9 resulted in the development of the ArgonCube, a next-generation LArTPC concept, at
10 LHEP. It aims to address the most important challenges met by future LArTPCs. The
11 problematic high fields at the cathodes as well as the scintillation light containment issue
12 are addressed by splitting up the detector into smaller ($\sim 1\text{ m}$), self-contained TPCs
13 sharing a common LAr bath. A pixelated charge readout makes the detector capable of
14 true 3D event recording. To keep the dead volume to a minimum, ArCLight is used as
15 the light readout system. All of this is described in Chapters 5.

16 Chapter 6 introduces the proposed ArgonCube LArTPC component for the DUNE
17 ND complex together with a feasibility study of a LArTPC in such an environment.
18 Combining the knowledge gained from Chapter 5 with the next-generation pixel electronics
19 briefly described in Chapter 4, enables the realisation of a true 3D LArTPC. However, it
20 remains to be shown that such a detector is actually able to cope with the event rates
21 expected in the ND. To assess this capability, a metric was needed representative of the
22 physics processes. ElectroMagnetic (EM) showers produced from the photons originating
23 from π^0 decays are notoriously complex to reconstruct. On the other hand, it is important
24 to get their energy reconstruction right in order not to skew the neutrino energy spectrum
25 because they are present in a significant fraction of the neutrino interaction expected in

1. Introduction

²⁶ DUNE. At the DUNE energies, EM showers deposit a plethora of apparently unconnected
¹ charge clusters in a LArTPC rather than a homogeneous cone. Associating all those
² separate charge blobs to the correct event is one of the most difficult reconstruction tasks,
³ even for a LArTPC. Therefore, this type of EM shower was chosen for this study. A
⁴ rather rudimentary algorithm was employed to assign the deposited charge to the correct
⁵ EM shower because all available LArTPC reconstruction algorithms are optimised for
⁶ wire readouts. The amount of misidentified charge from other events is a suitable metric
⁷ to assess the impact of pile-up on the ND physics.

⁸ Chapter 7 concludes the thesis.

2. Neutrinos and their Detection

¹ Neutrino physics has seen massive progress from first detection 60 years ago to planned
² billion dollar experiments in the near future. This chapter will give an overview of the
³ history of neutrino detectors, describe the current state of the field and then introduce
⁴ the most relevant physics.

2.1. History

⁶ In 1914, Chadwick proved that the energy spectrum of the β -decay was continuous. [5]
⁷ As an explanation for this, Wolfgang Pauli in 1930 proposed a new neutral, weakly
⁸ interacting fermion to the *Radioactive Ladies and Gentlemen* [6] which he called the
⁹ *neutron*. However, the same Chadwick in 1932 discovered the particle we today call
¹⁰ neutron. [7] Upon this, Fermi proposed the name *neutrino* and a little later came up
¹¹ with a new theory for β -decay. [8]

It took almost another quarter of a century until the neutrino was experimentally detected for the first time by Reines and Cowan in 1956. [9] They built a detector for the reaction

$$\bar{\nu}_e p \rightarrow e^+ n \quad (2.1)$$

¹² and put it next to a nuclear reactor on the Savannah River Site in South Carolina,

2. Neutrinos and their Detection

13 USA. It consisted of two water tanks sandwiched in between three liquid scintillator
1 tanks with PMTs on the sidewalls. The water was the target to induce the above
2 reaction while the scintillator tanks had the task of detecting the resulting positron
3 and neutron. A free positron slows down in matter and eventually gets captured by a
4 shell electron which produces two back-to-back photons with an energy of 511 keV each.
5 These produce scintillation light in the two adjacent tanks and thus can be detected
6 by forming a coincidence of the PMTs of the two tanks. Neutron detection is achieved
7 by doping the water target with cadmium which captures the free neutrons producing
8 multiple photons that can again be detected using the coincidence of the two adjacent
9 scintillator tanks. The neutron capture is much slower than the positron one. Therefore,
10 the process from Equation (2.1) produces a very distinct signal in the detector consisting
11 of a pulse with a lower amplitude from the positron capture and another one with a
12 higher amplitude from the neutron capture a few μs later. Backgrounds can be efficiently
13 rejected employing this technique. That drawback is that detection is limited to the $\bar{\nu}_e$
14 interaction in Equation (2.1).

In 1962, Lederman et al. proved the existence of the ν_μ at the Alternating Gradient Synchrotron (AGS) at Brookhaven National Laboratory (BNL) in New York, USA. [10] For the first time, they produced ν_μ using an accelerator. The protons from the AGS were guided onto a beryllium target producing pions which in turn decay according to

$$\pi^+ \rightarrow \mu^+ \nu_\mu \quad \text{and} \quad \pi^- \rightarrow \mu^- \bar{\nu}_\mu \quad (2.2)$$

15 producing a beam of muon (anti)neutrinos. *Spark chambers* were used to detect the
16 neutrinos. They were placed behind a 13.5 m wall of iron shielding used to stop the
17 muons and remaining hadrons from the beam.

18 A spark chamber consists of several parallel conducting plates immersed in a counting
19 gas, typically a mixture of helium and neon. Every other plate is connected to a pulsed

2. Neutrinos and their Detection

high-voltage power supply while the rest is grounded. At either end of the stack, triggering detectors (usually scintillators coupled to PMTs) are placed. When two coinciding signals from these are received, a high-voltage pulse is applied to the plates. If this happens fast enough ($\sim 10 \mu\text{s}$), a spark forms along the electric field lines where the counting gas has been ionised by the incident particle(s). The amplitude and the duration of the HV pulse need to be carefully tuned in order to reach the threshold of spark formation but to prevent random sparks on sharp edges and spacers etc. A gas amplification of 10^8 to 10^9 is required to achieve this. Furthermore, the rising edge of the HV pulse needs to be extremely short ($\sim 1 \text{ ns}$). If it was too long, it would drift the ionised track towards the electrodes before the field is high enough to initiate a discharge. Switching HV at this speed is not easy. Additionally, spark chambers have quite high dead times of $\sim 100 \text{ ms}$ which is needed for the ionisation charge to clear. A *clearing field* or an electronegative quenching gas additive can be used to speed up this process. [11]

In the 1960's, after Davis failed to measure the lepton-number-violating reaction



he decided to replace the $\bar{\nu}_e$ by solar ν_e . [12, 13] Surprisingly, they measured a flux approximately one third lower than predicted by the Standard Solar Model (SSM). This result became famous as the solar neutrino problem only to be resolved more than 30 years later by the Sudbury Neutrino Observatory (SNO). Davis' experiment was located 1478 m (4200 m water equivalent) underground in the Homestake Gold Mine in South Dakota, USA. The detector consisted of a tank filled with 615 t of tetrachloroethylene, C_2Cl_4 . As opposed to the two experiments above, this was a *radiochemical* detector which can only detect neutrino interactions offline. According to Equation (2.3), an incident neutrino converts one of the chlorine atoms in the detector into an unstable argon isotope. After exposure, the tank is purged by pumping helium gas through the

2. Neutrinos and their Detection

23 liquid which extracts the argon isotopes. In order for this to work, a certain amount
1 of ^{36}Ar is introduced into the tank as a carrier. Through a sophisticated system, the
2 argon is purified and finally, its ^{37}Ar content is measured in a *proportional counter*. By
3 counting the number of decaying argon isotopes and extrapolating using its half-life of 35
4 days, it is possible to calculate the number of neutrino interactions during the exposure.

5 A proportional counter is a container with two electrodes (usually a cylinder with a wire
6 in its centre) filled with a counting medium (usually gaseous). Incident charged particles
7 ionise the counting medium—neutral particles can be detected if they first produce
8 charged particles via interaction with matter in or surrounding the detector. If an electric
9 field is applied to the electrodes, the produced electron-ion pairs are separated and drift
10 towards the corresponding electrode. By reading out the current on the electrodes, one
11 can measure the amount of ionisation produced inside the detector. Usually, the anode
12 is read out because the drift velocity of electrons in an electric field is much higher than
13 the one of ions. If the ionisation charge is simply drifted towards the electrodes, the
14 detector is in fact an ionisation counter rather than a proportional counter. The problem
15 is that the charge produced by the ionisation is very low and the current detector needs
16 to be very sensitive. By increasing the voltage across the electrodes, the sensitivity can
17 be improved. If the field inside the counter is above a certain threshold, the drifting
18 ionisation electrons become energetic enough to ionise the counting medium themselves
19 and thus, start an avalanche and produce more charge. In the appropriate voltage range,
20 the produced charge is still proportional to the primary ionisation charge, thus the name
21 proportional counter. The voltage can be raised further to enter the Geiger regime
22 where the avalanches produce UV photons in addition to the ionisation. These UV
23 photons travel independently of the electric field and can start new avalanches via the
24 photoelectric effect. The process can only be stopped by quenching the discharge either
25 electrically (temporary voltage reduction) or chemically (quenching additive).

2. Neutrinos and their Detection

26 While the Homestake experiment provided a clean way of counting ν_e interactions, it
1 provided no information on the timing, direction and kinematics of the interaction. Only
2 a lower energy threshold is given by the fact, that the neutrino needs to have enough
3 energy to dissociate the chlorine atom from the tetrachloroethylene molecule. Due to
4 this, it was not possible to tell which reaction chain in the sun, the detected neutrinos
5 originated from. Furthermore, care needs to be taken for a very good understanding of
6 all background processes that can produce ^{37}Ar or its signature in the counting tube.
7 Finally, this experiment was only capable of detecting ν_e which proved to be crucial in
8 the solution to the solar neutrino problem; oscillation.

9 In 1988, the Kamioka Nucleon Decay Experiment (KamiokaNDE), in the Kamioka
10 mine in Japan, and the Irvine-Michigan-Brookhaven (IMB) detector [14], in a Morton Salt
11 mine in Ohio, USA, found a similar deficiency in atmospheric neutrinos which actually
12 were a background for the original experiments looking for proton decays. Atmospheric
13 neutrinos are produced in a similar fashion than Lederman et al. did in their muon neutrino
14 beam experiment. Cosmic rays strike the Earth atmosphere and produce secondary
15 particles many of which are pions, in turn, decaying according to Equation (2.2). Thus,
16 atmospheric neutrinos are mainly $\nu_\mu/\bar{\nu}_\mu$. However, the muon neutrino flux measured by
17 KamiokaNDE was only $(59 \pm 7)\%$ of the one predicted by Monte Carlo simulations. [15]
18 After an upgrade (KamiokaNDE-II), the collaboration furthermore confirmed the solar
19 neutrino problem discovered by the Homestake experiment. [16] The detector was a
20 3000 t water tank equipped with 1000 PMTs to detect *Cherenkov* radiation produced by
21 incoming charged particles.

Upon passage of a charge particle, the atoms of the medium become electric dipoles by means of polarisation. If the velocity of the incident particle v is greater than the speed of light inside the medium $\frac{c}{n}$, defined by the refractive index n , this polarisation is not symmetric anymore, resulting in a non-vanishing dipole moment. A characteristic

2. Neutrinos and their Detection

cone-shaped radiation in the direction of the particle is the result. The half opening angle of the cone is given by

$$\cos(\theta_c) = \frac{c}{n(\lambda)v} \quad (2.4)$$

and the radiation spectrum is

$$\frac{dN}{dx} = 2\pi\alpha z^2 \int_{\lambda_1}^{\lambda_2} \left(\frac{\sin(\theta_c(\lambda))}{\lambda} \right)^2 d\lambda \quad (2.5)$$

²² with the number of Cherenkov photons N , path length x , fine-structure constant α , and
¹ electric charge of the particle z . By recording the ring produced by this cone with light
² detectors, it is possible to determine the timing, direction, momentum and type of the
³ incident charged particle within certain restrictions. Often employed detection media
⁴ include water and oil while the photodetectors are usually PMTs. [11]

The charged particles detectable by a Cherenkov detector can be produced by neutrinos in multiple ways. Here, only the two most important processes shall be introduced, a more detailed description will be given in Section 2.4. Analogously to Equation (2.1), neutrinos of all three flavours can interact with nucleons according to

$$\nu_\ell n \rightarrow \ell^- p \quad \text{and} \quad (2.6)$$

$$\bar{\nu}_\ell p \rightarrow \ell^+ n \quad (2.7)$$

with $\ell = e, \mu, \tau$. It should be noted however, that usually τ leptons are too short-lived and heavy to produce enough Cherenkov radiation to be detected. A second interaction

2. Neutrinos and their Detection

path of neutrinos with matter is the scattering off shell electrons according to

$$\nu_\ell e^- \rightarrow \nu_\ell e^- \quad \text{and} \quad (2.8)$$

$$\bar{\nu}_\ell e^- \rightarrow \bar{\nu}_\ell e^-. \quad (2.9)$$

5 If the neutrino momentum is high enough, the electron recoil can be detected by a
1 Cherenkov detector for all three flavours.

2 While registering timing and directionality in addition to being able to detect and
3 distinguish ν_e and ν_μ was a huge improvement over the radiochemical Homestake
4 experiment, Cherenkov detectors still suffer from some deficiencies in particle identification.

5 One of them is that they can only detect charged particles with sufficient momentum
6 to produce Cherenkov radiation rather than detecting the whole event topology. The
7 detector cannot distinguish between processes producing the same ring signature. An
8 important example is a π^0 produced by a ν_μ which produces a signal in a Cherenkov
9 detector very similar to the one of a ν_e . This is a crucial background for neutrino
10 oscillation experiments.

11 Super-KamiokaNDE, the 50 kt successor of KamiokaNDE, solved the atmospheric
12 neutrino problem in 1998. [17, 18] It measured the flavour ratio of the atmospheric
13 neutrino flux as a function of the zenith angle. The ratio of the number of upward to
14 downward muon-like events was found to be $\approx 50\%$ while from Monte Carlo simulations
15 it was expected to be $\approx 100\%$. This result suggested a disappearance of ν_μ via neutrino
16 oscillations for atmospheric neutrinos that travelled along the much longer baseline
17 through the Earth.

The solar neutrino problem was solved in 2002 by SNO, in the INCO Ltd. Creighton
Mine in Ontario, Canada. [19] SNO is a 1 kt heavy water Cherenkov detector located
2039 m below the Earth surface (≈ 6000 m water equivalent). Its use of heavy water

2. Neutrinos and their Detection

(D₂O) allows it to detect neutrinos flavour-independently via

$$\nu_\ell d \rightarrow \nu_\ell pn \quad \text{and} \quad (2.10)$$

$$\bar{\nu}_\ell d \rightarrow \bar{\nu}_\ell pn \quad (2.11)$$

in addition to the interaction channels detectable by light water Cherenkov detectors given by Equations (2.6), (2.7), (2.8), and (2.9). For this to work, the emerging neutron needs to be detected which was achieved using ³He-filled proportional counters inside the heavy water tank. The additional neutrino detection channel allowed SNO to prove that only the solar ν_e flux is below the predictions by the SSM while the combined flux of all three flavours is consistent with the model, providing another strong evidence for neutrino oscillation.

The ν_τ was first detected by the Direct Observation of the Nu Tau (DONUT) experiment at Fermi National Accelerator Laboratory (FNAL) in Illinois, USA, in 2001. [20] Similarly to the ν_μ discovery, a neutrino beam was produced by shooting 800 GeV protons from the Tevatron onto a tungsten beam dump. The ν_τ were detected via the interactions described by Equations (2.6) and (2.7) for $\ell = \tau$. Therefore, it was required to detect very short-lived τ requiring a detector with a very good spatial resolution.

Nuclear emulsions were chosen as the core component of the detector. They consist of fine-grained silver-halide crystals (AgBr and/or AgCl) embedded in a gelatine substrate. Ionisation by passing charged particles causes some of the silver-halide molecules to be reduced to metallic silver. A subsequent development process reduces the silver-halide crystals, preferentially affecting those microcrystals already disturbed and partly reduced by the ionisation. Finally, the remaining crystals are dissolved in the fixation process leaving a stable image of elemental silver particles along the ionisation tracks. These charge images can be digitised using Charge-Coupled Device (CCD) cameras attached to computer controlled microscopes. Pattern recognition accelerated by Graphics Processing

2. Neutrinos and their Detection

22 Units (GPUs) can be employed for event reconstruction. [11]

1 The spatial resolution of the emulsion is limited by the size of the crystals. On the
2 other hand, they need to have a certain size in order for ionising particles to be able to
3 reduce enough silver-halide molecules to create a track inside the emulsion. A compromise
4 needs to be found based on the experimental requirements. The price for the high spatial
5 resolution is that emulsions are an offline detector that cannot be triggered or vetoed.
6 An external tracking detector (scintillating fibres in the case of DONUT) are required
7 to record event timing. Its data needs to be matched to the emulsion data before the
8 actual analysis.

9 Nowadays, the concept of neutrino oscillation is well-established and characterised
10 by the Daya Bay [21], Tokai To Kamioka (T2K) [22], Kamioka Liquid scintillation
11 AntiNeutrino Detector (KamLAND) [23], SNO, Super-KamiokaNDE and many other
12 experiments. Daya Bay and KamLAND essentially employ the same technique as Reines
13 and Cowan to look for disappearance of nuclear reactor $\bar{\nu}_e$. The only difference being
14 that instead of using multiple scintillator tanks in coincidence, they use one big tank
15 shielded and vetoed by water and/or mineral oil Cherenkov detectors. T2K directs a ν_μ
16 beam similar to the one of Lederman et al. towards Super-KamiokaNDE to look for ν_μ
17 disappearance and ν_e appearance over a long baseline.

18 2.2. Neutrino Oscillation

19 ArgonCube was selected as the LAr component of the ND for the DUNE long-baseline
20 neutrino oscillation experiment. Therefore, this section will give a basic introduction to
21 neutrino oscillation and DUNE.

The root cause of neutrino oscillation is that the flavour eigenstates (ν_α with $\alpha = e, \mu, \tau$)
of the three neutrinos are not equal to their three mass eigenstates (ν_i with $i = 1, 2, 3$).

2. Neutrinos and their Detection

The mass composition of the flavour eigenstates can be written as

$$\begin{pmatrix} \nu_e \\ \nu_\mu \\ \nu_\tau \end{pmatrix} = U_{\text{PMNS}} \begin{pmatrix} \nu_1 \\ \nu_2 \\ \nu_3 \end{pmatrix} \quad (2.12)$$

where

$$\begin{aligned} U_{\text{PMNS}} &= \\ U_{\text{sol}} \times U_{\text{rea}} \times U_{\text{atm}} \times U_{\text{maj}} &= \\ \begin{bmatrix} 1 & 0 & 0 \\ 0 & C_{23} & S_{23} \\ 0 & -S_{23} & C_{23} \end{bmatrix} \times \begin{bmatrix} C_{13} & 0 & S_{13}e^{-i\delta_{\text{CP}}} \\ 0 & 1 & 0 \\ -S_{13}e^{-i\delta_{\text{CP}}} & 0 & C_{13} \end{bmatrix} &\times \begin{bmatrix} C_{12} & S_{12} & 0 \\ -S_{12} & C_{12} & 0 \\ 0 & 0 & 1 \end{bmatrix} \times \begin{bmatrix} e^{i\frac{\alpha_1}{2}} & 0 & 0 \\ 0 & e^{i\frac{\alpha_2}{2}} & 0 \\ 0 & 0 & 1 \end{bmatrix} \end{aligned} \quad (2.13)$$

²² is the Pontecorvo-Maki-Nakagawa-Sakata (PMNS) matrix. It can be written as the
¹ product of three rotation matrices corresponding to the three Euler angles in 3D space,
² the mixing angles θ_{12} , θ_{13} and θ_{23} . In Eq. (2.13) they are represented by $S_{ij} = \sin \theta_{ij}$
³ and $C_{ij} = \cos \theta_{ij}$. Due to their first measurement with solar, reactor and atmospheric
⁴ neutrinos, respectively, the matrices and angles are often named accordingly. In addition
⁵ to the mixing angles, there is a Dirac, δ_{CP} , and two Majorana CP-violating phases,
⁶ α_1 and α_2 . The Majorana phases can only be measured by experiments sensitive to a
⁷ Majorana nature of the neutrinos, such as neutrinoless double beta decay experiments.
⁸ In neutrino oscillation experiments, they cancel out. Therefore, they are ignored for the
⁹ rest of this work. An illustration of the relation between the mass and flavour neutrino
¹⁰ eigenstates is shown in Figure 2.1.

2. Neutrinos and their Detection

The mass eigenstates ν_i from Eq. (2.12) evolve in time as

$$|\nu_i(t)\rangle = e^{-iE_i t} |\nu_i\rangle \quad (2.14)$$

where E_i is the energy of the mass eigenstate ν_i . Furthermore, Eq. (2.12) can be solved for ν_i

$$\begin{pmatrix} \nu_1 \\ \nu_2 \\ \nu_3 \end{pmatrix} = U_{\text{PMNS}}^\dagger \begin{pmatrix} \nu_e \\ \nu_\mu \\ \nu_\tau \end{pmatrix} \quad (2.15)$$

where U_{PMNS}^\dagger is the adjoint matrix of U_{PMNS} . This leads to

$$\begin{pmatrix} \nu_e \\ \nu_\mu \\ \nu_\tau \end{pmatrix} = U_{\text{PMNS}} D U_{\text{PMNS}}^\dagger \begin{pmatrix} \nu_e \\ \nu_\mu \\ \nu_\tau \end{pmatrix} \quad (2.16)$$

with the diagonal matrix

$$D_{ij} = \delta_{ij} e^{-iE_i t} \quad (2.17)$$

where δ_{ij} is the Kronecker delta. For relativistic particles,

$$E_i = \sqrt{p^2 + m_i^2} \approx p + \frac{m_i^2}{2p} \approx E + \frac{m_i^2}{2E} \quad (2.18)$$

can be approximated by the neutrino energy $E \approx p$ for $p \gg m_i$. After some further

2. Neutrinos and their Detection

conversions, one obtains

$$\begin{aligned} P(\nu_\alpha \rightarrow \nu_\beta) &= \left| \sum_i U_{\alpha i} U_{\beta i}^* e^{-iE_i t} \right|^2 \\ &= \sum_i |U_{\alpha i} U_{\beta i}^*| + 2 \operatorname{Re} \left\{ \sum_{i>j} U_{\alpha i} U_{\alpha j}^* U_{\beta i}^* U_{\beta j} e^{-i\Delta_{ij}} \right\} \end{aligned} \quad (2.19)$$

for the transition probability from ν_α into ν_β . The phase difference

$$\begin{aligned} \Delta_{ij} &= (E_i - E_j)t \\ &= \frac{\Delta m_{ij}^2}{2} \frac{L}{E}, \end{aligned} \quad (2.20)$$

11 depends on the mass splitting $\Delta m_{ij}^2 = m_i^2 - m_j^2$ and the length of the baseline $L = ct = t$.

1 To improve readability, U_{PMNS} was abbreviated by U .

2 The second term of Eq. (2.19) is of oscillatory nature. This implies that the frequency
3 of the oscillation is determined by the mass splitting and the amplitude by the matrix
4 elements of U_{PMNS} , i.e. the mixing angles θ_{12} , θ_{13} and θ_{23} . In particular, the consequence of
5 this is that the observation of neutrino oscillation between all three flavours proves a finite
6 mass of at least two of the three neutrinos. It is worth noting that this derivation is based
7 on a plain wave approximation which turns out to be wrong in a real localised experiment.
8 A wave packet approach would be needed to address the resulting deficiencies. However,
9 it can be shown that the plain wave approximation holds for most real experiments
10 anyway as wave packet effects cancel on average.

11 Despite predicting neutrino mixing and oscillation, the theory does not predict the
12 values of the oscillation parameters. They need to be measured by experiment. The
13 three-neutrino paradigm described above is well-established and has withstood tests by
14 many experiments in the last few decades. Table 2.1 shows the results of a recent global
15 fit. [24] In particular, it can be seen, that the uncertainties on δ_{CP} are huge and the sign

2. Neutrinos and their Detection

¹⁶ of Δm_{31}^2 is not yet known. The latter gives rise to two different orderings of the neutrino
¹ masses as depicted in Figure 2.1. What is needed to determine these parameters, is
² essentially much higher statistics than were achieved in neutrino experiments so far.

Table 2.1.: Oscillation parameters obtained from a recent global fit for the normal mass ordering case. The uncertainties are given for 1σ . [24]

Parameter	Value	Unit
θ_{12}	33.2(12)	$^\circ$
θ_{13}	8.45(15)	$^\circ$
θ_{23}	41.4(16)	$^\circ$
δ_{CP}	-100(50)	$^\circ$
Δm_{21}^2	$7.45(25) \times 10^{-5}$	eV ²
$ \Delta m_{31}^2 $	$2.55(5) \times 10^{-3}$	eV ²

³ However, various effects can be exploited to enhance the oscillation probability from
⁴ Equation (2.19), such as $\frac{L}{E}$ tuning, and matter effects. Tuning of $\frac{L}{E}$ is trivial to understand
⁵ from theory but not so easy to achieve in practice. Originally, neutrino oscillations were
⁶ discovered and characterised using solar and atmospheric neutrinos. While neutrinos
⁷ produced in the Earth atmosphere allow for some $\frac{L}{E}$ tuning by means of a zenith angle
⁸ selection, and similarly via time of year for solar neutrinos, the gain is limited. Much
⁹ more fine-grained control is possible by directing an artificially produced neutrino beam
¹⁰ with a well-defined energy spectrum at an underground detector at a optimised distance
¹¹ L .

¹² In matter, neutrino oscillation is different than in vacuum. The neutrinos are coherently
¹³ scattered off the shell electrons, similar to the propagation of light through matter. As will
¹⁴ be shown in Section 2.4, the interactions of ν_e and $\bar{\nu}_e$ differ from the other flavours, they
¹⁵ are possible through an additional channel. Thus, the interaction probability of electron
¹⁶ neutrinos is higher. From Figure 2.1, it can be seen, that ν_e are primarily present in ν_1
¹⁷ and ν_2 . Therefore, the propagation of these two is altered while ν_3 is almost unaffected.
¹⁸ Named after its discoverers, the Mikheyev-Smirnov-Wolfenstein (MSW) effect [25, 26]

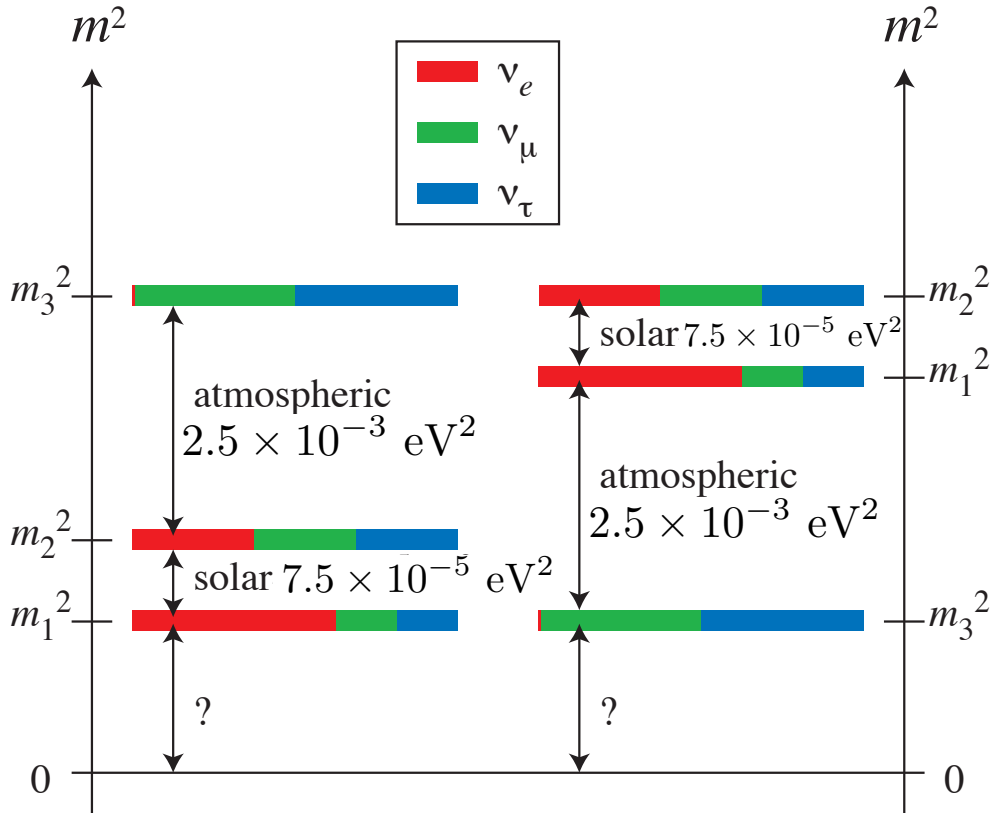


Figure 2.1.: The two possible neutrino mass orderings arising from the unknown sign of Δm_{31}^2 : normal ordering (NO) on the left and inverted ordering (IO) on the right. Neutrino oscillation experiments can only determine $\Delta m_{ij}^2 = m_i^2 - m_j^2$, not the absolute mass scale. Also shown is the flavour content (colour bars) of the three mass eigenstates. [24]

¹⁹ can be exploited to determine the mass ordering with a properly tuned $\frac{L}{E}$.

¹ 2.3. DUNE

² The Deep Underground Neutrino Experiment (DUNE) [27–30] is a long-baseline neutrino
³ oscillation experiment measuring $P(\nu_\mu \rightarrow \nu_e)$ and $P(\bar{\nu}_\mu \rightarrow \bar{\nu}_e)$, planned to start data
⁴ taking around 2025. It consist of a neutrino beamline at FNAL in Illinois, USA and
⁵ a LArTPC Far Detector (FD) at a baseline of 1300 km in the Sanford Underground

2. Neutrinos and their Detection

6 Research Facility (SURF) in South Dakota, USA. An artistic view of DUNE is shown in
 1 Figure 2.2.

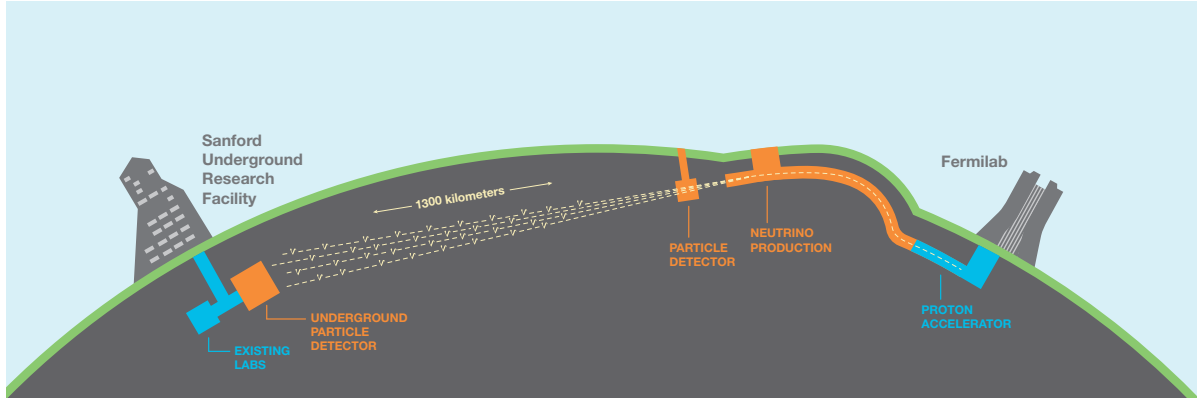


Figure 2.2.: DUNE. [27]

2 The beamline at FNAL produces pions by shooting a pulsed proton beam onto a
 3 graphite target. A variable proton energy of 60 GeV to 120 GeV allows for the production
 4 of different neutrino fluxes. One pulse is called a spill and has a duration of 10 μ s at
 5 a period of 0.7 s to 1.2 s, depending on the proton energy. During phase one of the
 6 experiment, each spill will contain 7.5×10^{13} protons resulting in a beam power of
 7 1.03 MW to 1.20 MW. In a later phase two, the number of protons per spill will be
 8 doubled, doubling the power as well as the average number of events per spill in the
 9 detectors. A summary of the various proton beam configurations is given in Table 2.2.
 10 In accordance with [28], most calculations in this work assume the 2 MW 80 GeV beam,
 11 i.e. 0.2 events per tonne of argon and beam spill. The produced pions pass through
 12 several EM focusing horns to enter a decay pipe where they decay to μ^+ (μ^-) and ν_μ
 13 ($\bar{\nu}_\mu$) according to Equation (2.2). By altering the polarity of the current in the focusing
 14 horns, either π^+ or π^- can be selected primarily, enhancing the ν_μ or $\bar{\nu}_\mu$ content of the
 15 beam, respectively. Alongside the pions, a small amount of kaons is produced as well.
 16 These in turn can decay to ν_e and $\bar{\nu}_e$ with a branching ratio of $\approx 5\%$ [31] producing
 17 a significant ν_e ($\bar{\nu}_e$) beam contamination. The (anti)neutrino beam flux is depicted in

2. Neutrinos and their Detection

¹⁸ Figure 2.3. More information on the beamline can be found in [28].

Table 2.2.: Summary of the DUNE proton beam parameters for various configurations.

Initially, the beamline will operate with the phase one parameters. Later, it will be upgraded to support the phase two parameters. The spill duration is 10 μs for all configurations. The last column gives the expected total number of neutrino interactions per tonne of argon and beam spill in the ND, excluding rock events. It is calculated by multiplying the expected neutrino flux with the cross-section on argon from the GENIE^a neutrino event generator. Note that these values are slightly different from the ones in Table 2.2 because the latter are outdated. In accordance with [28], most calculations in this work assume the 2 MW 80 GeV beam, i.e. 0.2 events per tonne or argon and beam spill. Taken from [29, 32].

Phase	E_p [GeV]	POT per spill	Spill period [s]	Power [MW]	ND rate [evt/t _{Ar}]
I	60	7.5×10^{13}	0.7	1.03	0.078
II	60	1.5×10^{14}	0.7	2.06	0.16
I	80	7.5×10^{13}	0.9	1.07	0.11
II	80	1.5×10^{14}	0.9	2.14	0.21
I	120	7.5×10^{13}	1.2	1.20	0.17
II	120	1.5×10^{14}	1.2	2.40	0.33

^a<https://genie.hepforge.org>

¹ The baseline and energy spectrum of DUNE are optimised to measure δ_{CP} and determine
² the mass ordering. Figure 2.4 shows the (anti)neutrino oscillation probability as a function
³ of neutrino energy at the DUNE baseline for the normal and inverted mass ordering. Put
⁴ into very simple terms, δ_{CP} can be derived from the difference in oscillation probability
⁵ between neutrino and antineutrino mode. The MSW effect enhances either neutrino or
⁶ antineutrino oscillation depending on the mass ordering, allowing for a determination of
⁷ the latter. For more thorough sensitivity treatments, see [24, 33, 34].

⁸ Figure 2.5 shows the sensitivities of DUNE to determination of the mass ordering
⁹ and discovery of CP violation. To reach a 3σ sensitivity for a 75 % coverage of the δ_{CP}
¹⁰ parameter space, an exposure of 1320 ktMW years is required. Assuming the reference
¹¹ design of a 40 kt FD and a 1 MW beam results in a data taking time of 33 years. Therefore,
¹² to reach the sensitivity goal earlier, a beam > 1 MW is required.

2. Neutrinos and their Detection

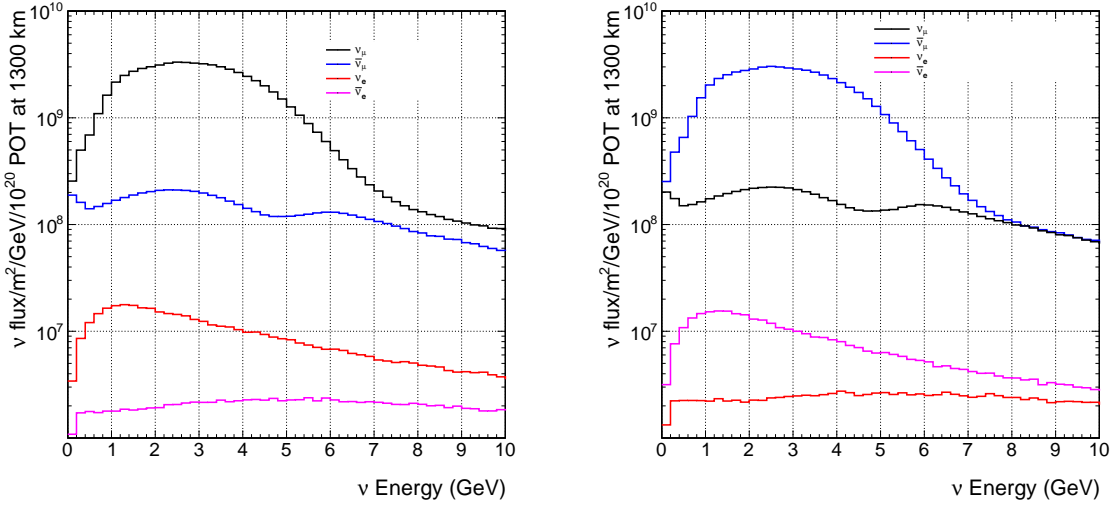


Figure 2.3.: Neutrino fluxes for the DUNE reference beam design operating in neutrino mode (left) and antineutrino mode (right), generated with a 120 GeV primary proton beam. [28]

Another important feature of Figure 2.5 are the indicated signal normalisation uncertainties. In particular the second number has a significant influence on sensitivity, the aforementioned exposure assumes an uncertainty of 5 % \oplus 2 %. A detailed explanation of this is out of the scope of this work and can be found in [28]. What shall be mentioned here however is that these uncertainties can be reached by a precise constraint of the flux rate and shape by means of a Near Detector (ND). It is placed at a distance of 574 m downstream of the proton beam target. To eliminate the introduction of further extrapolation uncertainties it is important to have a ND component employing the same target material and detector technology as the FD, i.e. a LArTPC.

As will be explained in Chapter 3, LArTPCs are slow detectors. This is problematic in the high-multiplicity ND environment of DUNE which is the reason why [28] and [30] do not mention an ND LAr component. The aforementioned MW beam intensity leads to ND event rates of 0.2 events per tonne of argon leading to significant event pile-up (see Table 2.2). Rock events—secondary particles produced by beam neutrino interactions in

2. Neutrinos and their Detection

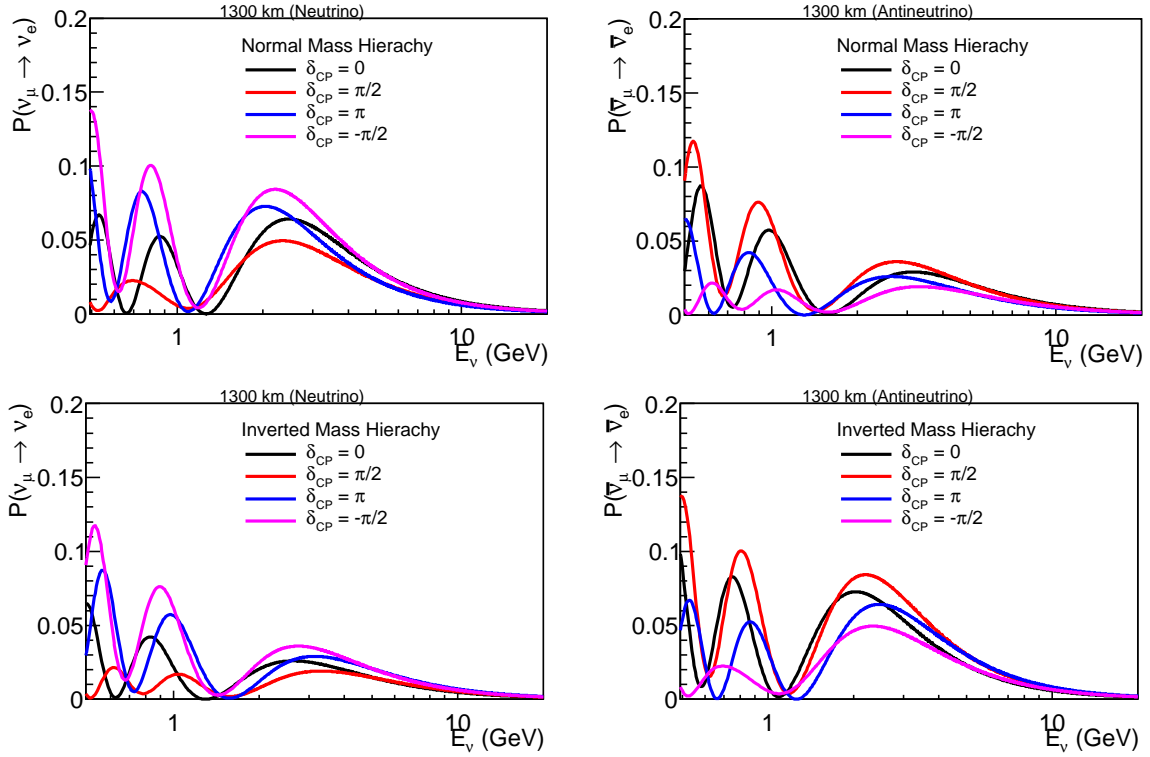


Figure 2.4.: Muon to electron neutrino (left) and antineutrino (right) oscillation probability for normal (top) and inverted (bottom) mass ordering (hierarchy in the figure). The oscillation probabilities are calculated from equation (2.19). δ_{CP} can be obtained from the difference between neutrino and antineutrino mode. The MSW effect either enhances the probability in neutrino or antineutrino mode depending on the mass ordering, allowing for a determination of the latter. [34]

¹⁴ the surrounding material, entering the detector—are not included in this estimate.

2. Neutrinos and their Detection

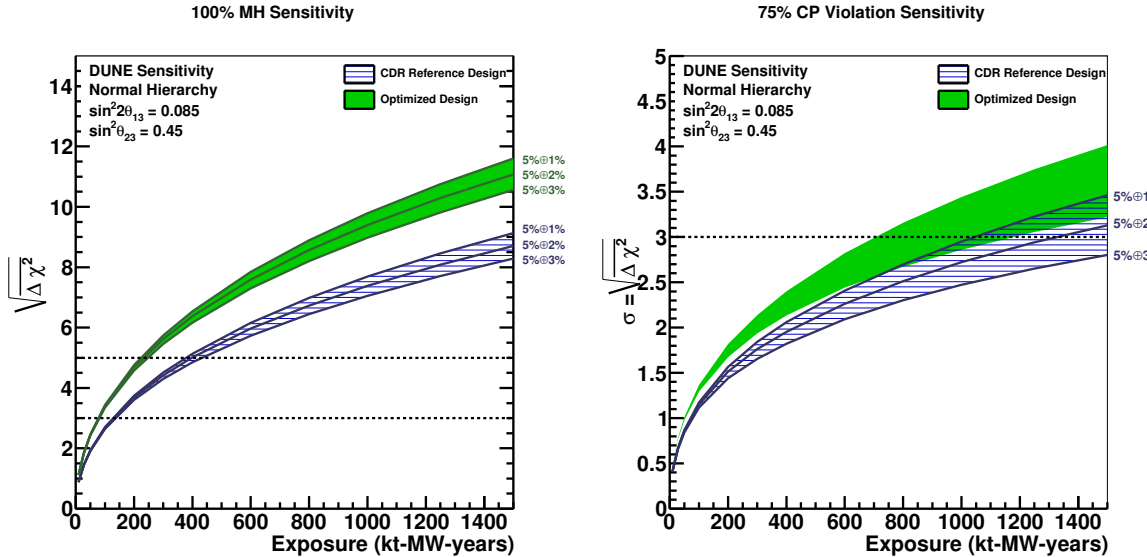


Figure 2.5.: Expected sensitivity of DUNE to determination of the neutrino mass ordering (hierarchy, left) and discovery of CP violation, i.e. $\delta_{CP} \neq 0$ or π , (right) as a function of exposure in ktMW years, assuming equal running in neutrino and antineutrino mode, for a range of values for the ν_e and $\bar{\nu}_e$ signal normalisation uncertainties from 5 % \oplus 3 % to 5 % \oplus 1 %. The sensitivities quoted are the minimum sensitivity for 100 % of δ_{CP} values in the case of mass ordering and 75 % of δ_{CP} values in the case of CP violation. The two bands on each plot represent a range of potential beam designs described in [28]: the blue hashed band is for the reference design and the solid green band is for the optimized design. Sensitivities are for true normal ordering; neutrino mass ordering and θ_{23} octant are assumed to be unknown. Taken from [28].

[remove octant or explain](#)

2.4. Neutrino Interaction with Matter

- ¹ Neutrinos cannot be directly detected, they need to pass on some of their energy and momentum to secondary particles that can be detected, i.e. they need to interact with a detection medium. This chapter will give a brief overview of the different types of these interactions. In general, neutrino interactions are divided into Charged Current (CC) and Neutral Current (NC) mediated by charged (W^\pm) or neutral (Z^0) gauge bosons. In a CC interaction, the neutrino is transformed into its corresponding charged lepton while it survives an NC interaction. Furthermore, they can be subdivided according to the

2. Neutrinos and their Detection

Table 2.3.: Estimated number of interactions per tonne of argon at the DUNE ND for approximately one month (1×10^{20} POT) exposure to an (anti)neutrino beam produced from a primary proton beam of 120 GeV and 1.2 MW, taken from [28]. Note that these rates are slightly different from the ones in Table 2.2. The reason for this is that the values below are outdated. However, their order of magnitude is correct and no such detailed breakdown is available for the more recent values. Therefore, they are presented as a rough estimate for the expected rates for the different interaction channels.

Production mode	Reaction	ν_μ beam	$\bar{\nu}_\mu$ beam
CC QE	$\nu_\mu n \rightarrow \mu^- p$	30 000	13 000
NC elastic	$\nu_\mu N \rightarrow \nu_\mu N$	11 000	6700
CC RES	$\nu_\mu p \rightarrow \mu^- p \pi^+$	21 000	0
CC RES	$\nu_\mu n \rightarrow \mu^- n \pi^+ (p \pi^0)$	23 000	0
CC RES	$\bar{\nu}_\mu p \rightarrow \mu^+ p \pi^- (n \pi^0)$	0	8300
CC RES	$\bar{\nu}_\mu n \rightarrow \mu^+ n \pi^-$	0	12 000
NC RES	$\nu_\mu p \rightarrow \nu_\mu p \pi^0 (n \pi^+)$	7000	0
NC RES	$\nu_\mu n \rightarrow \nu_\mu n \pi^+ (p \pi^0)$	9000	0
NC RES	$\bar{\nu}_\mu p \rightarrow \bar{\nu}_\mu p \pi^- (n \pi^0)$	0	3900
NC RES	$\bar{\nu}_\mu n \rightarrow \bar{\nu}_\mu n \pi^-$	0	4700
CC DIS	$\nu_\mu N \rightarrow \mu^- X$ or $\bar{\nu}_\mu N \rightarrow \mu^+ X$	95 000	24 000
NC DIS	$\nu_\mu N \rightarrow \nu_\mu X$ or $\bar{\nu}_\mu N \rightarrow \bar{\nu}_\mu X$	31 000	10 000
CC COH π^+	$\nu_\mu A \rightarrow \mu^- A \pi^+$	930	0
CC COH π^-	$\bar{\nu}_\mu A \rightarrow \mu^+ A \pi^-$	0	800
NC COH π^0	$\nu_\mu A \rightarrow \nu_\mu A \pi^0$ or $\bar{\nu}_\mu A \rightarrow \bar{\nu}_\mu A \pi^0$	520	450
NC elastic electron	$\nu_\mu e^- \rightarrow \nu_\mu e^-$ or $\bar{\nu}_\mu e^- \rightarrow \bar{\nu}_\mu e^-$	16	11
Inverse muon decay	$\nu_\mu e^- \rightarrow \mu^- \nu_e$	9.5	0
Total CC		170 000	59 000
Total CC+NC		230 000	84 000

⁸ type of interaction into Quasi-Elastic (QE), Resonant (RES), Deep Inelastic Scattering

¹ (DIS), and Coherent (COH).

QE is characterised by the reactions

$$\nu_\ell n \rightarrow \ell^- p \quad \text{and} \quad \bar{\nu}_\ell p \rightarrow \ell^+ n \quad (2.21)$$

² and the kinematics are similar to that of an elastic collision, hence called QE. Apparent

³ from the equation above, this can only happen as a CC interaction.

2. Neutrinos and their Detection

The NC equivalent is an actual elastic interaction of a neutrino with a target nucleon according to

$$\nu_\ell N \rightarrow \nu_\ell N. \quad (2.22)$$

RES involves the excitation of the involved nucleon to a resonant state, e.g.

$$\nu_\mu p \rightarrow \mu^- \Delta^{++} \rightarrow \mu^- p \pi^+ \quad (2.23)$$

⁴ where the Δ^{++} resonance is too short-lived to be seen by the detectors. There are a lot
¹ of different RES interactions which all work in a similar manner.

For DIS, the momentum transfer is high enough to destroy nucleon. The neutrino rips a quark out which, in turn, starts to hadronise and form jets. The reactions are

$$\nu_\ell N \rightarrow \ell X \quad \text{or} \quad \nu_\ell N \rightarrow \nu_\ell X \quad (2.24)$$

² where N is the target nucleon and X a group of hadrons. This reaction happens in a very
³ similar manner to deep inelastic electron scattering off nucleons.

In a COH reaction, the opposite happens. The neutrino interacts with a target nucleus (A) as a whole but the latter is left intact as a spectator. Instead, another particle is produced alongside the corresponding lepton. An example reaction is

$$\nu_\mu A \rightarrow \nu_\mu A \pi^0 \quad (2.25)$$

⁴ where a pion is produced from a muon neutrino interacting with a target nucleus.

The inverse muon decay,

$$\nu_\mu e^- \rightarrow \mu^- \nu_e, \quad (2.26)$$

2. Neutrinos and their Detection

⁵ requires neutrino energies above 11 GeV [28].

Of particular importance is elastic scattering off shell electrons,

$$\nu_\ell e^- \rightarrow \nu_\ell e^- \quad \text{or} \quad \bar{\nu}_\ell e^- \rightarrow \bar{\nu}_\ell e^-, \quad (2.27)$$

¹ which is possible for all (anti)neutrino flavours. For $\nu_e/\bar{\nu}_e$, the interaction is also possible
² in the CC channel via the exchange of a W^\pm boson as depicted in Figures 2.6 and 2.7.
³ This gives rise to a flavour-dependent term in the oscillation probability in matter, the
⁴ MSW effect (see Section 2.2).

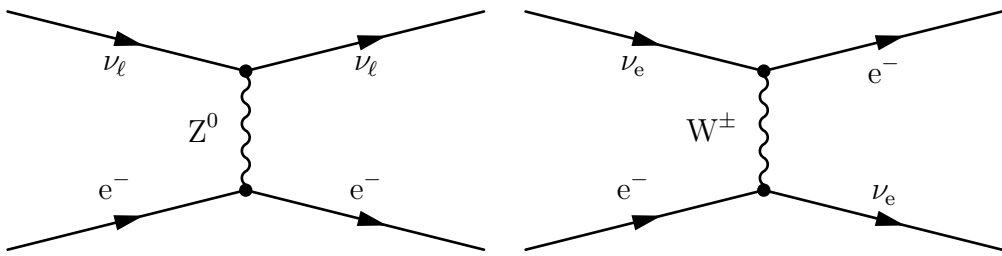


Figure 2.6.: NC (left) and CC (right) neutrino electron scattering.

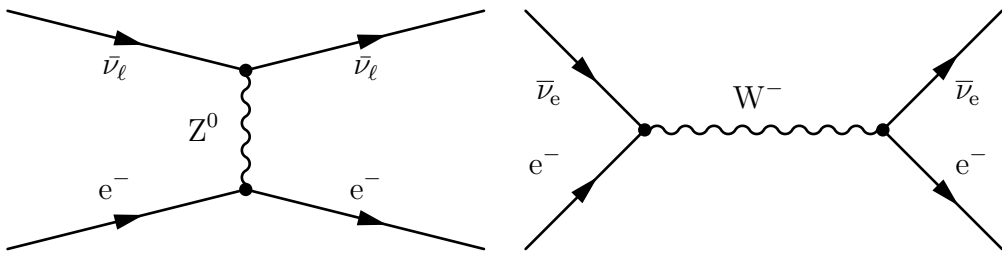


Figure 2.7.: NC (left) and CC (right) antineutrino electron scattering.

⁵ A summary of the expected rates of the different interactions in the DUNE ND is
⁶ given in Table 2.3. Figure 2.8 depicts the cross-section (see next paragraph) of neutrino
⁷ interactions as a function of neutrino energy. For comparison, the flux shapes of several
⁸ experiments are shown (in arbitrary units). The cross-section is split into contributions
⁹ from CC and NC interactions. For CC, the individual contributions from RES and
¹⁰ 1p1h+2p2h are shown. $xpyh$ refers to x particles and y holes, i.e. the target nucleus

2. Neutrinos and their Detection

- ¹¹ is missing y nucleons after the interactions. 1p1h corresponds to a CC QE interaction
¹ whereas in 2p2h interactions, a virtual meson is exchanged inside the target nucleus,
² also called Meson Exchange Current (MEC). Interactions involving MECs are important
³ because they can mimic the detector response of CC QE events.

To better understand the meaning of Figure 2.8, a brief explanation of the cross-section concept is given here. For a beam consisting of particles A , incident on a target made of particles B , the rate of the interaction $AB \rightarrow X$ is given by

$$R_X = \phi_A N_B \sigma_{ABX}, \quad (2.28)$$

where ϕ_A is the flux of beam particles, N_B is the number of target particles, and σ_{ABX} is the cross-section. Therefore, the cross-section

$$\sigma_{ABX} = \frac{R_X}{\phi_A N_B} \quad (2.29)$$

- ⁴ is a measure for the interaction rate R_X normalised by the number of both, beam and
⁵ target, particles. As flux is given in units of inverse time and area, and interaction rate
⁶ in inverse time, the cross-section needs to have the dimension of an area.

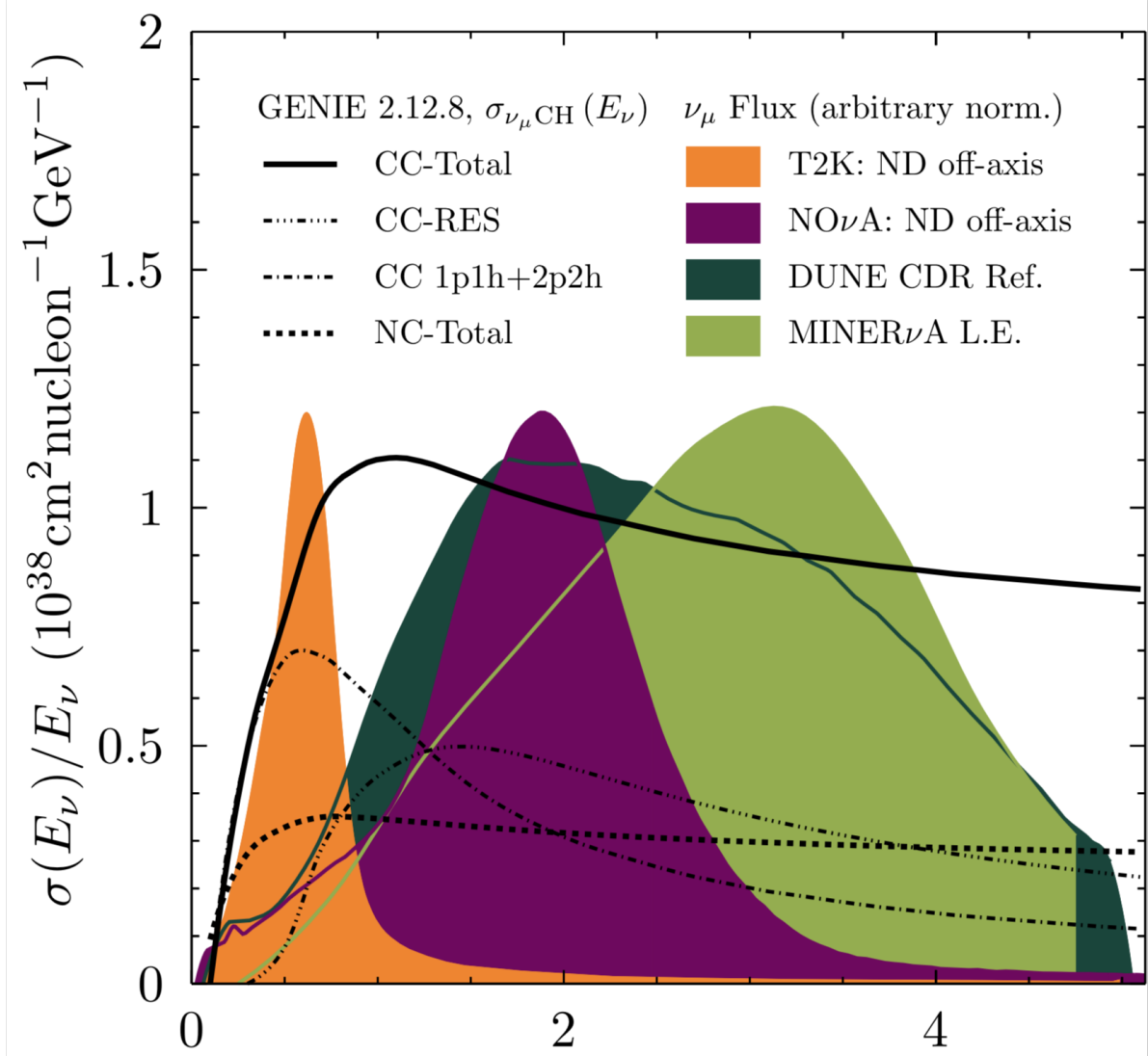


Figure 2.8.: Neutrino interaction cross-section per nucleon as a function of neutrino energy in GeV. Overlaid are the flux shapes of various beam experiments in arbitrary units. The cross-section is split into contributions from CC and NC interactions. For CC, the individual contribution from RES interactions is shown, as well as from the sum of 1p1h and 2p2h. The latter two correspond to the QE channel and interactions involving MECs, respectively.

sance

2.5. Final State Detection

- ¹ In order to be able to detect particles, they need to interact with a detection medium.
- ² This section will describe the most important interaction of charged particles as well as
- ³ neutral particles with matter. A special focus is laid on charged interactions as these are
- ⁴ the most important ones for LArTPCs. As a measure of the interaction strength, the
- ⁵ energy loss per distance or stopping power $\frac{dE}{dx}$ is used. Where not otherwise mentioned,
- ⁶ this section is based on [11].

The main interaction of charged particles with matter happens on atomic electrons. That is why for most of these interactions, one needs to treat the interaction of electrons separately. For all other charged particles, the stopping power is described by the Bethe-Bloch formula

$$-\frac{1}{\rho} \frac{dE}{dx} = 4\pi N_A r_e^2 m_e c^2 z^2 \frac{Z}{A} \frac{1}{\beta^2} \left[\ln \left(\frac{2m_e c^2 \gamma^2 \beta^2}{I} \right) - \beta^2 - \frac{\delta}{2} \right], \quad (2.30)$$

⁷ where

⁸ ρ is the density of the absorber material,

⁹ N_A is Avogadro's number,

¹⁰ $r_e = \frac{1}{4\pi\epsilon_0} \frac{e^2}{m_e c^2}$ is the classical electron radius using the permittivity of free space ϵ_0 ,

¹¹ m_e is the electron mass,

¹² z is the charge of the incident particle,

¹³ Z is the atomic number of the absorber,

¹⁴ A is the atomic weight of the absorber,

¹⁵ $\beta = \frac{v}{c}$ with v the velocity of the incident particle,

2. Neutrinos and their Detection

¹⁶ $\gamma = \frac{E}{m_0 c^2}$ with E the energy and m_0 the rest mass of the incident particle,

I is the mean excitation energy of the absorber material which can be approximated by

$$I = 16Z^{0.9} \text{eV} \quad \text{for } Z > 1, \quad (2.31)$$

¹ δ is a parameter describing the screening of the extended transverse electric field of
² relativistic incident particles by the charge density of the atomic electrons of the
³ absorber.

⁴ Equation (2.30) describes the stopping power of particles with $m_0 \gg m_e$ by ionisation and
⁵ excitation of the atoms in the absorber material. As the stopping power is proportional
⁶ to the electron density and thus to the mass density of the absorber material, it is
⁷ often divided by the latter. Thus, Equation (2.30) actually gives the so called mass
⁸ stopping power. The only remaining dependence on the absorber material is $\frac{Z}{A}$ which is
⁹ ≈ 0.5 for most light materials, and the mean excitation energy which only contributes
¹⁰ logarithmically.

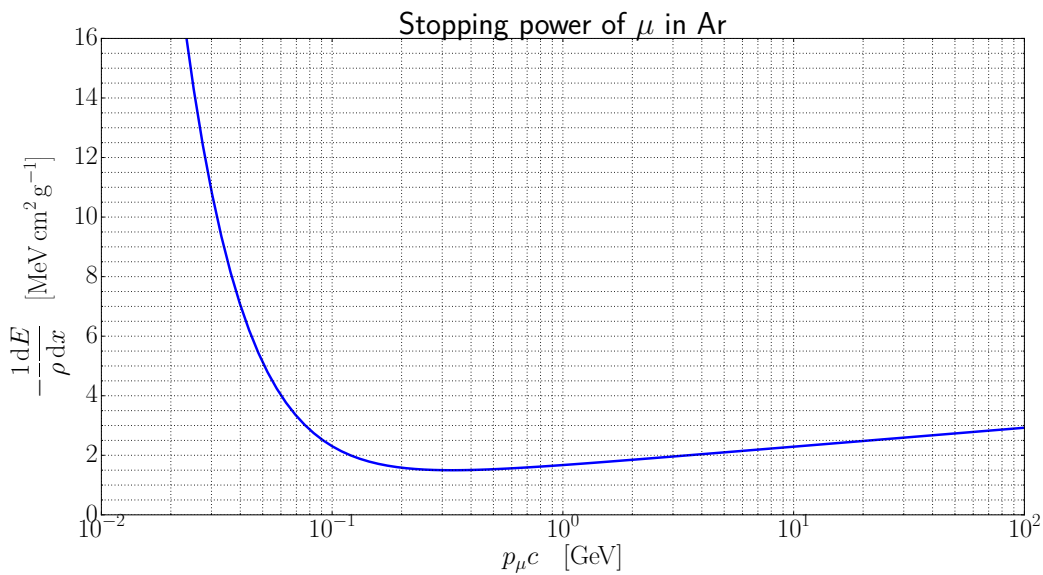


Figure 2.9.: Bethe-Bloch stopping power of μ in Ar.

2. Neutrinos and their Detection

Figure 2.9 shows the mass stopping power of muons in argon neglecting the $\frac{\delta}{2}$ term. As can be seen, there is a broad minimum which is characteristic of the Bethe-Bloch formula. Particles in this momentum range are called Minimum Ionising Particles (MIPs). They are important for detectors because this energy loss is a measure for the required energy resolution of a detector. As mentioned above, the mass stopping power only loosely depends on the absorber material and therefore, its minimum is

$$-\frac{1}{\rho} \frac{dE}{dx} \Big|_{\min} \approx 2 \text{ MeV cm}^2 \text{ g}^{-1} \quad (2.32)$$

for singly charged incident particles on most (light) absorbers. To the left of the minimum is the *Bragg peak* which is especially important for radiation therapy with heavy charged particles (e.g. protons). The Bragg peak falls off with a strong $\frac{1}{\beta^2}$ dependence. After the minimum, the stopping power rises again with a logarithmic dependence on β and the mean excitation energy of the absorber I . The reason for this so called *logarithmic rise* is the extension of the transverse electric field of the incident particle in the relativistic regime. Due to increasing shielding of the transverse electric field by the shell electrons of the absorber materials, taken into account by the $\frac{\delta}{2}$ term, the rise is only asymptotic. For electrons and positrons, Equation (2.30) does not hold because their mass is equal to the mass of the atomic electrons of the absorber. The stopping power changes further for electrons because the incident particle cannot be distinguished from its collision partner in that case. On the other hand, a positron will be annihilated upon stop by an electron which needs to be taken into account as well. The equivalent of Equation (2.30) for e^\pm can be found in [11].

At high velocities, further effects come into play. *Bremsstrahlung* describes the radiation energy loss of a fast charged particle in the Coulomb field of the absorber nuclei. It can

2. Neutrinos and their Detection

be described by

$$-\frac{1}{\rho} \frac{dE}{dx} = \frac{E}{X_0} \quad (2.33)$$

where

$$X_0 = \frac{A}{4\alpha N_A Z(Z+1) \left(\frac{1}{4\pi\varepsilon_0} \frac{e^2}{mc^2} \right)^2 \ln(183Z^{-\frac{1}{3}})} \quad (2.34)$$

¹⁴ is the *radiation length* of the absorber material using

¹ $\alpha \approx \frac{1}{137}$ the fine-structure constant and

² m the mass of the incident particle.

Again, the energy loss is proportional to the density of the absorber and for convenience, divided by the latter. Bremsstrahlung is emitted in interactions of the incident particle with the absorber nuclei ($\propto Z^2$) as well as with the atomic electrons of the absorber ($\propto Z$). By neglecting the latter, one obtains the important relation

$$X_0^{-1} \propto Z^2 \quad (2.35)$$

as opposed to the $\propto Z$ dependence of the Bethe-Bloch formula. Equation (2.33) also holds for electrons as long as $E \gg \frac{m_e c^2}{\alpha Z^{\frac{1}{3}}}$. Furthermore, looking at the dependence on the mass of the incident particle, one finds

$$X_0 \propto m^2 \quad (2.36)$$

using Equation (2.34). Therefore, the radiation length of an absorber material is usually

2. Neutrinos and their Detection

given for electrons and the relation

$$X_0 = X_0^e \frac{m^2}{m_e^2} \quad (2.37)$$

can be used to get the radiation length for any charged particle of mass m . Radiation losses play a significant role only at energies much higher than the energy of MIPs. Using Equations (2.30) and (2.33), one can define a *critical energy* E_c by

$$\left. \frac{dE}{dx}_{\text{ion}} \right|_{E_c} = \left. \frac{dE}{dx}_{\text{brems}} \right|_{E_c} \quad (2.38)$$

- ³ at which radiation losses take over from ionisation losses. Similar to the radiation length,
- ¹ the critical energy is proportional to m^2 . Thus, it is most important for electrons while for
- ² other particles it becomes significant only at very high energies. If we take the example
- ³ of an iron absorber again for instance, we get $E_c^e = 20.7 \text{ MeV}$ and $E_c^\mu = 890 \text{ GeV}$.
- ⁴ At high energies, there are additional types of radiation loss taking place, for instance
- ⁵ direct electron-pair production and photonuclear interactions. They shall not be described
- ⁶ here. Instead, only their $\propto E$ relation similar to bremsstrahlung losses shall be mentioned.
- ⁷ A description of those effects can be found in [11].

In addition to the processes described above, charged particles traversing matter also undergo scattering in the Coulomb field of the nuclei of the traversed medium. Accordingly, this process is called *Multiple Coulomb Scattering (MCS)*. The Root Mean Square (RMS) of the *scattering-angle distribution*

$$\Theta_{\text{RMS}} = \frac{13.6 \text{ MeV}}{\beta c p} z \sqrt{\frac{2x}{X_0}} \left[1 + 0.038 \ln \left(\frac{x}{X_0} \right) \right] \quad (2.39)$$

- ⁸ is defined by the momentum p , velocity βc and charge z of the scattered particle, and
- ⁹ the thickness of the scattering medium $\frac{x}{X_0}$ in radiation lengths. The distinct momentum
- ¹⁰ dependence of this so-called *Highland formula* can be used to reconstruct the momentum

2. Neutrinos and their Detection

¹¹ of the incident particle provided the angular resolution of the detector is fine enough.

¹ Concerning the interactions of charged particles with matter, there is one important
² note regarding detectors. While charge produced in interactions (i.e. ionisation) can be
³ detected directly, light (i.e. excitation photons and photon radiation) first needs to be
⁴ converted to charge to be detected.

The three most important interactions converting photons to charge are the *photoelectric effect*, *Compton Scattering*, and *pair production*. All of them have in common that they attenuate photon beams exponentially according to

$$I = I_0 e^{-\mu x} \quad (2.40)$$

where I_0 and I is the intensity before and after passing the absorber, respectively. The thickness of the absorber is given by x and

$$\mu = \frac{N_A}{A} \sum_i \sigma_i \quad (2.41)$$

⁵ is the *mass attenuation coefficient* defined by the sum of the cross-sections σ_i of the
⁶ different interaction processes.

At low energies (ionisation energy $\leq E_\gamma \leq 100 \text{ keV}$), photons primarily undergo conversion to charge by the photoelectric effect. The photon is absorbed by an atom of the absorber which in turn is ionised and thus ejects one of its shell electrons. The cross-section is given by

$$\sigma_{\text{photo}} = \left(\frac{32}{\epsilon^7} \right)^{\frac{1}{2}} \alpha^4 Z^5 \sigma_{\text{Th}}^e \quad (2.42)$$

⁷ where

⁸ $\epsilon = \frac{E_\gamma}{m_e c^2}$ is the reduced photon energy and

2. Neutrinos and their Detection

⁹ $\sigma_{\text{Th}}^{\text{e}} = \frac{8}{3}\pi r_{\text{e}}^2 = 6.65 \times 10^{-25} \text{ cm}^2$ is the *Thomson cross-section* for elastic scattering of
¹ photons on electrons.

For energies $\approx 1 \text{ MeV}$, Compton scattering dominates the interaction of photons with matter. Thereby, the photon is not absorbed by the atom but just scatters off one of its shell electrons with the cross-section

$$\sigma_{\text{c}} = 2\pi r_{\text{e}}^2 Z \left\{ \left[\frac{1+\epsilon}{\epsilon^2} \right] \left[\frac{2(1+\epsilon)}{1+2\epsilon} - \frac{1}{\epsilon} \ln(1+2\epsilon) \right] \right. \quad (2.43)$$

$$\left. + \frac{1}{2\epsilon} \ln(1+2\epsilon) - \frac{1+3\epsilon}{(1+2\epsilon)^2} \right\} \quad (2.44)$$

obtained from the Klein-Nishina formula. As only part of the photon's energy is absorbed while the rest is scattered, it makes sense to divide this cross-section into a scattering cross-section

$$\sigma_{\text{cs}} = \frac{E'_{\gamma}}{E_{\gamma}} \quad (2.45)$$

and an absorption cross-section

$$\sigma_{\text{ca}} = \sigma_{\text{c}} - \sigma_{\text{cs}} \quad (2.46)$$

² where E_{γ} and E'_{γ} is the energy of the photon before and after scattering, respectively.

At $E_{\gamma} \geq 2m_{\text{e}}c^2$, photons are capable of producing pairs of $e^+ e^-$. Because of momentum conservation, this process can only happen in the Coulomb field of a so called spectator particle. As pair-production in the field of an electron is strongly suppressed, the spectator is usually a nucleus of the absorber material. Therefore, the cross-section of pair-production depends on the shielding of the Coulomb field by the shell electrons and thus on the proximity to the nucleus. Eventually, this results in an energy dependence.

2. Neutrinos and their Detection

For $1 \ll \epsilon < \frac{1}{\alpha Z^{\frac{1}{3}}}$, the cross-section is given by

$$\sigma_{\text{pair}} = 4\alpha r_e^2 Z^2 \left(\frac{7}{9} \ln 2\epsilon - \frac{109}{54} \right) \quad (2.47)$$

and for $\epsilon \gg \frac{1}{\alpha Z^{\frac{1}{3}}}$, the cross-section is

$$\sigma_{\text{pair}} = 4\alpha r_e^2 Z^2 \left[\frac{7}{9} \ln \left(\frac{183}{Z^{\frac{1}{3}}} \right) - \frac{1}{54} \right]. \quad (2.48)$$

- ³ As mentioned above, for Compton scattering, two different cross-sections are defined,
- ¹ σ_{cs} for the scattered energy and σ_{ca} for the absorbed energy. Consequentially, there
- ² are also different definitions of the coefficient μ in Equation (2.41). Replacing the total
- ³ Compton cross-section σ_c by σ_{ca} from Equation (2.46), one gets the *mass absorption*
- ⁴ *coefficient* μ_a , only taking into account photon absorption processes. While μ is more
- ⁵ precisely called the *total mass attenuation coefficient*.

An interesting effect takes place for e^\pm traversing material at energies higher than the critical energy E_c defined by Equation (2.38). In this regime, the energy loss is dominated by bremsstrahlung for e^\pm and by pair production for photons. This leads to an *EM cascade* or *shower* where e^\pm and γ produce each other alternately in a self-sustaining process. The mean free path of a photon before pair production

$$\lambda_{\text{prod}} = \frac{9}{7} X_0 \quad (2.49)$$

is very close to the mean free path of an e^\pm before bremsstrahlung, the radiation length X_0 . Therefore, the number of particles participating in the shower doubles roughly every radiation length resulting in an exponential growth. This allows EM showers to be approximated by the following rather simple model. When the average energy per particle drops below the critical energy, ionisation losses begin to dominate over radiative losses

2. Neutrinos and their Detection

for e^\pm and Compton and photoelectric effect over pair production for photons. At this point, the shower reaches its maximum and

$$t_{\max}^{\text{EM}} = \frac{\ln\left(\frac{E}{E_c}\right)}{\ln(2)} \quad (2.50)$$

is its longitudinal extent in radiation lengths. The *Molière radius*

$$R_M^{\text{EM}} = \frac{21 \text{ MeV}}{E_c} X_0 \quad (2.51)$$

⁶ is the transversal extent of the shower divided by the material density. Both t_{\max}^{EM}
¹ and R_M^{EM} are important benchmarks for the dimensioning of EM calorimeters. Naturally,
² a photon in the energy range where pair production dominates will produce a shower as
³ well. On the other hand, also μ^\pm can start EM cascades, if there energy is high enough
⁴ to produce bremsstrahlung.

Similarly, hadrons interacting with matter via the strong force can produce cascades as well. As opposed to the EM showers governed only by e^\pm and γ , the hadronic process is much more complex because many different secondary particle can be involved. Hadrons start to shower because they mainly interact inelastically with matter, producing secondary strongly interacting particles. That is why the hadronic cross-section

$$\sigma_{\text{total}} = \sigma_{\text{elastic}} + \sigma_{\text{inel}} \quad (2.52)$$

is usually split. From σ_{inel} , one can derive the *interaction length*

$$\lambda_{\text{int}} = \frac{A}{N_A \rho \sigma_{\text{inel}}} \quad (2.53)$$

2. Neutrinos and their Detection

which describes the absorption of hadrons in matter according to

$$N = N_0 e^{-\frac{x}{\lambda_{\text{int}}}} \quad (2.54)$$

with the initial number of hadrons N_0 and number of hadrons N after a distance x of absorber material. For absorbers with $Z \geq 6$, the interaction length is much larger than the radiation length X_0 meaning that hadronic calorimeters usually need to be much larger than their EM counterparts. Experimental data shows that hadronic showers from a few GeV to a few 100 GeV can be approximated by similar parameters as EM showers.

The shower maximum is reached at

$$t_{\max}^{\text{had}} = 0.2 \ln\left(\frac{E}{\text{GeV}}\right) + 0.7 \quad (2.55)$$

interaction lengths. From this, the longitudinal extent containing 95 % is given by

$$L_{0.95}^{\text{had}} = t_{\max}^{\text{had}} + 2.5 \left(\frac{E}{\text{GeV}}\right)^{0.13}, \quad (2.56)$$

in interaction lengths again. Transversally, 95 % of the shower are contained within a cylinder of radius

$$R_{0.95}^{\text{had}} \leq \lambda_{\text{int}} \quad (2.57)$$

⁵ which is independent of the energy and smaller for high-Z materials. [35]

3. The Liquid Argon Time Projection Chamber

¹ The Time Projection Chamber (TPC) is a derivative of Charpak's Multi-Wire Proportional Chamber (MWPC)[36] developed by Nygren in the late 1970s [37]. Crossing charged particles ionise the detection medium which was gaseous in the original design. To prevent the recombination of the ions and electrons, an electric field is applied. In this field, the electrons drift towards a 2D readout plane (an MWPC in the original design). The charge readout is triggered by a scintillation light readout which also provides accurate timing of an event. Using this, one can measure the time for the ionisation electrons to reach the readout plane. As the drift speed of charged particles in the detection medium is constant and if it is known, the coordinate in drift direction can be calculated from the drift time.

¹² While gaseous TPCs already provide very accurate tracking, they have the disadvantage that the target mass and thus, the cross-section of the detection medium is quite low resulting in a low interaction rate. Therefore, in 1977, Rubbia proposed to use Liquid Argon (LAr) as a detection medium [38]. This requires a cryogenic detector while gaseous detectors can be operated at room temperature.

¹⁷ 3.1. Liquid Argon as a Detection Medium

¹ For an efficient particle detection by a TPC, several properties of the sensitive medium are
² of interest, such as ionisation and light yield, electron-ion pair recombination, dielectric
³ strength, length scales of EM and hadronic interactions, density, transparency to its own
⁴ scintillation light, and the boiling point. LAr is quite unique as it has all the necessary
⁵ properties while at the same time it is comparably cheap because it is readily available in
⁶ the Earth's atmosphere. A summary of its properties can be found in Table 3.1. Xenon for
⁷ instance slightly surpasses argon in many aspects but is prohibitively expensive to build
⁸ large detectors. A boiling point of $\approx 87\text{ K}$ raises the need for strong thermal insulation
⁹ and a potent cooling system for LAr, though the requirements are far less stringent than
¹⁰ for liquid helium. This section will outline the most important LAr properties.

Table 3.1.: Properties of LAr taken from [39] where not specified otherwise.

Property	Symbol	Value	Unit
Molar mass	μ	3.9948×10^1	g mol^{-1}
Boiling point at $1.013\,25 \times 10^5\text{ Pa}$	T_S	8.726×10^1	K
Density at T_S	ρ_S	1.399×10^3	kg m^{-3}
Dielectric constant [40]	ε_r	1.504	
Required energy per electron-ion pair	W_i	2.36×10^1	eV
Required energy per photon	W_{sc}	1.95×10^1	eV
Fano factor	F	1.07×10^{-1}	
EM radiation length	X_0	1.4×10^{-1}	m
Hadronic interaction length	λ_{int}	8.37×10^{-1}	m
Peak scintillation wavelength	λ_{scint}	1.28×10^{-7}	m
Scintillation attenuation length	λ_{att}	6.6×10^{-1}	m
Concentration in air by volume		9.34×10^{-1}	%

¹¹ In order to register the ionisations tracks of charged particles in a TPC, two processes
¹² are crucial: production and transportation of charge. The charge production needs
¹³ to be high enough to be detectable by the available electronics. This is given by the
¹⁴ energy required to produce an electron-ion pair W_i . The W_i value of 23.6 eV for LAr

3. The Liquid Argon Time Projection Chamber

¹⁵ is challenging but manageable with contemporary electronics as shown in Section 3.5.

¹ Naturally, this imposes a lower limit on detectable $\frac{dE}{dx}$.

Charge transport is mainly influenced by three processes: *recombination*, *diffusion*, and *lifetime*. The ultimate goal is to collect as much of the produced charge as possible. Recombination is the main process opposing this. While it can be partially mitigated by increasing the electric field, it cannot be eliminated completely. Even if that was possible, it would not be beneficial because the scintillation light needed for the drift time measurement is partly produced by recombining electron-ion pairs. The relation between the strength of the drift field and charge yield can be described by the *box model* [41]. It assumes that the ion-electron pairs are isolated and initially uniformly populate a box of a given size. Furthermore, the diffusion of electrons and ions as well as the ion drift velocity (1×10^5 times smaller than for electrons) are assumed to be negligible. For a produced charge Q_0 and a collected charge Q , the collection ratio is given by

$$\frac{Q}{Q_0} = \frac{1}{\xi} \ln(1 + \xi), \quad (3.1)$$

² with a parameter ξ depending on the drift field, electron mobility, initial number of
³ ion-electron pairs, chosen size of the box and recombination coefficient. Figure 3.1 shows
⁴ a measurement by LHEP of the collected charge in an 8 mm drift LArTPC for different
⁵ drift field intensities and nitrogen concentrations.

Due to thermal motion, ionisation charge clouds will start to diffuse over time. The process is characterised by the diffusion coefficient D . In the presence of a drift field, longitudinal (D_L) and transversal (D_T) components need to be treated separately. The resulting smearing of the ionisation charge cloud after drift time t is given by

$$\sigma_{L/T} = \sqrt{2D_{L/T}t} \quad (3.2)$$

3. The Liquid Argon Time Projection Chamber

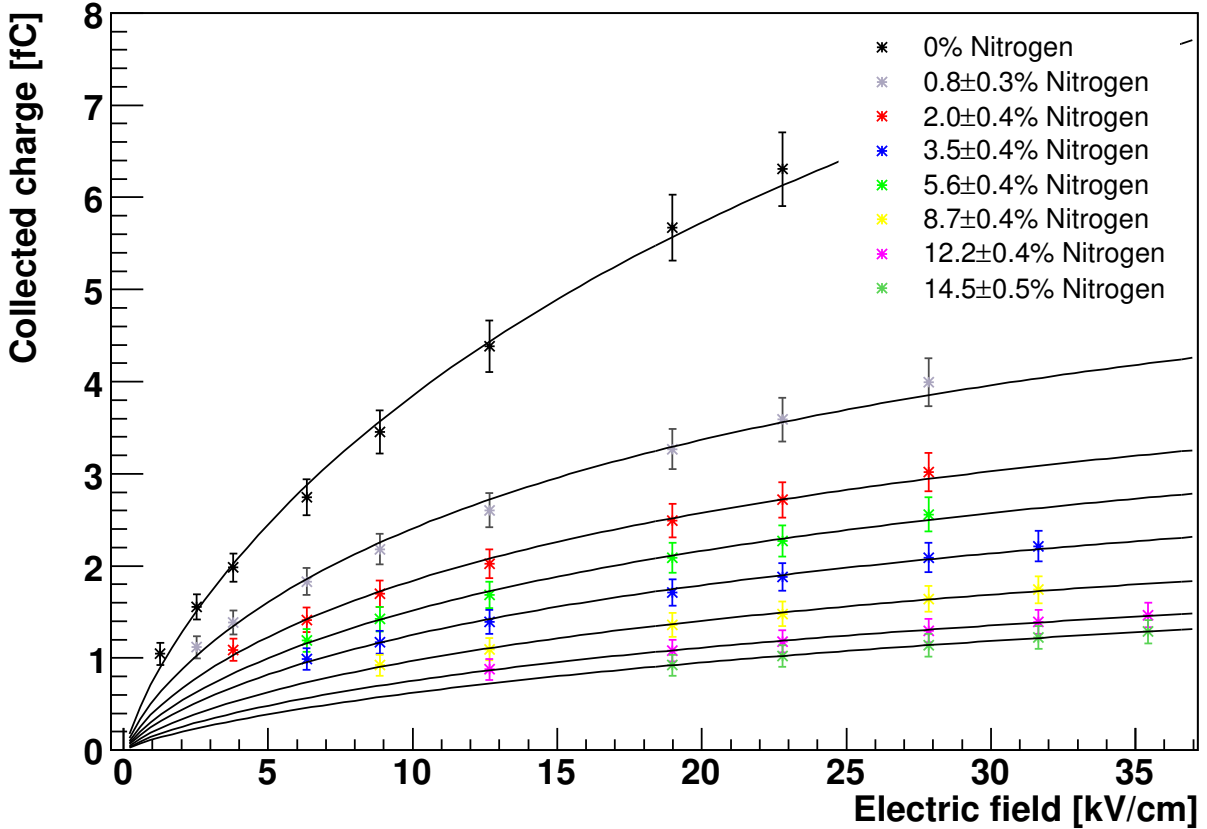


Figure 3.1.: Collected charge in an 8 mm-drift LArTPC as a function of electric field, at various levels of nitrogen concentration. The lines represent box model fits. [42]

for longitudinal and transversal diffusion respectively. Therefore, D has the dimension of area per time. [43]

A third process affecting charge transport is electron trapping by impurities, the probability of an electron becoming attached to an atom in the medium. For the argon itself, this is highly unlikely because its outer electron shell is fully populated. This is one of the reasons why (liquefied) noble gases are a prime choice for TPCs. Nevertheless, drifting electrons can be captured by impurities in the argon. Oxygen is particularly bad due to its high electronegativity. Impurities are therefore often measured in oxygen-equivalent concentration. Finite purity gives rise to a finite lifetime of free electrons in

3. The Liquid Argon Time Projection Chamber

the medium.

$$N_e(t) = N_e(0)e^{-\frac{t}{\tau}} \quad (3.3)$$

² is the charge left after a time t for an electron lifetime τ .

The velocity of the charge drifting in an electric field is related to the so-called mobility, μ , by

$$\vec{v} = \mu(\vec{E})\vec{E}, \quad (3.4)$$

¹ where μ in general depends on the electric field. This means, the higher the field is, the
² higher the charge velocity and thus, the lower the drift time. One wants to keep drift
³ times low for multiple reasons. One of them are the aforementioned impurities. They
⁴ cause the charge to posses a finite lifetime following an exponential decay with time. A
⁵ consequence is that higher impurities can be partially compensated by a higher field.

⁶ In a beam experiment with a given beam timing, increasing the drift time will increase
⁷ pile-up, i.e. the number of events simultaneously present in the detector. Pile-up in turn,
⁸ complicates event reconstruction. On the other hand, the readout electronics need to be
⁹ fast enough to guarantee the required spatial resolution in the drift coordinate which
¹⁰ defines an upper limit for the drift velocity. A reasonable value from a purity point of
¹¹ view is a drift time of ~ 1 ms. For a detector size of ~ 1 m, the required drift speed is
¹² $\sim 1 \text{ mm } \mu\text{s}^{-1}$ which requires a field of $\sim 1 \text{ kV cm}^{-1}$.

¹³ For detectors much larger than 1 m, a drift field of 1 kV cm^{-1} becomes challenging due
¹⁴ to the required high cathode voltage. Soon after entering LArTPC R&D, the LHEP group
¹⁵ realised that the reported dielectric strength of LAr is much lower [2] than measured by
¹⁶ Swan et al. in 1960 [3, 4]. It turned out, opposing the assumption of Swan et al., that
¹⁷ the dielectric strength is not independent of the absolute dimensions of the electrodes.

3. The Liquid Argon Time Projection Chamber

¹⁸ This led to a very detailed study of breakdowns in LAr in the course of this thesis which
¹ is presented in Section 4.1.

<p>¹ Check:</p> <ul style="list-style-type: none">• General specs• Electronegativity• Ionisation• Scintillation• Recombination• Diffusion• Dielectric strength• Single- and dual-phase?• Citations ([39])	
²	

³ 3.2. Electric Field Generation

⁴ For charge separation and drift, an electric field of $\sim 1 \text{ kV cm}^{-1}$ is needed inside the
⁵ fiducial volume of a LArTPC. An easy way to achieve this is by means of field shaping
⁶ rings fed by a resistive divider between cathode and anode. The drawback is the need
⁷ for a feedthrough capable of withstanding the full cathode voltage. One alternative is to
⁸ generate the HV inside the cryostat, for instance using a Greinacher voltage multiplier
⁹ circuit as the one used for the ARGONTUBE experiment at LHEP [44]. A Greinacher
¹⁰ multiplier works by pumping up a cascade of capacitors and diodes using a high frequency
¹¹ source. However, while the voltage generation itself worked well, this approach proved
¹² to be impractical because the high frequency voltage needed to charge the multiplier
¹³ interfered with the readout and therefore had to be turned off during data-taking.
¹⁴ Recharging, in turn, caused a lot of detector down time.

¹⁵ **3.3. Charge Readout**

¹ Classically, the charge readout of a LArTPC is done using wires with a diameter of
² ~ 0.1 mm. One wire plane delivers a 2D projection of the ionisation tracks in the
³ detection medium. This has two consequences:

- ⁴ 1. At least two parallel wire planes are needed to be able to reconstruct the 3D event
⁵ topology.
⁶ 2. In theory, the higher the complexity of the event, the more planes would be required
⁷ to be able to fully reconstruct it.

⁸ Multiple wire planes can be realised by operating only the last one (in drift direction) in
⁹ charge collection mode. All the preceding wire planes are biased in such a way that
¹⁰ they are transparent to the incoming charge but pick up an induction signal during the
¹¹ passage of the latter. A typical number of wire planes for currently operational detectors
¹² is three, tilted at 60° to each other.

¹³ **3.4. Light Readout**

¹⁴ In order to calculate the distance the charge has drifted along the electric field (i.e.
¹⁵ the space coordinate perpendicular to the readout plane), one needs to record the drift
¹⁶ time. The Data Acquisition (DAQ) can record the time of the arrival of the charge at
¹⁷ the readout plane. What is missing is the time of the charge production. This can be
¹⁸ acquired by registering the scintillation light produced alongside the ionisation of the
¹⁹ detection medium. Contemporary detector designs employ PMTs for this purpose. PMTs
²⁰ are a well established technology with a high quantum efficiency and a fast response.

²¹ The light impinging upon a PMT is converted to an electron by a photo cathode coated
²² on the sensitive surface of the PMT. These photo cathodes have a limited absorption

3. The Liquid Argon Time Projection Chamber

²³ spectrum. In particular, the scintillation light of LAr does not fall inside this spectrum
¹ for most photo cathodes. That is why the vacuum UV scintillation light needs to be
² converted to the visible range where it can be efficiently detected by a PMT. A widespread
³ WLS capable of achieving this is TetraPhenyl Butadiene (TPB). Therefore, a common
⁴ setup consists of either coating the PMT [45], or a surface in front of it [46] with TPB.

⁵ 3.5. Charge Readout Electronics

⁶ This section gives an overview of charge readout electronics from the physics perspective.
⁷ A more detailed review is given in Section 4.3. Using W_i , the energy required to produce
⁸ one electron ion pair, from Section 3.1 and assuming a MIP, one gets

$$\frac{dQ}{dx} = \frac{\frac{dE}{dx}\Big|_{\text{MIP}}}{W_i} e = \frac{210 \text{ keV mm}^{-1}}{23.6 \text{ eV}} e \approx 8900 e \text{ mm}^{-1} \approx 1.4 \text{ fC mm}^{-1}$$

⁹ as a rough estimation for the charge yield. This calculation does not incorporate
¹⁰ recombination, diffusion and charge lifetime, meaning that in a real experiment the value
¹¹ will be even lower. The result is that the readout electronics need to be capable of
¹² detecting $\sim 1 \text{ fC}$ charges.

¹³ That is why the charge signal needs to be amplified before digitisation. This is achieved
¹⁴ by means of an integrating amplifier which also converts the charge to a voltage. Early
¹⁵ LArTPC designs used preamplifiers outside the cryostat at room temperature for this.
¹⁶ From a noise point of view though, it is beneficial to put the amplifiers inside the cryostat
¹⁷ submerged in LAr for two reasons. Firstly, the closer to the source the amplifier is
¹⁸ located, the shorter the low-signal lines will be, resulting in less pick-up noise. Secondly,
¹⁹ the temperature-dependent Johnson-Nyquist noise of the amplifiers will be reduced at
²⁰ cryogenic temperatures.

3. The Liquid Argon Time Projection Chamber

For the same reasons it makes sense to operate the entire analogue signal chain at cryogenic temperatures. This would also help to eliminate ground loops which can pick-up noise inductively or provoke self-oscillation of the analog signal circuitry. On the other hand, in general it is not easy to operate a circuit at cryogenic temperatures. Usually, a complete redesign of the circuit is necessary due to most components operating outside their guaranteed temperature range. For some complex active components like the amplifiers and digitisers, even a redesign of the Integrated Circuit (IC) might be necessary. On the other hand, placing the digitisers too close to the readout might result in elevated noise levels due to the digital clocks coupling into the analogue signal path.

The requirements on the electronics are given by the required sensitivity of the detector. The necessary bit depth of the digitisers is given by the required dynamic range, i.e. the minimum and maximum amount of charge the readout needs to be able to register. While the spatial resolution in the two coordinates parallel to the readout plane is given by the pitch of the electrodes, the accuracy of the third coordinate is given by the timing accuracy. This in turn depends on three properties: the timing accuracy of the light readout, the sampling time of the digitisers and the peaking time of the preamplifiers. Peaking time is the time needed until the output of the preamplifier reaches its maximum (peak) for a delta pulse input.

3.6. Challenges of Future Detectors

To accomplish the physics goals of future neutrino detectors, outlined in Chapter 1, much higher statistics than with today's experiments are necessary. There are two obvious ways to do this: Increase the beam flux and detector size. Scaling up a LArTPC brings several challenges, in particular for the drift HV and wire readout planes.

At the same drift field, the cathode voltage scales with the size of the detector in drift direction. This in turn increases the required distance of the cathode from all grounded

3. The Liquid Argon Time Projection Chamber

25 parts. Where the cathode is close to the LAr vessel, this inevitably leads to more dead
1 volume that cannot be used for particle detection. HV problems are worsened by the
2 fact that an increased drift distance also means an increased drift time at the same field.
3 This can either be compensated by increasing the charge lifetime and thus the LAr purity
4 accordingly or by increasing the drift speed and thus the drift field. In summary, at the
5 same LAr purity, the cathode voltage scales more than linearly with detector size in drift
6 direction.

7 Further problems are associated with the classic wire readouts employed in LArTPCs,
8 such as mechanical construction and event pile-up. One of the mechanical requirements
9 on a wire readout is that it should be as planar as possible. Sagging wires caused by
10 insufficient mechanic tension lead to distortions in spatial reconstruction. For large
11 detectors, possessing thousands of wires on a single frame, this becomes quite challenging.
12 Every wire that has a slight deviation in tension from its neighbours will start to sag. This
13 is worsened by the fact that the construction needs to withstand extreme temperature
14 gradients during detector cool-down.

15 The second problem of wires, event pile-up is a consequence of the increased flux
16 required for future experiments. It is rooted in the way event reconstruction works
17 for wires. As mentioned above, effectively, wire planes do not produce real 3D event
18 topologies but rather multiple 2D projections. In order to achieve true 3D events, they
19 need to be disentangled from the 2D projections. If an event is complex enough, this
20 cannot be done unambiguously with a limited number of 2D projections. This problem
21 is especially serious in case of a ND. The envisioned DUNE ND, for instance, is expected
22 to see 0.2 neutrino events per tonne of argon and beam spill (see Table 2.2).

23 On top of the event reconstruction problems, event pile-up also poses a challenge for
24 trigger accuracy. In a monolithic detector, the scintillation light produced alongside
25 the ionisation charge scatters across a large volume triggering a big portion of the light

3. The Liquid Argon Time Projection Chamber

²⁶ readout system. Thus, matching a scintillation flash to the corresponding charge to get
¹ the correct timing of the event is a non-trivial task.

4. Experimental Studies on High Voltage, Charge Readout, and Light Collection

4.1. High Voltage

The difficulties involved with the necessary voltages have been highlighted by the LHEP Group's work, in which I have already played a key role[47]. For the first time, we took high speed footage of breakdowns in LAr, measured their current-voltage characterisitcs and recorded their optical spectral distribution. These measurements help to understand the physics of the breakdowns and develop ways to mitigate them and/or protect future detectors from catastrophic failures. Our High Voltage (HV) studies have already influenced the design of Micro Booster Neutrino Experiment (MicroBooNE) and will continue to impact the design of future experiments.

4.1.1. Experimental Setup

The setup used in this study is very similar to the one described in [2] and is shown in Figure 4.1. A spherical cathode and a plane anode electrode form the discharge gap. Three different diameters of the cathode sphere were tested: 4 cm, 5 cm and 8 cm. Two

4. Experimental Studies on High Voltage, Charge Readout, and Light Collection

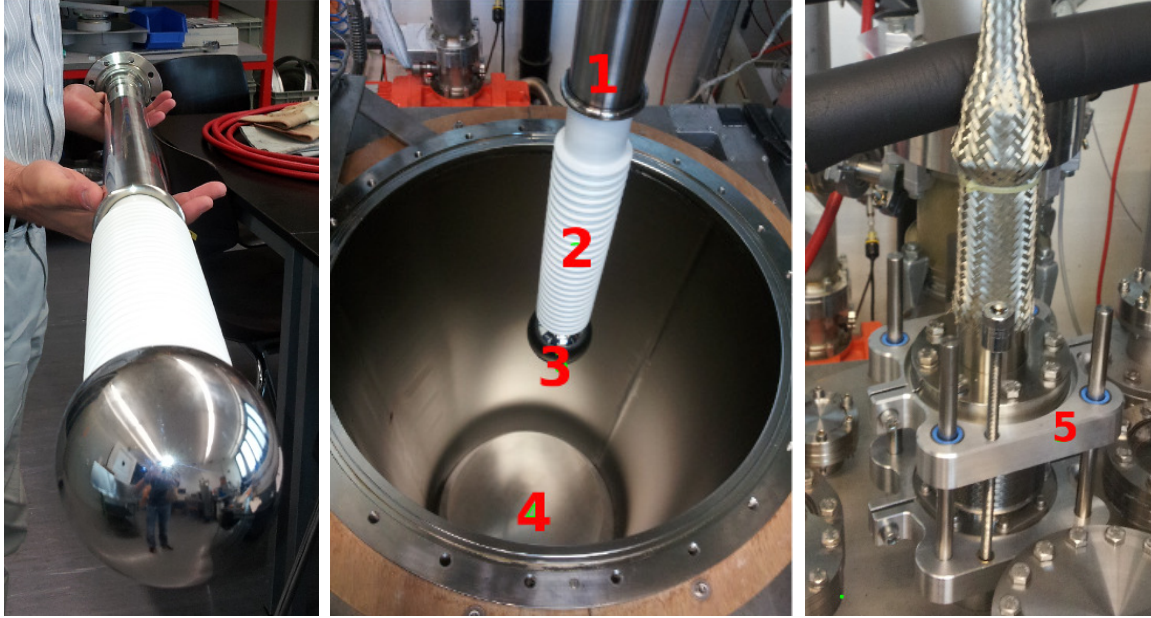


Figure 4.1.: Experimental setup. Left: HV feed-through with the spherical cathode. Middle: the feed-through before insertion into the cryostat. 1. ground shield of the feed-through; 2. ribbed PET-C dielectric; 3. cathode sphere; 4. anode plate sitting on a tripod on the grounded bottom of the cryostat; two of the tripod legs are insulated while the third one contains a 50Ω shunt resistor. Right: linear translation unit used to set the cathode-anode gap width (5).

¹⁶ types of surface treatment were used in the cathode preparation, namely mechanical fine
¹ polishing and electro-polishing. For the anode, mechanical fine polishing was used for all
² measurements. The anode-cathode gap width can be set in the range of 0 mm to 100 mm
³ with a precision of 0.3 mm. An example of the field distribution in the setup is shown in
⁴ Figure 4.2. The field map was calculated using the COMSOL Finite Element Method
⁵ (FEM) package.¹

⁶ The purity of the argon after filling was estimated with a small TPC chamber
⁷ (according to the method described in [48]) to be ~ 1 ppb of oxygen-equivalent impurity
⁸ concentration. More details of the setup can be found in [2].

⁹ The control circuit of the *Spellman SL150*² Power Supply Unit (PSU) outputs two low

¹<http://www.comsol.com>

²<http://www.spellmanhv.com>

4. Experimental Studies on High Voltage, Charge Readout, and Light Collection

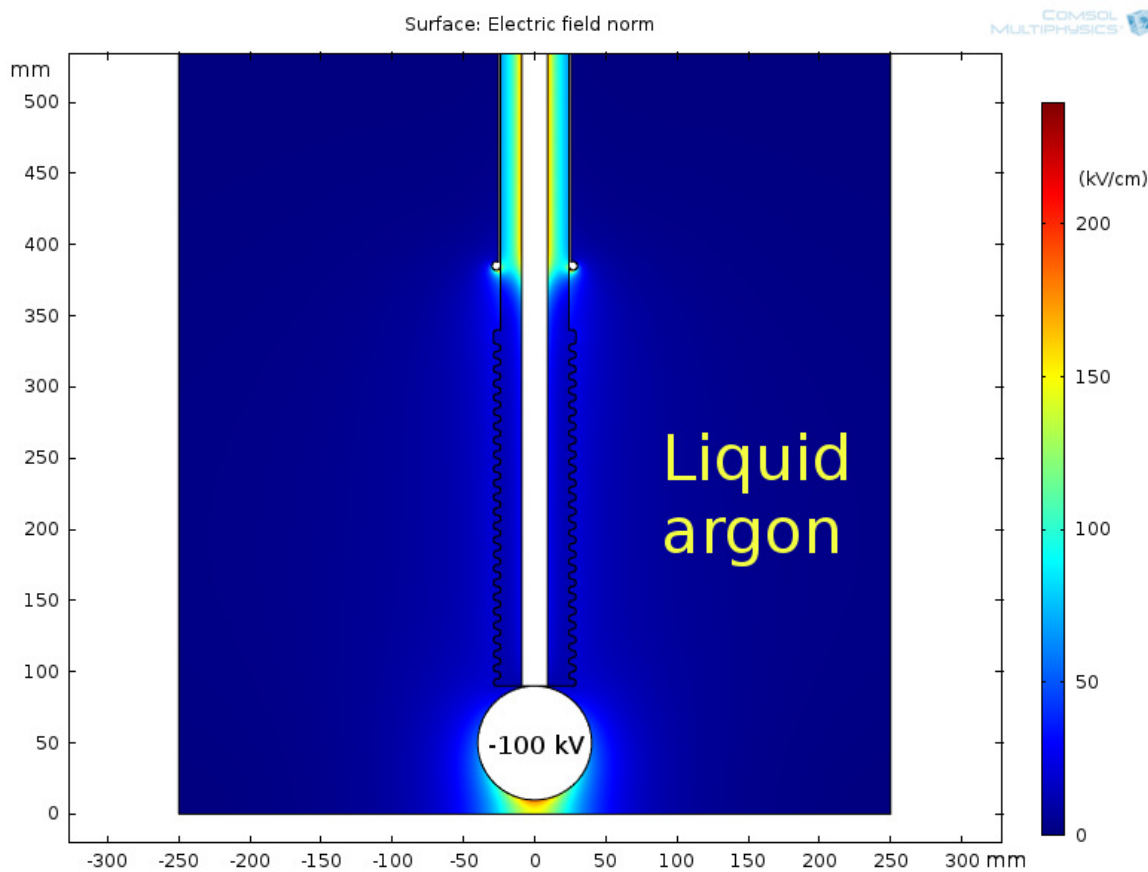


Figure 4.2.: Calculated electric field amplitude map for the test setup with -100 kV at the cathode and cathode-anode distance of 1 cm.

voltages proportional to the voltage and the current at the output, respectively. These voltages are recorded with a *Tektronix DPO 3054*³ digital oscilloscope. The output polarity of the PSU can be switched by replacing the output HV multiplier module. To measure the discharge current, a 50Ω shunt resistor is placed between the anode plate and the vessel ground which is connected to the ground return of the PSU. The voltage drop across the shunt resistor is transmitted via a matched coaxial line to the oscilloscope. The latter is controlled by a LabVIEW program. The equivalent electric schematic of the setup is shown in Figure 4.3. The voltage at the V_{mon} output of the power supply corresponds to the PSU output voltage divided by a factor K_V . The voltage at I_{mon}

³<http://www.tek.com>

4. Experimental Studies on High Voltage, Charge Readout, and Light Collection

is related to the PSU output current. However, according to the manufacturer of the PSU, an accurate reconstruction of the output current for frequencies above 100 Hz is not possible because of a filtering circuit in the current control loop. Therefore, for the measurement of the discharge current only the voltage drop across the shunt resistor is used.

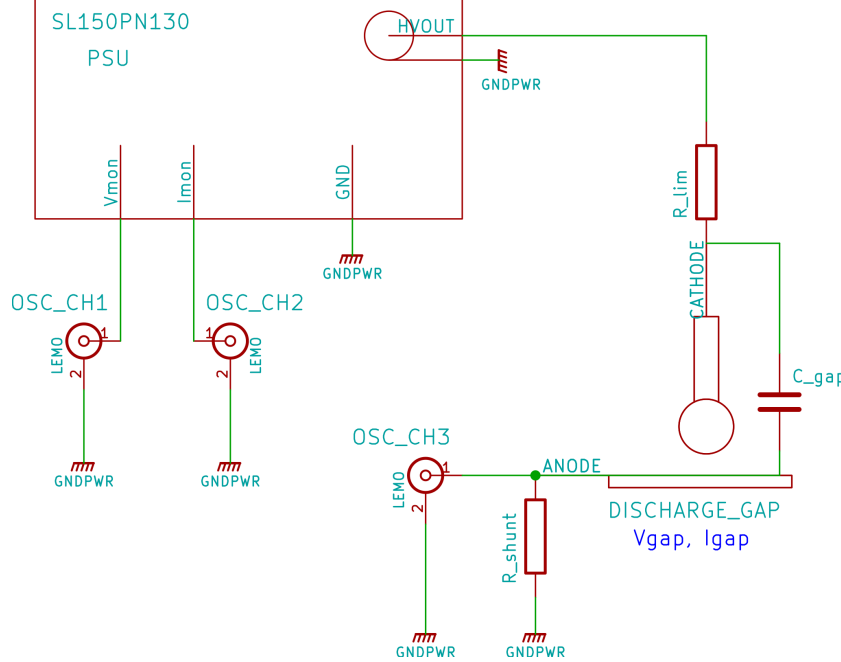


Figure 4.3.: Electric schematic of the experimental setup. The oscilloscope is connected to the control circuit of the HV power supply and to a shunt resistor on the ground return path. From the recorded voltages, the voltage and the current of the discharge can be derived.

The oscilloscope is triggered by the channel connected to the shunt resistor. The breakdown discharge current is composed of the output current of the PSU and the discharge current of the setup capacitance C_{gap} as $I_{\text{gap}} = I_{\text{out}} + C_{\text{gap}} \frac{dV_{\text{gap}}}{dt}$. To limit the PSU output current an additional resistor R_{lim} is inserted into the HV output circuit. The measured values for the circuit parameters are summarized in Table 4.1. The knowledge of these parameters allows to calculate the voltage across the gap during breakdown.

4. Experimental Studies on High Voltage, Charge Readout, and Light Collection

Table 4.1.: Summary of the measured parameters of the test circuit.

Parameter	Value	Unit
K_V	42.3×10^{-6}	
R_{shunt}	50	Ω
R_{lim}	200	$M\Omega$
C_{gap}	370	pF

11 In addition, the setup is equipped with an *AOS Technologies S-PRIPlus*⁴ high-speed
 1 camera to observe the development of the discharge. The camera is capable of recording
 2 700×400 pixel Red Green Blue (RGB) images at 1230 fps. The camera comprises a
 3 frame ring buffer and is triggerable by an external Transistor-Transistor-Logic (TTL)
 4 pulse. This allows a synchronous recording of the visual appearance of the discharge
 5 and its volt-ampere characteristics. The camera is triggered from the trigger output of
 6 the oscilloscope. The luminous part of the discharge is analysed for each frame of the
 7 recorded sequence.

8 The camera is mounted above a 5 cm diameter glass view port, located at the top
 9 flange of the cryostat and is looking downward. To observe a discharge from the side, a
 10 glass mirror plate is installed at the edge of the cathode plane located 20 cm from the
 11 cathode, in such a way as to not perturb the electric field in the discharge gap.

12 Finally, a custom built optical spectrometer is used to analyze the light emission of
 13 the discharges. The spectrometer is connected to an optical fiber entering the cryostat
 14 with its other end attached to the anode plate. The fiber is aligned such that its end
 15 directly faces the discharge gap resulting in a high angular acceptance. As will be shown
 16 later, the discharge emission spectra allow to better understand the processes at different
 17 stages of the discharge. This is due to the fact that the emission spectra of excited
 18 neutral atomic argon, singly-ionized and multiply-ionized atoms lay in different regions
 19 of the visible spectrum.

⁴<http://www.aostechnologies.com>

4. Experimental Studies on High Voltage, Charge Readout, and Light Collection

20 The possibility of creating gas bubbles near the discharge gap is inhibited by keeping
1 the pressure in the inner vessel at 100 mbar above atmospheric pressure, plus an additional
2 100 mbar due to the hydro-static pressure. The outer bath is opened to the atmosphere,
3 thus keeping the inner vessel temperature constant and well below the boiling point. No
4 boiling was detected anywhere near the discharge gap region during the measurements.

5 **4.1.2. Results**

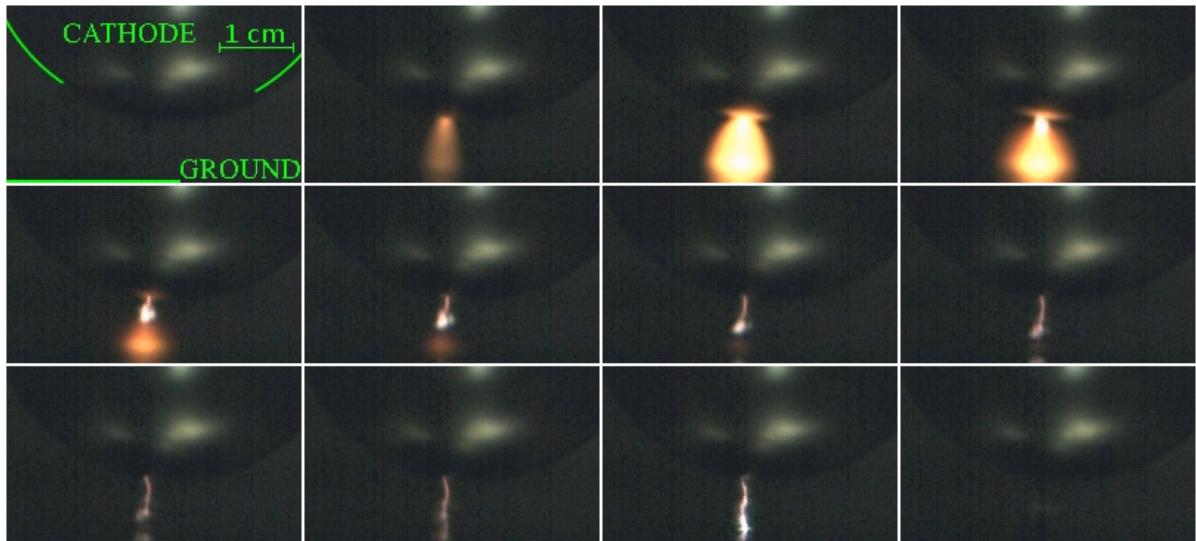


Figure 4.4.: Recorded camera image sequence for a breakdown from a 5 cm diameter cathode at -100 kV and 8.8 mm apart from the anode plate. The sequence is taken at 1250 fps, each frame takes 0.8 ms.

6 In earlier measurements [2], sporadic discharges were experienced across the ribs of
7 the dielectric of the HV feed-through. By rising the level of the LAr by about 20 cm,
8 it was possible to suppress these discharges completely. This improved the cooling of
9 the feed-through and reduced bubble production near the bottom of the feed-through
10 grounded shield, placed 60 cm below the liquid surface.

11 The measurement campaign comprised 5 runs with a total of more than 5000 measured
12 discharges, with varying sphere diameter, surface treatment and polarity. A summary is

4. Experimental Studies on High Voltage, Charge Readout, and Light Collection

13 shown in Table 4.2. A typical recorded camera image sequence for breakdown from a
 1 5 cm diameter cathode at -100 kV and 8.0 mm apart from the anode plate is shown in
 2 Figure 4.4. The movie can be found as *movie1.webm* in the ancillary files of [47].⁵

Table 4.2.: Summary of the breakdown measurement runs.

Run	$\varnothing_{\text{Sphere}}[\text{cm}]$	Surface finish	Sphere polarity	Events	$d_{\text{Gap}}[\text{mm}]$	$V_{\text{Breakdown}}[\text{kV}]$
1	4	Mech. polished	Cathode (-)	1086	0.5 to 8.0	3 to 130
2	5	Mech. polished	Cathode (-)	900	0.2 to 12.0	2 to 130
3	8	Mech. polished	Cathode (-)	2434	0.1 to 70.0	1 to 130
4	5	Mech. polished	Anode (+)	102	4.0 to 5.0	5 to 114
5	5	Electro-polished	Cathode (-)	1141	0.1 to 10.0	1 to 130

3 In Figure 4.5, the current and voltage features of a similar breakdown is shown from
 4 a 4 cm diameter cathode at 6.0 mm from the anode plate. The current was directly
 5 measured by observing the voltage drop across the shunt resistor, while the voltage
 6 was obtained by integrating the current taking into account the gap capacitance, the
 7 protection resistor and the output voltage of the power supply. When using the measured
 8 values of Table 4.1 for capacitance and resistance, this results in a negative voltage at
 9 the end of most discharges. This is an unphysical result as can be seen in the top plot of
 10 Figure 4.5. This behavior may be attributed to poor knowledge of the effective values of
 11 the current-limiting resistor and the setup capacitance in the frequency domain of the
 12 discharge. In order to better approximate these parameters, they are tuned in such a way
 13 that the minimum voltage for a maximum number of discharges approaches zero. The
 14 best result was achieved by lowering the resistance by a factor of 1.7 and increasing the
 15 capacitance by the same factor. Interestingly, this result leaves the *RC* characteristics

⁵<http://arxiv.org/src/1512.05968v2/anc/movie1.webm>

4. Experimental Studies on High Voltage, Charge Readout, and Light Collection

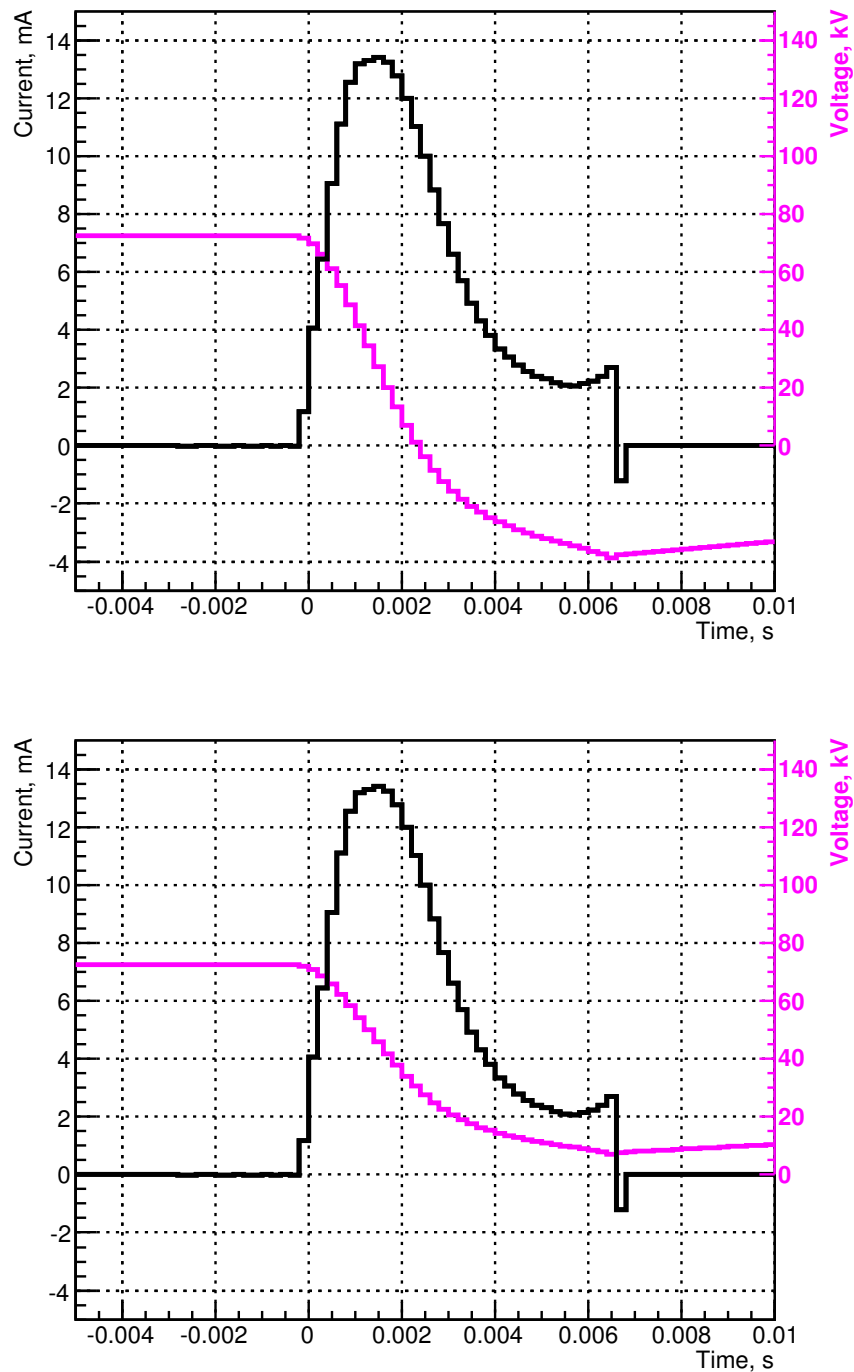


Figure 4.5.: Measured current through the gap (black) and voltage across the gap (magenta) for a typical breakdown at 6.0 mm distance between a 4 cm diameter cathode and the anode plate. The top plot shows the voltage obtained using the measured values of the protection resistor and the gap capacitance, while the bottom plot uses the tuned values.

4. Experimental Studies on High Voltage, Charge Readout, and Light Collection

of the system unchanged. The bottom plot of Figure 4.5 shows the result obtained by using the tuned values for capacitance and resistance.

Most of the discharges are localized in the area of high field concentration between the tip of the sphere and the anode plane. However, in rare cases, the discharge is initiated far from that region, sometimes at the side surface of the sphere. An example of such a discharge is shown in Figure 4.6 and the corresponding movie can be found as *movie2.webm* in the ancillary files of [47].⁶



Figure 4.6.: An image of the streamer stage of the discharge, initiated at the side surface of a 5 cm cathode sphere at -121.5 kV and 8.0 mm apart from the anode plate. The cone of electrons emitted into liquid from the streamer tip towards the anode (lower edge of the image) produces bright orange luminescence in LAr.

⁶<http://arxiv.org/src/1512.05968v2/anc/movie2.webm>

4.1.3. Interpretation

As it was shown in [49, 50], experimental data on breakdowns in liquefied noble gases suggest the following dependence for the maximum field at the breakdown: $E_{max} = C \cdot A^p$, where C is a material-dependent constant, A is the stressed area with an electric field intensity above 90 % of its maximum, and $p \approx -0.25$. In Figure 4.7, data available in literature is combined with those obtained from the measurements performed within the scope of this thesis as well with earlier measurements performed at LHEP. Each data point is the mean value of all measurements of one run taken at the same gap distance and therefore with the same stressed area. The global best fit gives the following values for the parameters: $C = 139 \pm 5$ and $p = -0.22 \pm 0.01$. The statistical uncertainties represented by the error bars (smaller than the marker where not shown) are small compared to the unknown systematic uncertainties. Indications for this are the high spread of the points around the fit line and the high reduced chi-square of 7283.

Figure 4.8 shows the recorded spectra of a typical event. The spectra are integrated over 1 ms and approximately correspond to frames 3 (blue) and 8 (red) in Figure 4.4. From the observation of the spectra of the emitted light and the discharge appearance, one can distinguish three phases of the breakdown development. The first phase starts with the field emission of electrons from a point of the cathode metal surface. The emitted electrons drift to the anode, ionizing and exciting argon atoms. Frames 2 and 3 of Figure 4.4, the broad current peak of the current in Figure 4.5, and the blue curve in Figure 4.8 show the development of the emission. Evidence for the presence of ionization comes from the analysis of the emission spectrum in the cone formed by drifting electrons.

The emission of light by charged particles drifting in noble liquids under the influence of an electric field (electro-luminescence) gained great interest in the last years. Recent studies in this field are well covered by [51–53] and references therein. The red electro-luminescence, namely the peak around 700 nm of the red curve in Figure 4.8, produced

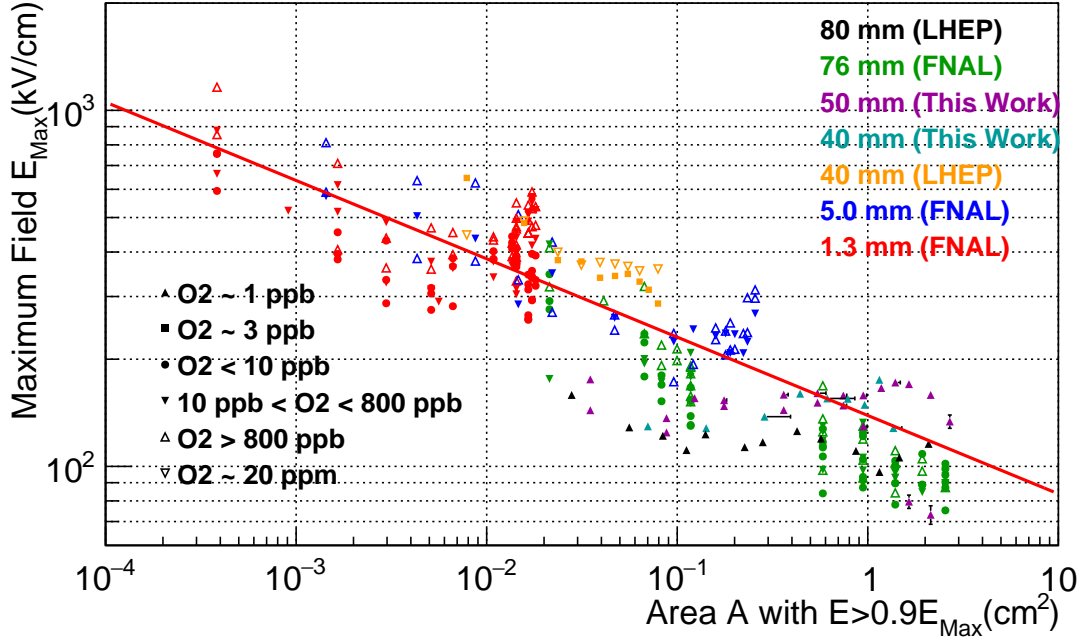


Figure 4.7.: Breakdown field versus stressed area of the cathode. The stressed area A is defined as the area with an electric field intensity greater than 90 % of the maximum electric field intensity in the gap. The fit line represents the dependence $E_{max} = C \cdot A^p$ with $C = 139 \pm 5$ and $p = -0.22 \pm 0.01$. The colours correspond to different cathode sphere diameters while the marker styles correspond to different oxygen-equivalent impurity concentrations. The data are taken from [49] (FNAL), [2] (LHEP), and [47] (this work).

26 by electrons drifting in argon gas is attributed to the $3p^54p - 3p^54s$ transition of neutral
 1 argon [54]. The energy needed for the excitation of the electrons to the $3p^54p$ states
 2 from the ground state in argon gas is 12.9 eV to 13.5 eV. The ionization potential of
 3 LAr is 13.84 eV [48]. For the condensed state, only the scintillation spectrum under
 4 ionization by high-energy charged particles has been described in literature so far [55].
 5 The electro-luminescence spectrum measured (blue curve in Figure 4.8) exhibits a broad
 6 continuum, similar to the scintillation spectrum. However, the center value at about
 7 580 nm does not correspond to any of the electron transitions of neutral, singly- or
 8 doubly-ionized argon atoms. The nearest candidate for such an emission is the residual

4. Experimental Studies on High Voltage, Charge Readout, and Light Collection

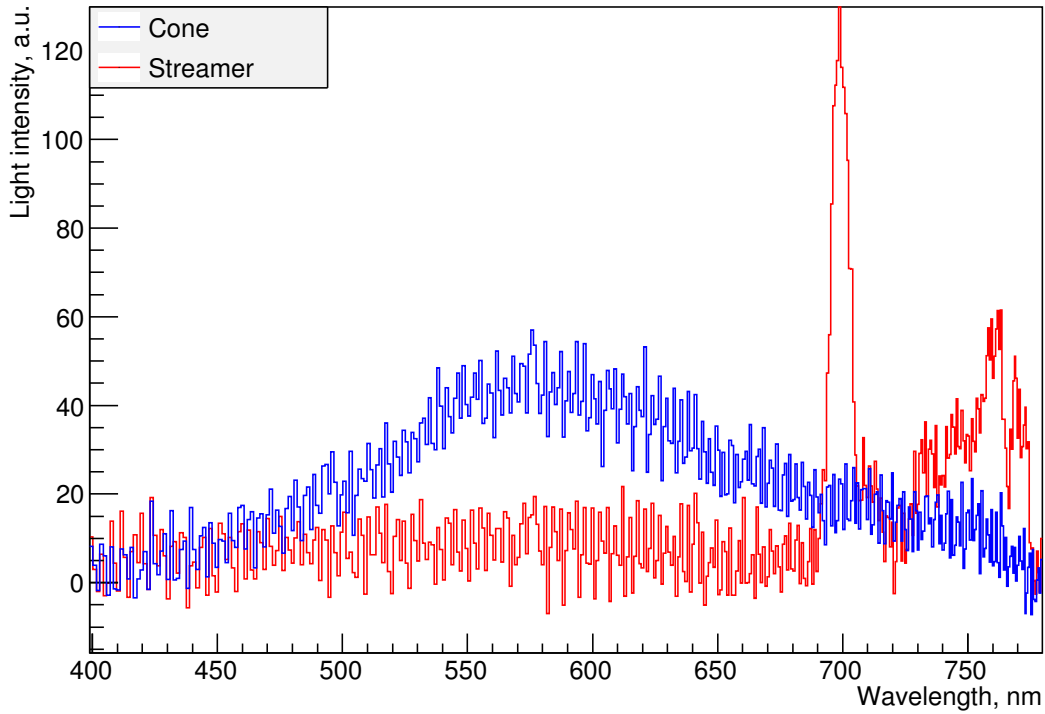


Figure 4.8.: Spectra of the field emission cone (blue) and the streamer (red) for a breakdown from a 4 cm diameter cathode at -56.2 kV and 3.0 mm apart from the anode plate. The spectra were integrated over a time of 1 ms with the spectrum of the streamer taken 2 ms after the spectrum of the cone. The blue curve is a broad continuum similar to the scintillation spectrum of LAr, while the red curve features a distinct peak around 700 nm which is attributed to the $3p^54p-3p^54s$ transition of neutral argon gas.

oxygen with its strong 557.7 nm emission line. However, if attributable to oxygen, this
line has to also be observed at the later stages of the discharge, which does not take
place in the measurements.

The broad width of the spectrum could be explained by smearing the energy levels
into bands due to inter-atomic interactions in liquid and by the formation of exciton
clusters [56, 57]. If the energy band structure of excitons in LAr is continuous, as
suggested by the scintillation spectrum, there might be a significant overlap of the band
corresponding to the $3p^54p$ atomic levels and the conduction band above 13.84 eV. The

4. Experimental Studies on High Voltage, Charge Readout, and Light Collection

⁸ presence of an observable emission at about 580 nm, in this case, is inevitably linked to a
¹ presence of ionized states.

² Another signature of avalanche ionization in this phase of the breakdown is the
³ increase of the cone brightness as it develops from the cathode towards the anode.
⁴ Figure 4.9 shows this increase together with the fit avalanche multiplication parameter
⁵ $\alpha = (0.15 \pm 0.03) \text{ mm}^{-1}$ for the following gap conditions: voltage across the 7.0 mm
⁶ gap $V = 54.0 \text{ kV}$, cathode sphere diameter of 4 cm, maximum field in the gap $E_{\max} =$
⁷ 96.1 kV cm^{-1} , mean field in the gap $\langle E \rangle = 87.0 \text{ kV cm}^{-1}$. To calculate the emission
⁸ intensity the raw values of all pixels of the camera image were summed up that were in a
⁹ row perpendicular to the cone direction. The distance from the cathode can be derived
¹⁰ from the known gap distance. From the fit, the given statistical uncertainty of α was
¹¹ obtained. As only one measurement was taken, it is not possible to state anything about
¹² unknown systematic uncertainties (for instance the calibration of the camera).

¹³ As already suggested in [2], positive ions produced in this process drift towards the
¹⁴ cathode, raising the surface field and provoking a rapid increase of the field emission
¹⁵ current to values $\sim 1 \text{ mA}$. Ions bombarding the cathode surface raise the local temperature
¹⁶ and, after 1 ms to 2 ms, the liquid near the initial discharge point transitions to a gas phase,
¹⁷ forming a bubble. Both the first and the second avalanche multiplication coefficients are
¹⁸ a few orders of magnitude higher in gas than in liquid. Therefore, the ionization density
¹⁹ in the gas bubble quickly rises along with the conductivity of the formed plasma. This
²⁰ leads to a decrease of the electric field in the close vicinity of the field emission point
²¹ and to the suppression of a further growth of the field emission current. Accelerated
²² electrons of the gas plasma hit the gas-liquid interface, forcing the bubble to elongate
²³ and grow. In the region behind the head of the streamer the filament is collapsed to
²⁴ a diameter below 200 μm (the spatial resolution of the camera) by surface tension and
²⁵ electro-striction forces. This second phase of the discharge is characterized by the growth

4. Experimental Studies on High Voltage, Charge Readout, and Light Collection

of the streamer-like filament in liquid. In Figure 4.4 (frames 4 to 10), one can see the development of such a filament. Unlike the electrons in the first phase the filament does not follow the electrostatic field lines but it rather rambles around their direction, being subject to thermodynamic fluctuations at the tip of the growing streamer where the liquid-gas transition happens. The spectrum of the light emission from the streamer has a distinct line at about 700 nm, a characteristic feature of the plasma in argon gas.

Finally, when the streamer reaches the anode a short peak of light emission is registered (frame 11 in Figure 4.4) with the blue-green spectral component dominating (Figure 4.10). This phase is characterized by an acoustic shock and a massive production of gas bubbles in the region of the discharge. These effects are typical for an arc discharge in argon gas. The spectrum of the light emission in this phase is shown in Figure 4.10.

As it was demonstrated in [55], the transition from the liquid phase to the gas phase for scintillation manifests itself by the appearance of sharp spectral lines while in liquid, the emission spectrum is continuous and without features. This behaviour is also suggested by the two spectra in Figure 4.8. While the spectrum is continuous during the field emission phase, there is a distinct peak at around 700 nm several ms later.

It is worth mentioning that not every streamer results in a third phase spark. For those streamers started from the side of the cathode sphere, the charge needed for streamer growth might exceed the total charge available in the system. Such streamers extinguish before reaching the anode without an acoustic shock or any other additional effects. On the other hand, in some cases the filament quickly transits to a third stage before it reaches the anode. One possible explanation for this is that, if the filament current exceeds a given threshold, the filament loses its thermodynamic stability and expands into a gas bubble in which the arc discharge quickly develops afterwards.

In Figures 4.11 to 4.15, several correlations of measured and calculated parameters of the breakdowns are shown. For some of these plots, 18 events were selected with

4. Experimental Studies on High Voltage, Charge Readout, and Light Collection

recorded current characteristics similar to Figure 4.5. As a comparison, the bottom plot of Figure 4.11 shows the data of all events with current characteristics including events not possessing a distinct plateau as the one visible in Figure 4.5. The discrepancy to the total number of events in Table 4.2 arises, on the one hand, because the shunt resistor was installed only in the last run and, on the other hand, since the latter was damaged after the events shown in the bottom plot of Figure 4.11. The low number of events in the selection is due to the fact that an automated analysis of the current characteristics can only detect very long streamers. This also explains the behaviour of the charge in Figure 4.11. The selected streamers last for several ms, almost always consume the whole charge in the system and then cease without transitioning to a spark. The slight excess in charge compared to the charge in the gap capacitance (red line) is likely supplied by the PSU before tripping. Contrary to this, the bottom plot showing all the events contains many events that do not consume all the stored charge and result in a spark. The good match between the red curve and the data points serves also as a cross-check of the tuned capacitance.

Figure 4.12 shows the behavior of the peak current versus the breakdown field, suggesting a proportionality between the two with the coefficient of about $60 \mu\text{A cm kV}^{-1}$. The field was calculated by dividing the breakdown voltage by the gap distance. Therefore, this is a mean value along shortest path and does not directly apply to the selected events as most of them emerged from the side of the sphere.

Figures 4.13 and 4.14 show the correlation of the current during the streamer phase (the plateau in Figure 4.5) with the peak current and the breakdown field. The plateau current clearly rises with both the breakdown field and the peak current. Together with Figure 4.12 this indicates that for higher fields, higher currents flow during both field emission as well as streamer phases. As mentioned above, the plateau current could only be reliably detected for the selected events which is why these plots are not shown for all

4. Experimental Studies on High Voltage, Charge Readout, and Light Collection

26 events.

1 Finally, Figure 4.15 depicts the dependence of the streamer velocity on the breakdown
2 field. Again, the velocity is only a lower limit as it was calculated by dividing the gap
3 distance by the duration of the streamer, which is not correct for streamers emerging
4 from the side of the sphere. There are two distinct types of events. While the selected
5 streamers are rather slow (velocity $\approx 300 \text{ mm s}^{-1}$, independent of the field), the whole
6 data set contains much faster events with the total time in the ns scale (not shown). The
7 knowledge of the streamer velocity can be applied in the design of protection circuits
8 for future LArTPCs. If a breakdown condition is detected during the streamer phase,
9 the HV can be killed prior to a disruptive spark phase potentially damaging sensitive
10 detector electronics.

11 **4.1.4. A Method to Suppress Electric Breakdowns in Liquid Argon**

12 As a result of the thorough characterisation of breakdowns in LAr, a way was found
13 to suppress them by coating the field cage with latex. It was possible to increase the
14 voltage by a factor of 10 using this technique. This study has been published in [58].

15 The setup was the same as the one used to study the breakdowns, described in
16 Section 4.1.1. Additionally, the cathode sphere was coated by a layer of polymer. In order
17 to effectively suppress electric breakdowns, the coating needs to have a high dielectric
18 strength while at the same time staying elastic at cryogenic temperatures (87 K for a
19 LAr detector). Furthermore, the excess electron mobility of the coating needs to be
20 significantly lower than the one of LAr. If this is the case, electrons emitted by the
21 cathode via field emission can accumulate inside the coating layer and in turn locally
22 reduce high fields and thus quench the field emission.

23 Natural polyisoprene (latex rubber) is a polymer that satisfies the above requirements.
24 Its dielectric strength is reported to be in the range of 1 MV cm^{-1} to 2 MV cm^{-1} [59],

4. Experimental Studies on High Voltage, Charge Readout, and Light Collection

its dielectric constant is 2.1 which is close to the 1.6 of LAr, and its room temperature resistivity is $1 \times 10^{16} \Omega \text{ cm}$. A polyisoprene layer of several 100 μm can be deposited on the sphere by dipping the latter in purified latex milk. After drying at room temperature, the coating is leached in deionised water for several hours and finally vulcanised at 70 °C for one hour. Leaching is needed to remove all soluble pollutants contained in natural latex while the vulcanisation increases the tear strength of the coating. Like this, the polyisoprene layer keeps its integrity and does not crack even after multiple fast cool-down and warm-up cycles to 87 K and back to room temperature, respectively.

In the first measurement, a 4 cm cathode sphere coated with 450 μm of polyisoprene was used. The test was started at cathode anode gap width of 5 mm and the voltage was ramped up from 0 kV to 130 kV at 50 V s^{-1} . After no breakdown could be observed for several hours, the gap width was decreased to 4 mm after ramping down the voltage. Again, no breakdown occurred for several hours and subsequently, the gap was decreased to 3 mm. During this third ramp-up, there was a breakdown at 112 kV. This corresponds to a maximum electric field intensity across the gap of 412 kV which is more than one order of magnitude higher than the required field intensity to provoke breakdowns from an uncoated cathode [2, 47]. A summary of the results is given in Table 4.3.

Table 4.3.: Summary of the breakdown test measurements with 200 μm and 450 μm thick polyisoprene layers coated 5 cm and 4 cm diameter spheric cathodes, respectively.

$d_{\text{Gap}} [\text{mm}]$	$E_{\text{max}} [\text{kV cm}^{-1}]$	$\varnothing_{\text{Sphere}} [\text{cm}]$	Polyisoprene thickness [μm]	Breakdown
5.0	298	4	450	no
4.0	358	4	450	no
3.0	412	4	450	yes
3.0	296	5	200	yes

4. Experimental Studies on High Voltage, Charge Readout, and Light Collection

¹⁷ 4.1.5. HV Summary

¹ A study of the visible light emission was performed for electrical breakdown in LAr near
² its boiling point with cathode-anode distances ranging from 0.1 mm to 10.0 mm with a
³ spherical cathode and a plane anode geometry. Three discharge development phases were
⁴ identified by observing the discharge appearance and the time development of visible
⁵ light emission. The dependence of several breakdown parameters on the critical field
⁶ was studied, as well. For the first time, it was found that the streamer propagation
⁷ velocity is about 300 mm s^{-1} and independent of the field intensity. The streamer phase
⁸ is characterized by a current peak of the order of 5 mA to 15 mA depending on the
⁹ breakdown field, followed by a plateau at about ten times lower current level.

¹⁰ The deposition of a few hundred μm thick polyisoprene layer on the surface of a spheric
¹¹ stainless steel cathode immersed in LAr allows to efficiently suppress field emission
¹² of electrons from the cathode surface and to reach significantly higher electric fields
¹³ intensities for cathode-ground distances of several mm. A field strength as high as
¹⁴ 412 kV cm^{-1} was reached. This solution allows to design and operate LArTPCs keeping
¹⁵ the volume of liquid outside of the electron drift region comparatively much smaller than
¹⁶ for the case of non coated cathode surfaces.

¹⁷ However, it was also found that the employed latex coating is very fragile. In particular,
¹⁸ it loses its protective function after a single breakdown. This makes an application in
¹⁹ a physics experiment impractical. Currently, a safe LArTPC operation can only be
²⁰ guaranteed by keeping electric fields below 40 kV cm^{-1} at all points in the detector.
²¹ Therefore, either low cathode voltages or large inactive volumes around the cathode are
²² required.

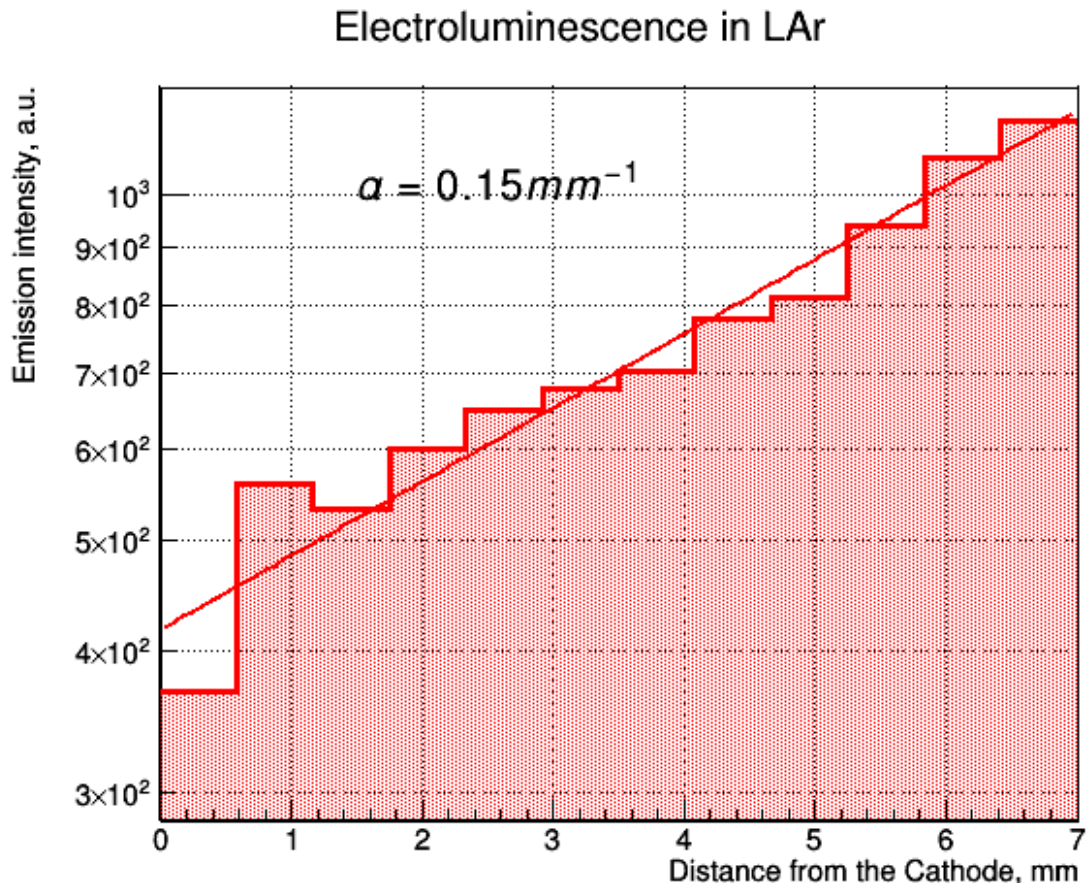


Figure 4.9.: Increasing brightness of the electro-luminescence cone as it develops towards the anode. The line represents the exponent with a fit avalanche multiplication parameter of $\alpha = (0.15 \pm 0.03) \text{ mm}^{-1}$ for gap conditions: voltage across the 7.0 mm gap $V = 54.0 \text{ kV}$, cathode sphere diameter of 4 cm, maximum field in the gap $E_{\max} = 96.1 \text{ kV cm}^{-1}$, mean field in the gap $\langle E \rangle = 87.0 \text{ kV cm}^{-1}$.

4. Experimental Studies on High Voltage, Charge Readout, and Light Collection

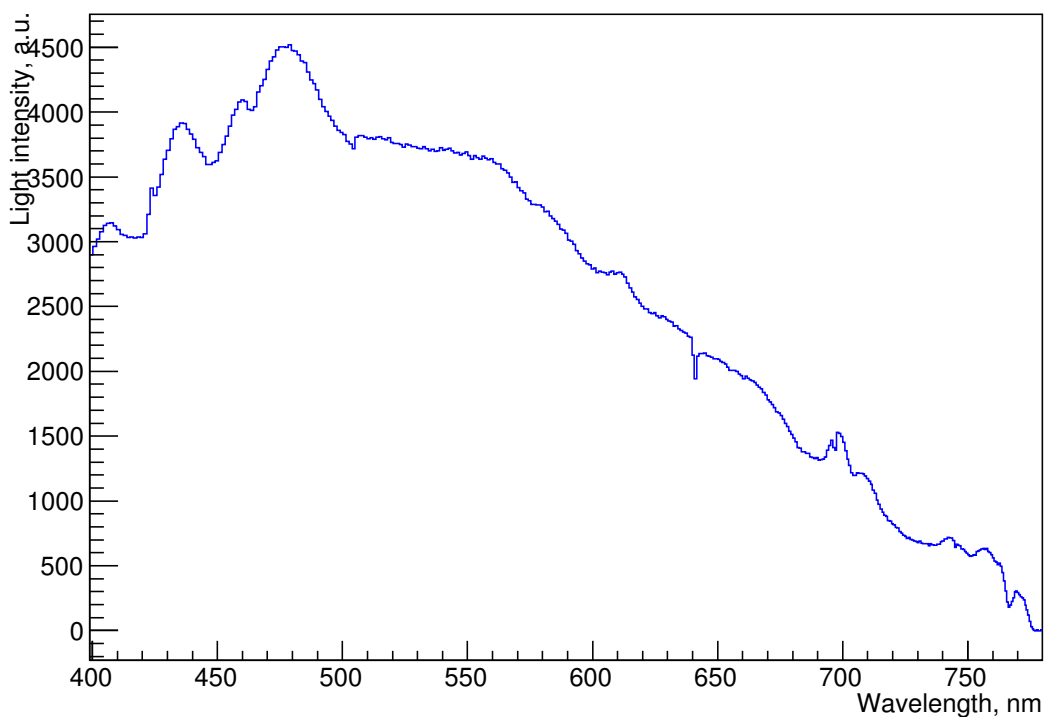


Figure 4.10.: Spectrum of the spark for a breakdown from a 4 cm diameter cathode at -39.7 kV and 4.0 mm apart from the anode plate. The spectrum was integrated over a time of 1 ms.

4. Experimental Studies on High Voltage, Charge Readout, and Light Collection

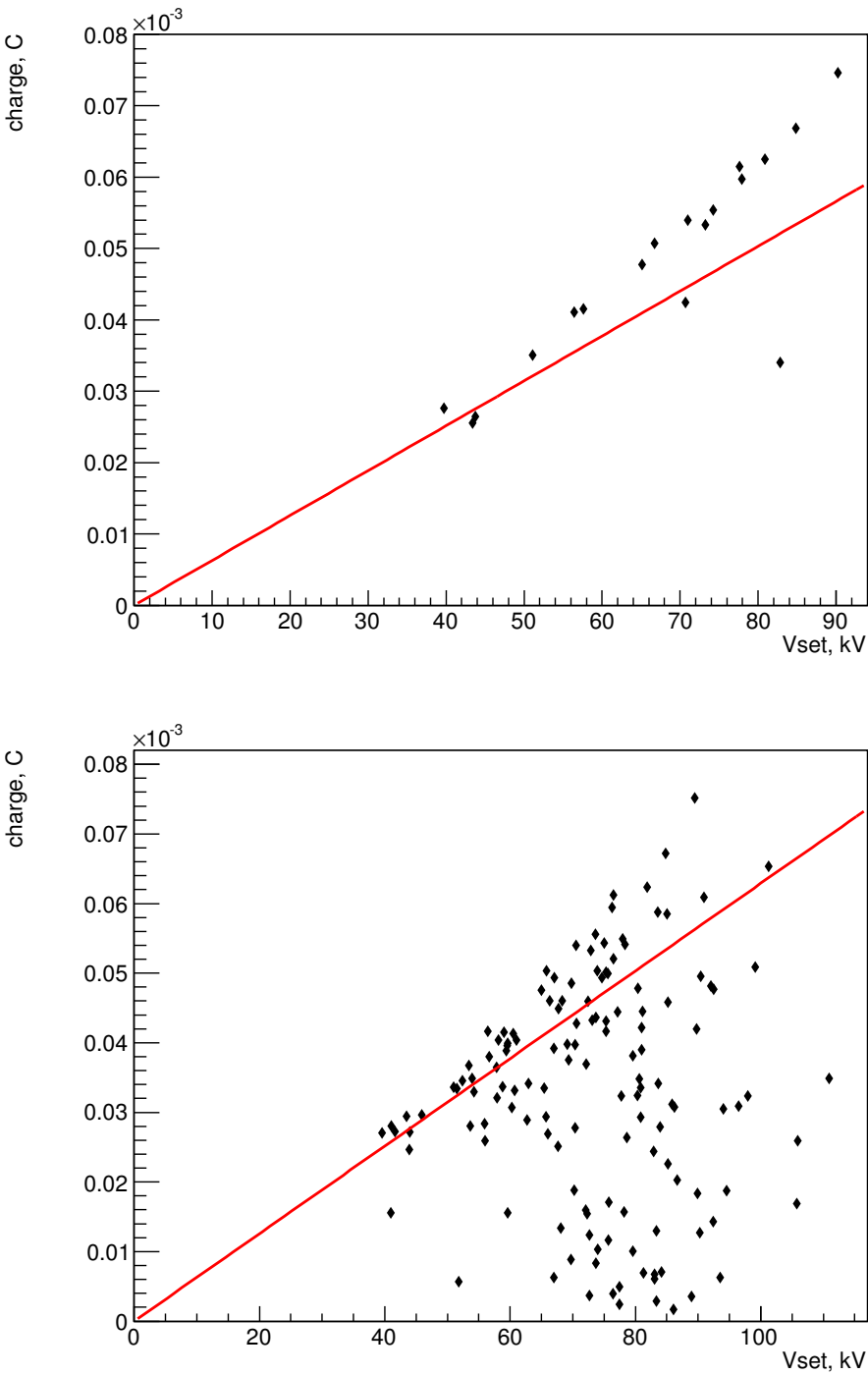


Figure 4.11.: Correlations between integrated charge and breakdown voltage V_{set} for the selected events with distinguishable slow streamer phase (top) and for all events with recorded current characteristics (bottom). The red line represents the charge stored in the gap capacitance using the tuned value of the latter.

4. Experimental Studies on High Voltage, Charge Readout, and Light Collection

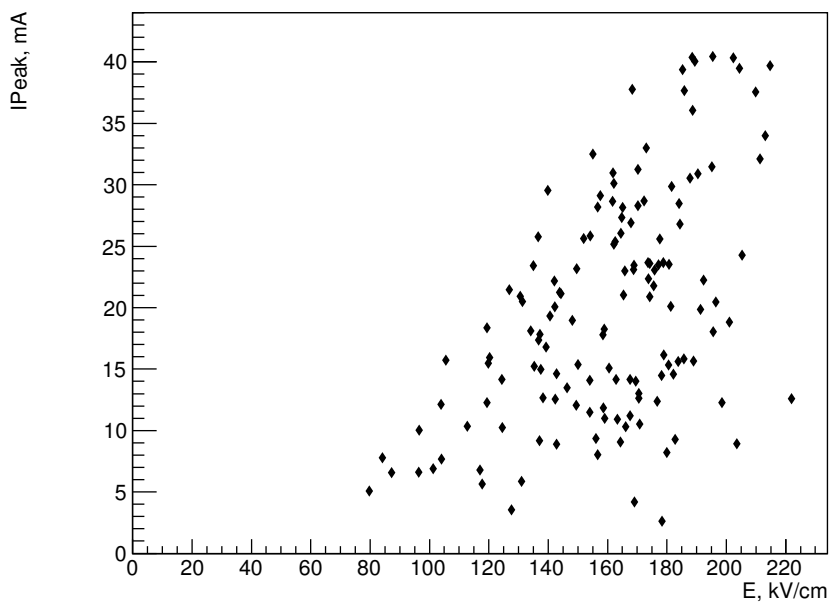


Figure 4.12.: Correlations between peak current I_{Peak} and maximum breakdown field E for all events with recorded current characteristics.

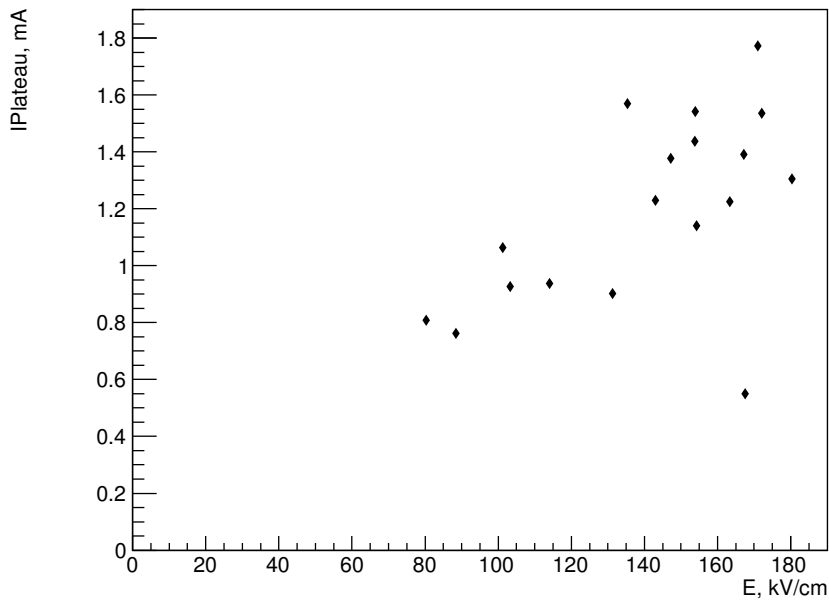


Figure 4.13.: Correlations between plateau current $I_{Plateau}$ and maximum breakdown field E for the selected events.

4. Experimental Studies on High Voltage, Charge Readout, and Light Collection

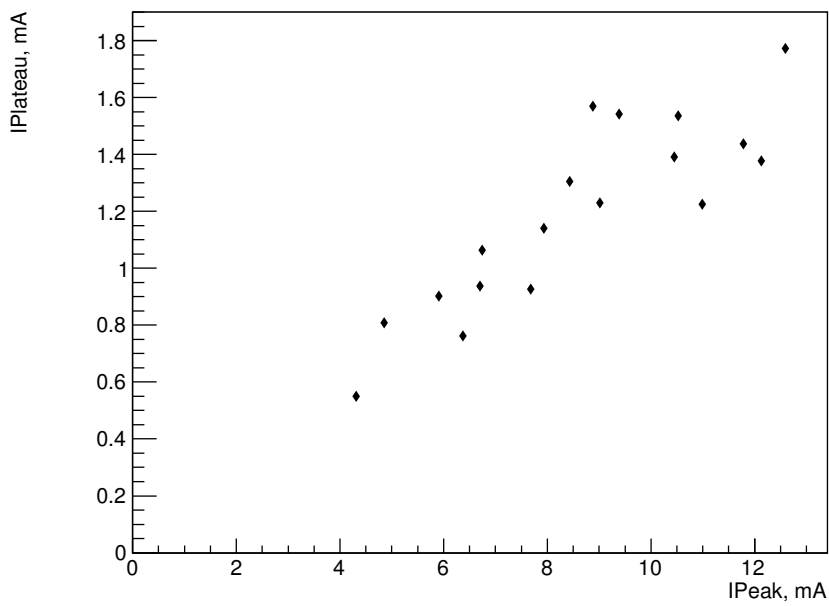


Figure 4.14.: Correlations between plateau current $I_{Plateau}$ and peak current I_{Peak} for the selected events.

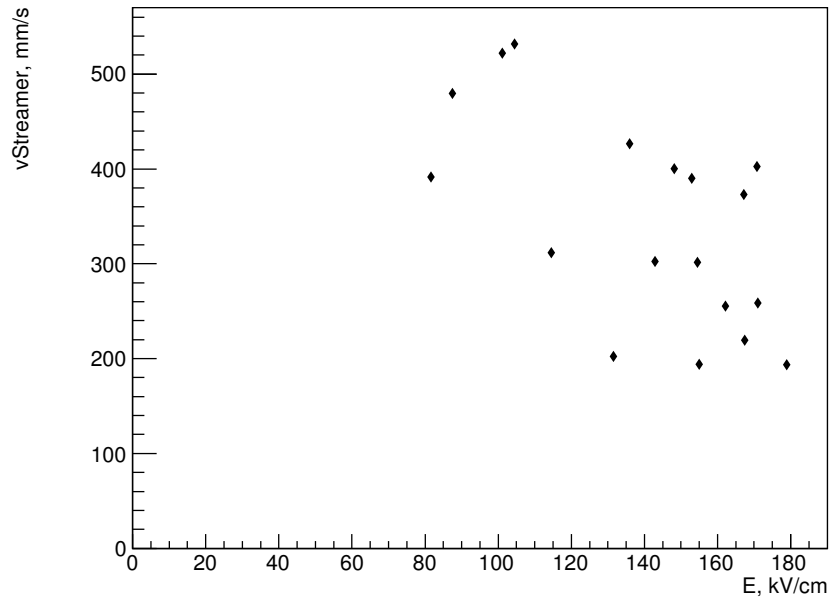


Figure 4.15.: Correlations between minimum streamer velocity $v_{Streamer}$ and maximum breakdown field E for the selected events with a distinguishable slow streamer phase.

²³ 4.2. Charge Readout

¹ As outlined in Section 3.6, classical wire readouts pose two big challenges to future
² LArTPCs: ambiguities and mechanical stability. Two new charge readout concepts were
³ tested for this work. Wires implemented as printed circuits solve the mechanical problems
⁴ but not the ambiguities. A pixelated charge readout solves both problems but introduces
⁵ a new one of a drastically increased number of readout channels.

⁶ 4.2.1. A More Robust Approach to TPC Readout Wires

⁷ A possible solution to the mechanical problems with wires is to not use actual wires but
⁸ instead print thin copper tracks on a support structure. To investigate this solution, a
⁹ proof of concept was performed at LHEP.

¹⁰ In a classical wire readout plane, the induction signal is produced by drifting the charge
¹¹ through one or multiple induction wire grids. With the proposed scheme of copper tracks
¹² on a support structure, it is no longer possible for the charge to actually drift through
¹³ the induction plane(s). Therefore, induction is only produced by the approach of the
¹⁴ charge. One consequence of this is, that induction signals will no longer be bipolar. As
¹⁵ opposed to the classic design, the collection plane will even be in front of the induction
¹⁶ plane(s). This means that the charge can only approach the induction plane(s) until
¹⁷ it is collected by the collection plane on the top layer of the support structure. That
¹⁸ is why it is crucial to make the support structure as thin as possible in order to get
¹⁹ induction signals as high as possible. Using a Flame Retardant 4 (FR4) structure as in
²⁰ classical Printed Circuit Board (PCB) designs is therefore not a viable option. Very thin
²¹ support structures can be provided by using a flexible PCB made from Kapton instead of
²² FR4. These can be made as thin as a few 10 µm. For this test, a Kapton layer of 50 µm
²³ was used with a single induction plane on the back (Fig. 4.16). The Kapton layer was
²⁴ supported by an FR4 frame for mounting on the TPC.

4. Experimental Studies on High Voltage, Charge Readout, and Light Collection

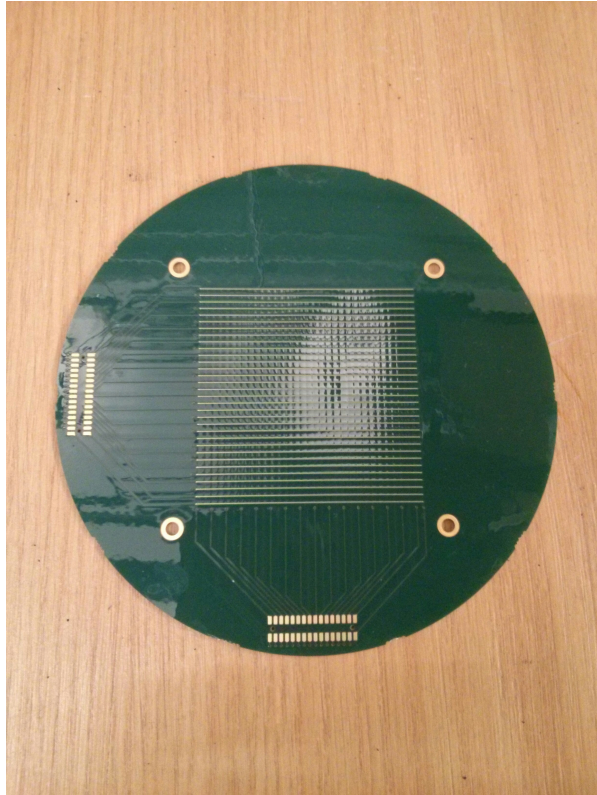


Figure 4.16.: Copper on Kapton readout plane.

25 The test was performed in a small vacuum-insulated double-batch cryostat with an inner
1 volume of 30 cm diameter and 50 cm height. Prior to filling, the cryostat was evacuated check dimensions
2 using a turbo-molecular pump and then purged with argon gas and evacuated a second
3 time. From earlier experiments [48], the purity can be assumed to be ~ 1 ppb after
4 filling. The cryostat is sealed using rubber o-rings which lose tightness at cryogenic
5 temperatures. Therefore, and due to the fact that no purification system was available,
6 the purity degraded slowly in the course of the experiment. The 8 cm long field cage
7 consists of 8 copper rings of 8 cm diameter terminated by a copper plate cathode. A field
8 of 1 kV cm^{-1} is generated using a resistive divider.

9 The charge readout electronics were adopted from ARGONTUBE without modifications.
10 Charge signals are amplified by cryogenic charge amplifiers and then digitised at room
11 temperature. More details can be found in Section 4.3.1.

4. Experimental Studies on High Voltage, Charge Readout, and Light Collection



Figure 4.17.: TPC used for the copper on Kapton readout test.

Because of the limited space inside the cryostat, no internal light triggering system could be used. Instead, the digitisers were either triggered on one of the charge collection channels or by an external muon telescope. The latter was formed of two scintillator panels with PMTs above and below the cryostat, respectively. Triggering directly on charge collection channels has the potential disadvantage of recording events only partially. If the triggering channel does not receive the first charge pulse of the event, all earlier pulses are lost, unless the DAQ implements a pre-trigger ring buffer of sufficient size. It is therefore preferable to trigger on the external muon telescope.

Using the above-described setup, cosmic muons were recorded over the course of multiple hours. A typical event is depicted in Figure 4.18. It can be seen that due to the event being almost parallel to the induction strips, the induction signal is in fact stronger than the collection signal. The reason for the bad Signal-To-Noise Ratio (SNR)

4. Experimental Studies on High Voltage, Charge Readout, and Light Collection

is improper grounding of the setup and high noise levels in the lab from the nearby train station and air conditioning. Due to time constraints and an upcoming test of a pixelated readout described in Chapter 6, no analysis was performed on this data. Anyhow, the fact that cosmic muons could be seen using this setup proves that there is no inherent problem with having the induction plane a few 10 μm behind the collection plane.

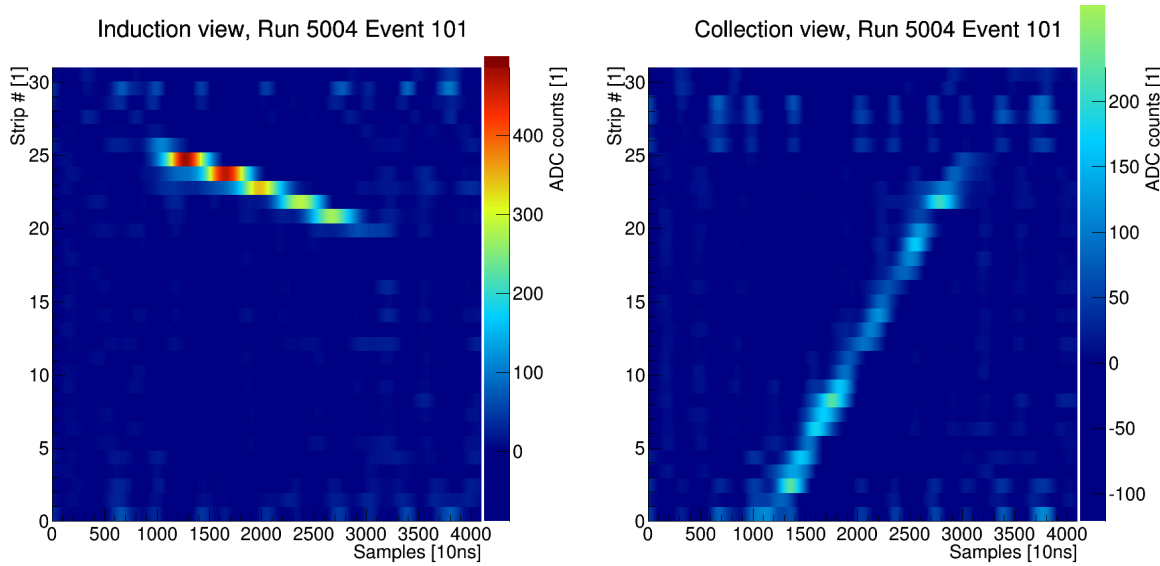


Figure 4.18.: Muon event recorded using the copper on Kapton readout.

While this technique can potentially solve the mechanical problems of classical wire readouts, it does not reduce the ambiguities inherent to 2D projective readouts outlined in Section 3.6. Because of this, it was decided not to further investigate copper on Kapton readouts and instead focus on pixelated readouts for LArTPCs providing real 3D data.

4.2.2. Pixel Readout

As outlined in Section 3.6, wire readouts are not suitable for LArTPCs the size of the envisioned future neutrino detectors. The ambiguities caused by the nature of wire readouts can be eliminated by using a fully pixelated readout. Such a readout will record a true 2D image of the charge for every time slice and thus directly produce 3D space

4. Experimental Studies on High Voltage, Charge Readout, and Light Collection

¹⁴ points of the event. On the other hand, this will increase the required number of DAQ
¹ channels and therefore the data throughput. To illustrate this, let us imagine a readout
² plane of $1\text{ m} \times 1\text{ m}$ and a desired resolution of 5 mm. For a conventional wire readout
³ with two planes, this results in

$$\left(\frac{1\text{ m}}{5\text{ mm}}\right) \times 2 = 40 \quad (4.1)$$

⁴ wires and thus DAQ channels. In order to reduce ambiguities, one can use more than
⁵ two planes which will increase the number of channels linearly with the number of planes.
⁶ For a pixelated readout,

$$\left(\frac{1\text{ m}}{5\text{ mm}}\right)^2 = 400 \quad (4.2)$$

⁷ DAQ channels are required. Scaling this up to the needed detector size, this leads to
⁸ an enormous number of DAQ channels and data throughput.
⁹ It is possible to reduce the number of channel by employing some form of multiplexing.
¹⁰ There are multiple options, one could imagine for this:

- ¹¹ • Digital multiplexing
- ¹² • Genetic multiplexing
- ¹³ • Regions Of Interest (ROIs)

¹⁴ Digital multiplexing means digitising all channels as close as possible to the readout
¹⁵ plane and then mutliplexing the digital data onto a high-speed digital link. An advantage
¹⁶ of this technique is that the technology for this already exists and is well established in
¹⁷ information technology. Ideally, one would feed the data stream into an optical fibre

4. Experimental Studies on High Voltage, Charge Readout, and Light Collection

which additionally would provide galvanic isolation of the readout from the DAQ. The challenging part is that all of this needs to happen at cryogenic temperatures which is far from trivial because most off-the-shelf components are not made for this. A detailed description of upcoming electronics capable of cold digitisation and multiplexing is given in Section 4.3.2. In contrast, genetic multiplexing and ROIs are forms of analogue multiplexing. The difference to digital multiplexing is that multiple readout channels are combined into a single analogue link before digitising them at room temperature outside the cryostat. In the two schemes described here, this happens by connecting multiple readout channels to a single DAQ channel.

In genetic multiplexing, the connections are done in a way that a certain event type (a single straight track for instance) forms a distinct pattern of DAQ channels activated. For simple events, it is possible to recover the full event from the pattern. Naturally, this reintroduces new ambiguities. Depending on the complexity of the event topology and the degree of multiplexing, they can potentially be resolved during reconstruction. In any case, if the event is too complex, it cannot be reconstructed properly. While genetic multiplexing has been shown to work for 1D readouts (wires), there is no known solution for two dimensions (pixels). sauce

A third technique is to subdivide a pixelated readout plane in so-called ROIs. This scheme was tested for an earlier PhD thesis at LHEP using a Micro-Mesh Gaseous Structure (MicroMeGaS) in a xenon gas TPC [60]. All pixels at the same position inside the ROIs are connected to the same DAQ channel. For instance, let us assume squared ROIs. One DAQ channel would connect to all the pixels in the top left corner of the ROIs. Another channel would connect to all the pixels in the top right corner and so on. To explain this a little better, let us assume a square pixel plane of $N \times N$ pixels where $N = n^2$ with an arbitrary integer n . Now, we divide the plane into $n \times n = N$, each consisting again of $n \times n = N$ pixels. For such a readout, we require N DAQ

4. Experimental Studies on High Voltage, Charge Readout, and Light Collection

26 channels for the ROIs and another N channels for the pixels. We need only as many pixel
1 channels as we have pixels per ROI because all the pixels at the same relative position
2 inside the ROIs are connected together to one DAQ channel. This means that we can
3 read out a $N \times N$ pixel plane using only $2N$ DAQ channels; the same number required
4 by a conventional 2-plane wire readout of the same size and pitch. If there is a signal
5 on a certain DAQ channel, the position inside the ROI is known but not the ROI. To
6 determine the full position, each ROI has its own inductive grid in between the pixels.
7 The grid is biased such that the charge is fully focussed onto the pixels and does not
8 collect any charge. Combining the bipolar pulse on the ROI grid with the collection
9 pulse from the pixels, it is possible to disentangle the true position. Again, the drawback
10 of this approach is that it is not free of ambiguities. It fails for multiple simultaneous
11 hits when it is impossible to say which pixel pulse belongs to which ROI pulse.

12 Independently of the amount of data one needs to bring out of the detector, a second
13 problem is heat dissipation. The more of the readout chain is sitting inside of the
14 detector, the more serious this problem becomes. It is especially problematic for digital
15 multiplexing which requires a lot of cryogenic electronics. A possible solution to this
16 is to power only that part of the readout that is actually needed. This would require
17 a means to wake up the part of the readout where the charge is arriving before it is
18 collected. Provided, the wake-up time is short enough, inductive grids on ROIs could
19 allow precisely for this.

20 **4.2.3. Charge Readout Summary**

21 As the ROI approach had already been demonstrated in a gas TPC, it was chosen for
22 the first prototype of a pixelated LArTPC. The readout plane could be realised as a
23 conventional Printed Circuit Board PCB because the detector is a single-phase LArTPC,
24 and thus no gas amplification as in MicroMeGaS is needed. Alongside the PCB, a new

4. Experimental Studies on High Voltage, Charge Readout, and Light Collection

25 TPC was designed which can be reused for future prototyping efforts. The design of
1 PCB and TPC as well as the results from the first tests are described in Section 5.1.

2 4.3. Charge Readout Electronics

3 For a heavy MIP with $\frac{dE}{dx} \approx 2.1 \text{ MeV cm}^{-1}$, a LArTPC has a charge yield of $\sim 1 \text{ fC mm}^{-1}$
4 as explained in Chapter 3. The readout electronics need to be able to reliably digitise
5 this charge. This section aims to outline the challenges based on present designs and
6 then present several tests of future approaches addressing them.

7 One of the biggest challenges to detect such low charges is the SNR. Noise can originate
8 from a plethora of sources. They can be divided into internal, originating inside the
9 electronic components, and pick-up from external sources.

The most important internal source is the *Johnson-Nyquist* noise. It is generated by the intrinsic motion of the charge carriers at non-zero temperature therefore often called thermal noise. In statistical thermodynamics, the energy of a system with one degree of freedom,

$$E = \frac{kT}{2}, \quad (4.3)$$

is proportional to its temperature T by the Boltzmann constant k . The stored energy in a capacitor is given by

$$E = \frac{CV^2}{2}, \quad (4.4)$$

where C is capacitance of and V the voltage across the capacitor. Therefore, the voltage

4. Experimental Studies on High Voltage, Charge Readout, and Light Collection

generated by the thermal noise power inside a single capacitor is

$$V = \sqrt{\frac{kT}{C}}. \quad (4.5)$$

Combining this with the charge in the capacitor,

$$Q = CV = \sqrt{kTC} \quad (4.6)$$

¹⁰ is the equivalent noise charge due to the capacitor's temperature. [61]

¹ Equation (4.6) has two important consequences for charge detectors: Noise scales with
² temperature and detector capacitance. The temperature dependences is one of the main
³ reasons to operate all analogue electronics at cryogenic temperatures. Due to their much
⁴ smaller capacitance, noise levels on pixels are significantly lower compared to wires.

⁵ Another internal noise source are resonances in the signal path that can start to oscillate.
⁶ Resonances can occur from the combination of the impedance of electronic components
⁷ such as cables and input impedances. The main culprits are usually parasitic impedances
⁸ not taken into account during the desing of the circuit. The resulting oscillations are
⁹ superimposed on the signal.

¹⁰ An example of such a resonance is the behaviour of the cryogenic LARASIC
¹¹ preamplifiers used for ARGONTUBE, described in Section 4.3.1. They include a user
¹² configurable shaping filter. With its change, the input capacitance of the amplifier
¹³ changes as well. Some configurations can form resonances with the circuit at the input.
¹⁴ Most passive electronic components change their values more or less significantly with
¹⁵ temperature. Therefore, the resonance behaviour of the detector circuit is different
¹⁶ at room temperature and in LAr. Additionally, every deviation from the final setup
¹⁷ potentially changes parasitic impedances. As a result, it is quite challenging to debug
¹⁸ such resonances in the signal path.

4. Experimental Studies on High Voltage, Charge Readout, and Light Collection

19 External sources can induce voltages on the signal path from variable magnetic fields,
1 as predicted by Faraday's law. Particularly prone to this are ground loops, any closed
2 circuit supposed to be entirely at ground potential. If the resistance at one place of the
3 loop is high enough, the induction results in a voltage difference along the loop. If the
4 same part of the loop is used as reference of a signal carrying connection, a difference in
5 the ground reference between signal source and signal sink will affect the signal.

6 There are several possibilities to make a circuit more resilient to external noise sources.
7 An obvious one is shielding all sensitive parts from external magnetic fields using a
8 Faraday cage. Implementing this effectively is extremely complicated and often not
9 practical for small experiments. Another approach is hardening the signal path itself
10 by using current-coupled and/or symmetric signals. Current-coupled signals are much
11 less sensitive to induced voltages, as long as they are small enough and do not result in
12 significant current across parasitic impedances. An example is Nuclear Instrumentation
13 Module (NIM) logic.

14 For conventional single-ended signalling, the signal is measured as the voltage or current
15 difference between a signal conductor and a ground common to the signal source and the
16 signal sink. Using a common ground as signal return path can have several undesired
17 effects. To shield the signal conductor, it is usually enclosed in a ground shield. If the
18 latter is connected on both sides, a ground loop can result for instance in combination
19 with a shared power supply ground. Ground loops can pick up noise through induction
20 if the resistance along the loop is high enough. A second way to couple noise into a
21 single-ended system is by shifting the potential on the common ground away from the
22 reference voltage or current, for instance due to high currents flowing through a lossy
23 ground connection. Because the signal is always measured against the common ground,
24 it will be distorted. In symmetric or differential signalling, the signal is not measured
25 between a signal conductor and ground but instead between two signal conductors. This

4. Experimental Studies on High Voltage, Charge Readout, and Light Collection

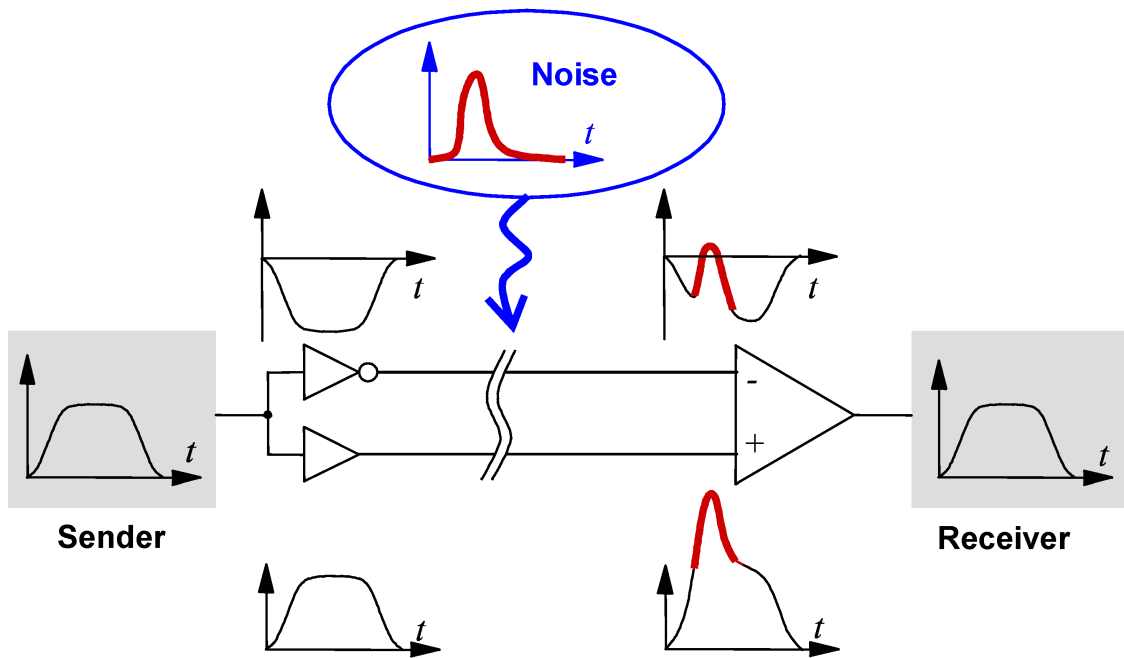


Figure 4.19.: Noise reduction using differential signalling. [62]

²⁶ works by putting an inverted (symmetric) waveform of the signal on a second conductor.

¹ The signal is recovered by taking the difference between two signal conductors. As a
² result, the signal sink needs not be connected to the same ground as the signal source
³ because the signal is independent of ground. Ground loops can thus be avoided in the
⁴ signal path. Furthermore, the effects of noise pick-up on the signal lines is drastically
⁵ reduced. Due to the completely symmetric signal path, inductive noise pick-up is equal
⁶ on both signal conductors as opposed to single-ended signals where the signal path is not
⁷ symmetric. In the signal sink, the difference between the two symmetric signal conductors
⁸ is formed and everything that is present on both of them, such as the inductively picked
⁹ up noise, cancels out.

¹⁰ Disentangling the three different sources of noise (thermal noise, resonances, and
¹¹ external pick-up) is not easy. Hints can often be found in the spectrum of the noise.
¹² Thermal noise is equal and uncorrelated over the full frequency spectrum. Resonances

4. Experimental Studies on High Voltage, Charge Readout, and Light Collection

13 usually occur at specific frequencies and thus produce regular patterns such as a sine at
1 the resonance frequency. External sources are more difficult to identify. If the source
2 produces EM fields at known frequencies (e.g. harmonics of a switched power supply) the
3 noise spectrum can be scanned for these. On the other hand if the source is unknown,
4 debugging is much more complex.

5 **4.3.1. ARGONTUBE Chain**

6 Contemporary electronics schemes shall be introduced by looking at the existing readout
7 chain at LHEP. It was originally designed for the ARGONTUBE experiment and a more
8 detailed description can be found in [63].

9 The charge collected by the readout plane is amplified by LARASIC4* [64] cryogenic
10 charge amplifiers developed by BNL for MicroBooNE [46]. A performance characterisation
11 of these Application-Specific Integrated Circuits (ASICs) can be found in [63]. Their
12 main features include

- 13 • 16 channels per ASIC;
- 14 • low noise charge amplifiers incorporating high-order filters;
- 15 • per channel programmable gain of 4.7 mV fC^{-1} , 7.8 mV fC^{-1} , 14 mV fC^{-1} or
16 25 mV fC^{-1} ;
- 17 • per channel programmable filter peaking time of $0.5 \mu\text{s}$, $1.0 \mu\text{s}$, $2.0 \mu\text{s}$ or $3.0 \mu\text{s}$;
- 18 • built-in test capacitance connected to dedicated external test pulse input for
19 calibration;
- 20 • and a power dissipation $< 10 \text{ mW}$ per channel.

21 The cryogenic preamplifiers are mounted as close as possible to the readout in order
22 to minimise noise pick-up on these very sensitive lines. Via an Inter-Integrated Circuit

4. Experimental Studies on High Voltage, Charge Readout, and Light Collection

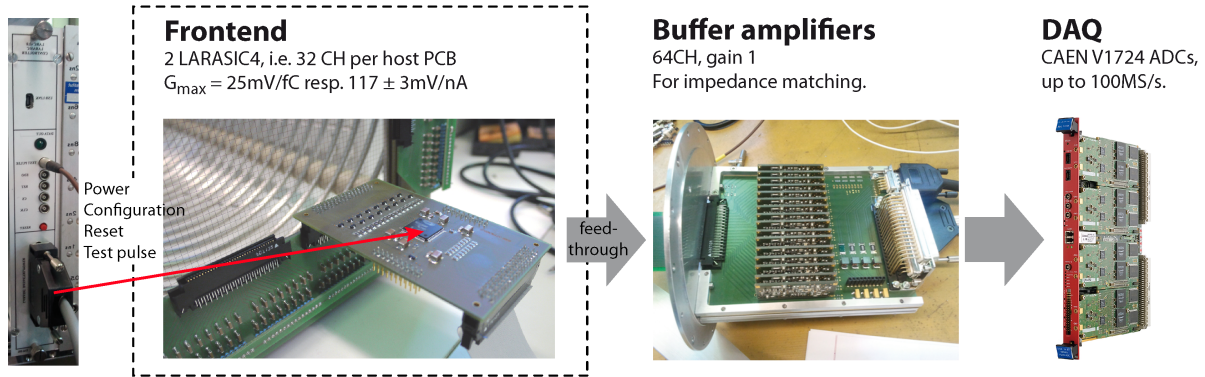


Figure 4.20.: ARGONTUBE readout chain. [63]

²³ (I^2C) bus, LARASICs can be programmed to the different aforementioned configurations.

¹ For this purpose, they are connected to a bespoke NIM module housing an Arduino
² which generates the I^2C signals, a test pulse generator, and multiple low-noise voltage
³ regulators providing power to the LARASICs. The output of the preamplifiers is fed to
⁴ buffer amplifiers mounted on top of the signal feedthrough by means of flexible Kapton
⁵ ribbon cables. The buffers operate at room temperature, have a unity gain, and match
⁶ the output impedance of the LARASICs to the 50Ω input impedance of the downstream
⁷ digitisers. From the buffers, the signals are routed via 50Ω unbalanced coaxial lines to
⁸ *CAEN V1724*⁷ 14 bit digitisers mounted in a VERSAmodule Eurocard (VME) crate. For
⁹ debugging purposes, the output of the buffers can be routed to an oscilloscope via a
¹⁰ coaxial T-piece. Finally, the digital data is read out from the VME crate via a fibre-optic
¹¹ link by a standard PC. Figure 4.20 depicts the entire readout chain. The complete
¹² analogue signal path from the pixel plane to the VME digitisers is single-ended and thus
¹³ prone to ground loops and all associated noise problems.

¹⁴ During the first pixelated readout measurement campaign (see Sections 4.2 and 5.1),
¹⁵ it became apparent that the data was significantly impaired by noise. As can be seen
¹⁶ in Figure 4.21, the noise amplitude is similar over multiple channels. This implies a
¹⁷ common mode component that cannot originate from inductive pick-up. Instead, the

⁷<http://www.caen.it>

4. Experimental Studies on High Voltage, Charge Readout, and Light Collection

18 noise is likely generated by self-oscillating parts of the signal path due to ground loops
1 and parasitic impedances. For the second measurement campaign, different steps were
2 taken to mitigate this behaviour through modifications to detector location, power supply,
3 signal path, and intrinsic capacitance.

4 A correlation between noise levels and the running state of the air condition in the
5 utility room next to the lab was found. Therefore, the experimental setup was moved
6 away from the wall facing the utility room.

7 A decoupled clean power grid was built in the lab. A Motor Generator (M-G set)
8 separates the lab grid mechanically from the building power supply. Thus, any noise
9 present on the latter is prevented from entering the experimental setup. Furthermore,
10 this decouples the lab grid entirely from the building ground preventing ground loops via
11 electric mains.

12 The signal path from the impedance-matching buffer amplifiers to the digitisers—i.e.
13 the warm signal path—was changed from single-ended to differential signalling. This
14 was achieved by replacing the buffer amplifiers by single-ended to differential amplifiers
15 and inserting another stage upstream of the digitisers to change the signal back to 50Ω
16 single-ended, matching the input of the digitisers. Like this, noise pick-up outside the
17 cryostat could be reduced as well as sensitivity to ground loops between the detector and
18 the DAQ rack. The design for the two buffer stages was kindly provided by the Liquid
19 Argon In A Testbeam (LArIAT) collaboration (see Section 5.2 and [65]).

20 A source of noise was identified in the layout of the pixel readout plane. It was found
21 that due to several ground planes and long tracks in the PCB, parasitic capacitances are
22 very high. Pixel channels are affected particularly due to the increased total track lengths
23 from connecting multiple pixels to the same DAQ channel. This is problematic because
24 for high enough frequencies (determined by RC), the input is shorted to ground creating
25 a ground loop again. Through this capacitive coupling to ground, the system can start to

4. Experimental Studies on High Voltage, Charge Readout, and Light Collection

26 oscillate. One evidence for this is that the noise is equal over multiple channels, so-called
1 common-mode noise. More specifically, the noise is equal for two respective groups of
2 channels (see Figure 4.21). Investigating this, it was found that these groups correspond
3 to channels of roughly equal parasitic capacitance: (150 ± 5) pF and (95 ± 5) pF. The
4 noise amplitude is higher on channels with higher capacitance (see Figure 4.22). To solve
5 this problem, the PCB design was optimised by removing unnecessary ground planes,
6 routing signal tracks outside necessary ground planes and increasing the thickness of
7 the PCB. Pixel capacitance could be improved to (65 ± 5) pF for all channels. ROI
8 capacitance improved only slightly from (25 ± 10) pF to (20 ± 10) pF which confirms the
9 hypothesis that the long tracks due to pixel multiplexing were the culprits. The reason
10 for the higher spread of the ROI capacitances is the larger difference in track length
11 between the different ROIs. For the sake of completeness, it should be noted here that
12 for the capacitance measurements, the old PCB was not populated while the new one
13 was populated as described in Section 5.1.1. However, the installed capacitors are either
14 not connected to ground or in series with a $10\text{ M}\Omega$ resistor. Therefore, their influence on
15 the measurements is negligible.

16 As can be seen from Figures 4.21 and 4.23, there is a significant decrease in noise
17 after commissioning all of the above improvements to the readout chain. This can also
18 be seen from Figures 4.22 and 4.24 depicting the noise amplitude distribution of the
19 two measurement campaigns. The data for the latter (5000 events in the first and 2000
20 events in the second campaign) was taken employing a 5 Hz random trigger. A more
21 detailed assessment of the noise after the implementation of the described noise mitigation
22 measures can be found in Section 5.1.4.

4.3.2. Improved Cold Electronics for Pixelated Readouts

This section describes the challenges met by electronics for pixelated LArTPCs and possible solutions. First, the cryogenic Analogue-to-Digital Converters (ADCs) for the DUNE FD, developed by BNL, are introduced, and an explanation is given why they are unsuitable for a pixelated ND. Therefore, the neutrino group at Lawrence Berkeley National Laboratory (LBNL) is developing bespoke pixel electronics for the ND, the Liquid Argon Pixel readout ASIC (LArPix). An overview of this effort is given in the second part of this section.

As mentioned in Section 3.5, cold digitisation can improve noise because of both shorter analogue signal lines and reduced thermal noise of the electronics. Furthermore, it enables the multiplexing of the data on high-speed digital links, reducing the number of needed signal cables and cryostat feedthroughs. However, designing reliable electronics at cryogenic temperatures is not an easy task. ADCs in particular are very sensitive to stable reference voltages required for proper analogue-to-digital conversion. Another problem arises from the fact that digital electronics in general require clocks with sharp edges for proper timing, usually realised as a square wave. According to Fourier analysis, a square wave produces a high level of harmonics. This is particularly problematic in case of readout wires that act as antennas and can pick up these clock signals. A further important aspect is power dissipation. All power dissipated by cryogenic electronics needs to be compensated for in order to prevent the LAr from boiling. This is particularly problematic for a pixelated readout that requires a much higher number of readout channels than a wire readout (see Section 4.2.2).

BNL is developing cold charge readout electronics for the DUNE FD. [66] In particular, the plan is to accompany the cryogenic LARASIC charge preamplifiers by cryogenic ADCs. They have 16 inputs, each capable of digitising the TPC signals at 2 MS/s and 12 bit with input characteristics optimised for the LARASIC output. A more detailed

4. Experimental Studies on High Voltage, Charge Readout, and Light Collection

26 description is given in [67].

1 In the course of this work, the cryogenic ADC ASICs developed by BNL were evaluated
2 to be used in the ND as well. The author joined the team at BNL in cold tests of the
3 devices. One of the results of these tests is presented here to illustrate the difficulties of
4 cryogenic ADCs. As a disclaimer, it should be noted that this is by no means the current
5 status of the ADCs at the time of this writing. The described tests were performed in
6 the Fall of 2016 at BNL.

7 An important characteristic of an ADC is linearity. It describes the relation between
8 the applied input voltage and the calculated digital number, the *ADC code*, at the output.

9 In the case of the BNL ADCs, this relation is expected to be strictly linear. To test this,
10 a voltage ramp is applied to the input and the converted digital values are recorded.

11 A typical measurement is shown in Figure 4.25. The expected shape is one straight
12 diagonal line from the bottom left to the top right corner, i.e. a linear relationship
13 between input voltage and ADC value. Two particular deviations from this are visible:
14 gaps accompanied by horizontal lines and a wobbly response around zero. Upon close
15 inspection, it can be seen that the gaps have the same voltage range as the horizontal
16 lines. The meaning of this is that for this input voltage range, the ADC output is *stuck*
17 at the same value. Both these effects mean that the detector response to detected charge
18 and thus energy deposition is not linear. While some non-linearities can be compensated
19 in offline data analysis, this is not possible for the sticking ADC values because they
20 correspond to a range of input voltages. This impairs the energy resolution of the
21 detector.

22 The cause for the non-linearities is rooted in the electronic design of the ASIC.
23 Additionally, it was not fully understood at the time of these tests. Therefore, an
24 explanation is out of the scope of this work and not given here. The measurements are
25 shown to illustrate the difficulties of designing a reliable cryogenic ADC.

4. Experimental Studies on High Voltage, Charge Readout, and Light Collection

26 Leaving aside the non-linear response, the BNL ADC ASICs are not suitable for
1 use in conjunction with a pixelated LArTPC charge readout. Being designed for wire
2 readouts, no strong focus was laid on power dissipation which is $\approx 5\text{ mW}$ per channel.
3 Combined with the one of the LARASIC (10 mW) [64], a total of 15 mW is dissipated.
4 For a pixelated DUNE ND with $\sim 10^7$ channels, the resulting required cooling power
5 would be 150 kW for 70 t of LAr (see Section 6.1). In comparison, MicroBooNE has a
6 total cooling power of $\approx 20\text{ kW}$ for 170 t of LAr. [46]

7 Due to their smaller geometric extent, pixels have a much lower capacitance than
8 wires. According to Equation (4.6), this reduces the intrinsic noise present on a pixelated
9 readout. LArPix, being developed by LBNL [68], exploits this fact to significantly reduce
10 the complexity of the cold electronics. Two key points distinguish them from the BNL
11 design for the wire-equipped FD. The complex shaping preamplifier required by wires for
12 noise filtering can be replaced by a simple charge integrator. Additionally, the low noise
13 levels allow for a self-triggering scheme; charge arriving at the LArPix is only digitised if
14 it is above a predefined thresholds. This, in turn, reduces the duty cycle and thus the
15 power dissipation of the ADC. If noise levels are well below the set threshold, power
16 dissipation becomes primarily a function of charge flux rate in the detector.

17 In addition to this, the digital circuitry of LArPix operates at lower frequencies than the
18 BNL design. For an Alternating Current (AC) of frequency f , the resistance presented
19 by a conductor is not simply given by its Ohmic resistance. There is an additional
20 component proportional to \sqrt{f} caused by the *skin effect*. [69] High frequency currents no
21 longer flow in the bulk of the conductor but only in a finite layer (skin) at its surface.
22 Therefore, the resistance is no longer proportional to the cross-section area but rather
23 the surface area of the conductor. The result of the skin effect is more power dissipation
24 at higher frequencies. By operating at lower frequencies, the power dissipation of LArPix
25 can be lowered further. The cost is a decrease in data transmission rates.

4. Experimental Studies on High Voltage, Charge Readout, and Light Collection

With its power dissipation (and consumption) dependent on the charge flux and the lowered data transmission rate, LArPix is susceptible to high event rates. Due to the triggered digitisation, the same goes for noise levels. For the successful operation of LArPix, it is of paramount importance to keep event rates and noise levels low. The latter can be achieved by minimising detector capacitance. To lower the susceptibility to high event rates, the DUNE ND design puts the TPC drift direction perpendicular to beam direction. This reduces the amount of charge per event arriving simultaneously at the readout. Furthermore, LArPix is equipped with a First In First Out (FIFO) buffer capable of holding 2048 charge pulses to cope with short peaks in event rate.

To accommodate the elevated number of channels of a pixelated readout, the first LArPix prototype chip has 32 inputs. Its resolution in time and charge are $2\text{ }\mu\text{s}$ and 8 bit, respectively. While currently inferior to the BNL design, these specifications are planned to be improved in the next design iteration, after a successful initial test. One of the goals of the first prototype is to assess the optimal size of the FIFO. [70]

4.3.3. Charge Readout Electronics Summary

Pixelated LArTPCs place high demands on the charge readout electronics. The very high number of readout channels required makes digitisation outside of the cryostat impractical due to the number of cable feedthroughs required. Cold digitisation inside the cryostat reduces the number of cables by channel aggregation on digital high-speed links. However, this worsens the problem of heat dissipation inside the LAr. The cold digitisers being developed for the charge readout wire planes of the DUNE FD were evaluated but found unsuitable for a pixelated LArTPC due to their high power dissipation. LArPix is a bespoke cold digitiser for pixelated LArTPCs. It is currently under development at LBNL and designed to meet the stringent heat dissipation requirements by means of a smart zero suppression.

4. Experimental Studies on High Voltage, Charge Readout, and Light Collection

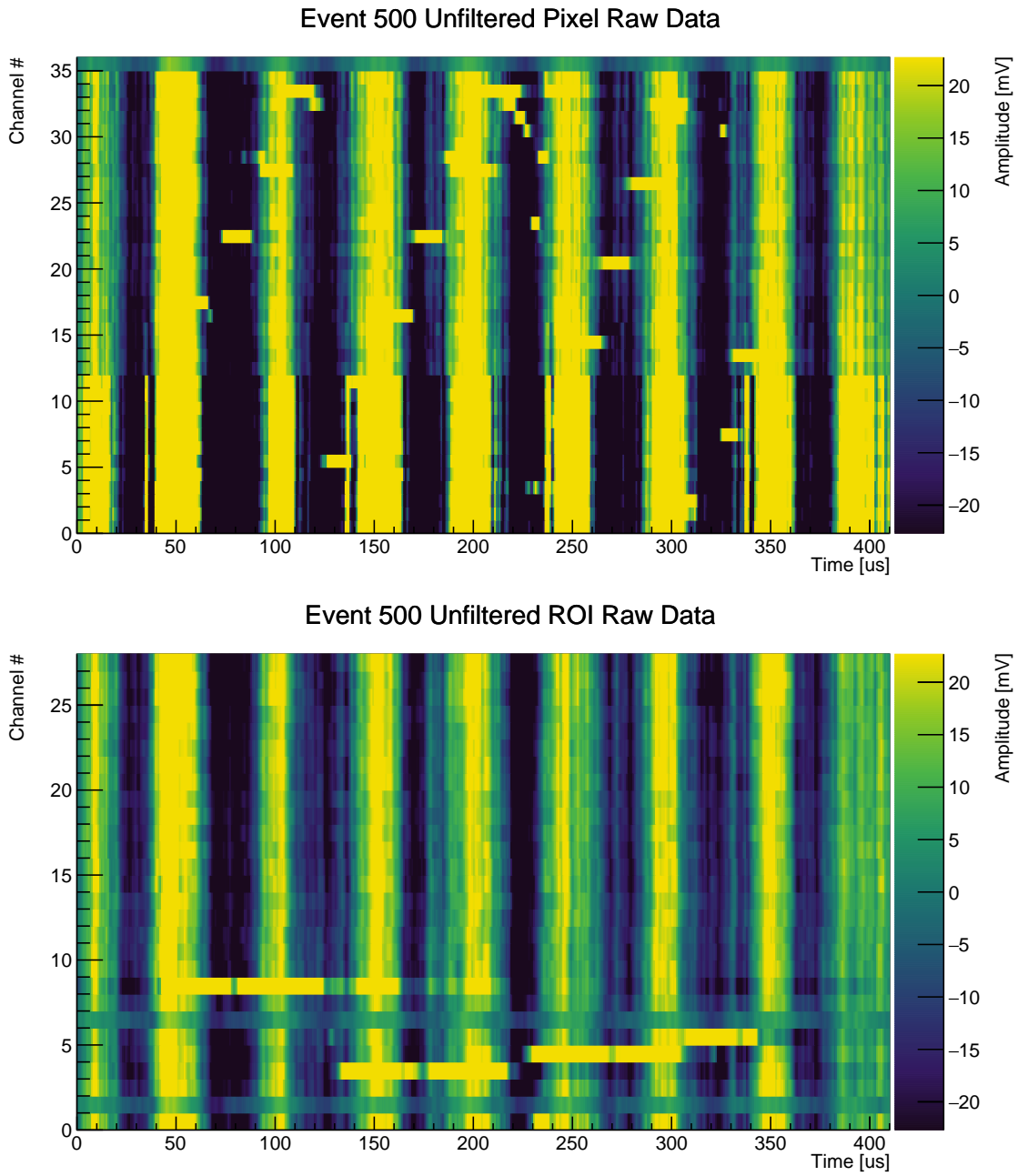


Figure 4.21.: Event from the first measurement campaign of the pixel demonstrator. The top plot shows pixel data while the bottom plot shows ROI data.

4. Experimental Studies on High Voltage, Charge Readout, and Light Collection

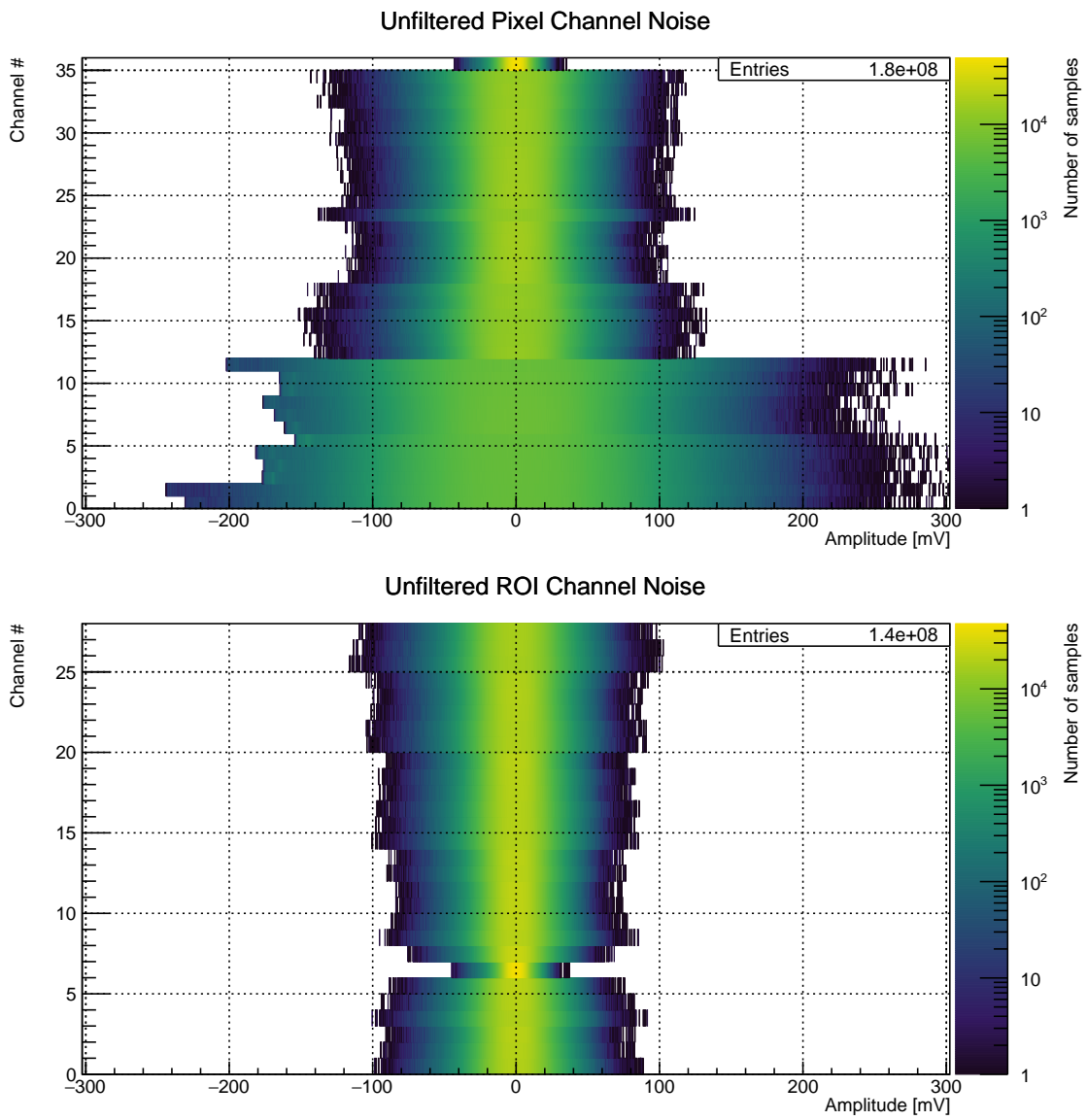


Figure 4.22.: Noise amplitude distributions of pixel (top) and ROI (bottom) channels of the first measurement campaign. 5000 events with 1000 410 ns samples each from a 5 Hz random trigger were combined.

4. Experimental Studies on High Voltage, Charge Readout, and Light Collection

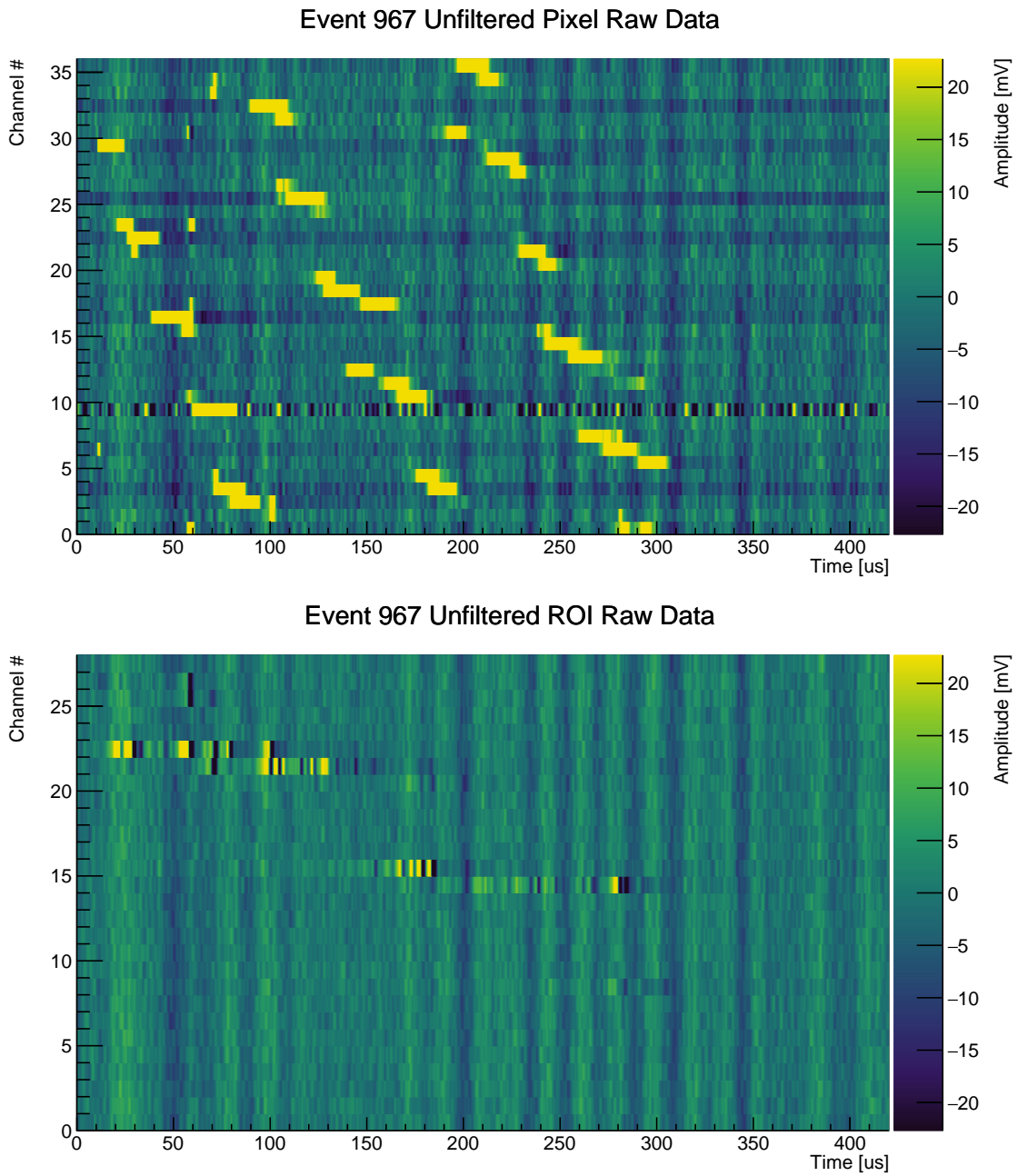


Figure 4.23.: Event from the second measurement campaign of the pixel demonstrator after improving the readout chain. The top plot shows pixel data while the bottom plot shows ROI data.

4. Experimental Studies on High Voltage, Charge Readout, and Light Collection

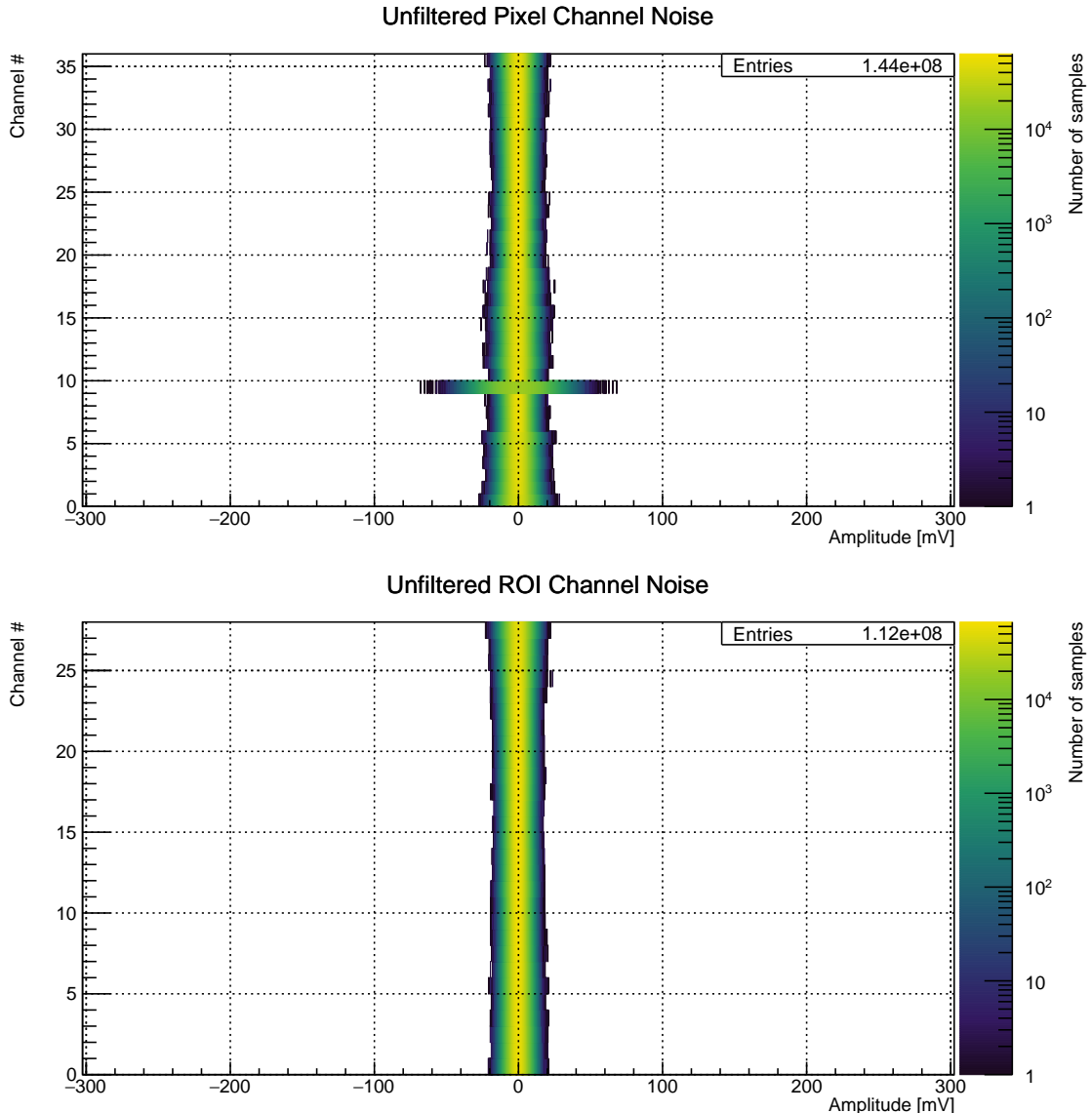


Figure 4.24.: Noise amplitude distributions of pixel (top) and ROI (bottom) channels of the second measurement campaign, after implementing hardware noise mitigation measures. 2000 events with 2000 210 ns samples each from a 5 Hz random trigger were combined.

4. Experimental Studies on High Voltage, Charge Readout, and Light Collection

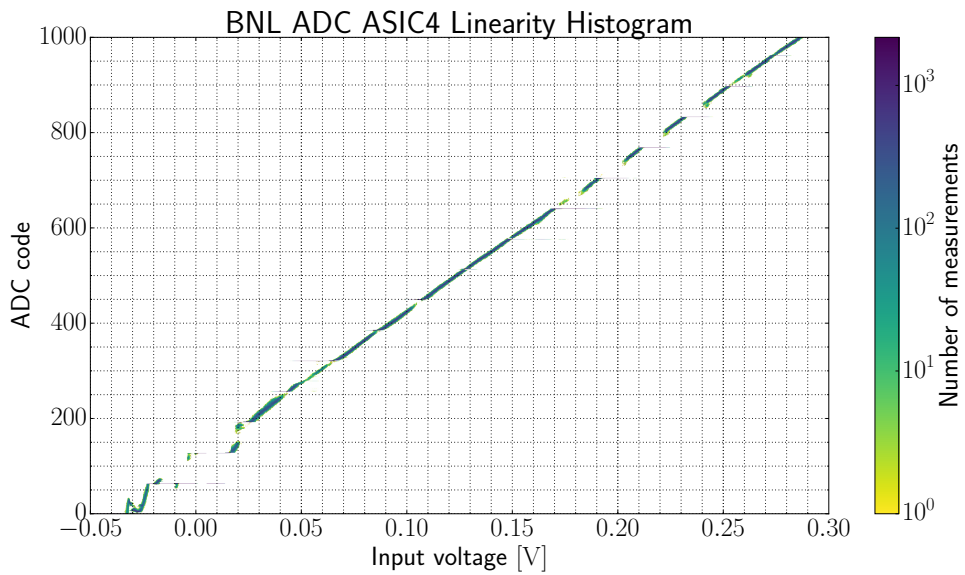


Figure 4.25.: Linearity measurement of the BNL cryogenic ADC ASICs with input voltage on the x-axis and ADC value (code) on the y-axis. Colour represents the number of measurements. The measurements were performed in liquid nitrogen.

25 4.4. Light Collection

1 For the ArgonCube detector concept detailed in Section 5.3, a slim and efficient light
 2 readout is needed. PMTs are not suitable because they occupy a lot of space and thus
 3 would require mounting on top of a module which in turn would reduce their efficiency.
 4 That is why the photon detectors of choice for such a detector are SiPMs. The following
 5 describes the light readout used in the ArgonCube pixel demonstrator described in
 6 Section 5.1. After that the ArgonCube Light readout, ArCLight, is introduced.

7 **4.4.1. Cryogenic SiPM Light Readout**

8 In 2016, LHEP developed a novel Cosmic Ray Tagger (CRT) system for LArTPCs which
 9 was subsequently installed in MicroBooNE [46] and will be installed in the Short Baseline
 10 Neutrino Detector (SBND) experiment [71] in the near future. The tagger consists of
 11 panels made from polystyrene based scintillating bars. On both long edges of the strips,
 12 the light is coupled into a *Kuraray Y11(200)M*⁸ WLS fibre of 1 mm diameter. One end of
 13 the fibre is coated with an aluminium mirror to increase collection efficiency. The other
 14 end is attached to a *Hamamatsu S12825-050P*⁹ SiPM. A bespoke Front-End Board (FEB)
 15 reads out the SiPM signal and provides power. It was developed at LHEP alongside the
 16 scintillator panels[72].

17 For the first pixel prototype described in Section 5.1, the CRT system was adapted to
 18 serve as the light trigger system. Except for operating everything up to the SiPMs in LAr,
 19 the polystyrene scintillating bars were replaced by acrylic rings. The latter are placed in
 20 between the aluminium field shaping rings of the TPC. To allow for proper convection of
 21 the LAr, only every other gap is completely filled by an acrylic ring. Perpendicularly
 22 to the rings(i.e. in drift direction), four WLS fibres collect the light from the rings and

⁸<http://kuraraypsf.jp>

⁹<http://www.hamamatsu.com>

4. Experimental Studies on High Voltage, Charge Readout, and Light Collection

23 guide it to the readout plane on the anode side where it is fed to the SiPMs. Residing
1 on the cryostat top-flange at room temperature, the FEB is connected to the SiPMs via
2 Teflon insulated coaxial cables.

3 The peak of scintillation light emission in LAr lies at 128 nm while the sensitivity sauce
4 wavelength peak of the SiPM is at 450 nm. Therefore, the scintillation light needs to be
5 shifted before it can be detected by the SiPMs. This happens in two stages. For the first
6 shift, TPB is applied to the inside of the acrylic rings. Their outside is not coated to
7 reduce the collected amount of scintillation light that originates outside the TPC while
8 their inside is machined to optimise light collection. TPB absorbs the 128 nm scintillation
9 light and re-emits with a peak at 440 nm [73] which is then propagated through the acrylic
10 and coupled into the WLS fibre. The latter has an absorption peak at 430 nm and an
11 emission peak at 476 nm. sauce

In the FEB, two coincidences of two out of four SiPMs are formed and combined by means of a logic *OR* operation. The trigger pattern is thus

$$T = (S_1 \wedge S_2) \vee (S_3 \wedge S_4) \quad (4.7)$$

12 for SiPMs S_1 through S_4 . The reason for this is that the same trigger logic is used for the
13 CRT panels to have a coincidence between two fibres of one scintillation bar. In order to
14 improve trigger purity, it was tried to change the firmware to trigger on the coincidence
15 of all four fibres in the TPC. Due to a firmware bug however this could not be achieved.

16 As will be explained in Section 5.1, the light readout scheme described above was
17 successfully used to trigger and record several thousand cosmic muon interactions with the
18 ArgonCube pixel demonstrator. However, when compared to a measurement triggered on
19 the charge readout directly, it became apparent that the efficiency of this light readout is
20 very poor. Due to limitations in the experimental setup, no quantitative measurement of
21 the trigger efficiency was performed. Triggering on the charge readout was only possible

4. Experimental Studies on High Voltage, Charge Readout, and Light Collection

22 using an oscilloscope because the used DAQ system was not capable of self-triggering.
1 Therefore the channel number was limited to four which would have enabled charge
2 readout triggering only on a subset of the readout area. An external reference trigger
3 source, such as a muon telescope was not available during the measurements. Furthermore,
4 after warming up the experiment, it was discovered that all four fibres were damaged
5 because the acrylic rings fell out of their mounting brackets and squeezed or even broke
6 the corresponding fibre.

7 Another drawback of the design is the optical coupling between the acrylic rings and
8 the LAr. Because the refractive indices are very close, a lot of light escapes from the
9 rings and is lost. Many other low-volume light readout systems based on light guides
10 developed for LAr [74–80] suffer from the same problem. As a solution, a dedicated light
11 readout system for the ArgonCube, ArCLight, was developed at LHEP.

12 **4.4.2. ArCLight**

13 The ArgonCube Light readout system (ArCLight) aims to minimise the occupied volume
14 by maximising the area coverage of SiPMs. This is achieved by coupling them to a passive
15 light collector. As mentioned above, principles based on full reflection on a polymer-LAr
16 interface are not suitable. Instead, ArCLight is based on the light trapping principle of
17 the Argon R&D Advanced Program at UniCamp (ARAPUCA) sensor [81]. The latter
18 works by trapping the photons inside a cavity made of walls covered by a highly reflective
19 materials. One of the walls is formed from a dichroic film, a material transparent to
20 certain wavelengths while highly reflective to others. On the outside, this film is covered
21 by TPB with the film transparent to the emitted blue light. The inside of the film is
22 covered by a second WLS, shifting the light to green which is reflected by the dichroic
23 film and therefore trapped inside the cavity. One or more SiPMs are mounted inside
24 the cavity to collect the trapped photons. In contrast, ArCLight replaces the void of

4. Experimental Studies on High Voltage, Charge Readout, and Light Collection

²⁵ ARAPUCA by a solid transparent polymer sheet, doped with a WLS dye. This makes it
¹ substantially more robust, compact and stable, especially when scaled up to larger areas.

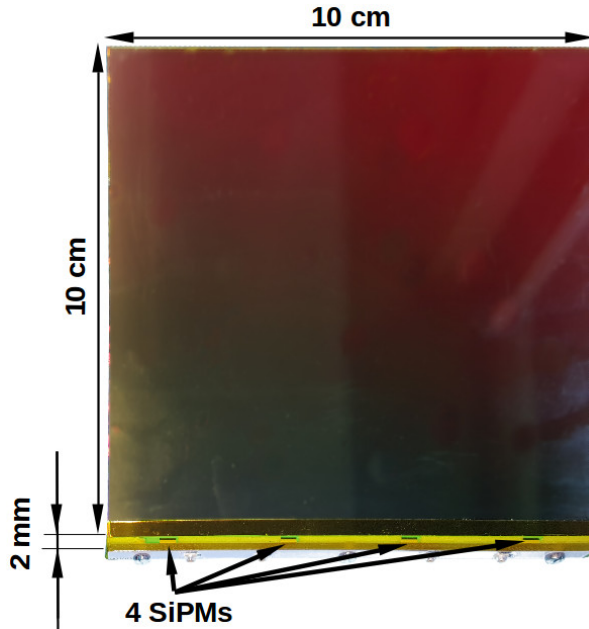


Figure 4.26.: 10 cm × 10 cm ArCLight prototype. Four SiPMs can be seen at the lower side, soldered to a narrow PCB providing coaxial connectors for signal readout. The rest of the sensor area is dielectric.

² A 10 cm × 10 cm ArCLight prototype is shown in Figure 4.26. The ratio of sensitive
³ area to total area is 98 % with the remaining 2 % occupied by a PCB carrying four
⁴ *Hamamatsu S13360-3050VE*¹⁰ SiPMs with a sensitive area of 3 mm × 3 mm each. The
⁵ inside of ArCLight is made of a 4 mm thick *Eljen Technology EJ-280*¹¹ WLS plate. Its
⁶ sides are laminated with reflective films. The back face and the edges are covered with a
⁷ *3M VM2000*¹² dielectric specular reflector foil having ≈ 98 % reflectance in the visible
⁸ light range. A *3M DF-PA Chill*¹² dichroic mirror covers the front face. It is transparent
⁹ in the blue and has a high reflectance in the green spectral range. Both films are held in
¹⁰ place by thin layers of transparent adhesive. To shift the Vacuum UltraViolet (VUV)

¹⁰ <http://www.hamamatsu.com>

¹¹ <http://www.eljentechnology.com>

¹² <https://www.3m.com>

4. Experimental Studies on High Voltage, Charge Readout, and Light Collection

11 scintillation light produced in LAr to the blue transparent range of the dichroic mirror,
 1 its outer surface is coated with TPB. A cross-section of the structure of ArCLight is
 2 depicted in Figure 4.27.

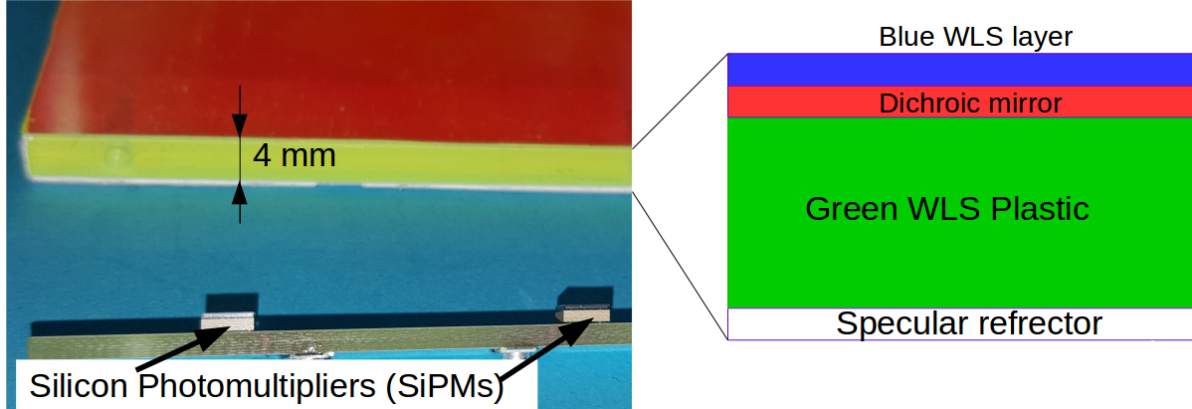


Figure 4.27.: ArCLight light collector cross-section near a corner. The structure is mechanically supported by a 4 mm thick WLS plastic. Its front is covered with a dichroic mirror film while the edges and the back face are covered with a dielectric specular reflector foil. The outer surface of the dichroic mirror is coated with TPB to shift the LAr VUV scintillation light to the blue range where the dichroic film is transparent. At the bottom of the left picture, two of the four SiPMs mounted to the carrier PCB are visible.

3 The Photon Detection Efficiency (PDE) was measured at room temperature using
 4 an ^{241}Am source, previously calibrated with a PMT. It was determined to be 0.8 % to
 5 2.2 %. Figure 4.28 shows PDE as a function of the position inside the light collector,
 6 overlaid onto a picture of the prototype for reference. The increase in PDE near the
 7 SiPMs is likely caused by photons hitting the SiPMs directly with no prior reflection
 8 off the dichroic mirror. Due to the angular dependence of the reflectance of the dichroic
 9 mirror, about 30 % of the light is lost during the first reflection on the dichroic mirror.
 10 Once reflected, a photon is trapped inside the ArCLight because of the specular nature of
 11 the reflection on all surfaces. In addition, the average PDE was calculated from theory to
 12 be (0.7 ± 0.4) % in agreement with the measurements. More details on the calculations
 13 and the calibration of the measurement can be found in [82].

4. Experimental Studies on High Voltage, Charge Readout, and Light Collection

¹⁴ The measurements described above were performed at room temperature. A
¹ 43 cm × 15 cm ArCLight module was successfully operated at LAr temperatures in the
² PixLAr test beam demonstrator at FNAL described in Section 5.2. Figure 4.29 shows the
³ time evolution of the average photo-electron yield per event in beam (red) and cosmic
⁴ ray (blue) mode. It can be seen that the yield is approximately constant over several
⁵ weeks. The jumps in the beam curve can be explained by the switching between different
⁶ beam configurations (e.g. momentum and intensity).

7 4.4.3. Light Collection Summary

⁸ Classic PMT-based light readout schemes for LArTPCs occupy large inactive volumes.
⁹ SiPMs are much smaller but so is their sensitive area. A SiPM-based light readout
¹⁰ was successfully used to trigger the charge readout of a pixelated LArTPC prototype.
¹¹ ArCLight is a new light readout system based on the ARAPUCA light trap principle to
¹² increase the sensitive area of SiPMs. Initial characterisations indicate a PDE of ∼ 1 %.
¹³ It can be installed inside the field cage of a LArTPC due to its low volume and the
¹⁴ dielectric nature of the light collector.

4. Experimental Studies on High Voltage, Charge Readout, and Light Collection

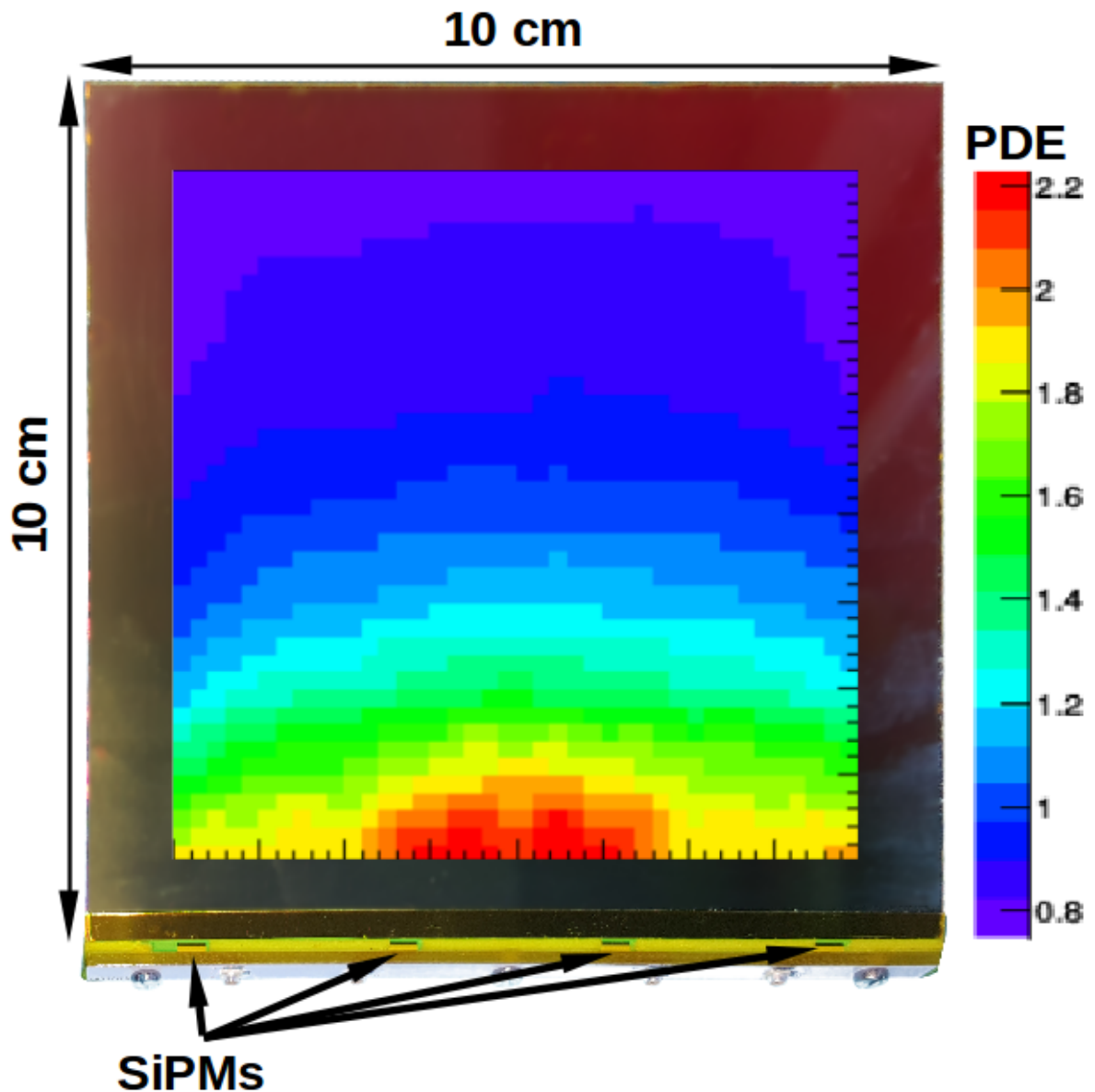


Figure 4.28.: Measured PDE for the 10 cm \times 10 cm ArCLight prototype (in the background), at room temperature. The PDE is given in %.

4. Experimental Studies on High Voltage, Charge Readout, and Light Collection

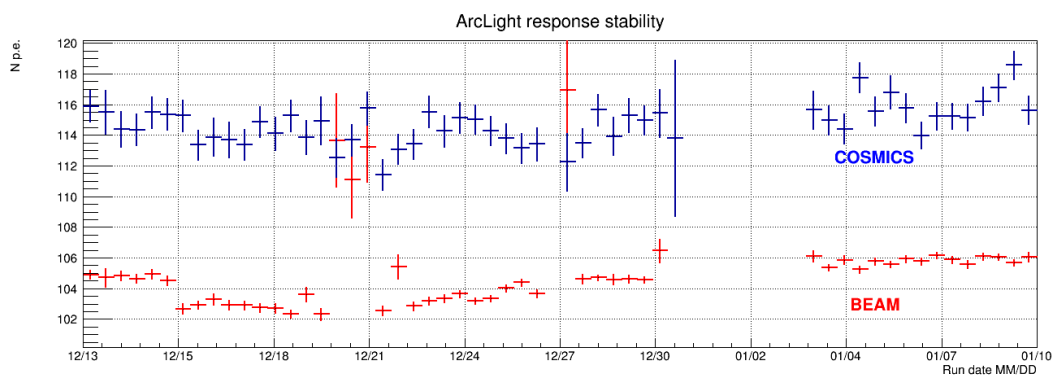


Figure 4.29.: Average observed number of photo-electrons (N p.e.) per event by the ArCLight module in the PixLAr test beam demonstrator at FNAL over several weeks. In addition to the beam response in red, the response to cosmic rays is shown in blue.

¹⁵ **5. A Novel Implementation of the 1 LArTPC Technology**

² **5.1. First Results from the ArgonCube Pixel 3 Demonstrator**

⁴ This chapter describes the results obtained from the first pixelated LArTPC prototype
⁵ for the ArgonCube project (see Chapter 5.3). While many of the individual systems, such
⁶ as the high-voltage system, light and charge readout, have been described in previous
⁷ chapters, a short overview of the implementation is given here.

⁸ **5.1.1. Pixel PCB Design**

⁹ The pixelated anode plane, shown in Figure 5.1, was produced as a conventional PCB.
¹⁰ The pixelated area is 100 mm across, the pixels are formed of 900 μm vias with a pitch
¹¹ of 2.54 mm. An inductive focusing grid surrounds the pixels, it is made from 152.4 μm
¹² copper traces split into 28 regions. There are 6×6 pixels per region, giving a total of
¹³ 1008 pixels.

¹⁴ Vias were used for pixels instead of pads in order to minimise capacitance. As detailed
¹⁵ in Section 4.3, it is important that capacitance is minimised when amplifying charge.
¹⁶ To further minimise parasitic capacitance, the PCB design was optimised by removing

5. A Novel Implementation of the LArTPC Technology

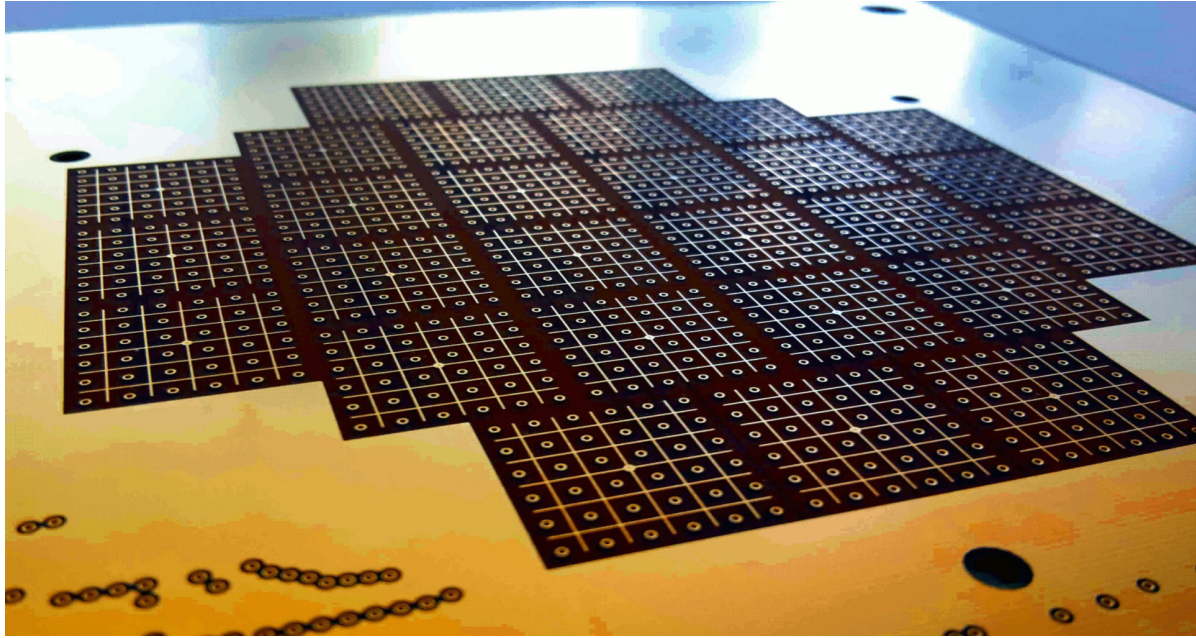


Figure 5.1.: First version of the pixelated anode PCB. The pixelated readout area is 100 mm in diameter. Each charge collection pixel is a $900\text{ }\mu\text{m}$, at a pitch of 2.54 mm , inductive focusing grids formed of $152.4\text{ }\mu\text{m}$ copper traces surround the pixels. There are 28 inductive focusing grids with 36 pixels per region, a total of 1008 pixels.

¹⁷ unnecessary ground planes, routing signal tracks outside necessary ground planes, and
¹ increasing the thickness of the PCB to 3.5 mm from an initial 1.75 mm. The resulting
² capacitance at each pixel is $\approx 50\text{ pF}$.

³ The pixels are directly connected to the preamplifiers while the inductive focusing
⁴ grids are decoupled via 10 nF capacitors. Additionally, the bias voltage is filtered at the
⁵ input by another 10 nF and $10\text{ M}\Omega$. The full schematic of the bias circuit is depicted in
⁶ Figure 5.2.

⁷ The bias on the inductive focusing grids had to be sufficient to allow full charge
⁸ transparency (all charge collected by the pixels), yet low enough to minimise any risk of
⁹ damaging the cold coupling capacitors. It was increased incrementally until transparency
¹⁰ was observed at 300 V. Simulation suggest this was only 95 % transparency, with 100 %
¹¹ at 350 V (see Figure 5.3). The simulation available at the time of the measurement

5. A Novel Implementation of the LArTPC Technology

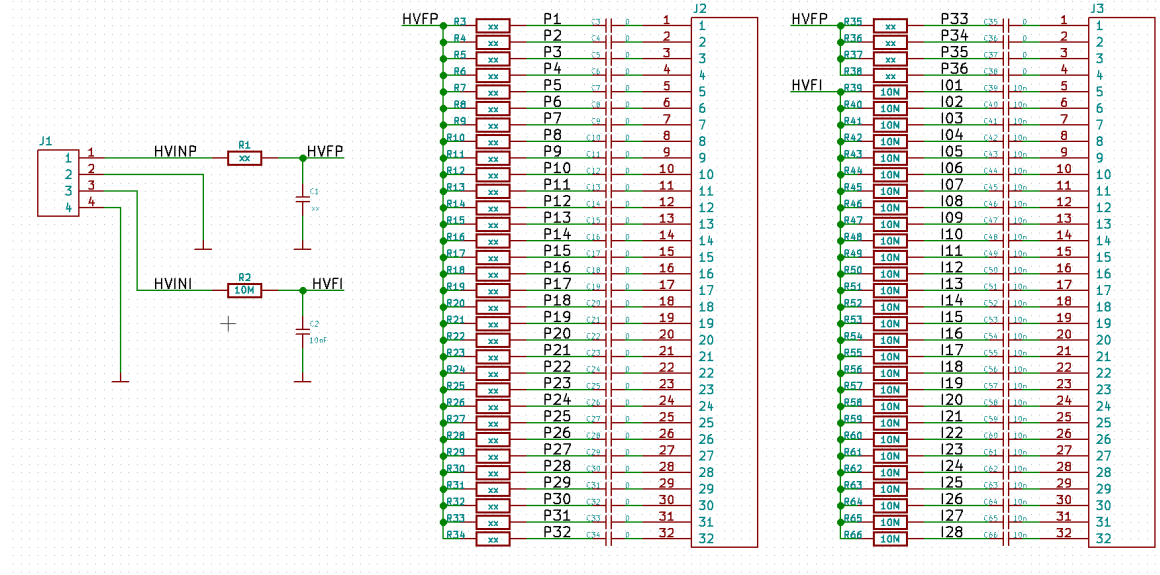


Figure 5.2.: Schematic of the bias circuit for the ArgonCube pixel demonstrator PCB. On the left, the pinheader connected to the bias HV power supply is shown. In the middle and on the right are the connections to the pixels and inductive ROI grids. The connections to the preamplifier inputs are located at the positions of numbers P1–P36 (pixels) and I1–I28 (ROIs). For simplicity and universality, the same circuit was used for both pixels and ROIs even though for the measurements described in this work, only the inductive ROI grids were biased. Therefore, the ROIs are connected as depicted (R2 and R39–R66, C2 and C39–C66). As the pixels need not be biased, they are directly connected to the preamplifiers by leaving R3–R38 unpopulated and replacing C3–C38 by 0Ω resistors. Additionally, R1 is 0Ω and C1 unpopulated, and by connecting pin 1 of J1 to ground, all unused PCB traces are grounded.

12 contained a bug resulting in an underestimation of the bias voltage required for full
 1 transparency. During measurements, the bug became apparent and full transparency had
 2 to be estimated by looking at live data from the detector. Due to the limited accuracy of
 3 this method, measurements were not taken up to the bias voltage for full transparency
 4 suggested by the (corrected) simulation. [83]

5 5.1.2. TPC

6 The pixel demonstration TPC, shown in Figures 5.4 and 5.5, is cylindrical with an inner
 7 diameter of 101 mm and a 590 mm drift length. The TPC operated with a drift field of

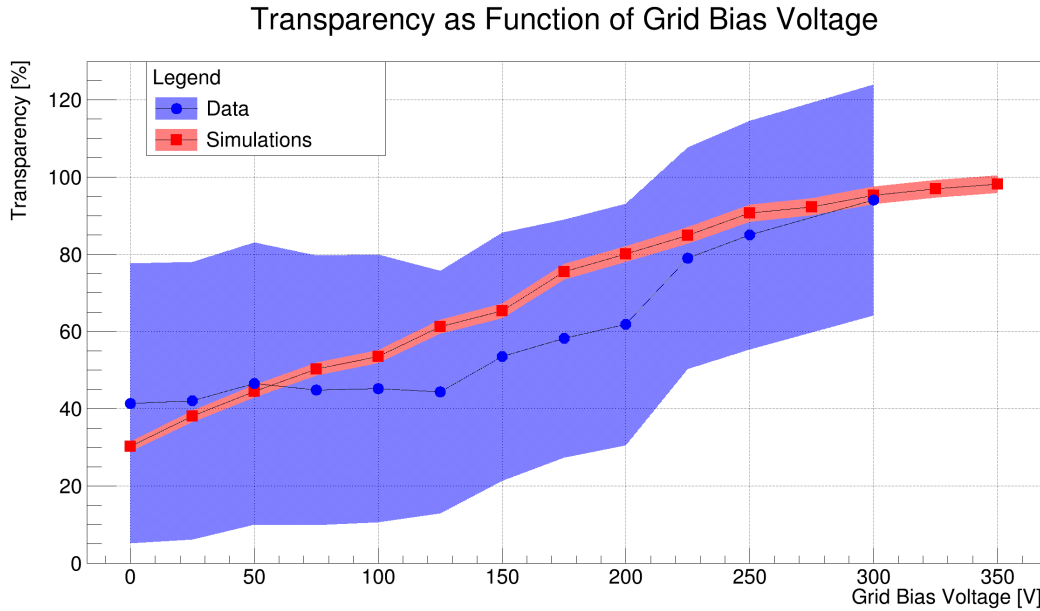


Figure 5.3.: Measured and simulated transparency versus bias voltage of the ArgonCube pixel demonstrator. [83]

⁸ 1 kV cm^{-1} , corresponding to a total drift time of $281 \mu\text{s}$ at $2.1 \text{ mm } \mu\text{s}^{-1}$. [84]

¹ The field-cage consists of aluminium rings supported by clear acrylic rings, with a
² cathode formed of a brass disc. The dimensions of the field-cage and cathode are shown
³ in Figure 5.4. Alternating acrylic rings are split, to allow for the circulation of purified
⁴ LAr within the TPC volume. Four square section PolyAmide-Imide (PAI) uprights
⁵ support the cathode and field cage, with PolyEther Ether Ketone (PEEK) screws fixing
⁶ the pillars to the acrylic rings. The four PAI uprights connect to a PAI frame which
⁷ supports the anode plane and the light readout SiPMs, see Figure 5.5.

⁸ The resistive divider consists of a chain of $100 \text{ M}\Omega$ Vishay Rox metal oxide resistors
⁹ (ROX100100MFKEL). Each resistor is soldered to its neighbour, and fixed to the field
¹⁰ cage at each joint with an M3 screw.

¹¹ The acrylic rings provide the light collection; their inner surfaces are machine-polished
¹² and coated with the WLS TPB. The coating method is based on [85]. 0.5 g of TPB and
¹³ 0.5 g of acrylic flakes were dissolved in 50 mL of toluene and then mixed with 12 mL of

5. A Novel Implementation of the LArTPC Technology

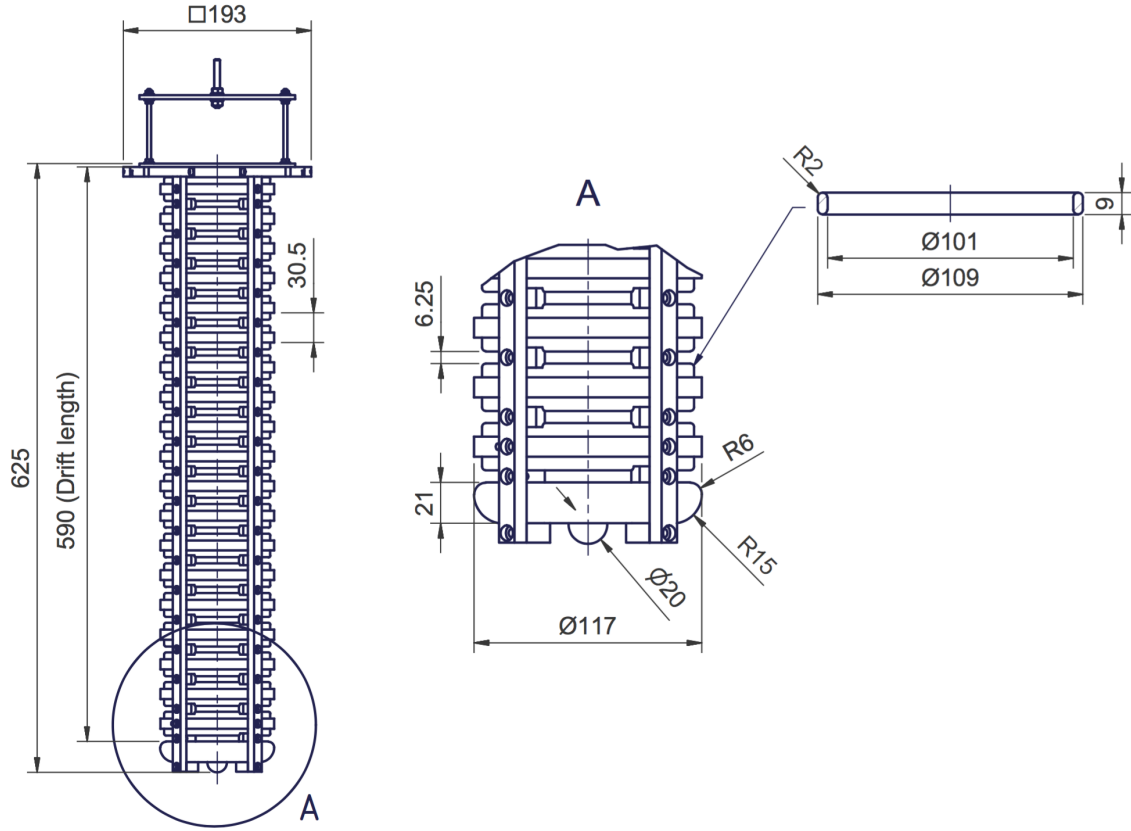


Figure 5.4.: Engineering drawing of the pixel demonstration TPC; 590 mm drift length; 6.25 mm field cage spacing; 101 mm internal diameter.

¹⁴ ethanol, which serves to increase the coating homogeneity. Three layers of the coating
¹ were applied by hand, with a fine brush.

² 1 mm diameter WLS fibres (Kuraray Y11(200)M) couple the acrylic rings to the four
³ Hamamatsu S12825-050P SiPMs mounted close to the anode, see Figure 5.5. The SiPMs
⁴ and their front-end electronics were adapted from those developed at LHEP for the CRTs
⁵ used in MicroBooNE and SBND [72, 86]. For operation in LAr, the SiPM bias voltages
⁶ had to be reduce from ≈ 70 V to 53 V, in order to limit the gain. In the front-end
⁷ electronics, two coincidences of two out of the four SiPMs are formed and combined by
⁸ means of a logic *OR* operation. This coincidence is used in order to improve trigger
⁹ purity.

5. A Novel Implementation of the LArTPC Technology



Figure 5.5.: Left: Photograph of the pixel demonstrator TPC at LHEP, with the HV feedthrough. Right: Close-up of the light collection system, showing WLS fibres coupling SiPMs to the TPB-coated light guides.

¹⁰ 5.1.3. Ancillary Infrastructure

¹ The pixel demonstration TPC is housed in a double-bath vacuum-insulated cryostat
² with the outer bath open to atmosphere. A diameter of 50 cm and a height of 110 cm
³ give an inner volume of $\approx 200\text{ l}$ of LAr. This is the same cryostat that was used for the
⁴ HV studies described in Section 4.1. The LAr filtering method is the same as described
⁵ in [48], with LAr filtered first on filling through a pair of Oxysorb-Hydrosorb filters, and
⁶ then recirculated through a single custom-made filter containing both activated copper
⁷ and silica gel. LAr purity is estimated to be in accordance with [48], with impurity
⁸ concentrations $\sim 1\text{ ppb}$ of oxygen-equivalent, which corresponds to a charge lifetime of
⁹ $(290 \pm 30)\text{ }\mu\text{s}$.

¹⁰ The Crystalline PolyEthylene Terephthalate (PET-C) HV feedthrough capable of

5. A Novel Implementation of the LArTPC Technology

11 potentials as high as -130 kV remains unchanged from the breakdown studies (Section 4.1).
1 A low-pass filter was added between the power supply and feedthrough, which consists
2 of an 800 pF decoupling capacitor grounded between two $100\text{ M}\Omega$ resistors connected in
3 series, i.e. a Resistor Capacitor (RC) low-pass filter with an additional protection resistor
4 at the output. For proper insulation, the whole assembly is submerged in transformer oil.

5 5.1.4. Signal-To-Noise Ratio

To assess the Signal-To-Noise Ratio (SNR), dedicated noise data was taken employing a 5 Hz random trigger. The data of 5000 events was combined. Subsequently, all pixel and ROI channels were combined separately and filled into respective amplitude distribution histograms. Finally, the standard deviation of the noise was calculated by fitting a Gaussian to the amplitude distribution. This value was used to calculate the noise for pixel and ROI channels according to

$$\text{SNR} = \frac{S}{\sigma}, \quad (5.1)$$

6 where S is the signal and σ is the noise standard deviation from the Gaussian fit. As
7 can be seen in the left plot in Figure 5.6, one of the pixel channels is significantly noisier
8 in comparison to others, likely caused by a broken preamplifier. Therefore, this channel
9 was blinded for the SNR calculations. The resulting equivalent noise charge is 1095 e for
10 the pixel channels and 982 e for the inductive ROI channels

The signal S is often taken for a MIP as this is at the lower end of the signal range interesting for neutrino physics. Getting a clean MIP sample from experimental data requires a calibrated reconstruction which was not available at the time of writing. Therefore, the MIP signal was estimated from theory assuming an energy loss of 2.1 MeV cm^{-1} (see Section 2.5). This can be converted to charge loss using the energy required to produce one electron-ion pair from Table 3.1: $W_i = 23.6\text{ eV }e^{-1}$. Additionally,

5. A Novel Implementation of the LArTPC Technology

charge recombination, diffusion and lifetime need to be taken into account (see Section 3.1). The recombination factor was measured by Imaging Cosmic And Rare Underground Signals (ICARUS) [87] and Argon Neutrino Test (ArgonNeuT) [88] and found to be $R_c \approx 0.7$ for a drift field of 1 kV cm^{-1} . With ARGONTUBE [44], LHEP measured a transverse diffusion coefficient $D_T = 5.3\text{ cm}^2\text{ s}^{-1}$ at 0.25 kV cm^{-1} while Gushchin et al. [89] report a value of $D_T = 13\text{ cm}^2\text{ s}^{-1}$ at 1 kV cm^{-1} . Even using the more conservative value, this results in a transverse spread of $\approx 0.9\text{ mm}$ for the pixel demonstrator drift time of $t = 281\mu\text{s}$, according to Equation (3.2). This value lies well below the pixel pitch of $d_p = 2.54\text{ mm}$. Considering that the longitudinal component is smaller than the transverse [43], diffusion is neglected completely for these calculations. Finally, the lifetime of $290\mu\text{s}$ will result in the reduction of charge by a factor of ≈ 0.38 over the full drift distance (Equation (3.3)). Combining this, the signal is

$$S = \frac{dE}{dx}_{\text{MIP}} \frac{R_c d_p}{W_i} = 15\,821\,e, \quad (5.2)$$

¹¹ for a charge deposited adjacent to the readout plane, and $S = 6004\,e$ for a charge
¹ deposited adjacent to the cathode.

² Table 5.1 lists the SNR values obtained from these signal values and the aforementioned
³ measured equivalent noise charge, using Equation (5.1).

Table 5.1.: SNR values obtained from Equation (5.1) using the theoretical signal of a MIP at the readout plane or cathode, respectively combined with the average equivalent noise charge for pixel and ROI channels obtained from measurements.

Channel	MIP at	SNR
Pixel	Readout plane	14
Pixel	Cathode	5.5
ROI	Readout plane	16
ROI	Cathode	6.1

5.1.5. 3D track reconstruction

¹ To demonstrate 3D track reconstruction, several thousand cosmic ray events were collected,
² many of which are MIPs, mostly muons. The charge readout was triggered by the light
³ readout described above.

⁴ The reconstruction procedure comprises five steps: noise filtering, hit finding, hit
⁵ matching, ambiguity rejection, and track fitting. These steps are explained in the
⁶ following and depicted in Figures 5.6 through 5.10, all taken from the same MIP (cosmic
⁷ muon) event.

⁸ In the first step, a noise-filtering algorithm is applied to the raw data. As can be
⁹ seen from Figure 5.6, the noise is largely correlated across all the channels.¹ This
¹⁰ common-mode correlation can be exploited by the noise filter algorithm. The following
¹¹ is done separately for the all pixel and ROI channels of each event. Similarly to the
¹² SNR calculation, all samples are filled into an amplitude distribution histogram for each
¹³ channel, and subsequently fitted with a Gaussian. A noise band is defined per channel
¹⁴ with its centre equal to the mean of the Gaussian and its width equal to the standard
¹⁵ deviation multiplied by a tunable scaling factor. The amplitudes of all channels within
¹⁶ the corresponding noise band are then averaged for each sample. Finally, this average is
¹⁷ subtracted from each channel at the corresponding sample. This technique was chosen
¹⁸ because it effectively suppresses the dominating common mode noise. At the same time,
¹⁹ spurious signals produced by high amplitudes from collected charge distorting the average
²⁰ are kept to a minimum by only accepting values within the noise band. The effectiveness
²¹ of the filtering can be seen in Figure 5.7, which shows the same data as Figure 5.6 post
²² filtering.

²³ The second step applies a recursive pulse finding algorithm. The following is performed
²⁴ for each channel independently. Most thresholds employed by the pulse finder are, again,

¹Due to the much higher signal levels, the noise is barely visible on the pixel channels on the left.

5. A Novel Implementation of the LArTPC Technology

defined in terms of noise amplitude. Therefore, noise mean and standard deviation are recalculated after noise filtering. A peak threshold is defined by multiplying the noise standard deviation by a variable scaling factor and adding the noise mean. Then, the sample with the highest amplitude is found. If it is below threshold, the process stops and proceeds to the next channel. Otherwise, the pulse is scanned in positive and negative directions until it crosses respective lower noise thresholds. After this, the whole pulse is deleted from the data and the process starts over with finding the new maximum sample and checking it against the peak threshold. For stability reasons, the peak threshold relative to noise levels is compared against an absolute threshold and the higher of the two is applied. The search is extended to the negative pulse for the bipolar ROI pulses. The different thresholds employed and samples found by this process are illustrated in Figure 5.8.

Identified pulses are then combined into 3D hits by matching pixels pulses to ROI pulses. For this proof of concept, this is done rather primitively by matching any pulses coinciding in time. In Figure 5.8, a pixel and ROI pulse are matched if their time slices, defined by the vertical dashed lines, overlap. This third step results in a rather high amount of ambiguities but assures that no hits are missed.

To resolve the ambiguities, a Principal Component Analysis (PCA) is applied to the 3D space points in a fourth step. This technique is well established and described in literature, e.g. [90]. Therefore, it shall be explained here only briefly. The basic idea is to calculate three orthogonal eigenvectors of the 3D space point cloud. A graphic interpretation of these eigenvectors are the three axis of an ellipsoid fitted to the data points. In case the points form a track, one of these eigenvectors will have a much higher eigenvalue than the other two. This eigenvector is taken as an estimate for the track direction. The ambiguities can be resolved by selecting the one closest to the track estimate. Furthermore, this procedure can be used to recursively reject outliers by

5. A Novel Implementation of the LArTPC Technology

26 forming a cylinder around the track estimate with a radius proportional to the second
1 largest eigenvalue. All hits outside this cylinder are rejected. The procedure can be
2 repeated by rerunning the PCA on the remaining points and performing another outlier
3 rejection. In a later stage of reconstructing more complex events, this algorithm can
4 potentially be used to cluster 3D space points in order to separate multiple tracks. The
5 PCA ambiguity rejection is illustrated in Figure 5.9.

6 The final step consists of a Kalman filter. For this, the well-established Generic
7 track-Fitting toolkit (GENFIT) package [91, 92] was used. Ionisation losses and MCS
8 are taken into account. The particle is assumed to be a minimum-ionising muon with an
9 initial momentum of $260 \text{ MeV } c^{-1}$ in the direction of the track estimate from the PCA. A
10 recursive algorithm capable of dealing with outliers was chosen, a so-called *deterministic*
11 *annealing filter*. This works by assigning successively lower weights to outliers with each
12 recursion step. For more details, see the respective publications [91, 92]. The resulting
13 track is shown in Figure 5.10.

14 Technically, the Kalman filter would be capable of fitting the particle momentum or
15 even particle type to the data. At the time of this writing, this is not implemented yet. In
16 particular, the momentum stays roughly at the initial guess of $260 \text{ MeV } c^{-1}$, assuming a
17 minimum ionising muon in LAr. A potential explanation for this is that the resolution of
18 the detector is too low to estimate momentum from MCS. Another explanation might be
19 the hit finder missing hits due to non-optimal tuning. Proper tuning of the reconstruction
20 requires a full simulation chain of the detector which is not yet available. Using data to
21 tune the reconstruction is prone to the introduction of circular biases. On the other hand,
22 most of the difficulties emerge from the multiplexing ambiguities and their resolution.
23 While the presented almost full 3D readout has already reduced the reconstruction
24 complexity compared to a classical wire readout, an ambiguity-free readout will make
25 reconstruction another big step easier by completely eliminating the need to resolve

5. A Novel Implementation of the LArTPC Technology

²⁶ ambiguities.

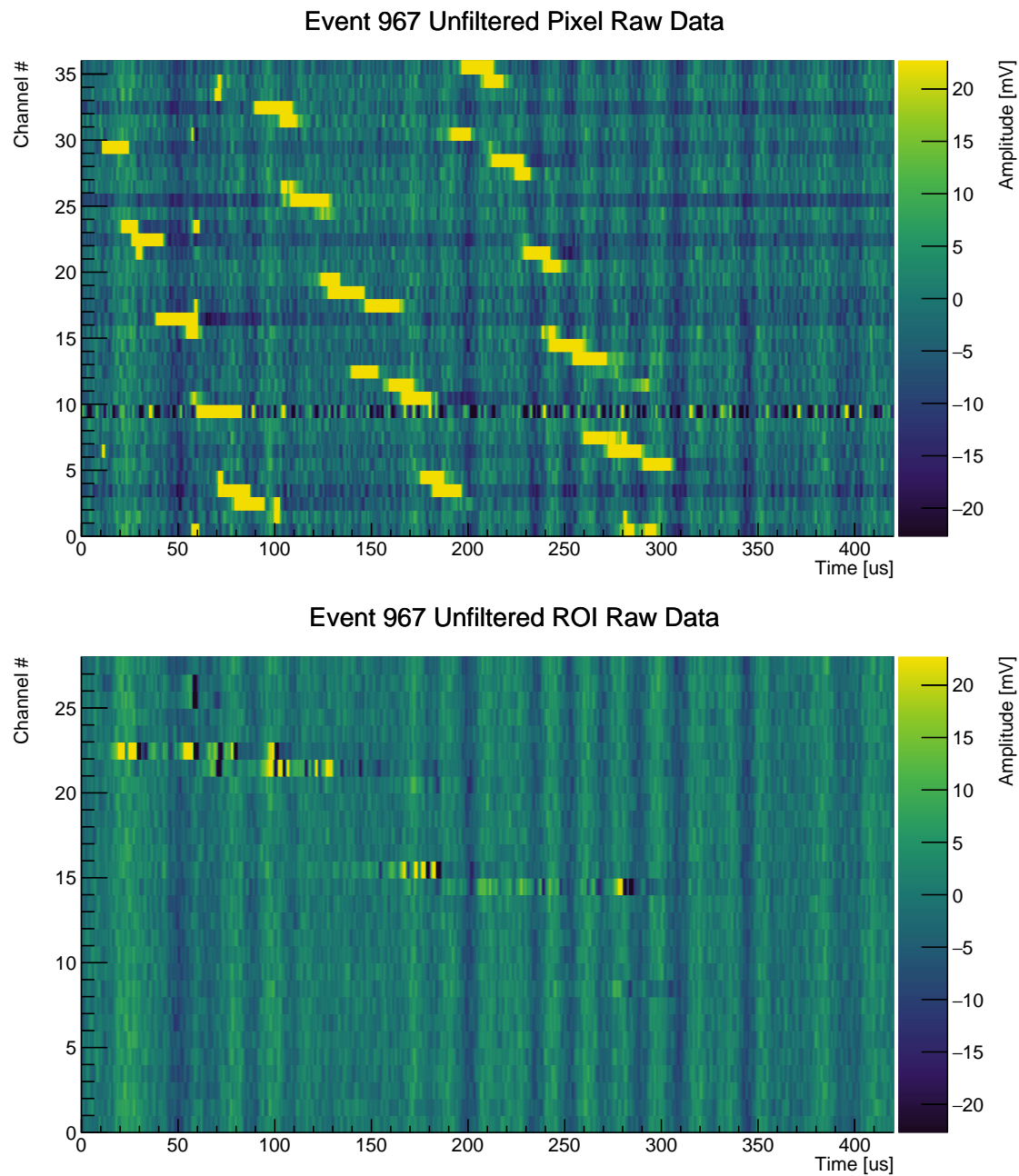


Figure 5.6.: Unfiltered raw data of a typical MIP event (the same event as in Figures 5.6 through 5.10). The top plot shows pixel data while the bottom plot shows ROI data.

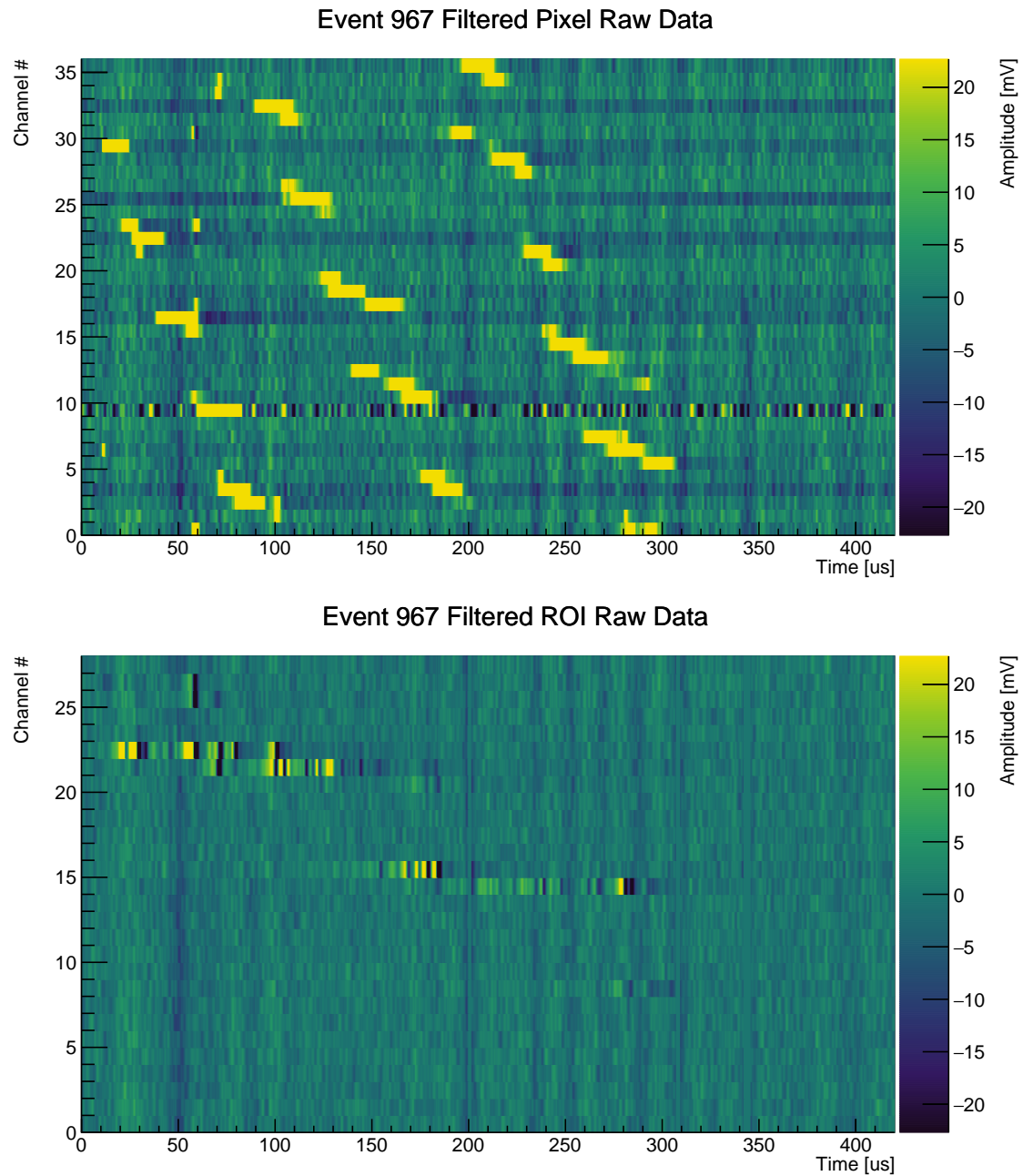


Figure 5.7.: Filtered data of a typical MIP event (the same event as in Figures 5.6 through 5.10). The top plot shows pixel data while the bottom plot shows ROI data.

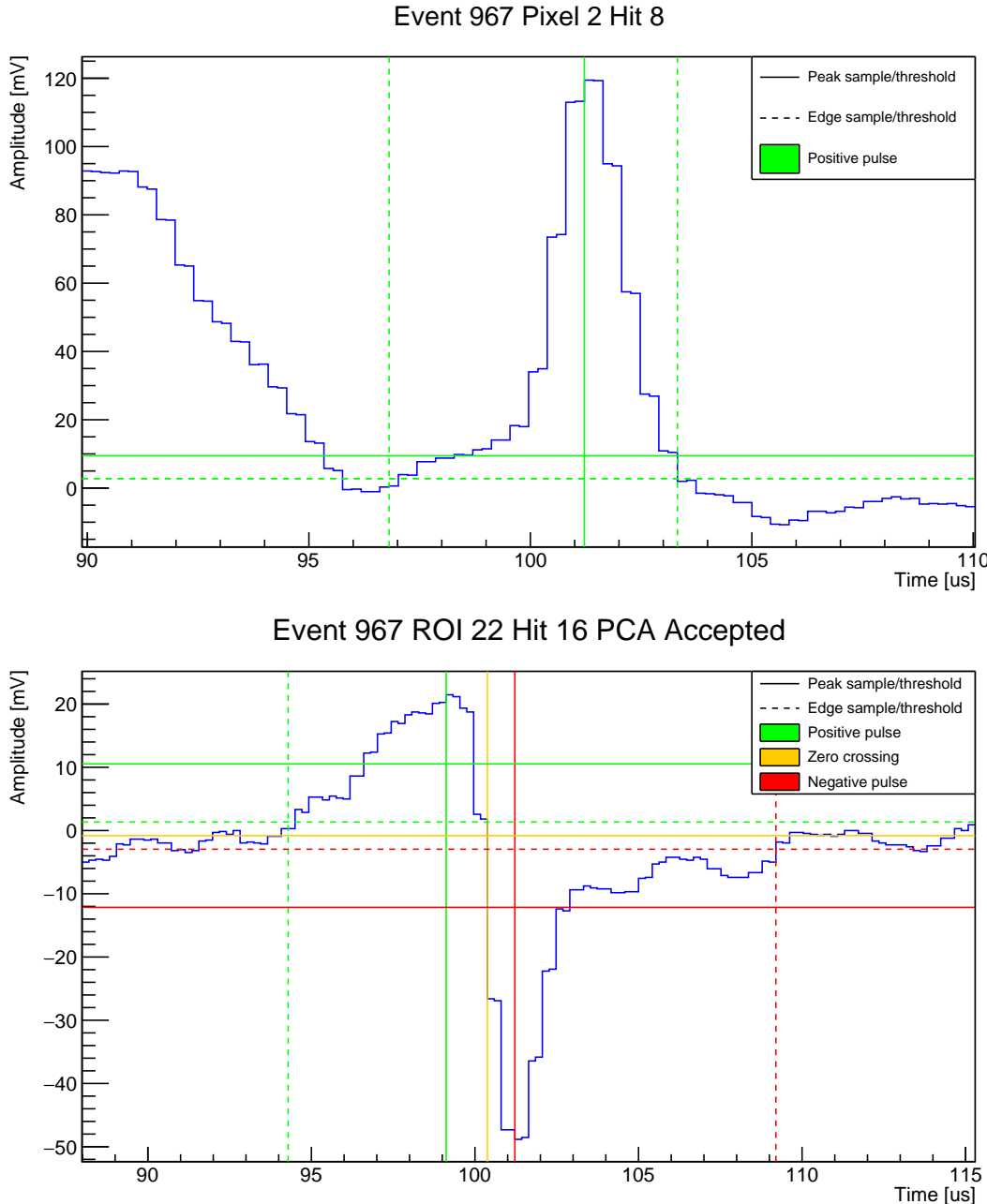


Figure 5.8.: Pulse shapes of a single pixel (top) and ROI (bottom) hit of a typical MIP event (the same event as in Figures 5.6 through 5.10). Superimposed are the thresholds of the hit finder algorithm. Horizontal lines represent thresholds: the solid is the minimum threshold required to be crossed for a pulse to be detected, and dashed are the thresholds used to detect the pulse edges. Vertical lines represent the corresponding detected peak/edge samples. Colour indicates a positive (green) or negative (red) pulse, or a zero crossing (yellow).

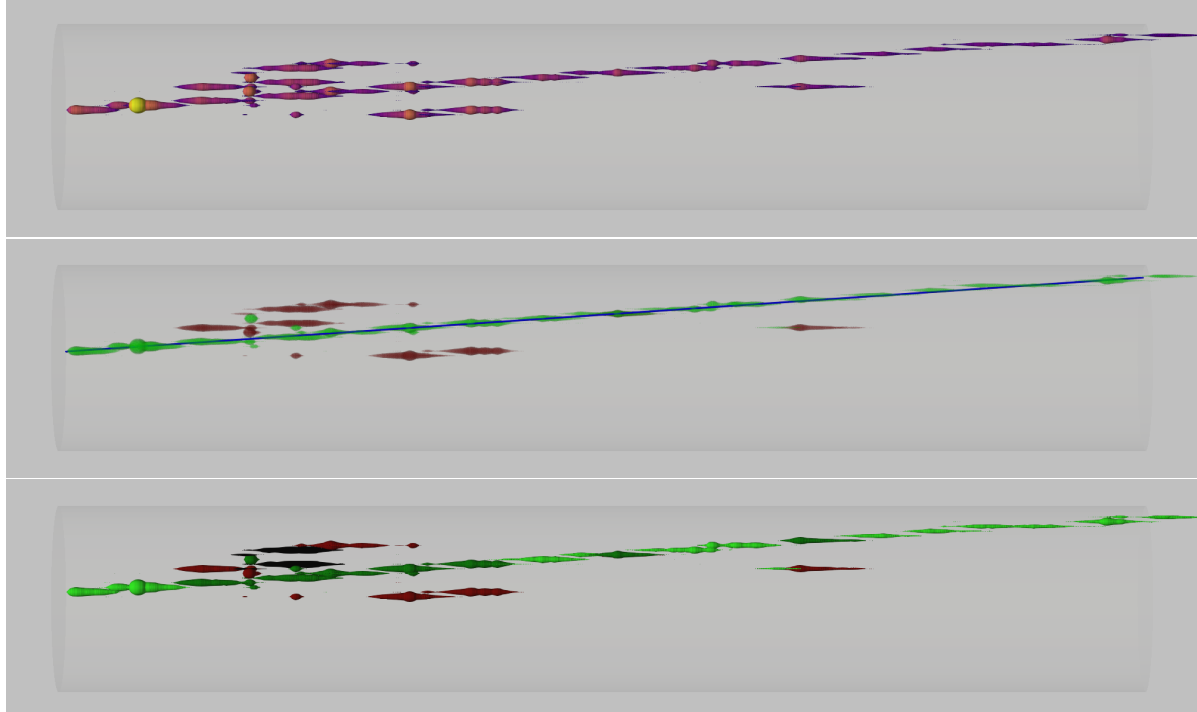


Figure 5.9.: Reconstructed 3D hits from the hit finder. The passing particle is most likely a cosmic μ entering from the left (the same event as in Figures 5.6 through 5.10). Drift direction is from right to left. Pulse shape is encoded as thickness. In the top plot, colour codes the amount of collected charge. The middle plot illustrates the ambiguity resolution employing a PCA. Green hits are accepted while dark red ones are rejected. This is achieved by selecting the ambiguity closest to the eigenvector of the point cloud with the largest eigenvalue, represented by the blue line. In the bottom plot, the degree of ambiguity is colour-coded: Light green are unambiguous hits while dark green are selected solutions of ambiguous hits. Dark red through black are rejected solutions of ambiguous hits where darker colour represents a higher degree of ambiguity. As this is a quite clean track with only few short δ rays, there are no outliers rejected other than the multiplexing ambiguities.

5. A Novel Implementation of the LArTPC Technology

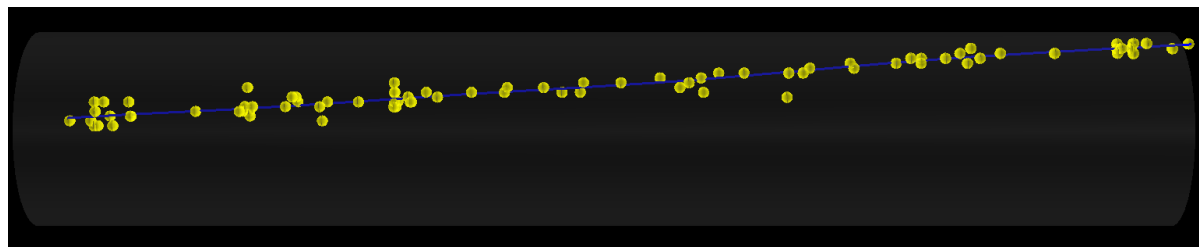


Figure 5.10.: Track fitted by the Kalman filter. The TPC volume is shown in faint grey. The passing particle is most likely a cosmic μ entering from the left (the same event as in Figures 5.6 through 5.10). Drift direction is from right to left. The yellow points are the input to the Kalman filter, the accepted hits from the PCA. Blue is the output, a fitted track taking into account ionisation losses and MCS in LAr.

¹ 5.2. PixLAr

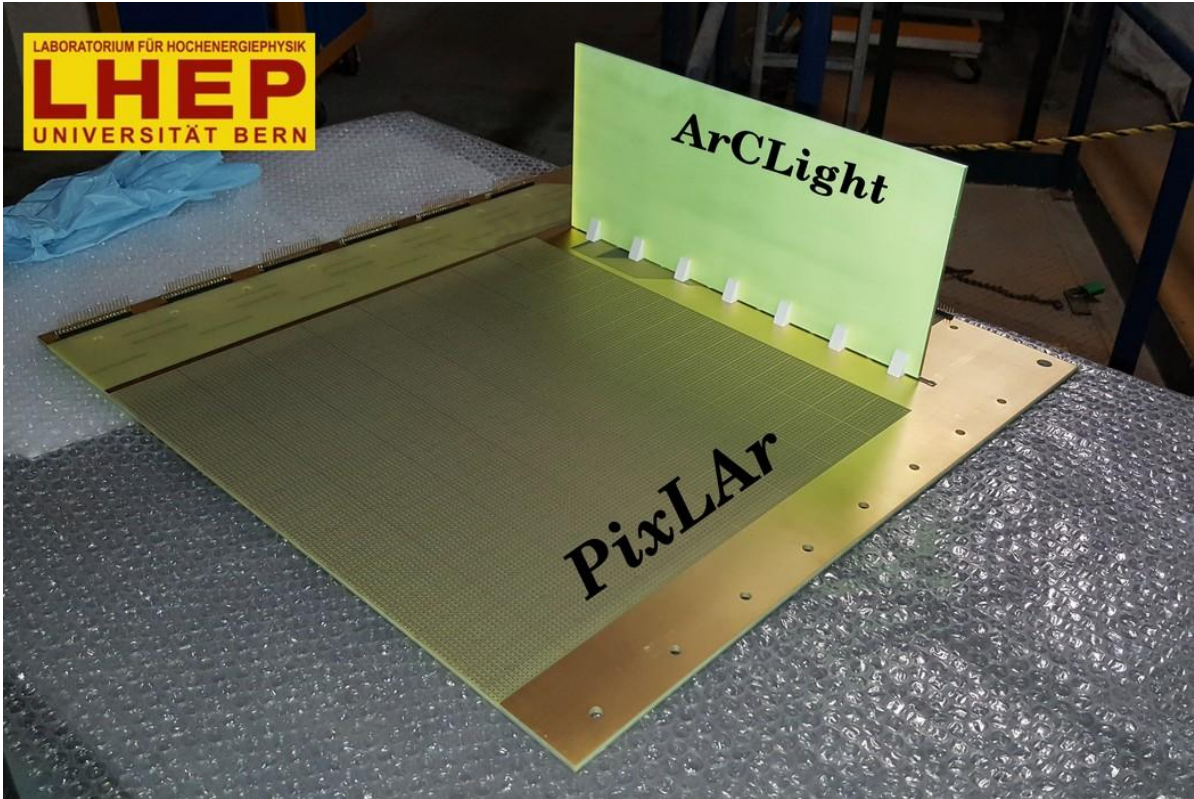


Figure 5.11.: One of the two PixLAr readout half planes with the ArCLight module attached.

¹ After the successful test with cosmic muons at LHEP, a bigger prototype of the pixel readout, employing the same multiplexing scheme, was built for a beam exposure in the LArIAT experiment [65] at FNAL. LArIAT consists of the former ArgonNeuT [93] cryostat and LArTPC put into a test beam. The tertiary beam line produces mainly pions and protons as well as electrons, muons and kaons at a lower rate. Their momentum spectrum can be tuned from $0.2 \text{ GeV } c^{-1}$ to $2.0 \text{ GeV } c^{-1}$. 550 l of LAr are contained in a cylindrical cryostat. It houses a TPC with 47 cm drift length and a $40 \text{ cm} \times 90 \text{ cm}$ readout plane parallel to the beam direction, resulting in an active volume of 170 l. For the pixel test, called PixLAr, the original wire planes were replaced by a 120×240 pixel readout. At 3 mm pitch, this gives an instrumented area of $36 \text{ cm} \times 72 \text{ cm}$. Due

5. A Novel Implementation of the LArTPC Technology

11 to constraints from the PCB manufacturer, the readout plane had to be split into two
 1 mirror-symmetric, electrically independent half planes. Each 120×120 pixel half plane is
 2 divided into 8×15 ROIs of 15×8 pixels each. The ROIs are oriented with their longer
 3 dimension parallel to the beam direction to reduce the multiplexing ambiguities. One of
 4 the noise mitigation measures implemented for the LHEP pixel demonstrator was to use
 5 the same differential warm signal path as used by LArIAT. Therefore, the charge readout
 6 electronics used in PixLAr are quite similar to the ARGONTUBE chain described in
 7 Section 4.3.1 after the upgrades. To trigger on scintillation light, one end of the TPC
 8 is equipped with a $43\text{ cm} \times 15\text{ cm}$ ArCLight module (see Section 4.4.2), while the other
 9 end features an ARAPUCA [81] detector for comparison. Figure 5.11 shows one of the
 10 readout half planes with the ArCLight module attached.

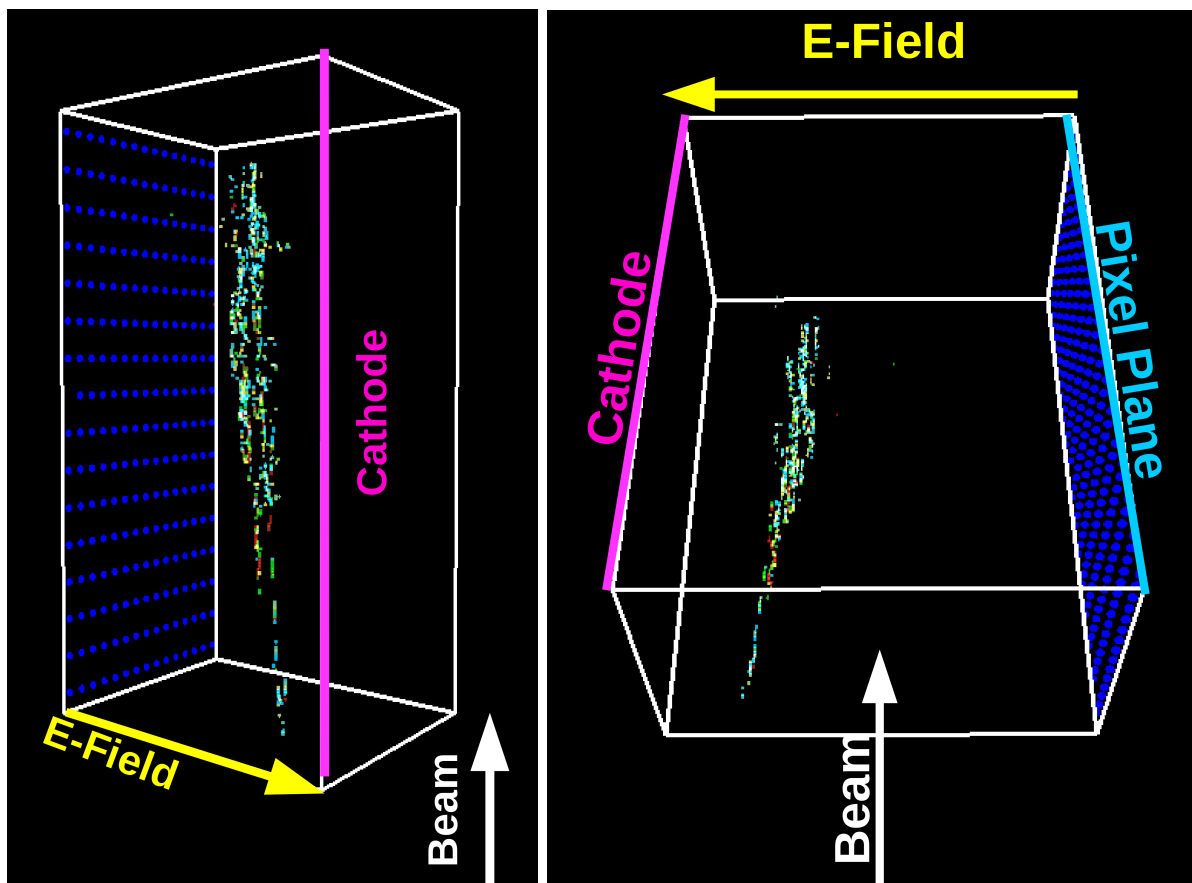


Figure 5.12.: PixLAr beam event.

5. A Novel Implementation of the LArTPC Technology

11 Over several weeks, beam and cosmic muon data was taken. At the time of writing,
1 no official results were available. Nevertheless, preliminary analyses indicate a successful
2 scale-up of the pixelated LArTPC concept. The achieved SNR seems to be comparable
3 to what was reached with the prototype at LHEP, described above. A recorded beam
4 event is depicted in Figure 5.12.

5 5.3. The ArgonCube Approach

6 To address the challenges mentioned in Section 3.6, the LHEP group has formed the
7 ArgonCube collaboration, with the goal of developing a new fully-modular type of
8 LArTPC. Modularity reduces pile-up and allows for shorter drift-times, thus slackens
9 the requirements on argon purity and HV. A modular detector also contains light within
10 each module, allowing for a more accurate trigger system. Maintenance and upgrading
11 of a modular detector is much easier than for a monolithic one.

12 5.3.1. Modularity

13 ArgonCube is made of self-contained TPC modules sharing a common cryostat. In case
14 of a fault condition the affected module(s) can be shut down and repaired or replaced
15 individually without affecting the rest of the detector. During construction, one can
16 start data taking as soon as the first module is operational and needs not wait for the
17 commissioning of the whole detector. A modular detector furthermore reduces event
18 pile-up because the acquisition time is reduced to the size of one half module. This is
19 crucial in the high-multiplicity environments of future LAr neutrino detectors. Finally,
20 also trigger purity profits from a modular approach because scintillation light is contained
21 within each module, allowing for a localised trigger.

22 A module is made of a rectangular box with a square footprint and the height required
23 by physics goals and/or sensitivity constraints. The top and bottom flanges are made

5. A Novel Implementation of the LArTPC Technology

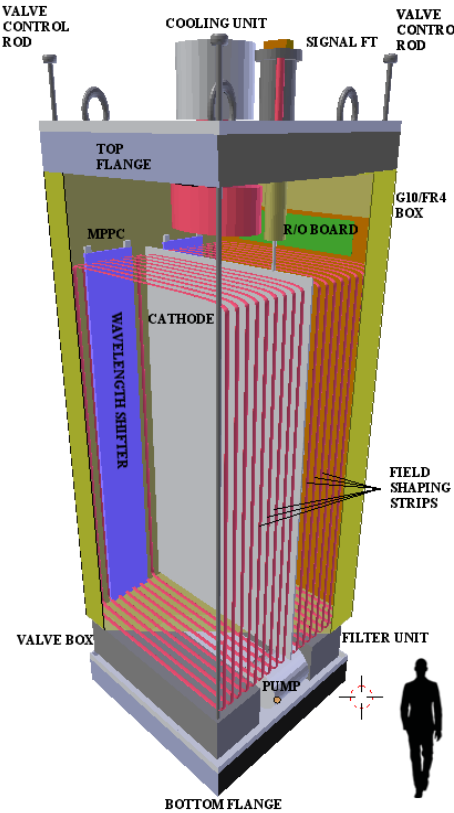


Figure 5.13.: Schematic of an ArgonCube module.

better, more recent picture

²⁴ of stainless steel while the side walls are made from 1 cm G10 sheets. G10 is a glass-reinforced epoxy composite formerly used for PCBs. Its low density makes it more transparent for passing particles allowing for a performance comparable to a monolithic detector. At the same time, the dead volume is drastically reduced compared to a monolithic design due to the comparably low cathode voltage (see Section 6.1). The modules are placed side-by-side in a bath of LAr where they can be extracted and reinserted as needed. Pressure inside the modules is kept close to the bath pressure putting almost no hydrostatic force on the module walls. Purity of the LAr is maintained within each module by means of a recirculation system (see Section 5.3.3). As a result, the argon surrounding the modules needs not meet as stringent purity requirements as the argon inside. Under normal operation conditions, all modules are inserted with only

5. A Novel Implementation of the LArTPC Technology

11 clearance distances between modules, and their top flanges sealed using indium. The
1 schematic of an ArgonCube module is shown in Figure 5.13.

2 To extract a module, the indium seal around the flange in question is removed. The
3 module is then slowly lifted up by a crane and the LAr is drained to the surrounding
4 bath through a hydrostatic outlet valve at the bottom of the module by means of gravity.
5 On the bottom of the module, a blind flange is located with equal dimensions as the
6 top flange but without any feedthroughs. When the bottom flange reaches the original
7 position of the top flange, it is sealed with indium again and then detached from the
8 module which is now free and can be brought to its destination. Upon reinsertion, the
9 procedure is reversed. First, the module is reattached to the blind flange and the indium
10 seals is removed. Then, it is slowly inserted into the argon bath while being filled through
11 a hydrostatic inlet valve at the bottom of the module by means of hydrostatic pressure.
12 As soon as the top flange of the module reaches the top flanges of the other modules, the
13 indium seal is reinstalled. Figure 5.14 shows the insertion (left) and extraction (right) of
14 a module, for the 2×2 prototype at LHEP (see Section 6.1.1).

15 5.3.2. Drift Field Generation

16 Another big problem that can be solved by a modular TPC design are the high electric
17 fields required for large detectors, and the resulting stored energy. Because each module
18 contains its own TPCs independent of all other modules, the required cathode potential
19 only depends on the module size not the detector size. To minimise the cathode voltage,
20 the field is applied along one of the short edges of a module and furthermore, the module
21 is split in half by the cathode reducing the voltage by another factor of two. Thus, for a
22 module footprint of $1\text{ m} \times 1\text{ m}$ and an electric field of 1 kV cm^{-1} , a cathode potential of
23 only 50 kV is required. Operating a LArTPC at this voltage is challenging but feasible
24 without a prohibitive loss in fiducial volume [44]. The HV is brought into the module

5. A Novel Implementation of the LArTPC Technology

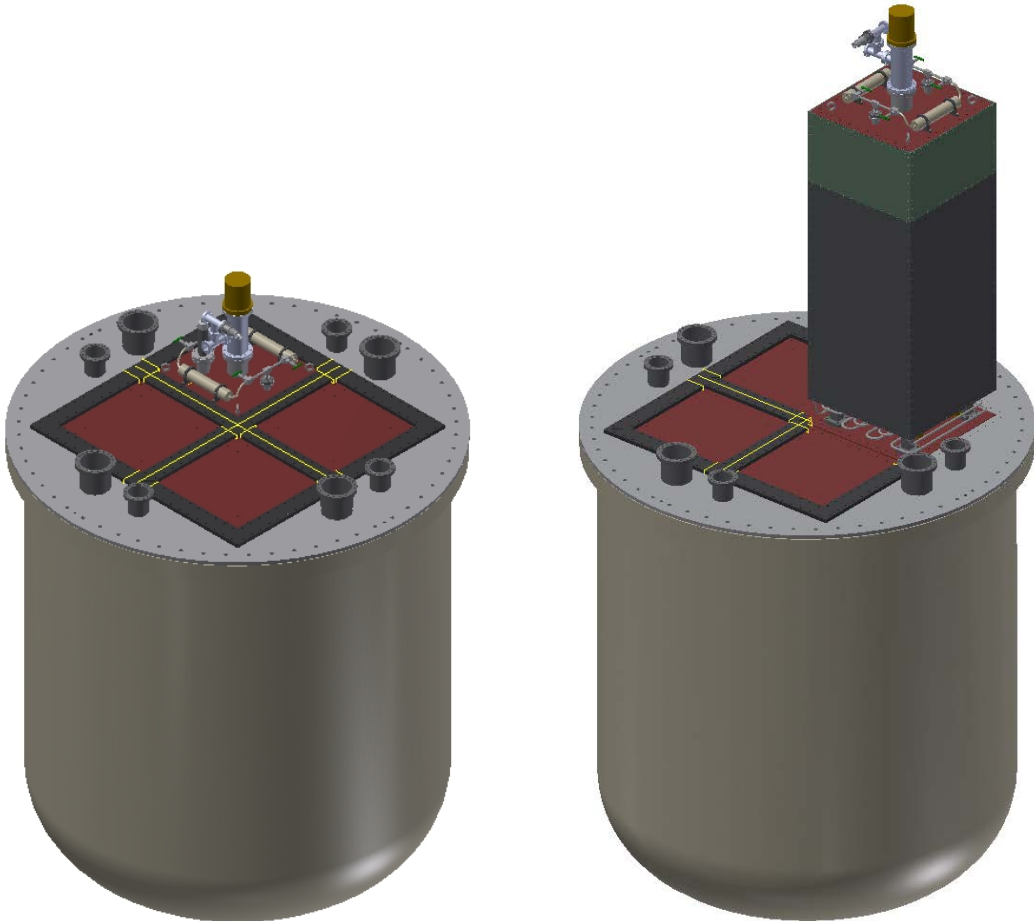


Figure 5.14.: Inserted (left) and extracted (right) module.

25 using a feedthrough similar to the one used for the breakdown studied presented in
1 Section 4.1. Due to the moderate cathode voltage, commercial alternatives are also
2 available. Using conventional PCB techniques, field-shaping rings can be realised as
3 copper traces directly printed onto the G10 module walls. They are connected via
4 high-voltage resistors in the same fashion as for a classic LArTPC. An improved solution
5 with a continuous resistive-plane field cage is under investigation. This could provide a
6 very homogeneous field paired with simple mechanics. The difficulty is to find a material
7 with the required sheet resistivity of $\sim 1 \text{ G}\Omega/\text{sq}^2$ that is stable at cryogenic temperatures

²Sheet resistivity only depends on the aspect ratio of the sheet but not its area. It is therefore quantified as a resistance per square.

8 and depositable on G10.

1 5.3.3. Cryogenics

2 During module insertion and extraction, the argon flow is controlled by hydrostatic
3 check valves located at the bottom of the module. They require a minimal differential
4 pressure to open. Purity inside to modules is maintained by means of continuous LAr
5 recirculation through oxygen traps. The dirty argon is sucked in at the module top and
6 then pushed through the oxygen traps. The clean argon is first routed through a heat
7 exchanger located below the module inside the outer bath for cooling, and then re-enters
8 the module at the bottom. For optimal heat transport, the argon flow is directed along
9 the cold electronics. To prevent dirty argon from the bath entering the modules, their
10 interior is held at a slight overpressure, just below the opening pressure of the check
11 valves. Cooling power to the bath is supplied by cryocoolers located in uninstrumented
12 volumes at the side of the detector called service volumes.

13 There are two slightly different options for the recirculation system. To maximise
14 module autonomy, each module can be equipped with its own oxygen trap and LAr
15 pump. One drawback of this is the very high cost of LAr pumps. Currently, the DUNE
16 ND complex is planned to consist of a magnetised detector besides an unmagnetised
17 LArTPC. The resulting magnetic stray fields might interfere with the electric motors of
18 LAr pumps on top of the modules. Using a shared recirculation circuit is more economic
19 but reduces module autonomy. The external system, comprising pump and oxygen traps,
20 can be located outside the argon bath (and potential magnetic stray fields) connected to
21 the modules via tubes.

²² **5.3.4. Charge Readout**

¹ The high rates present in a ND environment will lead to a significant amount of event
² pile-up. Disentangling the individual neutrino events requires a highly capable charge
³ readout. Solving this task with a projective wire readout is more than doubtful. To
⁴ enable true 3D tracking, the modules are equipped with a pixelated charge readout very
⁵ similar to the one described in Section 4.2.2. Pixelated anode planes are located on the
⁶ two outer walls parallel to the cathode. To achieve unambiguous 3D information, the
⁷ bespoke PixLAr cryogenic electronics described in Section 4.3.2 are used to digitise the
⁸ signals in cold.

⁹ **5.3.5. Light Readout**

¹⁰ One of the main challenges for the light readout are again the high rates faced by a ND.
¹¹ To get proper timing for the third spatial coordinate, scintillation signals need to be
¹² correctly matched to charge signals (flash matching). Furthermore attenuation due to
¹³ Rayleigh scattering becomes a problem for large detectors (see Table 3.1). Both problems
¹⁴ are greatly alleviated by using an opaque cathode and module walls, containing the
¹⁵ scintillation light inside a single module half (TPC). Therein, pile-up is reduced due to
¹⁶ the smaller volume. Having a position-resolving light readout helps as well. However,
¹⁷ a modular TPC introduces a new challenge: The dead spaces in between adjacent
¹⁸ TPCs have to be kept to a minimum because they introduce gaps in the recorded event
¹⁹ topologies accompanied by lost energy. Classic PMTs could therefore only be mounted
²⁰ at the top and/or bottom of the module but this would still waste active argon volume.
²¹ Additionally, the light would be collected at the far ends of a long narrow volume. Finally,
²² due to their operating principle, PMTs do not work well in high electric fields present
²³ near the field cage at the module top and bottom. Therefore, ArgonCube modules are
²⁴ instrumented with the ArCLight light collection system described in Section 4.4.2. With

5. A Novel Implementation of the LArTPC Technology

its light trap design, it allows light collection from a large area with a minimal dead volume. The location of the SiPMs at the edges of a dielectric sheet makes most of the light detector immune to electric fields. Splitting ArCLight into several horizontal strips stacked vertically gives some spatial resolution in the vertical direction. ArCLight sheets are mounted in between cathode and anode, parallel to the field cage, with the SiPMs directly attaching to the charge readout PCB. The additional dead volume of a few mm is similar to the one caused by the charge readout PCBs in perpendicular direction.

6. Towards the DUNE Near Detector

¹ The ArgonCube concept, described in Section 5.3, enables a LArTPC component in the
² DUNE Near Detector (ND) complex. This chapter will present a more detailed design
³ for the ND, together with a feasibility study of a LArTPC at the expected rates.

6.1. ArgonCube in the DUNE Near Detector

⁵ While Section 5.3 gave a general overview of the ArgonCube concept, this section focusses
⁶ on the detailed implementation for the DUNE ND. After the establishment of the key
⁷ technologies described in this work, the next step will be a 2×2 module prototype at
⁸ LHEP. Finally, the current status of an ArgonCube LArTPC component for the DUNE
⁹ ND complex is given.

6.1.1. 2×2 Module Prototype

¹¹ The goals of this prototype are testing the mechanical design and cryogenic systems,
¹² comparing different charge and light readout systems, and studying module insertion and
¹³ extraction procedures with a focus their influence on purity. For comparison, one of the
¹⁴ four modules will be equipped with a classic wire readout. To investigate purity, first tests
¹⁵ will be performed with the ArgonCube demonstrator TPC described in Section 5.1. The
¹⁶ TPC will be mounted inside an otherwise empty module, hanging from an intermediate

6. Towards the DUNE Near Detector

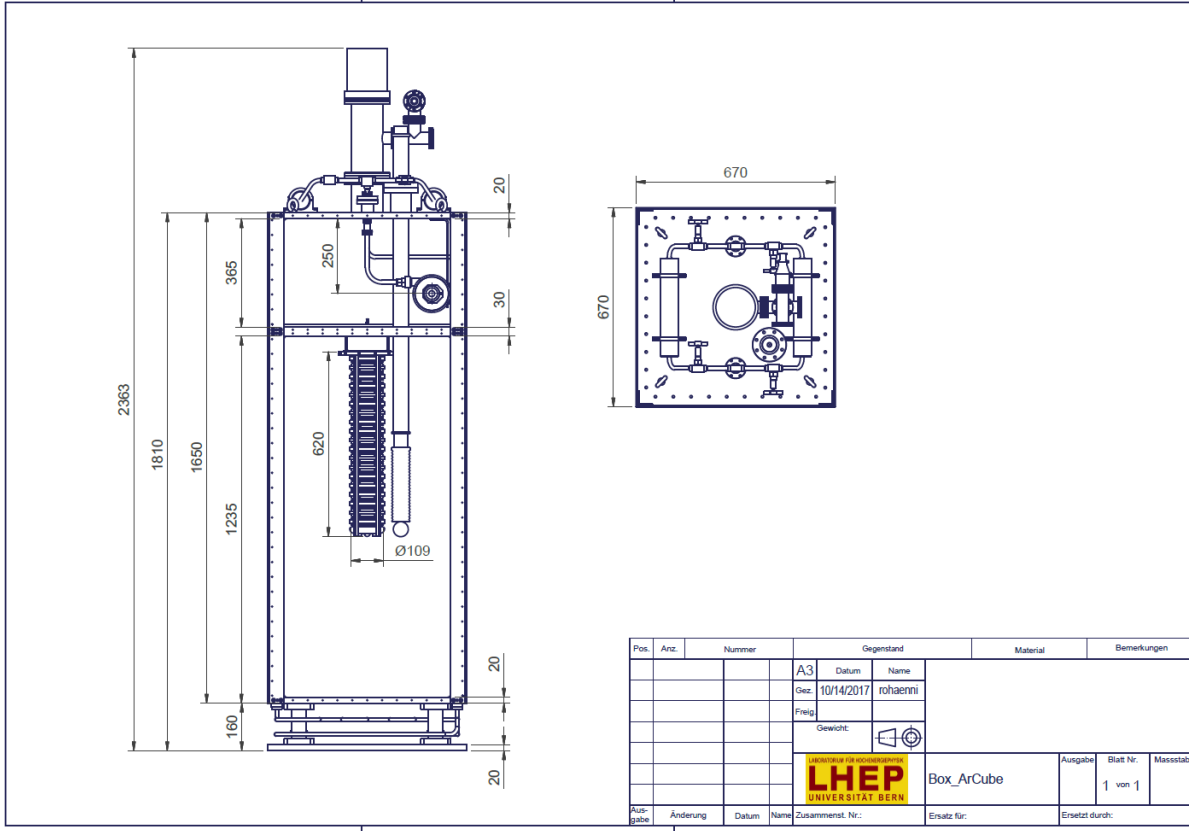


Figure 6.1.: Dimensions of a $0.67\text{ m} \times 0.67\text{ m} \times 1.81\text{ m}$ module with hanging pixel demonstrator TPC for the ArgonCube 2×2 module ArgonCube prototype at LHEP.

¹⁷ support layer. This will also serve as a first cryogenic stress-test of the module structure
¹ and LAr purification.

² The four modules will be housed in an existing cylindrical, vacuum-insulated cryostat
³ at LHEP. With its approximately 2 m diameter by 2 m height it provides a LAr bath
⁴ volume of roughly 6 m^3 . To fit inside the bath, the modules are scaled down to a footprint
⁵ of $0.67\text{ m} \times 0.67\text{ m}$ and a height of 1.81 m. Instead of service volumes, cooling is provided
⁶ by two liquid nitrogen turbo-cooling circuits attached to the inner cryostat wall inside
⁷ the insulation vacuum. They cool the LAr bath via evaporation of the liquid nitrogen.
⁸ The nitrogen flow has to be regulated precisely to keep the LAr stable and prevent it
⁹ from boiling or freezing.

6. Towards the DUNE Near Detector

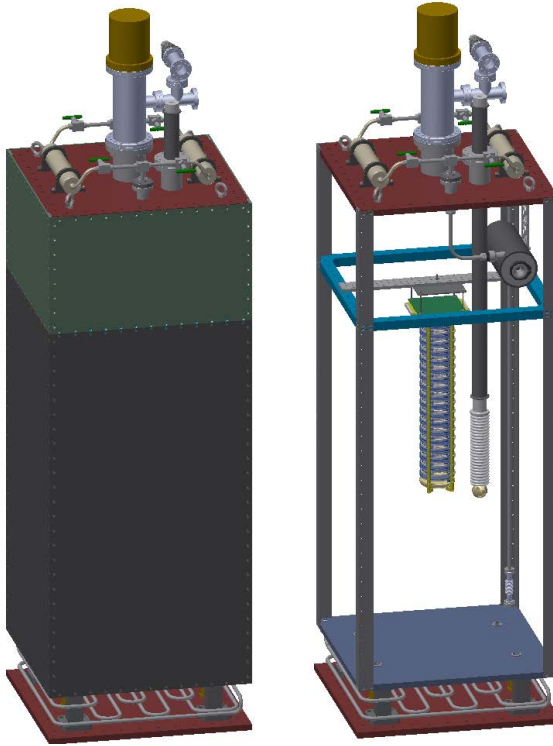


Figure 6.2.: Engineering drawings of a $0.67\text{ m} \times 0.67\text{ m} \times 1.81\text{ m}$ module with hanging pixel demonstrator TPC for the ArgonCube 2×2 module ArgonCube prototype at LHEP.

The height of the actual TPC in a fully equipped module is 1235 mm. Due to the split-TPC design, the resulting cathode voltage required for a 1 kV cm^{-1} field is below 35 kV. On the bottom, 160 mm are occupied by the heat exchanger and check valves for LAr exchange with the bath upon insertion and extraction. The remaining room on top of the TPC is filled up by the HV feedthrough, a buffer gas phase, and a potential recirculation pump. All support structures except for the flanges at the module top and bottom are made from G10, including most of the screws. The thickness of the side walls is 10 mm while the flanges are made of 20 mm stainless steel plates. Figure 6.1 gives the detailed dimensions of a prototype module. It depicts the first module that will be equipped with the demonstrator TPC. For this test, an internal pump salvaged from ARGONTUBE will be used in combination with oxygen traps mounted on top of the

6. Towards the DUNE Near Detector

11 module. Engineering drawings of this module are given in Figure 5.13.

1 Table 6.1 gives an overview of the most important dimensions of the 2×2 LHEP
2 prototype and the preliminary ND design (see Section 6.1.2). In particular the table
3 contains a rough estimate of dead space caused by the modular design and the
4 corresponding active volume fraction. For these calculations, a total charge readout
5 thickness of 20 mm and a total light readout thickness of 5 mm were assumed. The
6 difference is caused by the fact that charge readout electronics are located directly behind
7 the readout while the SiPMs are only mounted on the edges of ArCLight. Additionally,
8 a few mm clearance between the anode plane and the module wall are required for
9 convection cooling of the PixLAr electronics. Readout thicknesses also include the
10 clearance required between adjacent modules (~ 1 mm). The resulting total fraction of
11 active volume is 87.0 % for the 2×2 prototype.

12 In a first phase, the 2×2 prototype will be operated in the Grosslabor of LHEP,
13 taking cosmic ray data. After a successful test of all subsystems, it is planned to be
14 installed in a charged particle test beam at either CERN or FNAL to investigate the
15 influence of the module walls on calorimetry and tracking.

Is this still valid?

16 **6.1.2. Preliminary Near Detector Design**

17 The ArgonCube ND design is based on a scaled-up version of the 2×2 module design
18 described above. Modules will have a footprint of $1\text{ m} \times 1\text{ m}$ and a height of 3.5 m . Again,
19 0.1 m at the bottom are occupied by the heat exchanger and valves while 0.4 m at the
20 top are taken up by feedthroughs and the gas phase. This results in a TPC size of
21 $1\text{ m} \times 1\text{ m} \times 3\text{ m}$, split into two halves by the cathode. The full detector will consist of
22 4×5 modules with the longer dimension in beam direction. These dimensions were
23 optimised for maximum hadron containment by means of simulations done by the neutrino
24 group at LBNL [94]. While horizontal dimensions are unproblematic, the vertical 3 m are

6. Towards the DUNE Near Detector

Table 6.1.: ArgonCube dimensions for the 2×2 prototype at LHEP and preliminary DUNE ND design. Charge and light readout thicknesses are given per wall, i.e. the resulting dead space per module is twice as big. Both are preliminary estimates. For simplicity, clearance between adjacent modules is included in these numbers.

Dimension	2×2	ND	Unit
Detector size	2×2	4×5	mod
Module footprint	0.670×0.670	1.000×1.000	m^2
Module height	1.810	3.500	m
TPC height	1.235	3.000	m
Total TPC volume	2.218	60.000	m^3
Flange thickness	0.020	0.020	m
Side wall thickness	0.010	0.010	m
Charge readout thickness	0.020	0.020	m
Light readout thickness	0.005	0.005	m
Total dead volume	0.289	5.292	m^3
Active volume fraction	87.0	91.2	%

25 at the lower limit. According to the simulations, 2.5 m would be sufficient but provide no
 1 safety margin at all. Reducing the height by 0.25 m results in a significant loss of hadron
 2 containment already. Figure 6.3 illustrates this by means of the cross-section coverage as
 3 a function of neutrino energy. Cross-section coverage is similar to containment efficiency
 4 but should not be confused with the latter. To assess the efficiency, a detector of the
 5 corresponding size in the neutrino beam is simulated. While this indeed provides a good
 6 measure of the efficiency of the detector to contain different events, it is not necessarily a
 7 good quantity to assess the required detector size. Many events are simply not contained
 8 because of their specific location and/or orientation inside the detector. Cross-section
 9 coverage remedies this deficiency by looking at the actual extent of the event instead of
 10 its containment at a random position inside a realistic detector. On the other hand, an
 11 event extending through the full detector will very likely never be contained in a real
 12 detector due to the low probability of exactly happening in the right location. Therefore,
 13 the maximum event size needs to be selected smaller than the full detector size. For the

400cm wide x 500cm long

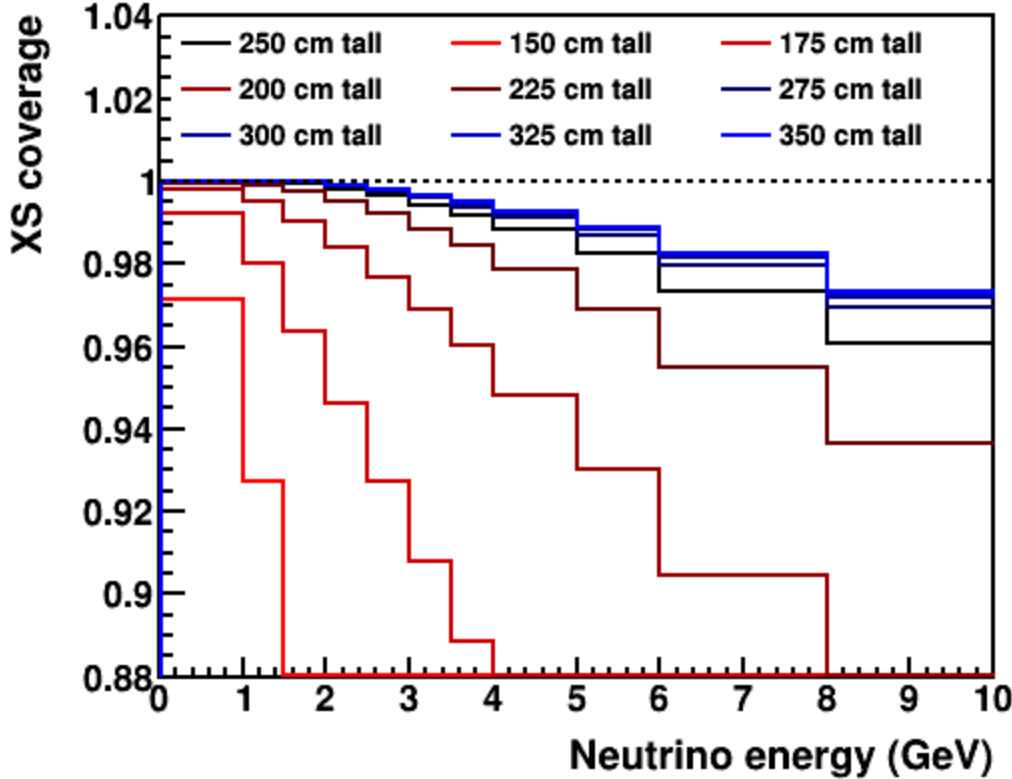


Figure 6.3.: Influence of the LArTPC size in the DUNE ND complex on hadron containment. Given in cross-section coverage as a function of neutrino energy. Horizontal dimensions are held constant at their nominal values of 4 m × 5 m. Height is indicated by colour. See text for explanation of cross-section coverage.

¹⁴ ND simulation, this was chosen as 0.5 m on all edges. Like this, cross-section coverage
¹ allows to probe for phase space regions inaccessible to a particular detector configuration.

² In Figure 6.3, it can be seen that cross-section coverage decreases rapidly for detector
³ heights below 2.5 m. A height of 3 m is therefore preferable to have some buffer for yet
⁴ unknown uncertainties in the simulation.

⁵ Inspired by the design of the DUNE 35 t prototype at FNAL [30], the LAr bath is
⁶ held in a foam-insulated membrane cryostat. The outer support structure is a 0.3 m

6. Towards the DUNE Near Detector

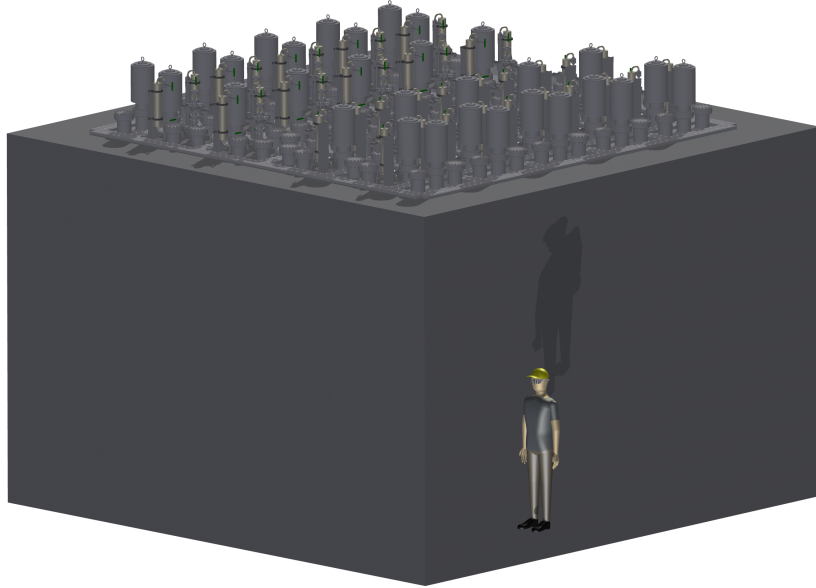


Figure 6.4.: Artistic view of the DUNE ND ArgonCube component. Shown with individual pump and oxygen traps for each module. On two sides, the half-width service modules are visible. Cabling for HV as well as charge and light readout is not shown.

7 thick steel-reinforced concrete layer, followed by a 0.4 m thick polyurethane foam layer
1 for thermal insulation. Inside of this is a 2 mm thick stainless steel membrane sealing
2 the LAr bath from the environment. There are several other support layers, all of
3 which with a thickness of \sim 1 mm, with a more detailed description in [30]. The total
4 thickness of the cryostat wall amounts to 2.88 radiation lengths. Cooling is provided by
5 10 uninstrumented $0.5 \text{ m} \times 1 \text{ m}$ service modules equipped with cryocoolers arranged on
6 the two detector faces parallel to beam direction. The total required cryostat footprint is
7 therefore $5 \text{ m} \times 5 \text{ m}$.

8 Table 6.1 gives an overview of the most important ArgonCube ND dimensions, in
9 comparison to the 2×2 LHEP prototype. Due to the bigger modules, the total fraction
10 of active volume is increased to 91.2 %. Drift direction is perpendicular to beam direction.
11 The reason for this is to reduce the rate on single pixels. If drift direction is parallel

6. Towards the DUNE Near Detector

to beam direction, particle tracks highly parallel to drift direction lead to a very high rate on single channels potentially leading to a buffer overflow and thus data loss in the LArPix chip. In addition, power dissipation increases proportionally to the event rate due to the smart zero suppression scheme of LArPix. Another advantage is that dead space in beam direction between adjacent modules will only be 30 mm due to the very slim dimensions of ArCLight. Figure 6.4 shows an artistic view of the ArgonCube ND component.

6.2. Feasibility Study of a Pixelated LArTPC for the DUNE Near Detector

Before ArgonCube selected as the LAr component of the DUNE ND complex, there were two main questions that needed to be addressed:

1. Is a pixelated LArTPC feasible?
2. Can the LAr detector handle the high rates?

Number one was addressed in Section 5.1. This chapter will address question number two. As described in Section 2.3, the DUNE beam will have an intensity of 2 MW. Paired with the slow (ms) nature of LArTPCs described in Chapter 3, this will result in multiple neutrinos interacting inside the detector for each beam spill, so-called event pile-up. A more precise phrasing of question number two is therefore: Can a LArTPC disentangle these piled up events? To assess this, one of the most difficult reconstruction tasks— π^0 -induced EM showers—was simulated in an ArgonCube ND component (see Section 6.1.2).

LArTPCs are intrinsically slow detectors with a readout time of $\approx 0.5 \text{ ms m}^{-1}$ for a 1 kV cm^{-1} drift field (see Chapter 3). This causes a pile-up of events in the detector; if

6. Towards the DUNE Near Detector

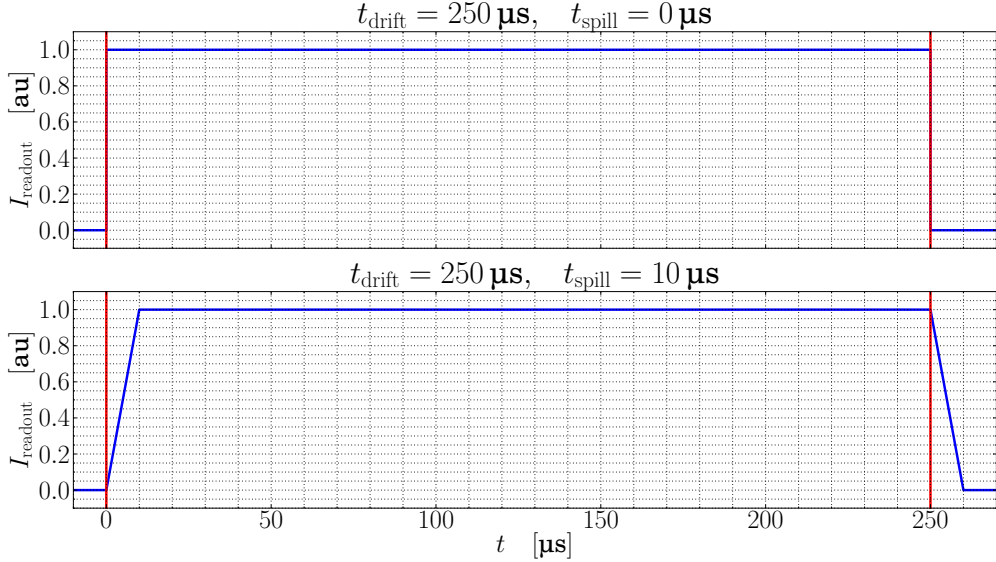


Figure 6.5.: Average current collected for one spill as a function of time. The current is given in arbitrary but equal units for both plots. Anode and cathode are represented by the vertical red lines, relative to the trigger timestamp. The upper plot assumes the whole charge is deposited instantaneously while for the lower plot, the actual spill duration from [28] is used.

the readout was infinitely fast, all neutrino interactions could be separated in time. In reality, even the ArgonCube TPCs with a drift length of only 0.5 m, corresponding to a full readout cycle of 250 μ s, are significantly slower than the spill duration of 10 μ s of the DUNE beamline reference design (see Table 2.2). Figure 6.5 visualises this effect. The charge arriving at the readout is represented as an average current in arbitrary units (same for both plots). Anode and cathode are represented by the vertical red lines, relative to the trigger timestamp. The amplitude of the readout current is a direct measure for event pile-up in the corresponding time slice. For simplicity, an infinitely short spill duration was assumed for the pile-up study (top), i.e. the whole ionisation charge produced by one beam spill is deposited instantaneously inside the TPC volume. As the time in between beam spills is ~ 1 s, all this charge can be read out within one drift time. In this case, the average current (pile-up) seen by the readout is constant over the whole readout cycle. The realistic case with the spill duration of the DUNE reference

6. Towards the DUNE Near Detector

beam is depicted in the bottom plot. At the beginning of the readout cycle, there is no charge deposited yet, the current (pile-up) is zero. Over the duration of the beam spill, ionisation charge accumulates inside the TPC volume while the existing charge is transported towards the readout by the drift field. After the beam spill is over, the remainder of the initial drift volume (240 μs) contains a uniform charge density. Due to the finite spill duration, there is an additional 10 μs (falling) ramp after the first 250 μs readout cycle, entering the next readout cycle. In short, a spill duration shorter than but comparable to the drift time results in the shape of the ionisation current (event pile-up) seen over time to become a trapezoid rather than a square. The integral, i.e. the total ionisation charge (deposited energy) is the same but part of it is shifted from the spill time slice to the beginning of the next readout cycle. In addition, the peak current (pile-up) is the same, as long as the spill duration is shorter than the drift time. If the spill duration becomes longer than the drift time, the charge is distributed over more than two readout cycles and the peak current (pile-up) begins to decrease. Therefore, the assumption of an infinitely short spill is a worst-case scenario slightly improved by the real, finite spill duration. However, for 96 % of the drift time (240 μs), pile-up is unchanged.

6.2.1. π^0 pile-up simulation

Reconstruction complexity paired with potential impact on physics measurements make photons produced by π^0 decays a good sample to study the robustness to pile-up of a pixelated LArTPC in the DUNE ND environment. Energy misidentifications lead to a misreconstructed neutrino energy. The resulting discrepancy to the true neutrino energy has the potential to skew the measured energy spectrum and, thus, influence the oscillation measurements. A significant amount of π^0 are produced in several RES and

6. Towards the DUNE Near Detector

Table 6.2.: Parameters of the π^0 pile-up simulation.

Parameter	Value	Unit
X-axis	Drift	
Y-axis	Vertical	
Z-axis	Beam	
Resolution X	3	mm
Resolution Y	3	mm
Resolution Z	3	mm
Target volume X	-100 to 500	cm
Active volume X	0 to 400	cm
Fiducial volume X	30 to 370	cm
Target volume Y	-100 to 350	cm
Active volume Y	0 to 250	cm
Fiducial volume Y	30 to 220	cm
Target volume Z	-400 to 500	cm
Active volume Z	0 to 500	cm
Fiducial volume Z	30 to 470	cm
Detection threshold	0.1	MeV
Cone extent	10	X_0
Cone aperture (full angle)	30	$^\circ$
Cylinder diameter	5	cm
Beam intensity	2.14	MW
Proton energy	80	GeV
Events per beam spill	0.21	evt/t _{Ar}

COH neutrino interactions (see Table 2.3, Section 2.4 and [28]). They decay according to

$$\pi^0 \rightarrow \gamma\gamma \quad (6.1)$$

with a branching ratio of 98.8 % [31]. The photons subsequently produce EM showers in LAr (see Section 2.5). At the energies of the DUNE beam (see Figure 2.3), most showers do not deposit a homogenous cone of charge but rather a lot of individually resolvable e^\pm tracks. More importantly, there often are significant gaps in between these charge clusters. A main challenge of shower reconstruction is to associate these well-separated charge blobs to the correct event.

6. Towards the DUNE Near Detector

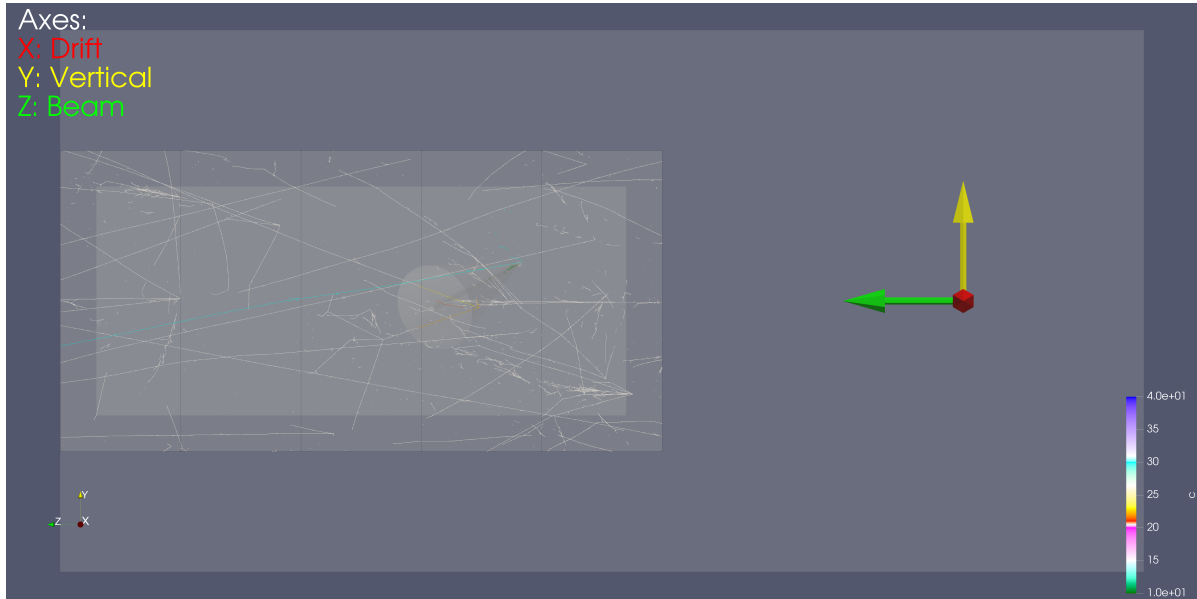


Figure 6.6.: Example event display of a simple π^0 -induced EM shower reconstruction algorithm based on a cone-cylinder union, simulated for the ArgonCube ND component. Visible are the three different volumes used for the simulation. The outermost volume is used to simulate rock events. The active detector volume is represented by the intermediate volume, divided into modules by vertical black lines. In order to reduce the number of EM showers not depositing any energy inside the detector, a fiducial volume (the innermost) is defined, and photons are required to be produced therein. Depicted is a side view of the detector, looking in drift direction. The detailed orientation is indicated by the coloured arrows.

6 One way to assess the performance of an analysis of experimental data is to run it on
 1 a simulated dataset. In the simulation, the quantities to be measured by the experiment
 2 are known a priori. They are called truth information and can be compared to the
 3 output of the analysis run on the simulated dataset. To simulate the expected neutrino
 4 interactions in the ND, the Argon Box¹ simulation tool was used. The neutrino group at
 5 LBNL is developing it with the goal of providing an easy-to-use simulation of particle
 6 interactions in the LAr component of the ND. Primary particles can either be provided by
 7 a particle gun (e.g. e^- , n , p , μ^+) or in form of a *HEPEVT* file². For this study, 6.6×10^6

¹https://github.com/dadwyer/argon_box

²A file format standard for passage of particle events between different simulation tools

6. Towards the DUNE Near Detector

8 neutrino events were produced with the GENIE³ neutrino event generator. Secondary
1 particle transport and interaction in Argon Box is performed by Geant4⁴. Finally, the
2 energy deposition in LAr is voxelised and stored together with all the necessary ancillary
3 information about the depositing particle. The data is stored in the tree format of the
4 ROOT data analysis framework⁵. This allows for convenient further processing using
5 ROOT.

6 To investigate the effects of pile-up on energy reconstruction, a working reconstruction
7 algorithm is necessary. However, at the time of writing, official reconstruction tools were
8 only available for LArTPCs read out by wire planes⁶. Therefore, a simple algorithm for
9 true 3D space points was implemented, under the assumption that a positive outcome of
10 such a pile-up study would imply an even better performance of a more sophisticated
11 reconstruction. This algorithm is explained in the following, its parameters are listed in
12 Table 6.2, an example of a simulated event is shown in Figures 6.6 and 6.7.

13 The basic underlying assumption is that a pixel readout without analogue multiplexing
14 will yield unambiguous 3D space points of charge deposition with a given resolution,
15 depending on the geometry of the pixel plane, time resolution of the readout electronics,
16 and charge transport effects. Section 5.1 proves that this is feasible provided the current
17 reconstruction ambiguities can be eliminated by a successful deployment of the LArPix
18 charge readout electronics described in Section 4.3.2. The spatial resolution of the pixel
19 readout is assumed to be 3 mm in both directions based on the ND design specified
20 in Section 6.1.2. A conservative value of 3 mm was chosen in drift direction. This has
21 several advantages. Choosing the same resolution as the pixel pitch makes the simulation
22 independent of the orientation of the TPC. MicroBooNE has achieved a resolution in
23 drift direction < 0.3 cm [46], making it safe to assume LArPix will enable a similar

justify!

³<https://genie.hepforge.org>

⁴<http://geant4.cern.ch>

⁵<https://root.cern>

⁶<http://larsoft.org>

6. Towards the DUNE Near Detector

²⁴ performance with ArgonCube. A conservative value also accounts for charge diffusion.
¹ Furthermore, it is assumed that EM showers can be identified and their starting point
² and direction reconstructed with negligible errors and inefficiencies, i.e. this information
³ is taken from the simulation truth. In reality, the direction and starting point can be
⁴ derived from the vertex producing the π^0 , and a rough shower direction obtained from a
⁵ pattern recognition. A cone is calculated in the direction of the shower with its tip at the
⁶ first charge deposition of the initial photon. The opening angle and length of the cone
⁷ were optimised by looking at the distributions of the distance from the starting point and
⁸ angle w.r.t. the direction of the shower. The finite resolution of the detector is emulated
⁹ by voxelising (via rounding) the charge deposition with the corresponding resolution in
¹⁰ all three spatial coordinates. This leads to problems near the tip of the cone where the
¹¹ transversal extent is lower than the voxel dimensions. In particular, it can happen that
¹² most of the initial charge is shifted outside the cone. Furthermore, MCS at lower energies
¹³ makes the cone model suboptimal near the tip. Therefore, the acceptance volume for the
¹⁴ reconstruction is taken as the union of the cone with a cylinder around the direction of
¹⁵ the shower of the same length as the cone. The cylinder radius was tuned to optimise
¹⁶ the trade-off between missed and misidentified energy deposition as defined below.

¹⁷ Argon Box propagates the neutrino interaction events it gets from GENIE through LAr,
¹⁸ the output is a ROOT tree of neutrino interaction events. To get a realistic simulation
¹⁹ of beam events in the detector, these events need to be distributed randomly in time
²⁰ and space. Beam spills are simulated by drawing the number of events for each spill
²¹ from a Poisson distribution whose mean is calculated from the beam intensity and the
²² target mass according to the values in Table 2.2. The resulting number of events is taken
²³ from the Argon Box ROOT tree and their vertices are placed within the LAr volume at
²⁴ coordinates drawn from a uniform distribution. Combined with the target mass given in
²⁵ Table 6.2, this results in an equivalent of $\approx 1.5 \times 10^{19}$ Protons On Target (POT). The

6. Towards the DUNE Near Detector

26 seemingly low number (compared to Table 2.3) is the result of many neutrino interactions
1 happening outside of the active detector.

2 Three different argon volumes are assumed for the simulation: target, active, and
3 fiducial volume. The actual detector dimensions are represented by the active volume.
4 It is inside the target volume which is the volume within which the neutrino vertices
5 are placed randomly. This is done to crudely emulate rock events, secondary particles
6 from beam neutrino interactions outside the detector volume. The additional target
7 mass is 1 m in all four directions transverse to the beam, and 4 m in upstream beam
8 direction. According to Equations (2.56) and (2.57), hadronic showers up to 10 GeV are
9 contained $> 95\%$ longitudinally and $> 50\%$ transversally (because Equation (2.57) gives
10 the radius for 95 % containment) in the additional volume. In other words, increasing the
11 target volume further will not result in significantly more rock events entering the active
12 volume. For transversal containment, it is enough to use the radius for 95 % containment
13 because the location of the shower is defined by its centre, i.e. showers further away than
14 one 95 % radius from the detector only deposit a minimal amount of energy inside the
15 detector. These numbers are supported by Geant4 simulations [95]. As mentioned in
16 Section 2.5, EM interactions happen on smaller scales than hadronic interactions. The
17 big exception are muons due to their high range. However, as will be explained below,
18 it makes sense to ignore pile-up from muons due to their high reconstruction efficiency.
19 Finally, a fiducial volume 30 cm ($\approx 2 X_0$) smaller than the active volume on all six faces
20 is defined. Without fiducialisation, there is a significant number of photons produced
21 by π^0 decays inside the detector but only showering outside the detector. This selection
22 results in $\approx 5.5 \times 10^5$ processed π^0 photons from the initial 6.6×10^6 neutrino events.
23 Table 6.2 contains a summary of all the LAr volume dimensions, Figure 6.6 shows an
24 example event with all three volumes drawn.

25 Active volume dimensions are taken from the preliminary DUNE ND design described

6. Towards the DUNE Near Detector

in Section 6.1.2. Note that the height was taken as 2.5 m as opposed to the 3 m of the ND design. The reason is that another 0.5 m safety margin were added after this pile-up simulation had been completed. However, the influence on the pile-up study should be negligible. The hadron containment studies described in Section 6.1.2 indicated that 2.5 m height is the bare minimum. A safety margin was added to account for unknown uncertainties in the simulation. However, the same simulation framework was used for both the containment and the pile-up study. Therefore, the 2.5 m height is sufficient for the pile-up study.

Cosmic ray induced backgrounds are neglected. The ND hall will have an overburden of 53 m, 33 m of rock (2.43 g cm^{-3}) plus 20 m of dirt (1.7 g cm^{-3}). Simulations predict a muon rate of 2.7 Hz m^{-2} at the top of the hall [96]. Scaled up to the ArgonCube ND footprint of $4 \text{ m} \times 5 \text{ m}$, this results in a rate of 54 Hz for the whole LArTPC component. However, the majority of these events can be rejected by means of a beam spill trigger gate. Looking at Figure 6.5, the total readout time for one beam spill is 260 μs . Events outside of this window cannot originate from beam neutrinos. On average, this results in 0.014 cosmic events per beam spill compared to 14.7 beam events in the simulated detector. Therefore, contributions from cosmic rays can be safely neglected.

After all events of one spill are placed inside the target volume, all π^0 photons produced inside the fiducial volume are reconstructed using the cone algorithm. All energy depositions inside the active volume are considered. To assess the performance of the algorithm and the influence of pile-up on neutrino energy reconstruction, the following two errors on the reconstructed energy are calculated for each π^0 photon:

Missed energy is the energy deposited by the corresponding π^0 photon (or its descendants) that is outside of the cone-cylinder union and therefore “missed” by the algorithm. This is a measure of the reconstruction performance and can be used to ensure optimum tuning of the union parameters.

6. Towards the DUNE Near Detector

26 **Misidentified energy** is the energy inside the cone-cylinder union deposited by descendants of a different (“wrong”) parent neutrino. This is a measure of event pile-up: the higher the charge deposition by other events inside the union, the higher the event pile-up.

4 Using this general definition of misidentified energy leads to quite mediocre results.
5 However, there are some assumptions that can be taken even without knowing the
6 actual reconstruction algorithm. From results of earlier experiments [97], the muon
7 reconstruction can be assumed to be very efficient. Assuming 100% reconstruction
8 efficiency for muons and 0% for all other particles can therefore serve as an upper limit
9 for misidentified energy. It can be calculated by ignoring energy deposited by muons
10 originating from other parent neutrinos. A lower limit for misidentified energy can be
11 calculated by assuming 100% reconstruction efficiency for all charged particles and 0% for
12 neutral particles (γ and n). This is calculated by only taking into account misidentified
13 energy deposited by neutral particles. Even assuming 0% reconstruction efficiency for
14 neutral particles is potentially too pessimistic. Future, more sophisticated reconstruction
15 algorithms (e.g. based on machine learning) might be able to partially reconstruct the
16 topology of charge depositions originating from neutral particles and thus prevent their
17 misidentification. Therefore, it can be assumed that the actual pile-up-related energy
18 reconstruction error is closer to the lower limit and potentially even below. It should
19 be noted that the upper limit excludes only energy deposited by muons directly and
20 not by their descendants (e.g. δ rays or Michel electrons). Whereas the lower limit
21 excludes charge deposited by photons, neutrons, and any of their descendants. Figure 6.7
22 illustrates the distinction of various energy depositions for an example event. In particular,
23 it can be seen that δ rays (orange) are not counted towards energy deposited by muons
24 (yellow). The long red track is an example of a deposition originating from a photon or
25 neutron (descendant) included in the lower limit sample but very likely reconstructible

²⁶ by future algorithms.

¹ 6.2.2. Results

² Missed and misidentified energy by the cone-cylinder union are analysed as a function of
³ true photon and neutrino energy, respectively. As mentioned above, the missed energy
⁴ is used to measure the performance of the employed photon reconstruction algorithm.
⁵ Therefore, it is sensible to compare it to the true photon energy rather than the true energy
⁶ of its parent neutrino. On the other hand, the primary goal of this study is to assess the
⁷ effect of event pile-up on the neutrino energy spectrum. The misidentified energy is thus
⁸ compared to the true neutrino energy. For this, the total missed energy of each neutrino
⁹ event is first calculated by summing up the contributions of all descending π^0 photons.
¹⁰ Additionally, it is illustrative to look at the fraction of events with a certain misidentified
¹¹ or missed energy. All the aforementioned information is contained in 2D histograms of all
¹² events with the true neutrino (photon) energy on one axis and the misidentified (missed)
¹³ energy on the other axis. The energy dependence of the error can be obtained by looking
¹⁴ at the true energy axis and calculating the mean misidentified (missed) energy for each
¹⁵ bin (a profile of the 2D histogram). Looking at the misidentified (missed) energy axis and
¹⁶ summing over all true energy bins yields the number of events with the corresponding
¹⁷ misidentified (missed) energy (a projection of the 2D histogram). The corresponding
¹⁸ fraction of events is obtained by normalising the histogram, i.e. dividing every bin by
¹⁹ the total number of entries. It should be noted that for the projections all values in the
²⁰ corresponding y-bin are taken into account, including the ones outside the boundaries of
²¹ the histogram (under- and overflow). For the profiles, only events with energies from
²² 0 GeV to 6 GeV or energy fractions from 0 to 1 are taken into account.

²³ The results for a 2 MW beam at 80 GeV proton energy are shown in Figures 6.8
²⁴ through 6.14. To illustrate the relation between the different histograms, all of them are

6. Towards the DUNE Near Detector

25 shown for the missed energy in Figures 6.8 through 6.10. The initial 2D histogram is
1 shown in Figure 6.8. Note that it actually depicts the missed photon energy as a fraction
2 of the true photon energy rather than an absolute value. Figure 6.9 is the profile of the
3 x-axis, i.e. the mean missed energy fraction for each true energy bin. The projection of
4 the y-axis is depicted in Figure 6.10. This is the fraction of photons with a certain missed
5 energy. It is drawn as a cumulative fraction which means that the curve represents the
6 fraction of photons on the y-axis with a missed energy fraction equal to or lower than the
7 corresponding value on the x-axis. A consequence of this is that the curve monotonically
8 approaches one towards the right, 100 % of the reconstructed photons have a missed
9 energy fraction of 100 % or less. For reference, Figure 6.11 shows the mean absolute
10 missed energy per true energy bin.

11 It can be seen that the absolute missed energy rises more or less linearly with the true
12 energy (Figure 6.11). This indicates that the cone models the shower well, as expected
13 from theory (see Section 2.5). Indeed, it can be seen from Figure 6.9 that the missed
14 energy fraction stays almost constant at 3 % from 1 GeV to 6 GeV. It starts to increase
15 below 1 GeV, reaching 10 % in the lowest energy bin (0 MeV to 125 MeV). This can be
16 explained by the increase in MCS at lower momenta. Similarly, the Compton scattering
17 cross-section increases as well. Both these effects lead to a higher angular distribution of
18 the energy deposited by electrons (and positrons) and photons. Consequentially, more
19 energy is missed because the cone angle is independent of energy. From Figure 6.10, it
20 can be seen that for roughly half of the photons 3 % of the energy is missed, indicating a
21 symmetric distribution of missed energy around the mean value. It should be noted that
22 energy deposited outside the detector, so-called leakage, is included in the missed energy.
23 Despite the fiducial volume, some events still exit the detector.

24 The behaviour of the misidentified energy is almost opposite to the missed energy: The
25 absolute energy is almost constant with the true neutrino energy (Figure 6.12), while

6. Towards the DUNE Near Detector

the fraction of the total energy is inversely proportional to the true energy, accordingly (Figure 6.13). This is expected as the amount of charge deposited inside the cone originating from other neutrinos should only depend on the geometry of the acceptance volume (i.e. the parameters of the cone-cylinder union) and on the event rate, but not on the true energy of the reconstructed photon or its parent neutrino. The effect of the different misidentified energy selections can be seen well. As mentioned above, the actual error on the reconstructed neutrino energy is probably somewhere in between the red curve, only rejecting misidentified energy deposited by muons, and the dark blue curve, rejecting all but misidentified energy deposited by photons and neutrons or any of their descendants. From Figure 6.13, this can be determined to be about 2% at the flux peak ($\approx 3 \text{ GeV}$, see Figure 2.3). The cumulative neutrino fraction versus the misidentified energy fraction reveals another interesting fact; it can be seen that about 70% of the events experience a pile-up-related error on reconstructed neutrino energy of 1% or less. For roughly 50% of the events, it is even below 0.1%. If it was possible to identify the other 50% somehow in the real experiment, they could be ignored, giving an essentially pile-up-free sample. Given the high event rates in the ND, this would be easily affordable. Using the cone-base algorithm described here, EM shower pile-up could be detected via overlapping cones for instance.

To get a rough idea of the performance of a 2D wire readout in an identical environment, the same study was performed ignoring the Y-coordinate completely, leaving everything else untouched. Of course, this is a gross underestimation of the capabilities of existing reconstruction algorithms for 2D charge readout data. In particular, contemporary experiments use at least three 2D projections whereas only one was used here. Even though, doing this comparison serves to show that the simple cone-cylinder union reconstruction algorithm breaks down for two dimensions as can be seen in Figures 6.15 through 6.18. The fraction of events not suffering from pile-up is below 10%, and 50%

6. Towards the DUNE Near Detector

have 10 % or more misidentified energy (Figure 6.18). Similarly, the error on energy reconstruction has increased to 10 % to 20 % at the flux peak (Figure 6.17). On the other hand, the error due to missed energy has improved from 3 % to 2 % compared to 3D (Figure 6.15). An explanation for this is that all the energy in Y-direction was summed up, due to the projection on XZ. Therefore, the cone (or rather triangle) cannot miss energy in the former direction.

Finally, as a cross-check, the (3D) pile-up study was performed for a hypothetical 10 MW beam in Figures 6.19 through 6.22. As explained above the missed energy only depends on the geometry of the acceptance volume, it should be independent of beam intensity. Therefore it is expected to be very similar to the 2 MW case as can be confirmed by comparing Figure 6.19 to Figure 6.9. As expected, the error due to misidentified energy is increased to 7 % to 15 % at the flux peak (Figure 6.21) but still better than for the XZ projection. Similarly, only about 10 % of the neutrino events remain pile-up free, and 50 % suffer from more than 4 % misidentified energy (Figure 6.22).

In summary, this study shows that even a very simple EM shower reconstruction algorithm, employing a cone-cylinder union selection, performs well in the high-multiplicity environment of the DUNE ND, when fed with unambiguous 3D spatial coordinates of energy depositions. The mean deposited energy missed by the algorithm is less than 3 %. More importantly, the pile-up-related misidentification of energy depositions from other events has a mean of 2 % to 3 %. For more than 50 % of the neutrino events, this error is even smaller than 0.1 %. In comparison, the FD is required to have an energy resolution for stopping hadrons below 10 % and an electron energy scale uncertainty of about 5 % [30]. Provided that a successful LArPix enables unambiguous 3D tracking information, ArgonCube will be capable of handling the high rates expected in the DUNE ND environment. The employed reconstruction algorithm clearly fails when reduced to two dimensions or presented with a much higher beam intensity.

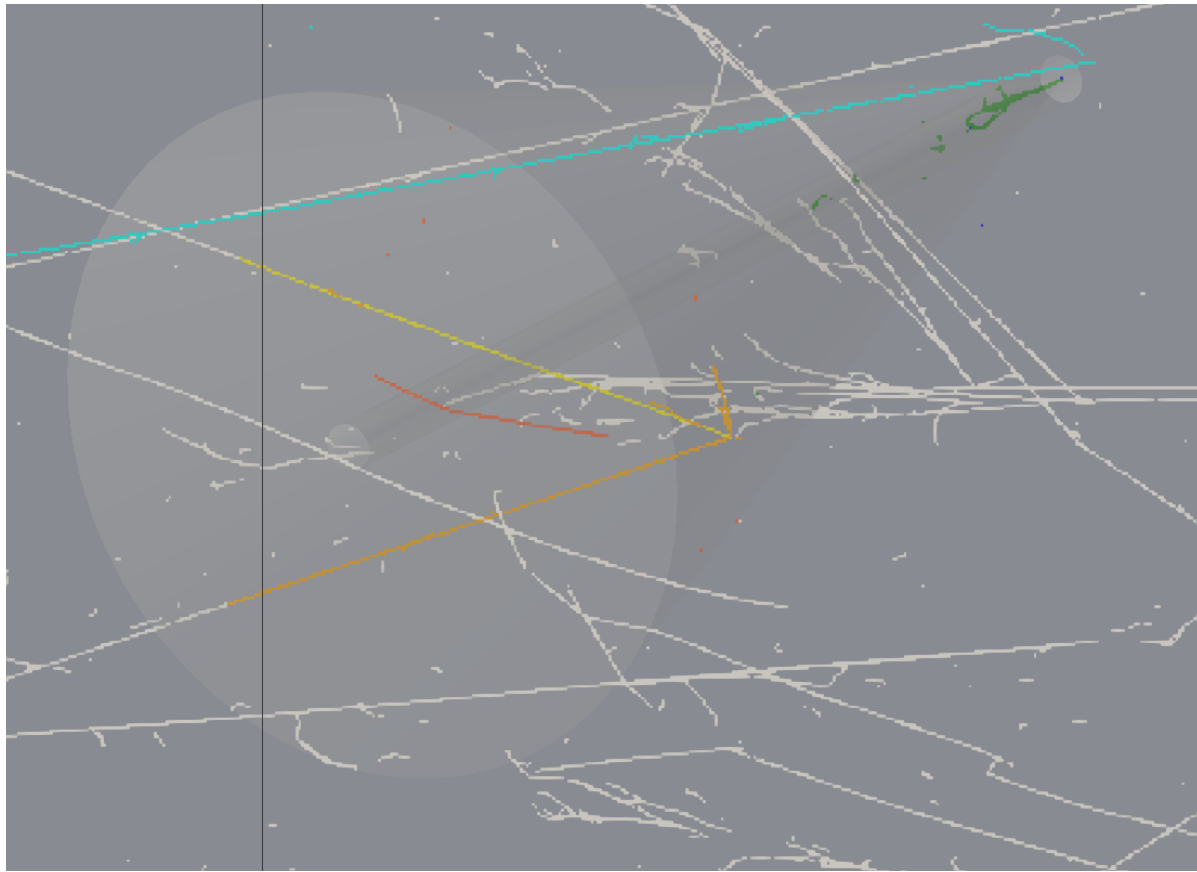


Figure 6.7.: Detailed view of the pile-up simulation event shown in Figure 6.6. The acceptance volume is defined by the union of cone and cylinder. Charge depositions are depicted by white and coloured squares whose size represents the applied resolution of 3 mm in all directions. Colour indicates type and acceptance of energy deposition. White: Different neutrino event, outside acceptance volume. Cyan: Correct neutrino event but not part of considered EM shower, outside acceptance volume. Dark blue: Correct neutrino event and EM shower, outside acceptance volume (missed energy). Green: Correct neutrino event and EM shower, inside acceptance volume. Magenta: Correct neutrino event but not part of considered EM shower, inside acceptance volume (not present in this example). Yellow (muons), red (γ , n and descendants), orange (neither): Different neutrino event, inside acceptance volume (misidentified energy).

6. Towards the DUNE Near Detector

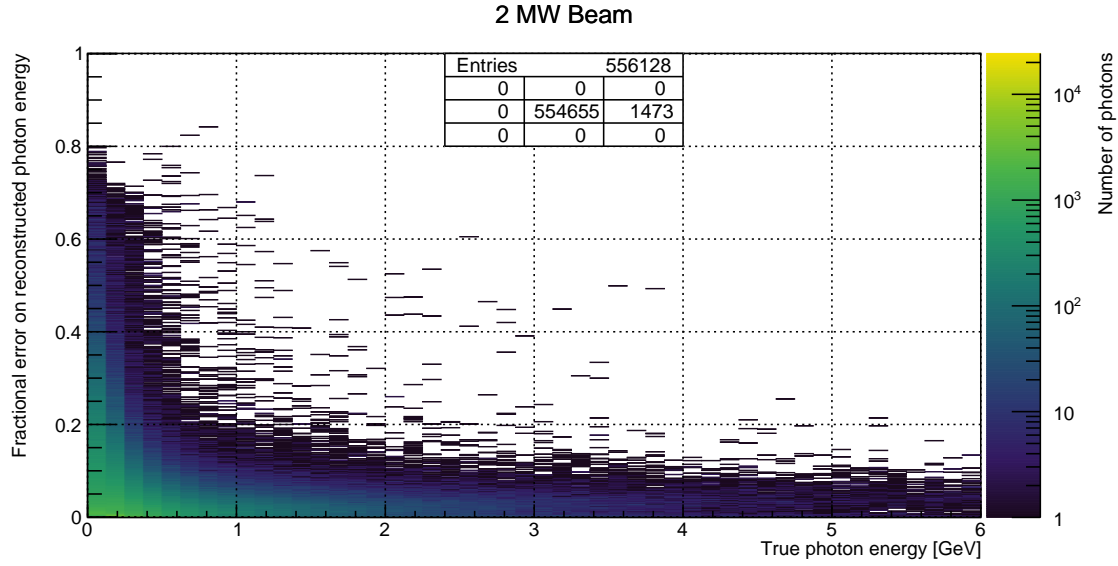


Figure 6.8.: Missed energy fraction versus true photon energy for a simple π^0 -induced EM shower reconstruction algorithm based on a cone-cylinder union. All energy deposited outside of the cone-cylinder union is counted as missed. 2 MW beam of 80 GeV protons. Entries: Central cell shows plotted entries, other cells show overflow entries in direction w.r.t. central cell.

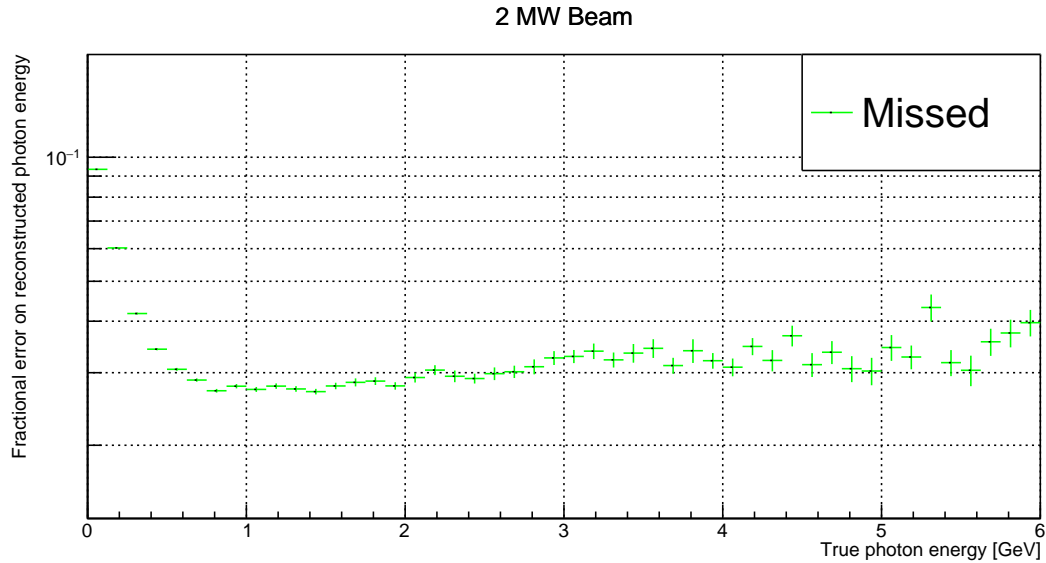


Figure 6.9.: Mean missed energy fraction versus true photon energy for a simple π^0 -induced EM shower reconstruction algorithm based on a cone-cylinder union. All energy deposited outside of the cone-cylinder union is counted as missed. 2 MW beam of 80 GeV protons.

6. Towards the DUNE Near Detector

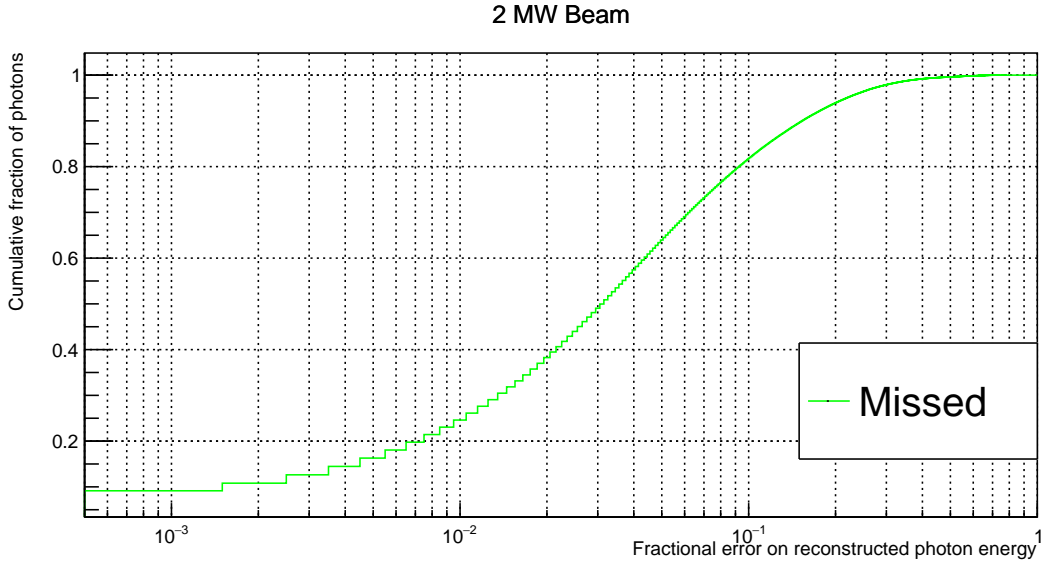


Figure 6.10.: Cumulative fraction of photons versus missed energy fraction for a simple π^0 -induced EM shower reconstruction algorithm based on a cone-cylinder union. All energy deposited outside of the cone-cylinder union is counted as missed. The curve depicts the fraction of photons on the y-axis with a missed energy fraction equal to or lower than the corresponding value on the x-axis. 2 MW beam of 80 GeV protons.

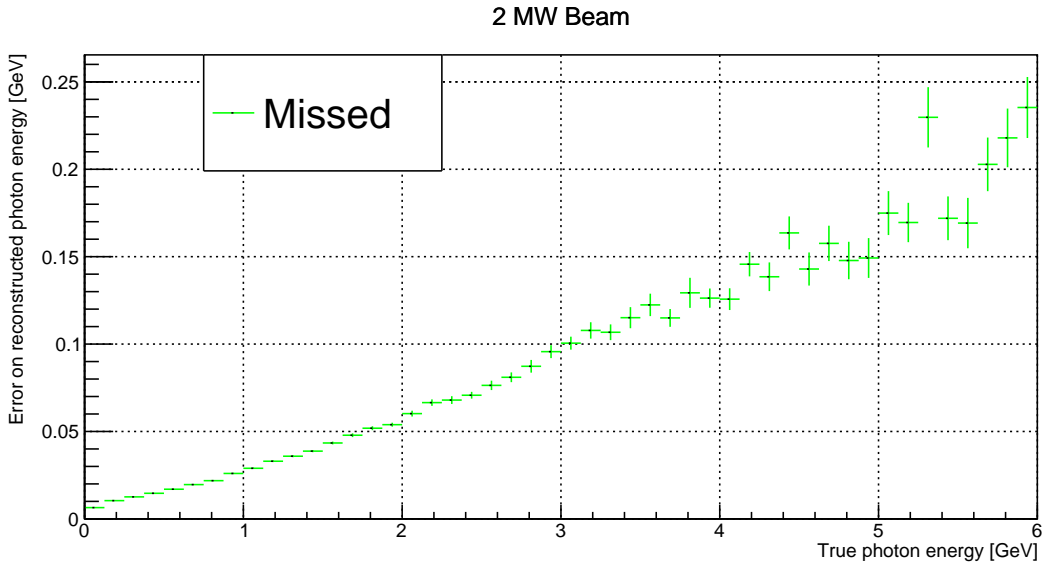


Figure 6.11.: Mean missed energy versus true photon energy for a simple π^0 -induced EM shower reconstruction algorithm based on a cone-cylinder union. All energy deposited outside of the cone-cylinder union is counted as missed. 2 MW beam of 80 GeV protons.

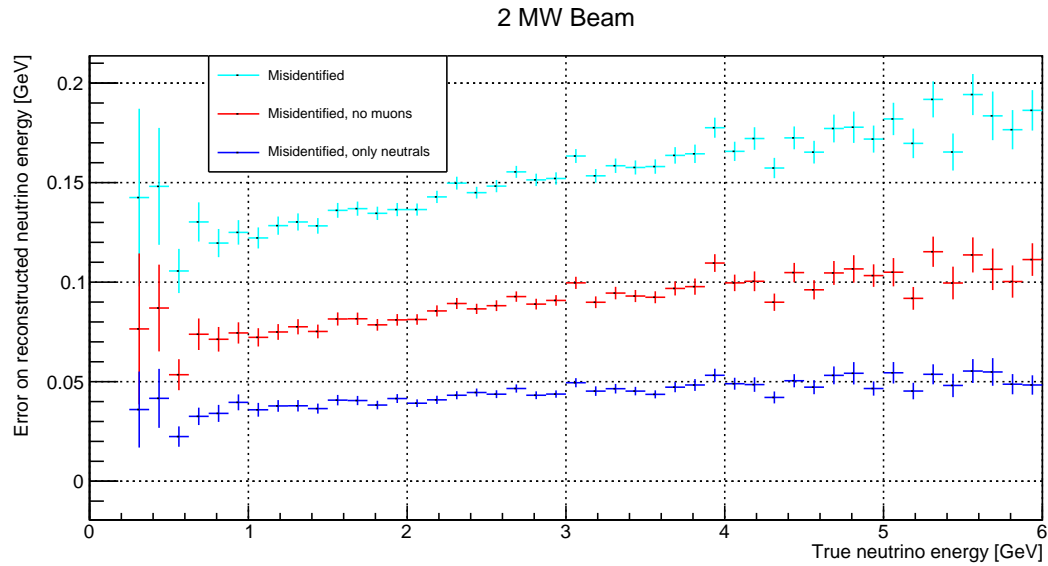


Figure 6.12.: Mean misidentified energy versus true neutrino energy for a simple π^0 -induced EM shower reconstruction algorithm based on a cone-cylinder union. All energy deposited inside the cone-cylinder union by descendants of neutrinos different from the parent of the corresponding π^0 photon is counted as misidentified. Colour indicates different selections of misidentified energy: total (cyan); excluding depositions from muons (red); deposition from photons, neutrons, and their descendants only (blue). 2 MW beam of 80 GeV protons.

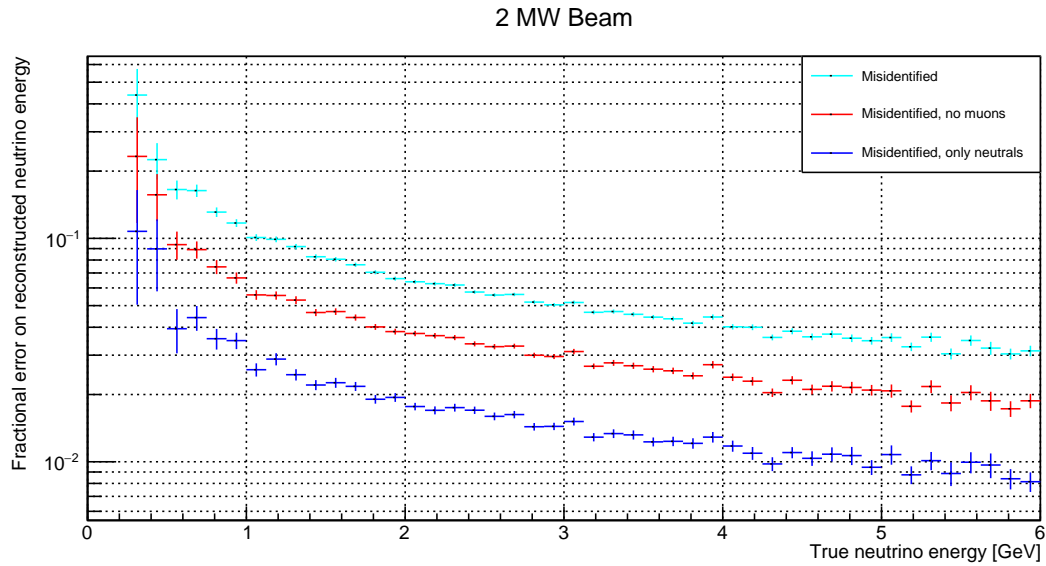


Figure 6.13.: Mean misidentified energy fraction versus true neutrino energy for a simple π^0 -induced EM shower reconstruction algorithm based on a cone-cylinder union. All energy deposited inside the cone-cylinder union by descendants of neutrinos different from the parent of the corresponding π^0 photon is counted as misidentified. Colour indicates different selections of misidentified energy: total (cyan); excluding depositions from muons (red); deposition from photons, neutrons, and their descendants only (blue). 2 MW beam of 80 GeV protons.

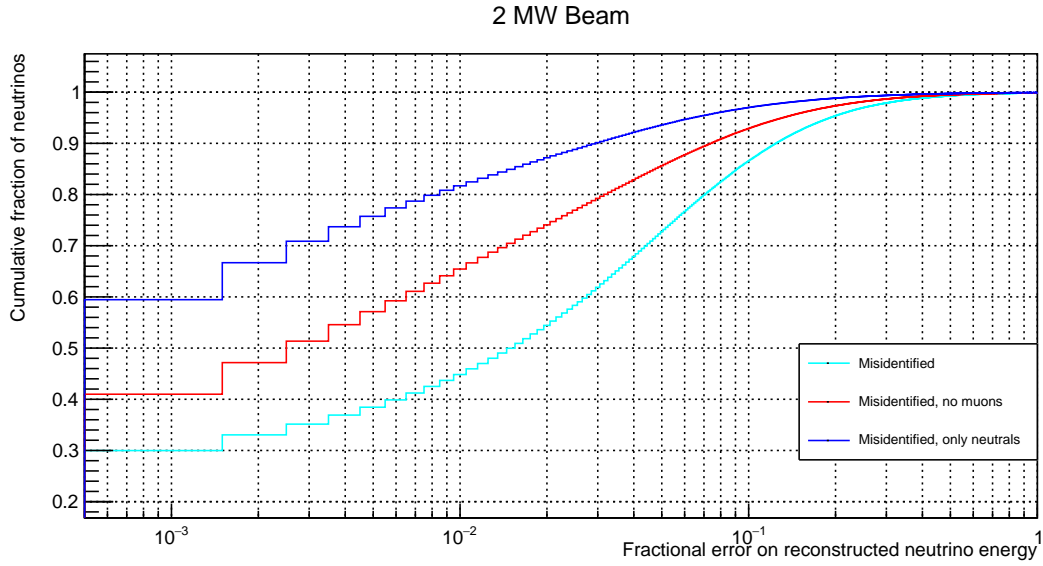


Figure 6.14.: Cumulative fraction of neutrinos versus misidentified energy fraction for a simple π^0 -induced EM shower reconstruction algorithm based on a cone-cylinder union. All energy deposited inside the cone-cylinder union by descendants of neutrinos different from the parent of the corresponding π^0 photon is counted as misidentified. Colour indicates different selections of misidentified energy: total (cyan); excluding depositions from muons (red); deposition from photons, neutrons, and their descendants only (blue). The curve depicts the fraction of neutrinos on the y-axis with a misidentified energy fraction equal to or lower than the corresponding value on the x-axis. 2 MW beam of 80 GeV protons.

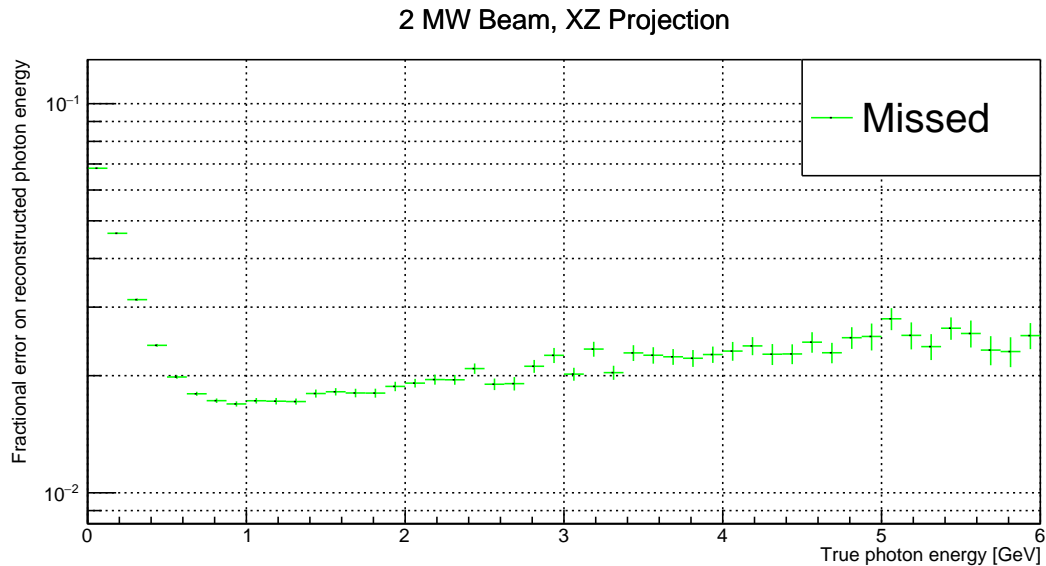


Figure 6.15.: Mean missed energy fraction versus true photon energy for a simple π^0 -induced EM shower reconstruction algorithm based on a cone-cylinder union. All energy deposited outside of the cone-cylinder union is counted as missed. 2 MW beam of 80 GeV protons. As a primitive simulation of a 2D wire readout, only X- and Z-coordinates are used for the energy reconstruction.

6. Towards the DUNE Near Detector

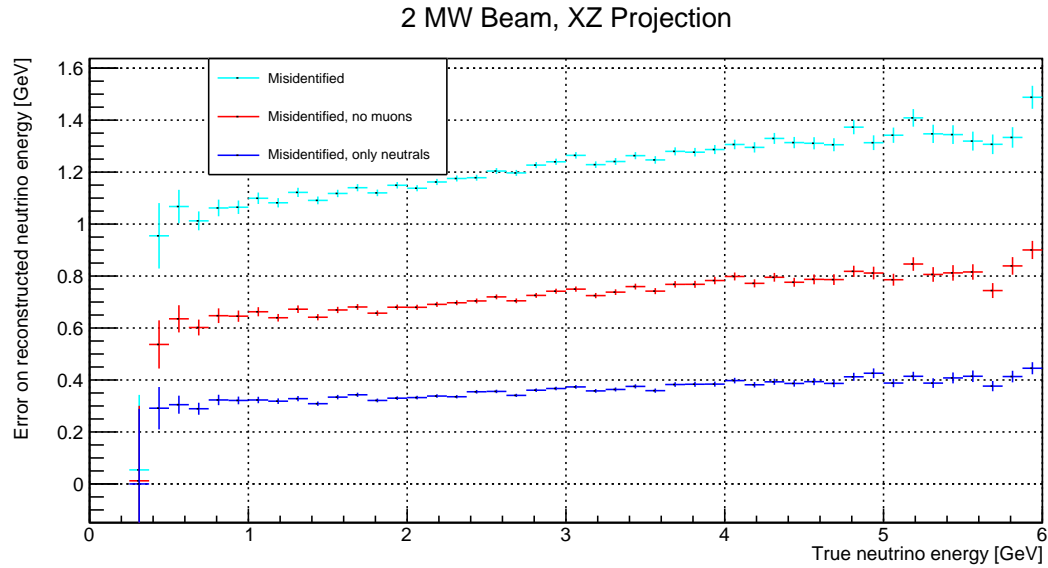


Figure 6.16.: Mean misidentified energy versus true neutrino energy for a simple π^0 -induced EM shower reconstruction algorithm based on a cone-cylinder union. All energy deposited inside the cone-cylinder union by descendants of neutrinos different from the parent of the corresponding π^0 photon is counted as misidentified. Colour indicates different selections of misidentified energy: total (cyan); excluding depositions from muons (red); deposition from photons, neutrons, and their descendants only (blue). 2 MW beam of 80 GeV protons. As a primitive simulation of a 2D wire readout, only X- and Z-coordinates are used for the energy reconstruction.

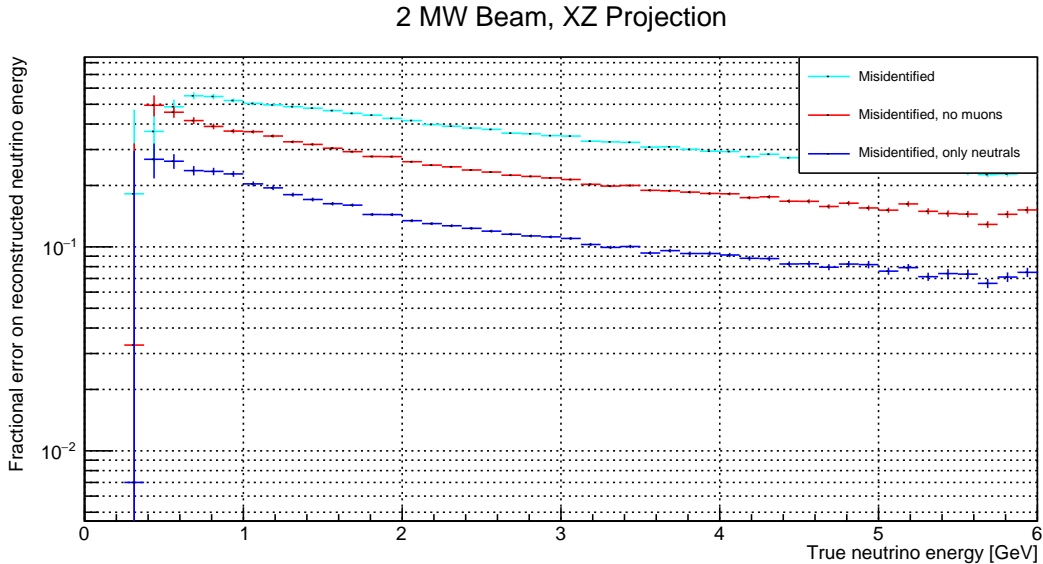


Figure 6.17.: Mean misidentified energy fraction versus true neutrino energy for a simple π^0 -induced EM shower reconstruction algorithm based on a cone-cylinder union. All energy deposited inside the cone-cylinder union by descendants of neutrinos different from the parent of the corresponding π^0 photon is counted as misidentified. Colour indicates different selections of misidentified energy: total (cyan); excluding depositions from muons (red); deposition from photons, neutrons, and their descendants only (blue). 2 MW beam of 80 GeV protons. As a primitive simulation of a 2D wire readout, only X- and Z-coordinates are used for the energy reconstruction.

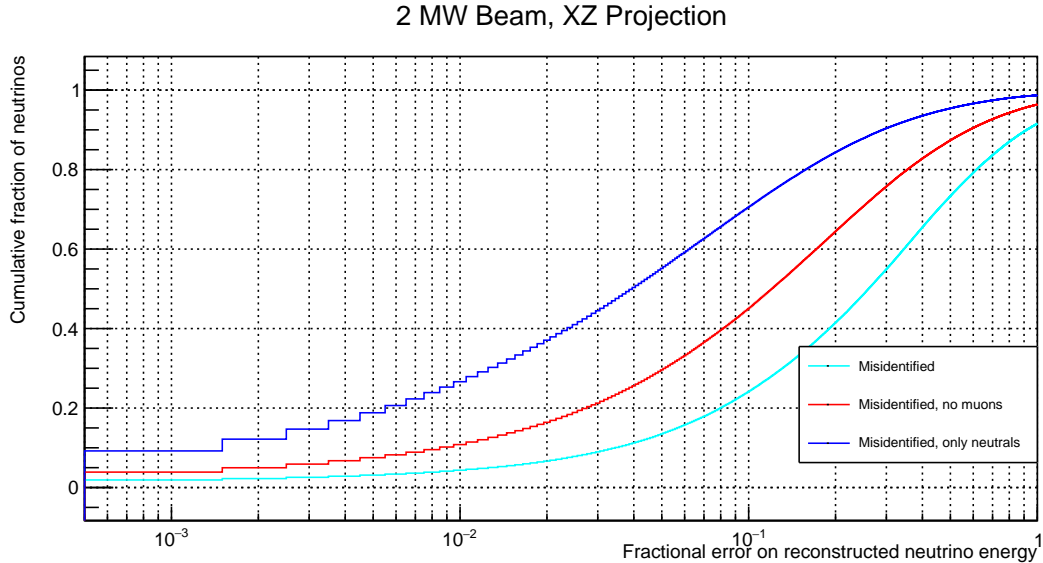


Figure 6.18.: Cumulative fraction of neutrinos versus misidentified energy fraction for a simple π^0 -induced EM shower reconstruction algorithm based on a cone-cylinder union. All energy deposited inside the cone-cylinder union by descendants of neutrinos different from the parent of the corresponding π^0 photon is counted as misidentified. Colour indicates different selections of misidentified energy: total (cyan); excluding depositions from muons (red); deposition from photons, neutrons, and their descendants only (blue). The curve depicts the fraction of neutrinos on the y-axis with a misidentified energy fraction equal to or lower than the corresponding value on the x-axis. 2 MW beam of 80 GeV protons. As a primitive simulation of a 2D wire readout, only X- and Z-coordinates are used for the energy reconstruction.

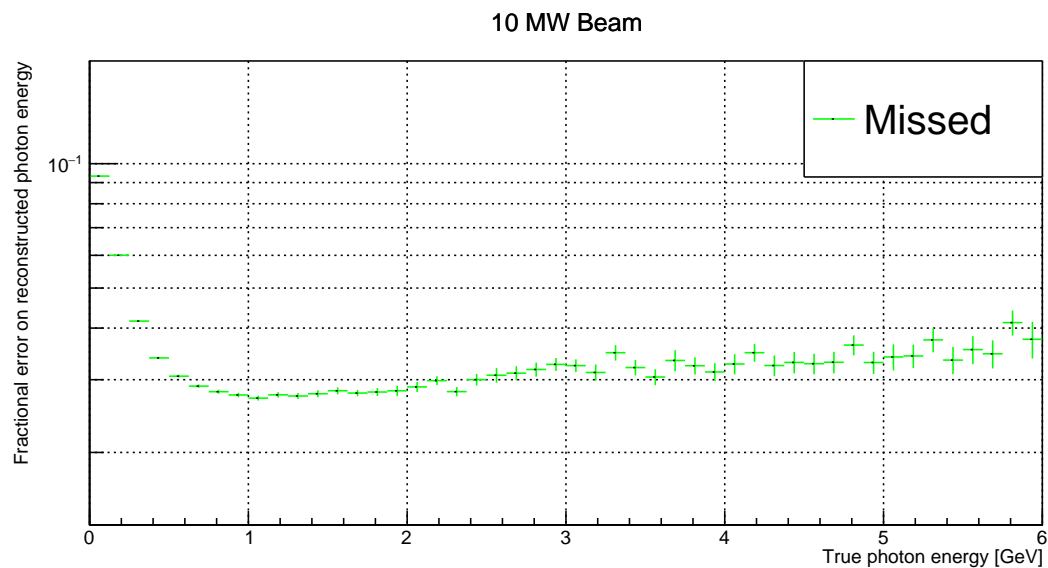


Figure 6.19.: Mean missed energy fraction versus true photon energy for a simple π^0 -induced EM shower reconstruction algorithm based on a cone-cylinder union. All energy deposited outside of the cone-cylinder union is counted as missed. 10 MW beam of 80 GeV protons.

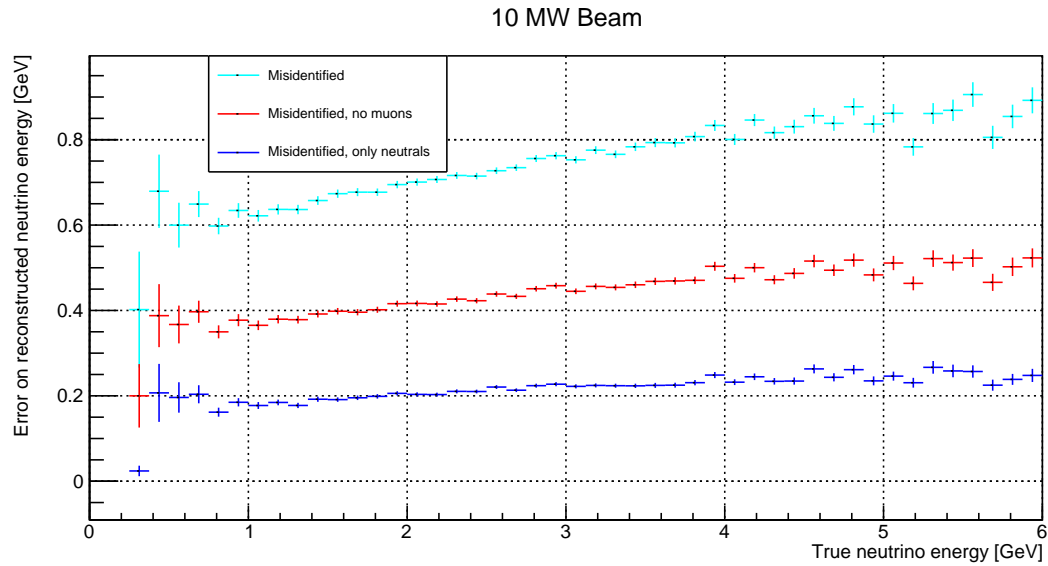


Figure 6.20.: Mean misidentified energy versus true neutrino energy for a simple π^0 -induced EM shower reconstruction algorithm based on a cone-cylinder union. All energy deposited inside the cone-cylinder union by descendants of neutrinos different from the parent of the corresponding π^0 photon is counted as misidentified. Colour indicates different selections of misidentified energy: total (cyan); excluding depositions from muons (red); deposition from photons, neutrons, and their descendants only (blue). 10 MW beam of 80 GeV protons.

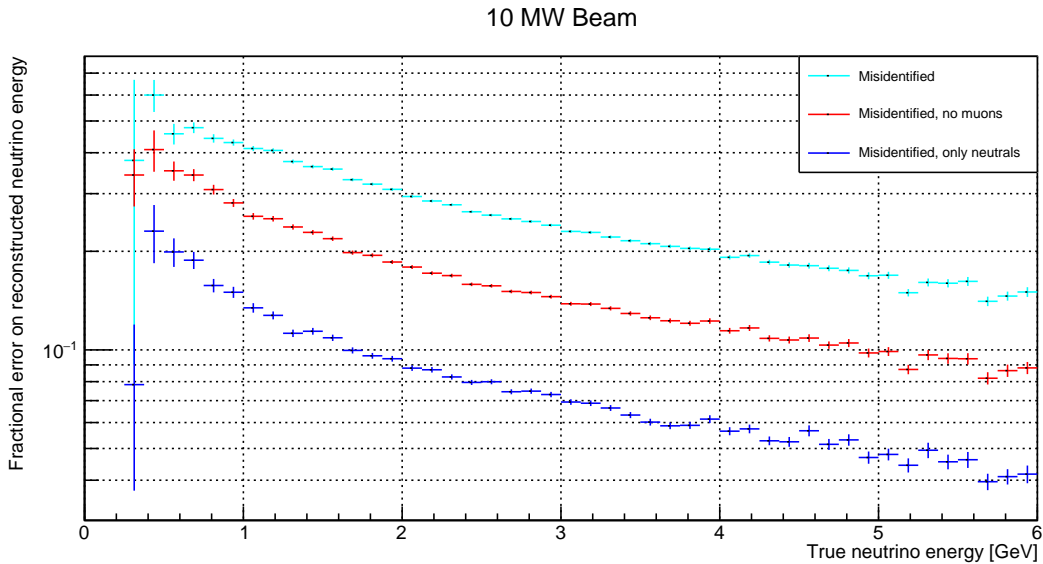


Figure 6.21.: Mean misidentified energy fraction versus true neutrino energy for a simple π^0 -induced EM shower reconstruction algorithm based on a cone-cylinder union. All energy deposited inside the cone-cylinder union by descendants of neutrinos different from the parent of the corresponding π^0 photon is counted as misidentified. Colour indicates different selections of misidentified energy: total (cyan); excluding depositions from muons (red); deposition from photons, neutrons, and their descendants only (blue). 10 MW beam of 80 GeV protons.

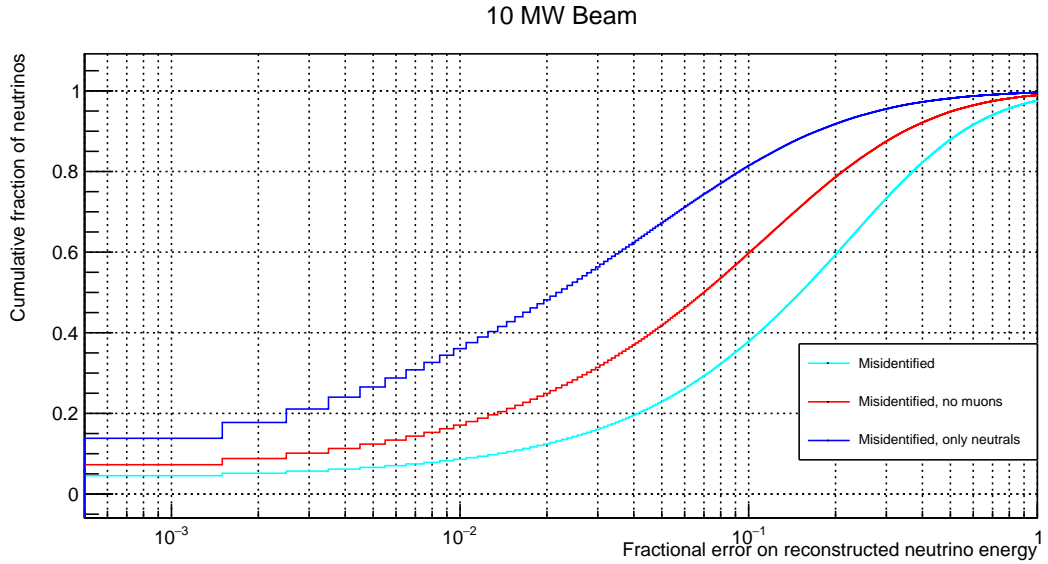


Figure 6.22.: Cumulative fraction of neutrinos versus misidentified energy fraction for a simple π^0 -induced EM shower reconstruction algorithm based on a cone-cylinder union. All energy deposited inside the cone-cylinder union by descendants of neutrinos different from the parent of the corresponding π^0 photon is counted as misidentified. Colour indicates different selections of misidentified energy: total (cyan); excluding depositions from muons (red); deposition from photons, neutrons, and their descendants only (blue). The curve depicts the fraction of neutrinos on the y-axis with a misidentified energy fraction equal to or lower than the corresponding value on the x-axis. 10 MW beam of 80 GeV protons.

²⁶ 7. Conclusion

¹ In this thesis, all relevant challenges for a ND LArTPC were studied, namely the dielectric
² strength of LAr, new charge and light readout methods, as well as the required next-
³ generation charge readout electronics. After the ARGONTUBE experiment [44] at
⁴ LHEP found the dielectric strength of LAr to be much lower than the $\approx 1 \text{ MV cm}^{-1}$
⁵ predicted by studies in the fifties, a systematic study of dielectric breakdowns in LAr
⁶ was undertaken. In particular, it was found that the dielectric strength is dependent on
⁷ absolute dimensions [2]. I recorded high-speed footage, current-voltage characteristics,
⁸ and spectrometry of breakdowns. From this, a conclusive theory of dielectric breakdowns
⁹ in LAr at the centimetre scale was developed [2]. The phenomenon is governed by three
¹⁰ distinct phases: field emission, streamer, and breakdown. Understanding the process
¹¹ enabled the development of a technique to mitigate the breakdowns [58]. However, this
¹² solution proved to be unreliable. Only keeping fields below 40 kV cm^{-1} everywhere in
¹³ the detector guarantees a safe operation.

¹⁴ In a preliminary study, I showed that the mechanical challenges met by wire plane
¹⁵ charge readouts can be alleviated by replacing the wires with copper tracks printed on a
¹⁶ thin Kapton layer. However, this does not solve the inherent ambiguities caused by wires.
¹⁷ Instead, a true 2D readout in form of pixels is needed. To address the high number of
¹⁸ channels required by a pixelated charge readout, I evaluated the cold digitisers foreseen
¹⁹ for the DUNE FD and found them unsuitable for a pixelated ND. Being optimised for
²⁰ wire readouts, their power dissipation is much too high given the required number of

7. Conclusion

21 channels. With no suitable cold electronics at hand, I implemented a form of analogue
1 multiplexing to demonstrate a pixelated LArTPC. Like this, it was possible to use the
2 existing charge readout electronics from ARGONTUBE.

3 I helped design and build a further prototype TPC to test the pixelated charge readout
4 scheme. Besides, it was also used to test the operation of SiPMs in LAr for the light
5 trigger system. Together with the LAr group of LHEP, I successfully recorded several
6 thousand cosmic muon tracks. The first measurement campaign still had some noise
7 on the charge readout. With the help of the electronics workshop, I extended the
8 ARGONTUBE readout electronics by a differential warm signal path, and reduced the
9 parasitic capacitances in the pixel readout PCB. In the second run, a SNR of 14 on the
10 pixel channels could be reached, proving a sufficient performance of pixels for operation in
11 a real physics experiment. These results triggered the development of bespoke cold pixel
12 electronics, LArPix, by LBNL, aimed to eventually enable an ambiguity-free pixelated
13 LArTPC charge readout.

14 To reconstruct the cosmic muon tracks, I developed a new software framework. The
15 hit finder had to be written from scratch because all existing LArTPC reconstruction
16 frameworks are optimised for wire readouts. A PCA was employed to solve the ambiguities
17 stemming from the analogue multiplexing. Finally, the unambiguous 3D measurements
18 were fed to GENFIT, an existing generic track-fitting toolkit based on a Kalman filter.
19 Therewith, I obtained fully reconstructed cosmic muon tracks.

20 Finally, I performed an event pile-up study using π^0 decay photons to demonstrate the
21 capability of ArgonCube to cope with the high event rates expected in the DUNE ND.
22 Based on the results from the pixel prototype test, I assumed unambiguous 3D position
23 information for the charge depositions. I employed a simple cone-based algorithm to
24 associate the charge to the corresponding photon. The mean deposited energy missed
25 by the algorithm was found to be less than 3 %. More importantly, the pile-up-related

7. Conclusion

²⁶ misidentification of energy depositions from other events was found to have a mean of
¹ 2% to 3%. For more than 50% of the neutrino events, this error is even smaller than
² 0.1%.

³ The combination of results from all of this work builds the groundwork for the
⁴ ArgonCube, a novel, fully modular LArTPC concept, addressing the most important
⁵ challenges of future neutrino detectors, in particular the DUNE ND. High cathode
⁶ voltages are prevented by splitting the detector into several small, self-contained TPCs
⁷ requiring only a moderate 50 kV cathode voltage. A pixelated readout enables the true
⁸ 3D tracking required to cope with the high event rates resulting from the high-intensity
⁹ neutrino beam. The ArCLight readout [82] minimises the dead volume in between the
¹⁰ modules, resulting in a similar performance to a monolithic detector while containing the
¹¹ scintillation light within the modules, simplifying association to the correct ionisation
¹² signals. The improvements I made led to ArgonCube being the LAr component of the
¹³ DUNE ND complex.

¹⁴ Acknowledgements

1

acknowledgements

2

So long, and thanks for all the fish.

³ Bibliography

- ¹ [1] C. Giunti and C. W. Kim. *Fundamentals of Neutrino Physics and Astrophysics*.
² 2007. ISBN: 9780198508717 (cit. on p. viii).
- ³ [2] A. Blatter et al. ‘Experimental study of electric breakdowns in liquid argon at
⁴ centimeter scale’. In: *Journal of Instrumentation* 9.04 (2014), P04006. URL: <http://stacks.iop.org/1748-0221/9/i=04/a=P04006> (cit. on pp. 5, 47, 54, 55, 59,
⁵ 64, 66, 70, 170).
- ⁶ [3] D. W. Swan and T. J. Lewis. ‘Influence of Electrode Surface Conditions on the
⁷ Electrical Strength of Liquified Gases’. In: *Journal of The Electrochemical Society*
⁸ 107.3 (1960), pp. 180–185. DOI: 10.1149/1.2427647. eprint: <http://jes.ecsdl.org/content/107/3/180.full.pdf+html>. URL: <http://jes.ecsdl.org/content/107/3/180.abstract> (cit. on pp. 5, 47).
- ⁹ [4] D. W. Swan and T. J. Lewis. ‘The Influence of Cathode and Anode Surfaces on
¹⁰ the Electric Strength of Liquid Argon’. In: *Proceedings of the Physical Society* 78.3
¹¹ (1961), p. 448. URL: <http://stacks.iop.org/0370-1328/78/i=3/a=314> (cit. on
¹² pp. 5, 47).
- ¹³ [5] J. Chadwick. ‘The intensity distribution in the magnetic spectrum of beta particles
¹⁴ from radium (B + C)’. In: *Verh. Phys. Gesell.* 16 (1914), pp. 383–391 (cit. on p. 9).
- ¹⁵ [6] W. Pauli. ‘Dear radioactive ladies and gentlemen’. In: *Phys. Today* 31N9 (1978),
¹⁶ p. 27 (cit. on p. 9).

Bibliography

- [7] J. Chadwick. ‘Possible Existence of a Neutron’. In: *Nature* 129 (1932), p. 312. DOI: 10.1038/129312a0 (cit. on p. 9).
- [8] E. Fermi. ‘Versuch einer Theorie der β -Strahlen. I’. In: *Zeitschrift für Physik* 88.3 (Mar. 1934), pp. 161–177. ISSN: 0044-3328. DOI: 10.1007/BF01351864. URL: <https://doi.org/10.1007/BF01351864> (cit. on p. 9).
- [9] F. Reines et al. ‘Detection of the Free Antineutrino’. In: *Phys. Rev.* 117 (1 Jan. 1960), pp. 159–173. DOI: 10.1103/PhysRev.117.159. URL: <https://link.aps.org/doi/10.1103/PhysRev.117.159> (cit. on p. 9).
- [10] G. Danby et al. ‘Observation of High-Energy Neutrino Reactions and the Existence of Two Kinds of Neutrinos’. In: *Phys. Rev. Lett.* 9 (1 July 1962), pp. 36–44. DOI: 10.1103/PhysRevLett.9.36. URL: <https://link.aps.org/doi/10.1103/PhysRevLett.9.36> (cit. on p. 10).
- [11] C. Grupen and B. Schwartz. *Particle detectors*. 2008 (cit. on pp. 11, 14, 17, 33, 35, 37).
- [12] R. Davis, D. S. Harmer and K. C. Hoffman. ‘Search for Neutrinos from the Sun’. In: *Phys. Rev. Lett.* 20 (21 May 1968), pp. 1205–1209. DOI: 10.1103/PhysRevLett.20.1205. URL: <https://link.aps.org/doi/10.1103/PhysRevLett.20.1205> (cit. on p. 11).
- [13] B. T. Cleveland et al. ‘Measurement of the Solar Electron Neutrino Flux with the Homestake Chlorine Detector’. In: *The Astrophysical Journal* 496.1 (1998), p. 505. URL: <http://stacks.iop.org/0004-637X/496/i=1/a=505> (cit. on p. 11).
- [14] D. Casper et al. ‘Measurement of atmospheric neutrino composition with the IMB-3 detector’. In: *Phys. Rev. Lett.* 66 (20 May 1991), pp. 2561–2564. DOI: 10.1103/PhysRevLett.66.2561. URL: <https://link.aps.org/doi/10.1103/PhysRevLett.66.2561> (cit. on p. 13).

Bibliography

- [15] K. Hirata et al. ‘Experimental study of the atmospheric neutrino flux’. In: *Physics Letters B* 205.2 (1988), pp. 416–420. ISSN: 0370-2693. DOI: [http://dx.doi.org/10.1016/0370-2693\(88\)91690-5](http://dx.doi.org/10.1016/0370-2693(88)91690-5). URL: <http://www.sciencedirect.com/science/article/pii/0370269388916905> (cit. on p. 13).
- [16] K. S. Hirata et al. ‘Real-time, directional measurement of ${}^8\text{B}$ solar neutrinos in the Kamiokande II detector’. In: *Phys. Rev. D* 44 (8 Oct. 1991), pp. 2241–2260. DOI: [10.1103/PhysRevD.44.2241](https://doi.org/10.1103/PhysRevD.44.2241). URL: <https://link.aps.org/doi/10.1103/PhysRevD.44.2241> (cit. on p. 13).
- [17] Y. Fukuda et al. ‘Measurement of a small atmospheric ν_μ/ν_e ratio’. In: *Physics Letters B* 433.1 (1998), pp. 9–18. ISSN: 0370-2693. DOI: [http://dx.doi.org/10.1016/S0370-2693\(98\)00476-6](http://dx.doi.org/10.1016/S0370-2693(98)00476-6). URL: <http://www.sciencedirect.com/science/article/pii/S0370269398004766> (cit. on p. 15).
- [18] Y. Fukuda et al. ‘Study of the atmospheric neutrino flux in the multi-GeV energy range’. In: *Physics Letters B* 436.1 (1998), pp. 33–41. ISSN: 0370-2693. DOI: [http://dx.doi.org/10.1016/S0370-2693\(98\)00876-4](http://dx.doi.org/10.1016/S0370-2693(98)00876-4). URL: <http://www.sciencedirect.com/science/article/pii/S0370269398008764> (cit. on p. 15).
- [19] Q. R. Ahmad et al. ‘Direct Evidence for Neutrino Flavor Transformation from Neutral-Current Interactions in the Sudbury Neutrino Observatory’. In: *Phys. Rev. Lett.* 89 (1 June 2002), p. 011301. DOI: [10.1103/PhysRevLett.89.011301](https://doi.org/10.1103/PhysRevLett.89.011301). URL: <https://link.aps.org/doi/10.1103/PhysRevLett.89.011301> (cit. on p. 15).
- [20] K. Kodama et al. ‘Observation of tau neutrino interactions’. In: *Physics Letters B* 504.3 (2001), pp. 218–224. ISSN: 0370-2693. DOI: [http://dx.doi.org/10.1016/S0370-2693\(01\)00307-0](http://dx.doi.org/10.1016/S0370-2693(01)00307-0). URL: <http://www.sciencedirect.com/science/article/pii/S0370269301003070> (cit. on p. 16).

Bibliography

- [21] F. P. An et al. ‘Measurement of electron antineutrino oscillation based on 1230 days of operation of the Daya Bay experiment’. In: *Phys. Rev. D* 95 (7 Apr. 2017), p. 072006. DOI: 10.1103/PhysRevD.95.072006. URL: <https://link.aps.org/doi/10.1103/PhysRevD.95.072006> (cit. on p. 17).
- [22] K. Abe et al. ‘Measurements of neutrino oscillation in appearance and disappearance channels by the T2K experiment with 6.6×10^{20} protons on target’. In: *Phys. Rev. D* 91 (7 Apr. 2015), p. 072010. DOI: 10.1103/PhysRevD.91.072010. URL: <https://link.aps.org/doi/10.1103/PhysRevD.91.072010> (cit. on p. 17).
- [23] A. Gando et al. ‘Reactor on-off antineutrino measurement with KamLAND’. In: *Phys. Rev. D* 88 (3 Aug. 2013), p. 033001. DOI: 10.1103/PhysRevD.88.033001. URL: <https://link.aps.org/doi/10.1103/PhysRevD.88.033001> (cit. on p. 17).
- [24] S. King. ‘Unified models of neutrinos, flavour and CP Violation’. In: *Progress in Particle and Nuclear Physics* 94.Supplement C (2017), pp. 217–256. ISSN: 0146-6410. DOI: <https://doi.org/10.1016/j.ppnp.2017.01.003>. URL: <http://www.sciencedirect.com/science/article/pii/S0146641017300042> (cit. on pp. 20–22, 24).
- [25] S. P. Mikheyev and A. Y. Smirnov. ‘Resonance enhancement of oscillations in matter and solar neutrino spectroscopy’. In: *Yadernaya Fizika* 42 (1985), pp. 1441–1448 (cit. on p. 21).
- [26] L. Wolfenstein. ‘Neutrino oscillations in matter’. In: *Phys. Rev. D* 17 (9 May 1978), pp. 2369–2374. DOI: 10.1103/PhysRevD.17.2369. URL: <https://link.aps.org/doi/10.1103/PhysRevD.17.2369> (cit. on p. 21).
- [27] R. Acciari et al. ‘Long-Baseline Neutrino Facility (LBNF) and Deep Underground Neutrino Experiment (DUNE): Volume 1: The LBNF and DUNE Projects’. In: (2016). arXiv: 1601.05471 [physics.ins-det] (cit. on pp. 22, 23).

Bibliography

- [28] R. Acciarri et al. ‘Long-Baseline Neutrino Facility (LBNF) and Deep Underground Neutrino Experiment (DUNE): Volume 2: The Physics Program for DUNE at LBNF’. In: (2015). arXiv: 1512.06148 [physics.ins-det] (cit. on pp. 22–25, 27, 28, 30, 143, 145).
- [29] J. Strait et al. ‘Long-Baseline Neutrino Facility (LBNF) and Deep Underground Neutrino Experiment (DUNE): Volume 3: Long-Baseline Neutrino Facility for DUNE’. In: (2016). arXiv: 1601.05823 [physics.ins-det] (cit. on pp. 22, 24).
- [30] R. Acciarri et al. ‘Long-Baseline Neutrino Facility (LBNF) and Deep Underground Neutrino Experiment (DUNE): Volume 4: The DUNE Detectors at LBNF’. In: (2016). arXiv: 1601.02984 [physics.ins-det] (cit. on pp. 22, 25, 140, 141, 155).
- [31] C. Patrignani et al. ‘Review of Particle Physics’. In: *Chinese Physics C* 40.10 (2016), p. 100001. URL: <http://stacks.iop.org/1674-1137/40/i=10/a=100001> (cit. on pp. 23, 145).
- [32] L. Fields. Personal Memo. Fermi National Accelerator Laboratory, Batavia, IL, USA. Jan. 2018 (cit. on p. 24).
- [33] P. Ballett et al. ‘Sensitivities and synergies of DUNE and T2HK’. In: *Phys. Rev. D* 96 (3 Aug. 2017), p. 033003. DOI: 10.1103/PhysRevD.96.033003. URL: <https://link.aps.org/doi/10.1103/PhysRevD.96.033003> (cit. on p. 24).
- [34] X. Qian and P. Vogel. ‘Neutrino mass hierarchy’. In: *Progress in Particle and Nuclear Physics* 83.Supplement C (2015), pp. 1–30. ISSN: 0146-6410. DOI: <https://doi.org/10.1016/j.ppnp.2015.05.002>. URL: <http://www.sciencedirect.com/science/article/pii/S0146641015000307> (cit. on pp. 24, 26).
- [35] C. W. Fabjan and T. Ludlam. ‘Calorimetry in High-Energy Physics’. In: *Annual Review of Nuclear and Particle Science* 32.1 (1982), pp. 335–389. DOI: 10.1146/annurev.ns.32.120182.002003. eprint: <https://doi.org/10.1146/annurev>.

Bibliography

- 25 ns . 32 . 120182 . 002003. URL: <https://doi.org/10.1146/annurev.ns.32.120182.002003> (cit. on p. 42).
- 2 [36] G. Charpak et al. ‘The use of multiwire proportional counters to select and localize
3 charged particles’. In: *Nuclear Instruments and Methods* 62.3 (1968), pp. 262–
4 268. ISSN: 0029-554X. DOI: [http://dx.doi.org/10.1016/0029-554X\(68\)90371-6](http://dx.doi.org/10.1016/0029-554X(68)90371-6). URL: <http://www.sciencedirect.com/science/article/pii/0029554X68903716> (cit. on p. 43).
- 7 [37] D. R. Nygren. ‘The Time Projection Chamber: A New 4 pi Detector for Charged
8 Particles’. In: *eConf* C740805 (1974), p. 58 (cit. on p. 43).
- 9 [38] C. Rubbia. *The Liquid Argon Time Projection Chamber: A New Concept for*
10 *Neutrino Detectors*. Tech. rep. CERN-EP-INT-77-08. CERN, 1977 (cit. on p. 43).
- 11 [39] E. Aprile et al. *Noble Gas Detectors*. Wiley, 2008. ISBN: 9783527405978. DOI:
12 10.1002/9783527610020 (cit. on pp. 44, 48).
- 13 [40] R. L. Amey and R. H. Cole. ‘Dielectric Constants of Liquefied Noble Gases and
14 Methane’. In: *The Journal of Chemical Physics* 40.1 (1964), pp. 146–148. DOI:
15 10.1063/1.1724850. eprint: <https://doi.org/10.1063/1.1724850>. URL:
16 <https://doi.org/10.1063/1.1724850> (cit. on p. 44).
- 17 [41] J. Thomas and D. A. Imel. ‘Recombination of electron-ion pairs in liquid argon
18 and liquid xenon’. In: *Phys. Rev. A* 36 (2 July 1987), pp. 614–616. DOI: 10.1103/
19 PhysRevA.36.614. URL: <https://link.aps.org/doi/10.1103/PhysRevA.36.614> (cit. on p. 45).
- 21 [42] M. Zeller et al. ‘Ionization signals from electrons and alpha-particles in mixtures of
22 liquid Argon and Nitrogen – perspectives on protons for Gamma Resonant Nuclear
23 Absorption applications’. In: *Journal of Instrumentation* 5.10 (2010), P10009. URL:
24 <http://stacks.iop.org/1748-0221/5/i=10/a=P10009> (cit. on p. 46).

Bibliography

- [43] V. Chepel and H. Araújo. ‘Liquid noble gas detectors for low energy particle physics’. In: *Journal of Instrumentation* 8.04 (2013), R04001. URL: <http://stacks.iop.org/1748-0221/8/i=04/a=R04001> (cit. on pp. 46, 116).
- [44] M. Zeller et al. ‘First measurements with ARGONTUBE, a 5 m long drift Liquid Argon TPC’. In: *Nuclear Instruments and Methods in Physics Research Section A: Accelerators, Spectrometers, Detectors and Associated Equipment* 718 (2013). Proceedings of the 12th Pisa Meeting on Advanced DetectorsLa Biodola, Isola d’Elba, Italy, May 20 – 26, 2012, pp. 454–458. ISSN: 0168-9002. DOI: <https://doi.org/10.1016/j.nima.2012.11.181>. URL: <http://www.sciencedirect.com/science/article/pii/S0168900212015288> (cit. on pp. 48, 116, 130, 170).
- [45] S. Amerio et al. ‘Design, construction and tests of the ICARUS T600 detector’. In: *Nuclear Instruments and Methods in Physics Research Section A: Accelerators, Spectrometers, Detectors and Associated Equipment* 527.3 (2004), pp. 329–410. ISSN: 0168-9002. DOI: <https://doi.org/10.1016/j.nima.2004.02.044>. URL: <http://www.sciencedirect.com/science/article/pii/S0168900204004966> (cit. on p. 50).
- [46] R. Acciarri et al. ‘Design and construction of the MicroBooNE detector’. In: *Journal of Instrumentation* 12.02 (2017), P02017. URL: <http://stacks.iop.org/1748-0221/12/i=02/a=P02017> (cit. on pp. 50, 88, 94, 101, 147).
- [47] M. Auger et al. ‘On the Electric Breakdown in Liquid Argon at Centimeter Scale’. In: *JINST* 11.03 (2016), P03017. DOI: [10.1088/1748-0221/11/03/P03017](https://doi.org/10.1088/1748-0221/11/03/P03017). arXiv: [1512.05968 \[physics.ins-det\]](https://arxiv.org/abs/1512.05968) (cit. on pp. 54, 60, 62, 64, 70).
- [48] I. Badhrees et al. ‘Measurement of the two-photon absorption cross-section of liquid argon with a time projection chamber’. In: *New Journal of Physics* 12.11 (2010), p. 113024. URL: <http://stacks.iop.org/1367-2630/12/i=11/a=113024> (cit. on pp. 55, 64, 78, 114).

Bibliography

- [49] R. Acciarri et al. ‘Liquid argon dielectric breakdown studies with the MicroBooNE purification system’. In: *Journal of Instrumentation* 9.11 (2014), P11001. URL: <http://stacks.iop.org/1748-0221/9/i=11/a=P11001> (cit. on pp. 63, 64).
- [50] J. Gerhold, M. Hubmann and E. Telser. ‘Gap size effect on liquid helium breakdown’. In: *Cryogenics* 34.7 (1994), pp. 579–586. ISSN: 0011-2275. DOI: [http://dx.doi.org/10.1016/0011-2275\(94\)90183-X](http://dx.doi.org/10.1016/0011-2275(94)90183-X). URL: <http://www.sciencedirect.com/science/article/pii/001122759490183X> (cit. on p. 63).
- [51] A. Bondar et al. ‘Study of infrared scintillations in gaseous and liquid argon. Part I: methodology and time measurements’. In: *Journal of Instrumentation* 7.06 (2012), P06015. URL: <http://stacks.iop.org/1748-0221/7/i=06/a=P06015> (cit. on p. 63).
- [52] A. Bondar et al. ‘Study of infrared scintillations in gaseous and liquid argon. Part II: light yield and possible applications’. In: *Journal of Instrumentation* 7.06 (2012), P06014. URL: <http://stacks.iop.org/1748-0221/7/i=06/a=P06014> (cit. on p. 63).
- [53] A. Buzulutskov. ‘Advances in Cryogenic Avalanche Detectors’. In: *Journal of Instrumentation* 7.02 (2012), p. C02025. URL: <http://stacks.iop.org/1748-0221/7/i=02/a=C02025> (cit. on p. 63).
- [54] J. B. Boffard et al. ‘Electron-impact excitation of argon: Optical emission cross sections in the range of 300-2500 nm’. In: *Atomic Data and Nuclear Data Tables* 93.6 (Nov. 2007). DOI: [10.1016/j.adt.2007.06.004](https://doi.org/10.1016/j.adt.2007.06.004) (cit. on p. 64).
- [55] T. Heindl et al. ‘The scintillation of liquid argon’. In: *EPL (Europhysics Letters)* 91.6 (2010), p. 62002. URL: <http://stacks.iop.org/0295-5075/91/i=6/a=62002> (cit. on pp. 64, 67).

Bibliography

- ²⁴ [56] P. Laporte et al. ‘Evolution of intermediate excitons in fluid argon and krypton’. In: ¹ *Phys. Rev. B* 35 (12 Apr. 1987), pp. 6270–6280. DOI: 10.1103/PhysRevB.35.6270.
² URL: <https://link.aps.org/doi/10.1103/PhysRevB.35.6270> (cit. on p. 65).
- ³ [57] M. Förstel et al. ‘Energy band dispersion in photoemission spectra of argon ⁴ clusters’. In: *Journal of Electron Spectroscopy and Related Phenomena* 184.3–6 ⁵ (2011). Advances in Vacuum Ultraviolet and X-ray PhysicsThe 37th International ⁶ Conference on Vacuum Ultraviolet and X-ray Physics (VUVX2010), pp. 107–112. ⁷ ISSN: 0368-2048. DOI: <http://doi.org/10.1016/j.elspec.2010.09.001>. URL: ⁸ <http://www.sciencedirect.com/science/article/pii/S0368204810001969> ⁹ (cit. on p. 65).
- ¹⁰ [58] M. Auger et al. ‘A method to suppress dielectric breakdowns in liquid argon ¹¹ ionization detectors for cathode to ground distances of several millimeters’. In: ¹² *JINST* 9 (2014), P07023. DOI: 10.1088/1748-0221/9/07/P07023. arXiv: 1406. ¹³ 3929 [physics.ins-det] (cit. on pp. 69, 170).
- ¹⁴ [59] G. I. Skanavi. *Fizika Dielektrikov; Oblast Silnykh Polei (Physics of dielectrics; ¹⁵ Strong Fields)*. Moscow: Gos. Izd. Fiz. Mat. Nauk (State Publ. Hause for Phys. ¹⁶ and Math. Scis.), 1958 (cit. on p. 69).
- ¹⁷ [60] M. Auger. ‘New Micromegas based Readout techniques for Imaging in Time ¹⁸ Projection Chambers’. PhD thesis. University of Bern, Switzerland, 2012 (cit. on ¹⁹ p. 82).
- ²⁰ [61] R. Sarpeshkar, T. Delbrück and C. A. Mead. ‘White noise in MOS transistors and ²¹ resistors’. In: *IEEE Circuits and Devices Magazine* 9.6 (Nov. 1993), pp. 23–29. ²² ISSN: 8755-3996. DOI: 10.1109/101.261888 (cit. on p. 85).

Bibliography

- [23] [62] Linear77. *Noise reduction using differential signaling*. Wikimedia Commons. Feb. 1 2012. URL: <https://commons.wikimedia.org/wiki/File:DiffSignaling.png> (cit. on p. 87).
- [3] [63] A. Ereditato et al. ‘Performance of cryogenic charge readout electronics with the ARGONTUBE LAr TPC’. In: *Journal of Instrumentation* 9.11 (2014), P11022. 4 URL: <http://stacks.iop.org/1748-0221/9/i=11/a=P11022> (cit. on pp. 88, 89).
- [6] [64] G. D. Geronimo et al. ‘Front-End ASIC for a Liquid Argon TPC’. In: *IEEE Transactions on Nuclear Science* 58.3 (June 2011), pp. 1376–1385. ISSN: 0018-9499. 7 DOI: [10.1109/TNS.2011.2127487](https://doi.org/10.1109/TNS.2011.2127487) (cit. on pp. 88, 94).
- [9] [65] F. Cavanna et al. ‘LArIAT: Liquid Argon In A Testbeam’. In: (2014). arXiv: 10 1406.5560 [physics.ins-det] (cit. on pp. 90, 126).
- [11] [66] B. Abi et al. ‘The Single-Phase ProtoDUNE Technical Design Report’. In: (2017). 12 arXiv: 1706.07081 [physics.ins-det] (cit. on p. 92).
- [13] [67] C. Thorn et al. ‘Cold Electronics Development for the LBNE LAr TPC’. In: 14 *Physics Procedia* 37 (2012). Proceedings of the 2nd International Conference on 15 Technology and Instrumentation in Particle Physics (TIPP 2011), pp. 1295–1302. 16 ISSN: 1875-3892. DOI: <https://doi.org/10.1016/j.phpro.2012.02.473>. URL: 17 <http://www.sciencedirect.com/science/article/pii/S187538921201838X> 18 (cit. on p. 93).
- [19] [68] A. Krieger et al. ‘A micropower readout ASIC for pixelated liquid Ar TPCs’. 20 In: *Topical Workshop on Electronics for Particle Physics*. 2017. URL: <https://pos.sissa.it/313> (cit. on p. 94).
- [22] [69] P. Horowitz and W. Hill. *The Art of Electronics*. Cambridge University Press, 2015. 23 ISBN: 9780521809269. URL: <https://books.google.ch/books?id=LAIWPwAACAAJ> 24 (cit. on p. 94).

Bibliography

- 25 [70] D. A. Dwyer. Personal Memo. Lawrence Berkeley National Laboratory, Berkeley,
1 CA, USA. Jan. 2018 (cit. on p. 95).
- 2 [71] M. Bass. ‘The Short Baseline Neutrino Oscillation Program at Fermilab’. In: *PoS*
3 ICHEP2016 (2016), p. 481. arXiv: 1702.00990 [physics.ins-det] (cit. on p. 101).
- 4 [72] M. Auger et al. ‘Multi-channel front-end board for SiPM readout’. In: *Journal*
5 *of Instrumentation* 11.10 (2016), P10005. URL: <http://stacks.iop.org/1748-0221/11/i=10/a=P10005> (cit. on pp. 101, 113).
- 7 [73] R. Francini et al. ‘VUV-Vis optical characterization of Tetraphenyl-butadiene films
8 on glass and specular reflector substrates from room to liquid Argon temperature’. In:
9 *Journal of Instrumentation* 8.09 (2013), P09006. URL: <http://stacks.iop.org/1748-0221/8/i=09/a=P09006> (cit. on p. 102).
- 11 [74] B. Howard et al. ‘A Novel Use of Light Guides and Wavelength Shifting Plates for
12 the Detection of Scintillation Photons in Large Liquid Argon Detectors’. In: (2017).
13 arXiv: 1710.11233 [physics.ins-det] (cit. on p. 103).
- 14 [75] Z. Moss et al. ‘Improved TPB-coated light guides for liquid argon TPC light
15 detection systems’. In: *Journal of Instrumentation* 10.08 (2015), P08017. URL:
16 <http://stacks.iop.org/1748-0221/10/i=08/a=P08017> (cit. on p. 103).
- 17 [76] C. Ignarra. ‘A Demonstration of Light Guides for Light Detection in Liquid
18 Argon TPCs’. In: *Physics Procedia* 37 (2012). Proceedings of the 2nd International
19 Conference on Technology and Instrumentation in Particle Physics (TIPP 2011),
20 pp. 1217–1222. ISSN: 1875-3892. DOI: <https://doi.org/10.1016/j.phpro.2012.02.455>. URL: <http://www.sciencedirect.com/science/article/pii/S1875389212018160> (cit. on p. 103).

Bibliography

- [77] B. Baptista et al. ‘Benchmarking TPB-coated Light Guides for Liquid Argon TPC Light Detection Systems’. In: (2012). arXiv: 1210.3793 [physics.ins-det] (cit. on p. 103).
- [78] B. J. P. Jones. ‘A simulation of the optical attenuation of TPB coated light-guide detectors’. In: *Journal of Instrumentation* 8.10 (2013), p. C10015. URL: <http://stacks.iop.org/1748-0221/8/i=10/a=C10015> (cit. on p. 103).
- [79] L. Bugel et al. ‘Demonstration of a lightguide detector for liquid argon TPCs’. In: *Nuclear Instruments and Methods in Physics Research Section A: Accelerators, Spectrometers, Detectors and Associated Equipment* 640.1 (2011), pp. 69–75. ISSN: 0168-9002. DOI: <https://doi.org/10.1016/j.nima.2011.03.003>. URL: <http://www.sciencedirect.com/science/article/pii/S0168900211005158> (cit. on p. 103).
- [80] D. Whittington. ‘Photon detection system designs for the Deep Underground Neutrino Experiment’. In: *Journal of Instrumentation* 11.05 (2016), p. C05019. URL: <http://stacks.iop.org/1748-0221/11/i=05/a=C05019> (cit. on p. 103).
- [81] A. Machado and E. Segreto. ‘ARAPUCA a new device for liquid argon scintillation light detection’. In: *Journal of Instrumentation* 11.02 (2016), p. C02004. URL: <http://stacks.iop.org/1748-0221/11/i=02/a=C02004> (cit. on pp. 103, 127).
- [82] M. Auger et al. ‘ArCLight—A Compact Dielectric Large-Area Photon Detector’. In: *Instruments* 2.1 (2018), p. 3. ISSN: 2410-390X. DOI: <10.3390/instruments2010003>. URL: <http://www.mdpi.com/2410-390X/2/1/3> (cit. on pp. 105, 172).
- [83] F. Stocker. ‘A Novel Approach to Liquid Argon Time Projection Chambers’. MA thesis. University of Bern, Switzerland, 2017 (cit. on pp. 111, 112).
- [84] B. Rossi et al. ‘A prototype liquid Argon Time Projection Chamber for the study of UV laser multi-photonic ionization’. In: *Journal of Instrumentation* 4.07 (2009),

Bibliography

- 25 P07011. URL: <http://stacks.iop.org/1748-0221/4/i=07/a=P07011> (cit. on
1 p. 112).
- 2 [85] Z. Moss et al. ‘A Factor of Four Increase in Attenuation Length of Dipped
3 Lightguides for Liquid Argon TPCs Through Improved Coating’. In: (2016). arXiv:
4 1604.03103 [physics.ins-det] (cit. on p. 112).
- 5 [86] M. Auger et al. ‘A Novel Cosmic Ray Tagger System for Liquid Argon TPC
6 Neutrino Detectors’. In: *Instruments* 1.1 (2017), p. 2. ISSN: 2410-390X. DOI: 10.
7 3390/instruments1010002. URL: <http://www.mdpi.com/2410-390X/1/1/2>
8 (cit. on p. 113).
- 9 [87] S. Amoruso et al. ‘Study of electron recombination in liquid argon with the
10 ICARUS TPC’. In: *Nuclear Instruments and Methods in Physics Research Section
11 A: Accelerators, Spectrometers, Detectors and Associated Equipment* 523.3 (2004),
12 pp. 275–286. ISSN: 0168-9002. DOI: <https://doi.org/10.1016/j.nima.2003.11.423>. URL: <http://www.sciencedirect.com/science/article/pii/S0168900204000506> (cit. on p. 116).
- 15 [88] R. Acciarri et al. ‘A study of electron recombination using highly ionizing particles
16 in the ArgoNeuT Liquid Argon TPC’. In: *Journal of Instrumentation* 8.08 (2013),
17 P08005. URL: <http://stacks.iop.org/1748-0221/8/i=08/a=P08005> (cit. on
18 p. 116).
- 19 [89] E. M. Gushchin, A. A. Kruglov and I. M. Obodovskil. ‘Electron dynamics in
20 condensed argon and xenon’. In: *Journal of Experimental and Theoretical Physics*
21 55.4 (Apr. 1982), p. 650 (cit. on p. 116).
- 22 [90] I. Jolliffe. *Principal Component Analysis*. Springer Series in Statistics. Springer,
23 2002. ISBN: 9780387954424. URL: https://books.google.ch/books?id=%5C_olByCrhjwIC (cit. on p. 118).

Bibliography

- [91] C. Höppner et al. ‘A novel generic framework for track fitting in complex detector systems’. In: *Nuclear Instruments and Methods in Physics Research Section A: Accelerators, Spectrometers, Detectors and Associated Equipment* 620.2 (2010), pp. 518–525. ISSN: 0168-9002. DOI: <https://doi.org/10.1016/j.nima.2010.03.136>. URL: <http://www.sciencedirect.com/science/article/pii/S0168900210007473> (cit. on p. 119).
- [92] J. Rauch and T. Schlüter. ‘GENFIT — a Generic Track-Fitting Toolkit’. In: *Journal of Physics: Conference Series* 608.1 (2015), p. 012042. URL: <http://stacks.iop.org/1742-6596/608/i=1/a=012042> (cit. on p. 119).
- [93] C. Anderson et al. ‘The ArgoNeuT detector in the NuMI low-energy beam line at Fermilab’. In: *Journal of Instrumentation* 7.10 (2012), P10019. URL: <http://stacks.iop.org/1748-0221/7/i=10/a=P10019> (cit. on p. 126).
- [94] C. M. Marshall. ‘LArTPC - optimal height of detector’. In: *DUNE Collaboration Meeting*. Feb. 2018. URL: <https://indico.fnal.gov/event/14581/session/5/contribution/86> (cit. on p. 138).
- [95] C. M. Marshall. ‘Containment, acceptance, and event rates in LAr’. In: *3rd DUNE Near Detector Workshop*. Nov. 2017. URL: <https://indico.fnal.gov/event/14737/session/2/contribution/28> (cit. on p. 149).
- [96] T. Alion et al. *DUNE Near Detector Task Force Report*. DUNE document 1792. DUNE, 2017. URL: <https://web.archive.org/web/20180224162141/http://www.neutrino.bnl.gov/q/DUNE/DUNE-doc-1792-v2.pdf> (cit. on p. 150).
- [97] R. Acciarri et al. ‘The Pandora multi-algorithm approach to automated pattern recognition of cosmic-ray muon and neutrino events in the MicroBooNE detector’. In: *The European Physical Journal C* 78.1 (Jan. 2018), p. 82. ISSN: 1434-6052. DOI:

Bibliography

²⁴ 10.1140/epjc/s10052-017-5481-6. URL: <https://doi.org/10.1140/epjc/s10052-017-5481-6> (cit. on p. 151).

² A. DUNE ND Event Pile-up Study ¹ Data

² A.1. 2 MW Beam at 80 GeV Proton Energy

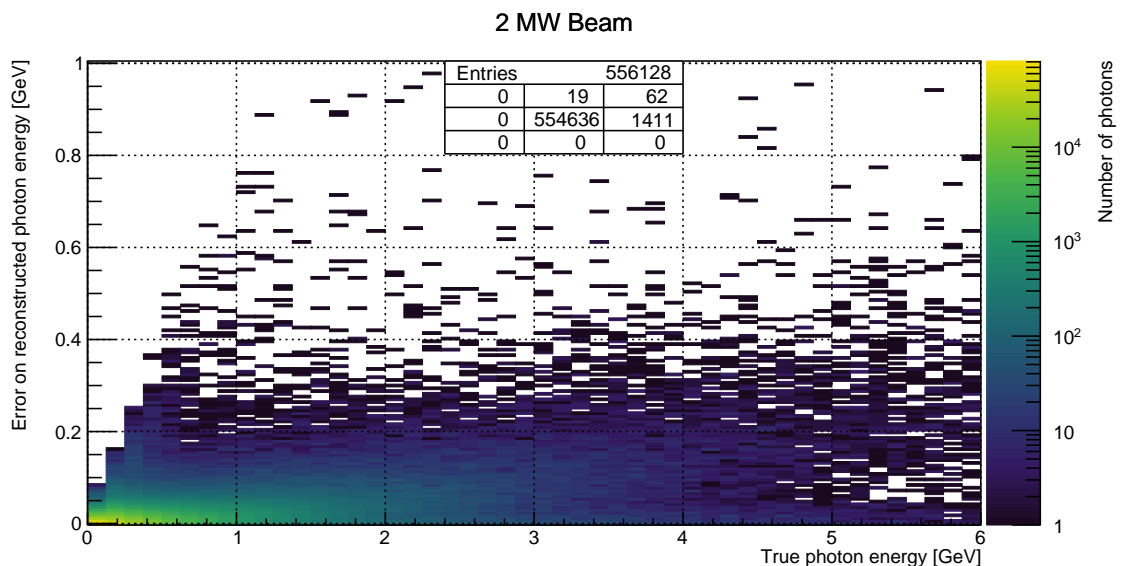


Figure A.1.: Missed energy versus true photon energy for a simple π^0 -induced EM shower reconstruction algorithm based on a cone-cylinder union. All energy deposited outside of the cone-cylinder union is counted as missed. 2 MW beam of 80 GeV protons. Entries: Central cell shows plotted entries, other cells show overflow entries in direction w.r.t. central cell.

A. DUNE ND Event Pile-up Study Data

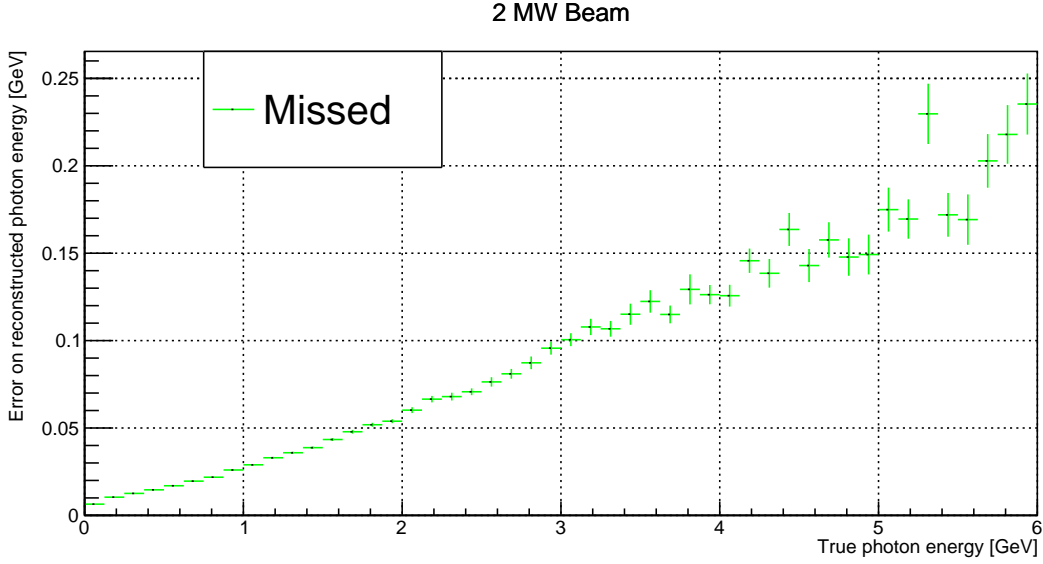


Figure A.2.: Mean missed energy versus true photon energy for a simple π^0 -induced EM shower reconstruction algorithm based on a cone-cylinder union. All energy deposited outside of the cone-cylinder union is counted as missed. 2 MW beam of 80 GeV protons.

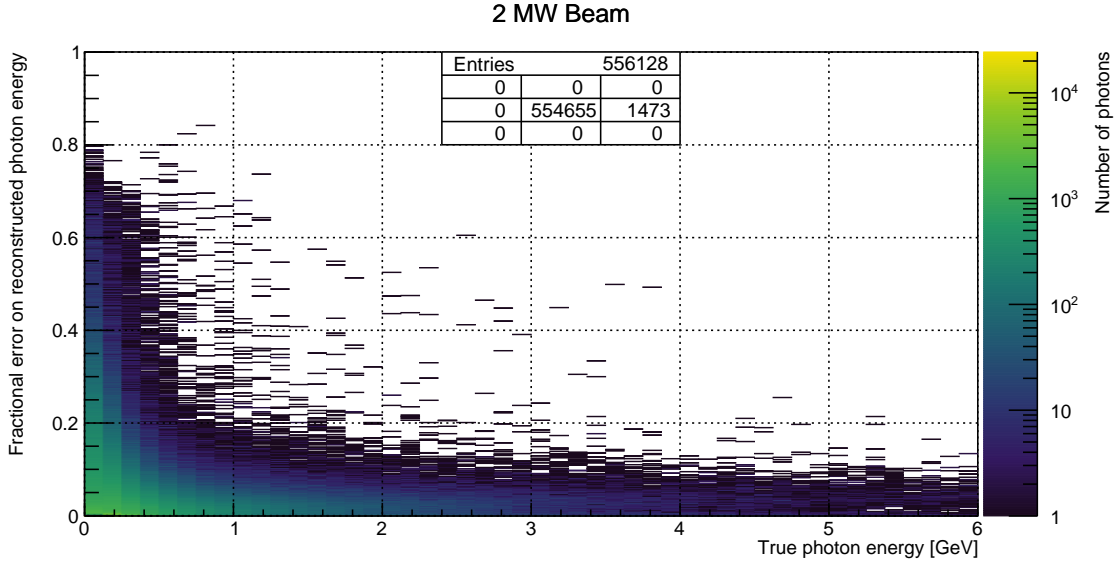


Figure A.3.: Missed energy fraction versus true photon energy for a simple π^0 -induced EM shower reconstruction algorithm based on a cone-cylinder union. All energy deposited outside of the cone-cylinder union is counted as missed. 2 MW beam of 80 GeV protons. Entries: Central cell shows plotted entries, other cells show overflow entries in direction w.r.t. central cell.

A. DUNE ND Event Pile-up Study Data

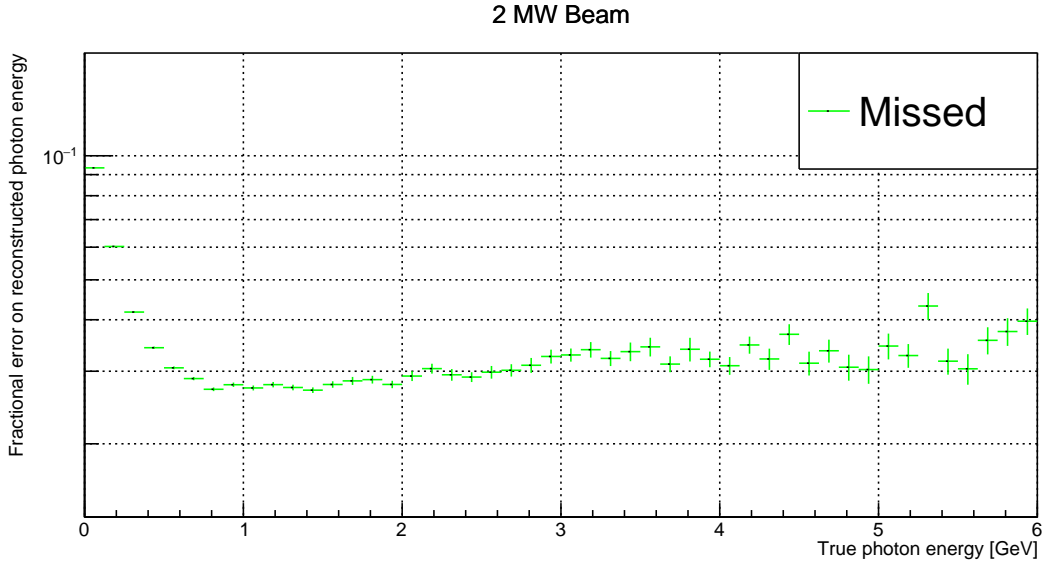


Figure A.4.: Mean missed energy fraction versus true photon energy for a simple π^0 -induced EM shower reconstruction algorithm based on a cone-cylinder union. All energy deposited outside of the cone-cylinder union is counted as missed. 2 MW beam of 80 GeV protons.

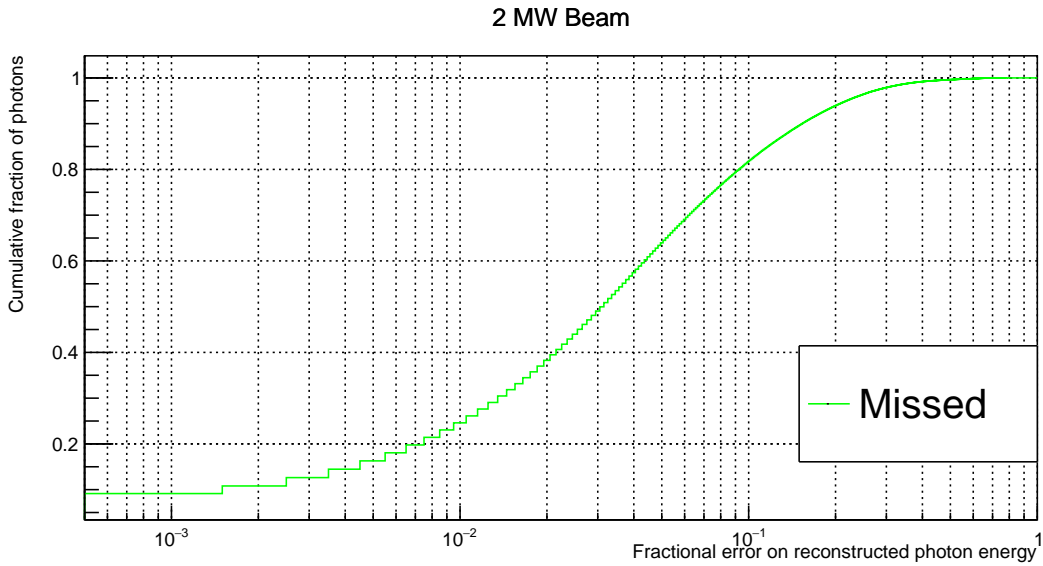


Figure A.5.: Cumulative fraction of photons versus missed energy fraction for a simple π^0 -induced EM shower reconstruction algorithm based on a cone-cylinder union. All energy deposited outside of the cone-cylinder union is counted as missed. The curve depicts the fraction of photons on the y-axis with a missed energy fraction equal to or lower than the corresponding value on the x-axis. 2 MW beam of 80 GeV protons.

A. DUNE ND Event Pile-up Study Data

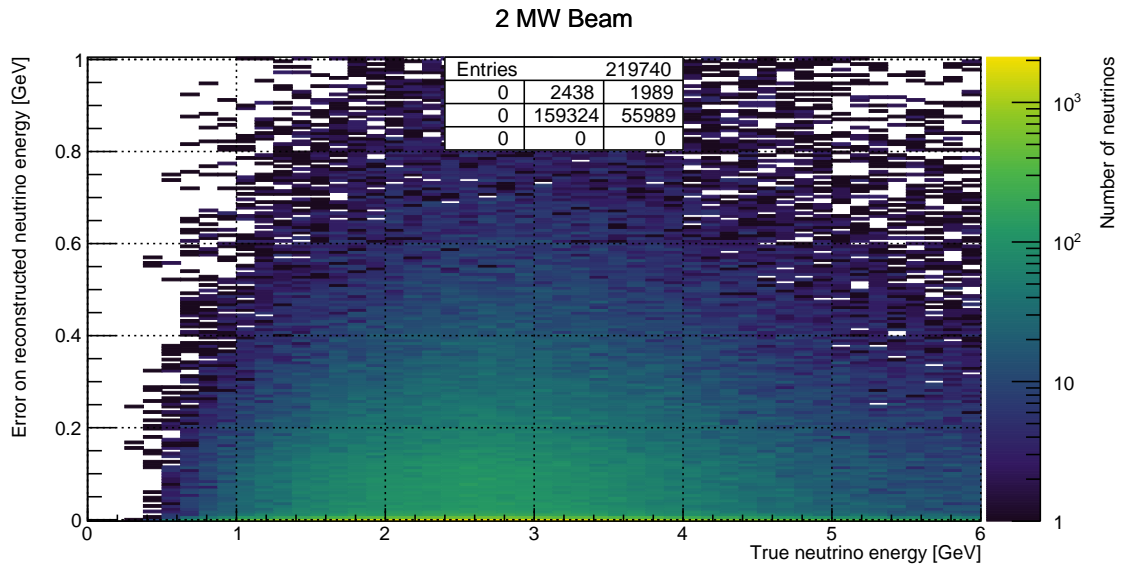


Figure A.6.: Misidentified energy versus true neutrino energy for a simple π^0 -induced EM shower reconstruction algorithm based on a cone-cylinder union. All energy deposited inside the cone-cylinder union by descendants of neutrinos different from the parent of the corresponding π^0 photon is counted as misidentified. 2 MW beam of 80 GeV protons. Entries: Central cell shows plotted entries, other cells show overflow entries in direction w.r.t. central cell.

A. DUNE ND Event Pile-up Study Data

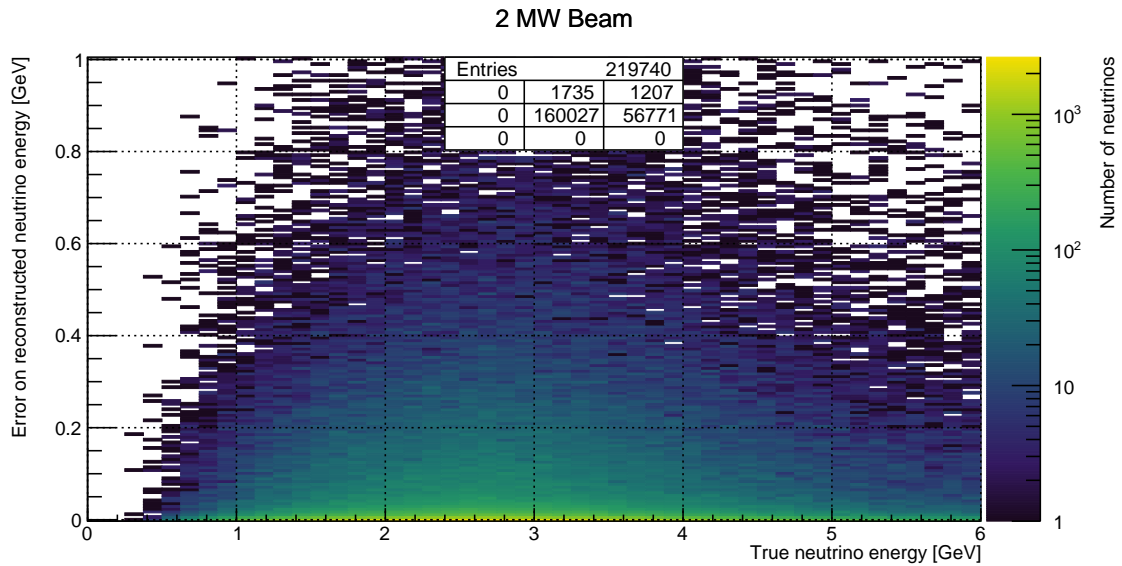


Figure A.7.: Misidentified energy versus true neutrino energy for a simple π^0 -induced EM shower reconstruction algorithm based on a cone-cylinder union. Energy deposited inside the cone-cylinder union by descendants of neutrinos different from the parent of the corresponding π^0 photon is counted as misidentified. Any energy deposited by muons is excluded. 2 MW beam of 80 GeV protons. Entries: Central cell shows plotted entries, other cells show overflow entries in direction w.r.t. central cell.

A. DUNE ND Event Pile-up Study Data

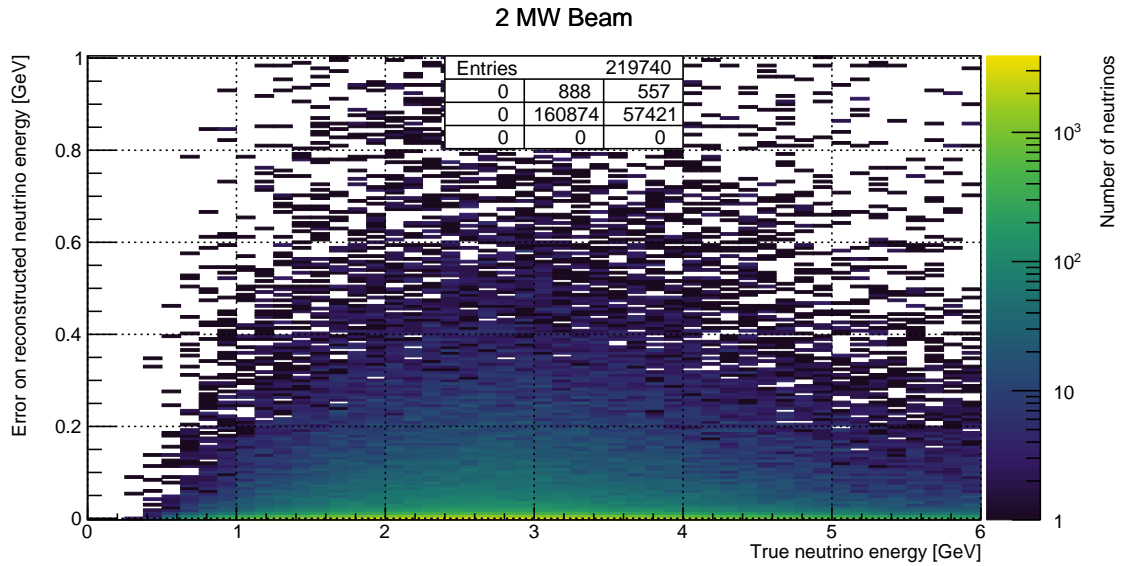


Figure A.8.: Misidentified energy versus true neutrino energy for a simple π^0 -induced EM shower reconstruction algorithm based on a cone-cylinder union. Energy deposited inside the cone-cylinder union by descendants of neutrinos different from the parent of the corresponding π^0 photon is counted as misidentified. Only energy deposited by photons, neutrons, or any of their descendants is included. 2 MW beam of 80 GeV protons. Entries: Central cell shows plotted entries, other cells show overflow entries in direction w.r.t. central cell.

A. DUNE ND Event Pile-up Study Data

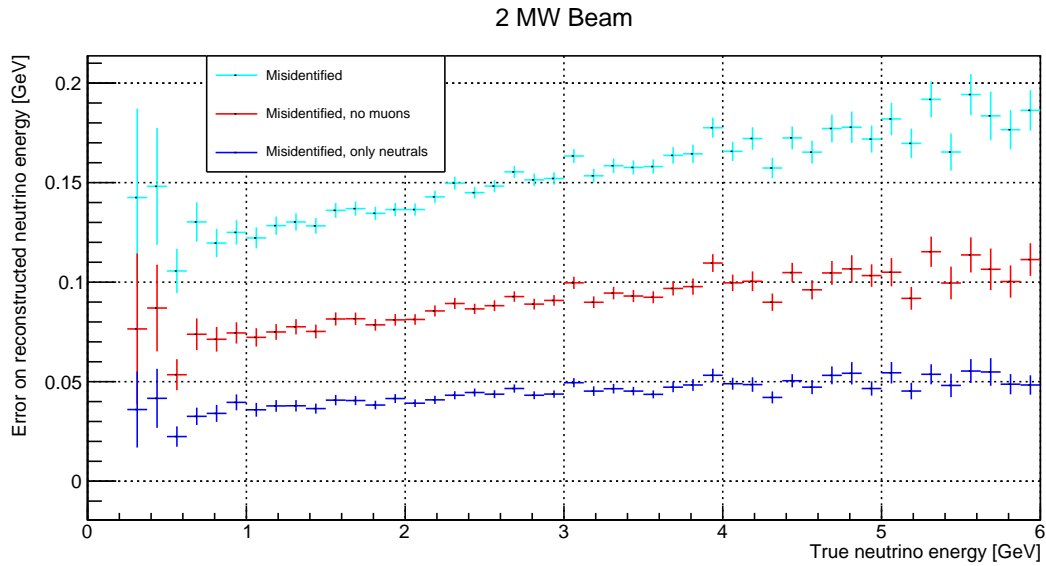


Figure A.9.: Mean misidentified energy versus true neutrino energy for a simple π^0 -induced EM shower reconstruction algorithm based on a cone-cylinder union. All energy deposited inside the cone-cylinder union by descendants of neutrinos different from the parent of the corresponding π^0 photon is counted as misidentified. Colour indicates different selections of misidentified energy: total (cyan); excluding depositions from muons (red); deposition from photons, neutrons, and their descendants only (blue). 2 MW beam of 80 GeV protons.

A. DUNE ND Event Pile-up Study Data

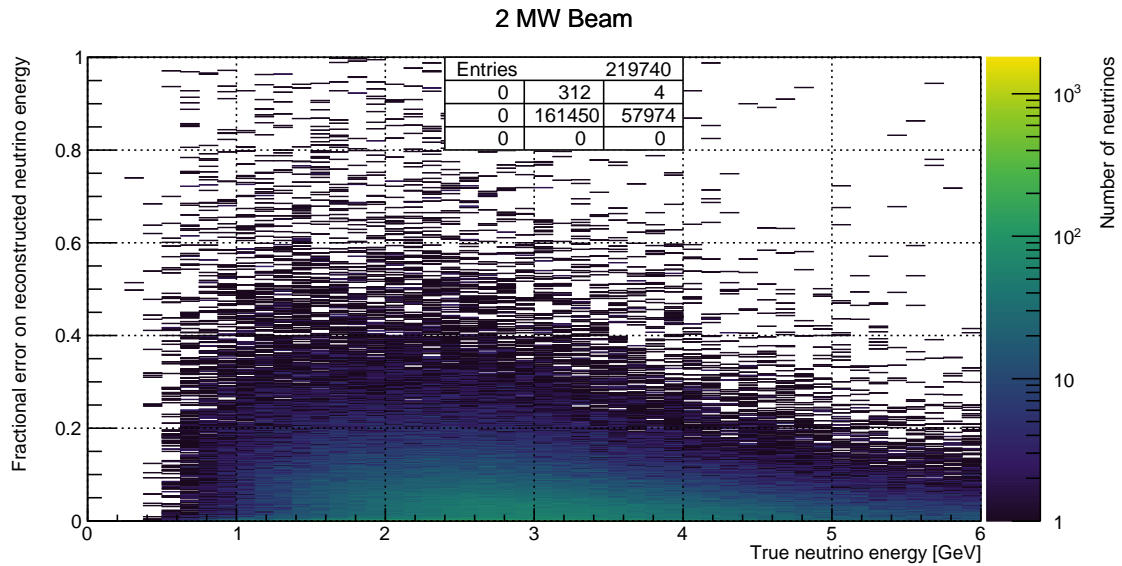


Figure A.10.: Misidentified energy fraction versus true neutrino energy for a simple π^0 -induced EM shower reconstruction algorithm based on a cone-cylinder union. All energy deposited inside the cone-cylinder union by descendants of neutrinos different from the parent of the corresponding π^0 photon is counted as misidentified. 2 MW beam of 80 GeV protons. Entries: Central cell shows plotted entries, other cells show overflow entries in direction w.r.t. central cell.

A. DUNE ND Event Pile-up Study Data

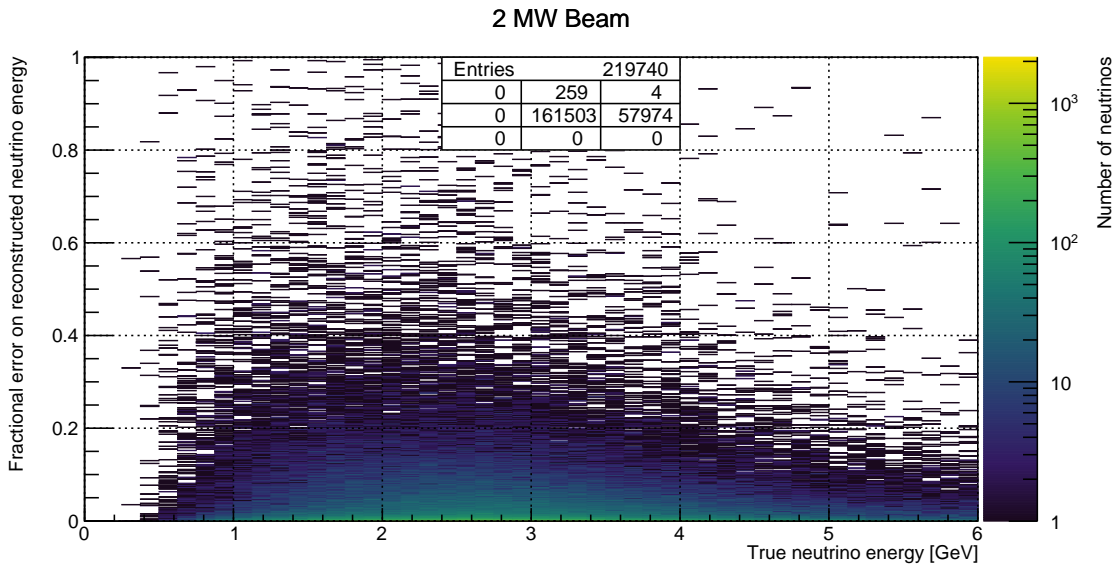


Figure A.11.: Misidentified energy fraction versus true neutrino energy for a simple π^0 -induced EM shower reconstruction algorithm based on a cone-cylinder union. Energy deposited inside the cone-cylinder union by descendants of neutrinos different from the parent of the corresponding π^0 photon is counted as misidentified. Any energy deposited by muons is excluded. 2 MW beam of 80 GeV protons. Entries: Central cell shows plotted entries, other cells show overflow entries in direction w.r.t. central cell.

A. DUNE ND Event Pile-up Study Data

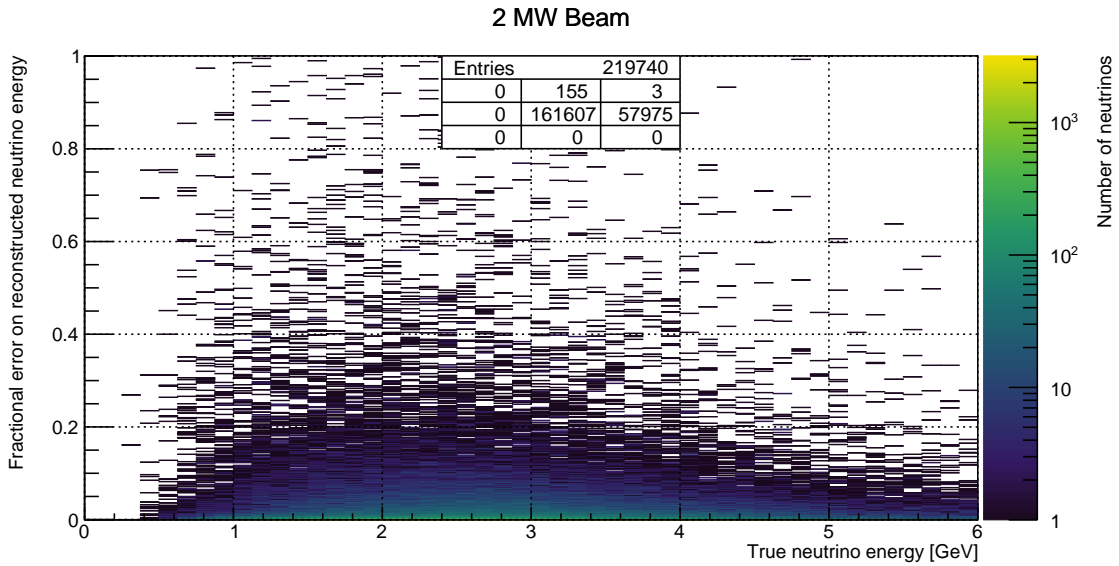


Figure A.12.: Misidentified energy fraction versus true neutrino energy for a simple π^0 -induced EM shower reconstruction algorithm based on a cone-cylinder union. Energy deposited inside the cone-cylinder union by descendants of neutrinos different from the parent of the corresponding π^0 photon is counted as misidentified. Only energy deposited by photons, neutrons, or any of their descendants is included. 2 MW beam of 80 GeV protons. Entries: Central cell shows plotted entries, other cells show overflow entries in direction w.r.t. central cell.

A. DUNE ND Event Pile-up Study Data

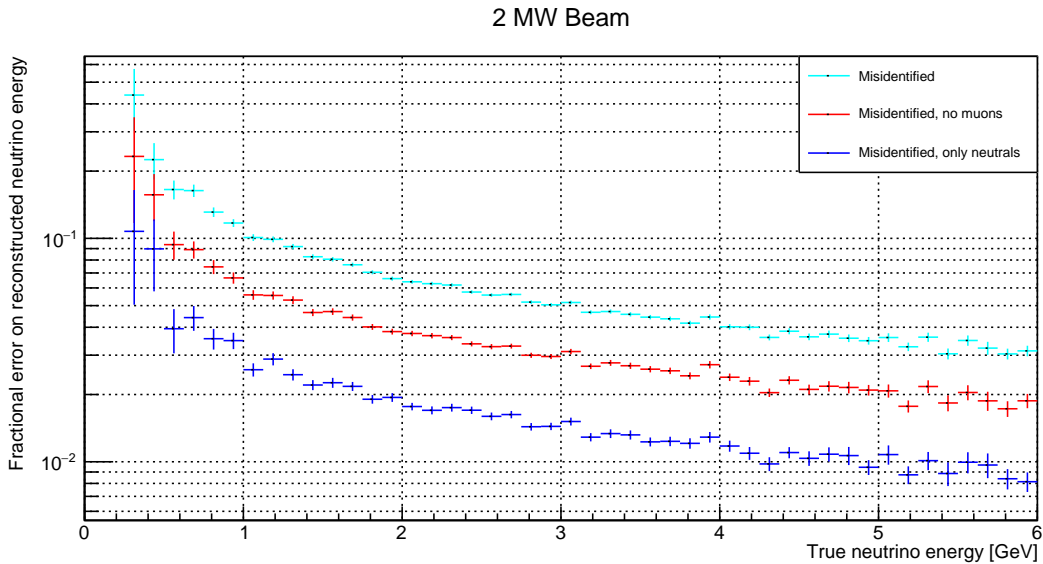


Figure A.13.: Mean misidentified energy fraction versus true neutrino energy for a simple π^0 -induced EM shower reconstruction algorithm based on a cone-cylinder union. All energy deposited inside the cone-cylinder union by descendants of neutrinos different from the parent of the corresponding π^0 photon is counted as misidentified. Colour indicates different selections of misidentified energy: total (cyan); excluding depositions from muons (red); deposition from photons, neutrons, and their descendants only (blue). 2 MW beam of 80 GeV protons.

A. DUNE ND Event Pile-up Study Data

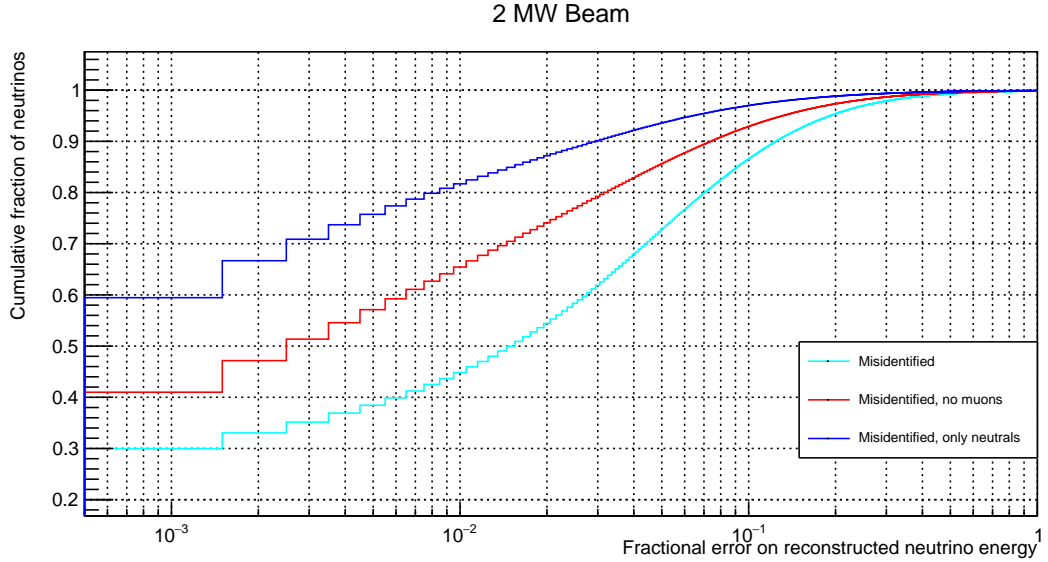


Figure A.14.: Cumulative fraction of neutrinos versus misidentified energy fraction for a simple π^0 -induced EM shower reconstruction algorithm based on a cone-cylinder union. All energy deposited inside the cone-cylinder union by descendants of neutrinos different from the parent of the corresponding π^0 photon is counted as misidentified. Colour indicates different selections of misidentified energy: total (cyan); excluding depositions from muons (red); deposition from photons, neutrons, and their descendants only (blue). The curve depicts the fraction of neutrinos on the y-axis with a misidentified energy fraction equal to or lower than the corresponding value on the x-axis. 2 MW beam of 80 GeV protons.

A. DUNE ND Event Pile-up Study Data

³ **A.2. 2 MW Beam at 80 GeV Proton Energy, XZ**

¹ **Projection**

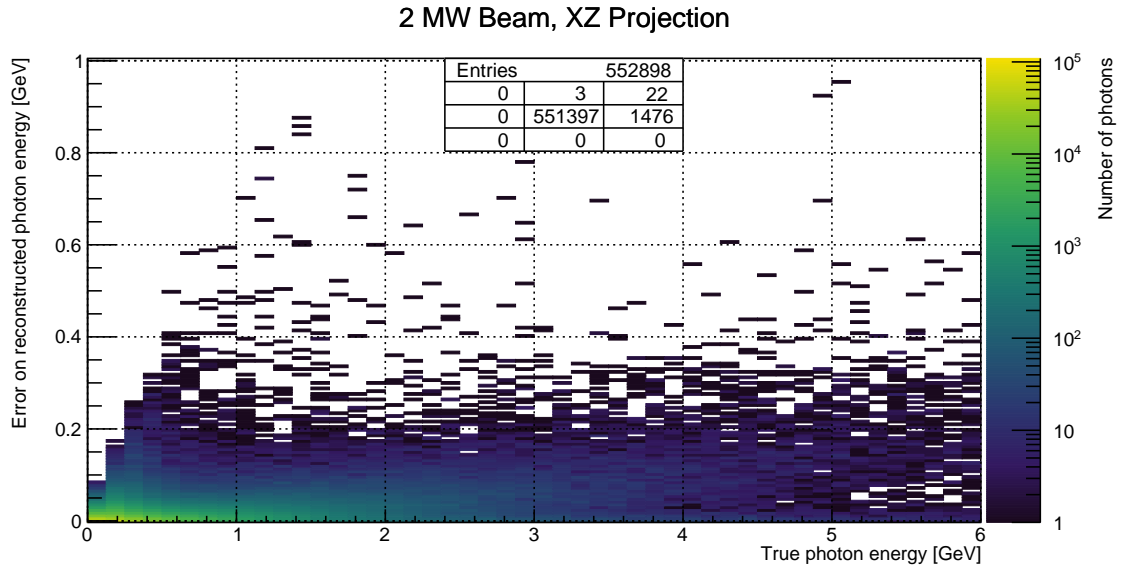


Figure A.15.: Missed energy versus true photon energy for a simple π^0 -induced EM shower reconstruction algorithm based on a cone-cylinder union. All energy deposited outside of the cone-cylinder union is counted as missed. 2 MW beam of 80 GeV protons. As a primitive simulation of a 2D wire readout, only X- and Z-coordinates are used for the energy reconstruction. Entries: Central cell shows plotted entries, other cells show overflow entries in direction w.r.t. central cell.

A. DUNE ND Event Pile-up Study Data

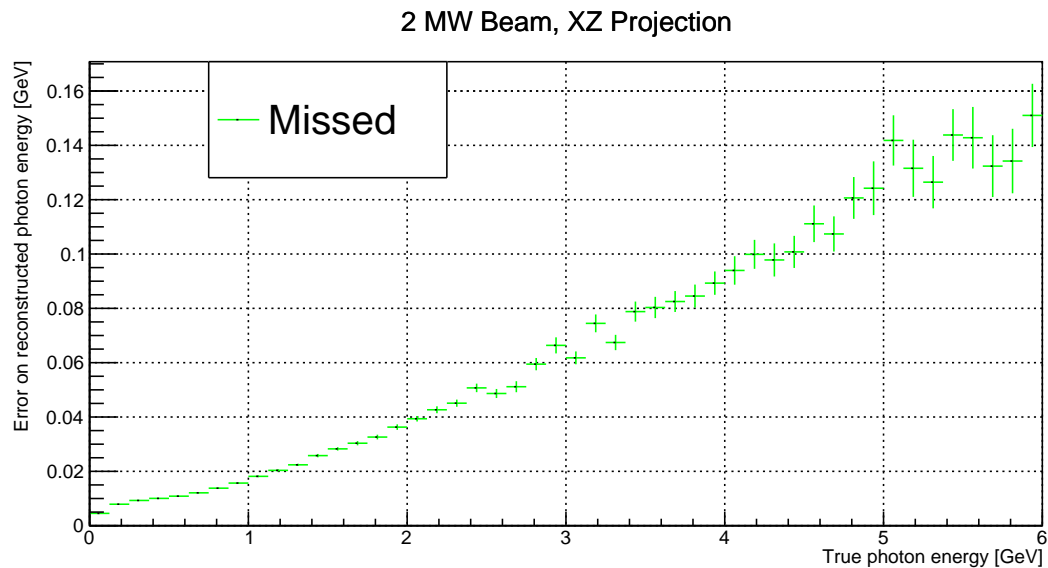


Figure A.16.: Mean missed energy versus true photon energy for a simple π^0 -induced EM shower reconstruction algorithm based on a cone-cylinder union. All energy deposited outside of the cone-cylinder union is counted as missed. 2 MW beam of 80 GeV protons. As a primitive simulation of a 2D wire readout, only X- and Z-coordinates are used for the energy reconstruction.

A. DUNE ND Event Pile-up Study Data

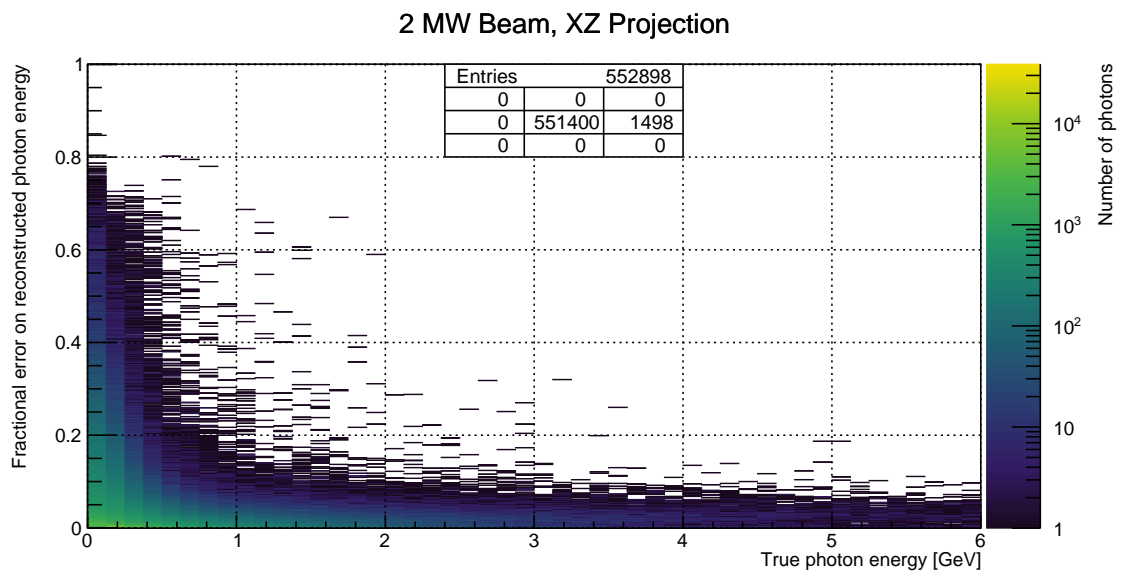


Figure A.17.: Missed energy fraction versus true photon energy for a simple π^0 -induced EM shower reconstruction algorithm based on a cone-cylinder union. All energy deposited outside of the cone-cylinder union is counted as missed. 2 MW beam of 80 GeV protons. As a primitive simulation of a 2D wire readout, only X- and Z-coordinates are used for the energy reconstruction. Entries: Central cell shows plotted entries, other cells show overflow entries in direction w.r.t. central cell.

A. DUNE ND Event Pile-up Study Data

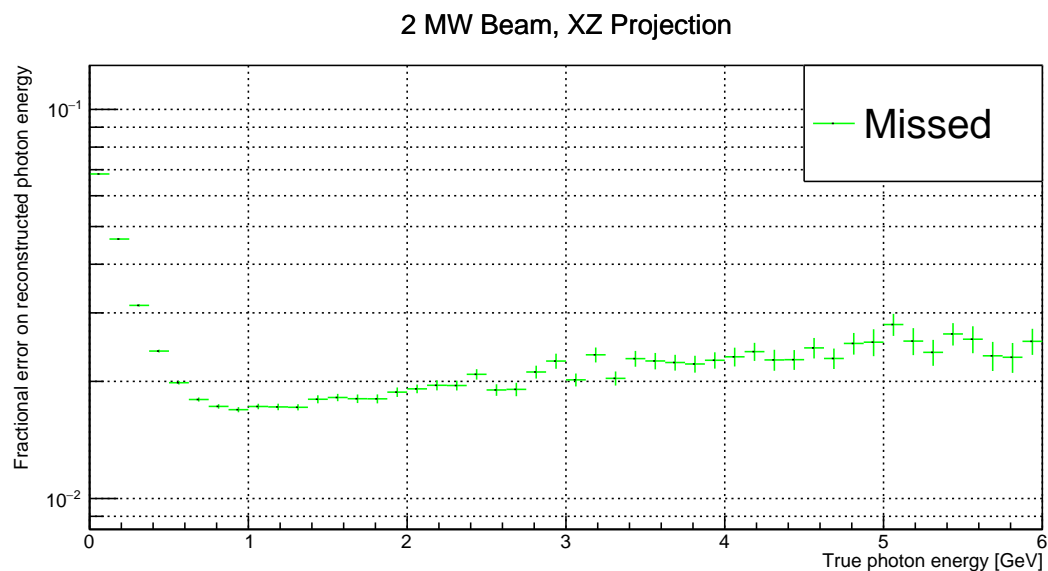


Figure A.18.: Mean missed energy fraction versus true photon energy for a simple π^0 -induced EM shower reconstruction algorithm based on a cone-cylinder union. All energy deposited outside of the cone-cylinder union is counted as missed. 2 MW beam of 80 GeV protons. As a primitive simulation of a 2D wire readout, only X- and Z-coordinates are used for the energy reconstruction.

A. DUNE ND Event Pile-up Study Data

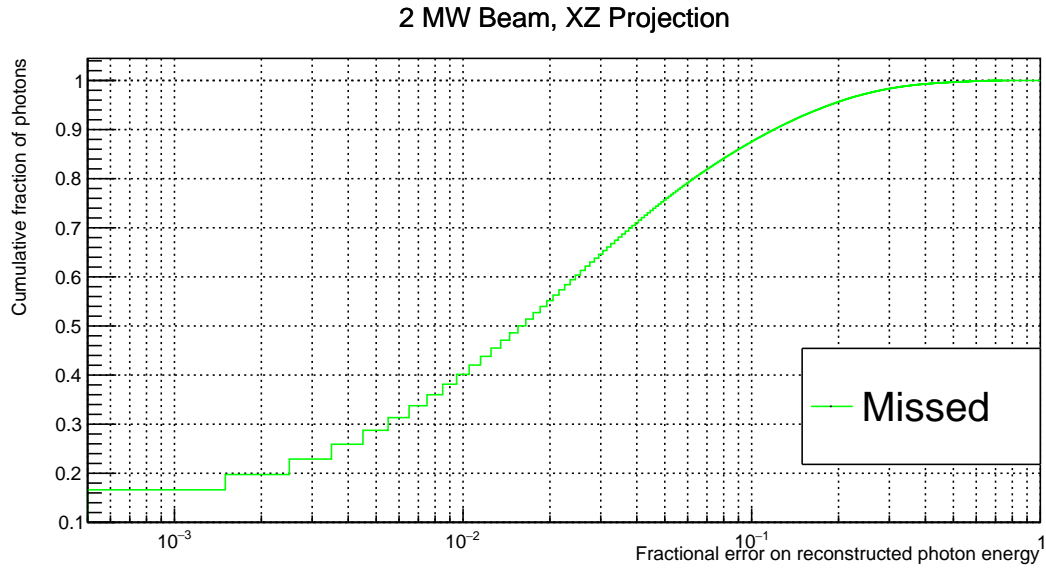


Figure A.19.: Cumulative fraction of photons versus missed energy fraction for a simple π^0 -induced EM shower reconstruction algorithm based on a cone-cylinder union. All energy deposited outside of the cone-cylinder union is counted as missed. The curve depicts the fraction of photons on the y-axis with a missed energy fraction equal to or lower than the corresponding value on the x-axis. 2 MW beam of 80 GeV protons. As a primitive simulation of a 2D wire readout, only X- and Z-coordinates are used for the energy reconstruction.

A. DUNE ND Event Pile-up Study Data

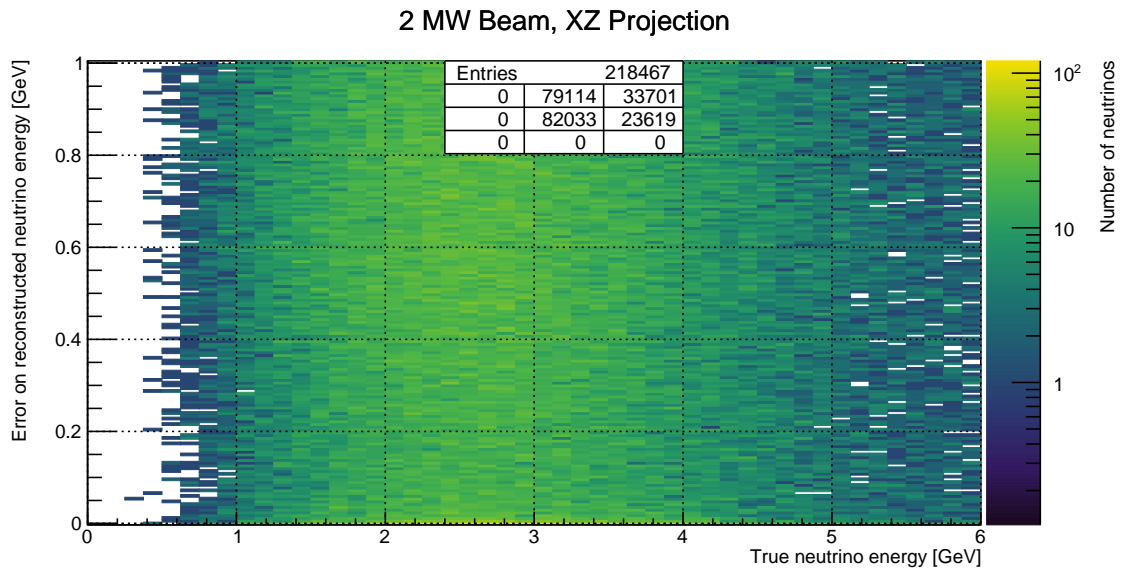


Figure A.20.: Misidentified energy versus true neutrino energy for a simple π^0 -induced EM shower reconstruction algorithm based on a cone-cylinder union. All energy deposited inside the cone-cylinder union by descendants of neutrinos different from the parent of the corresponding π^0 photon is counted as misidentified. 2 MW beam of 80 GeV protons. As a primitive simulation of a 2D wire readout, only X- and Z-coordinates are used for the energy reconstruction. Entries: Central cell shows plotted entries, other cells show overflow entries in direction w.r.t. central cell.

A. DUNE ND Event Pile-up Study Data

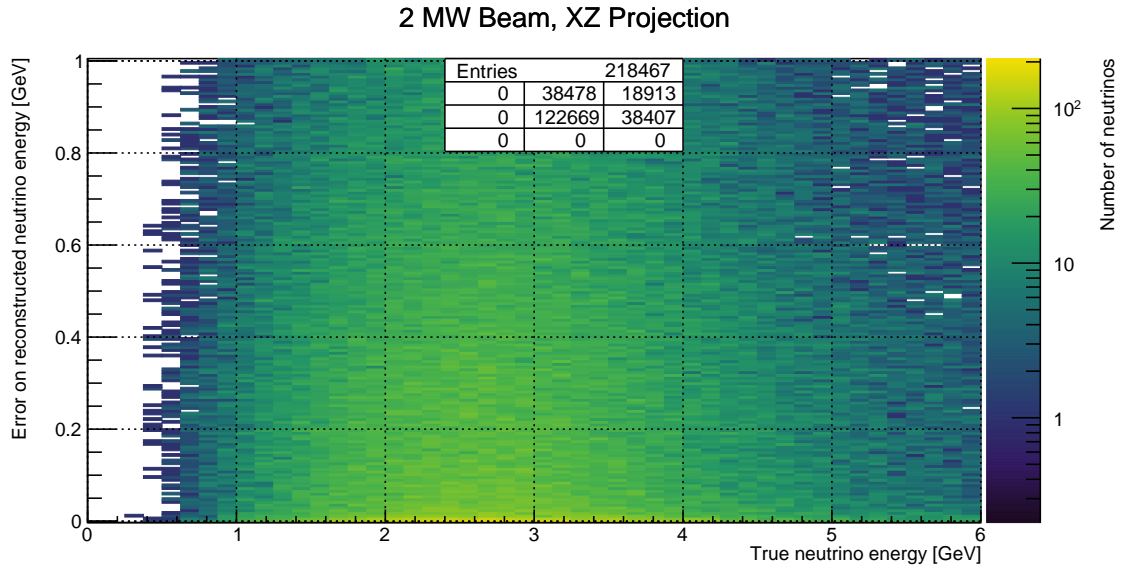


Figure A.21.: Misidentified energy versus true neutrino energy for a simple π^0 -induced EM shower reconstruction algorithm based on a cone-cylinder union. Energy deposited inside the cone-cylinder union by descendants of neutrinos different from the parent of the corresponding π^0 photon is counted as misidentified. Any energy deposited by muons is excluded. 2 MW beam of 80 GeV protons. As a primitive simulation of a 2D wire readout, only X- and Z-coordinates are used for the energy reconstruction. Entries: Central cell shows plotted entries, other cells show overflow entries in direction w.r.t. central cell.

A. DUNE ND Event Pile-up Study Data

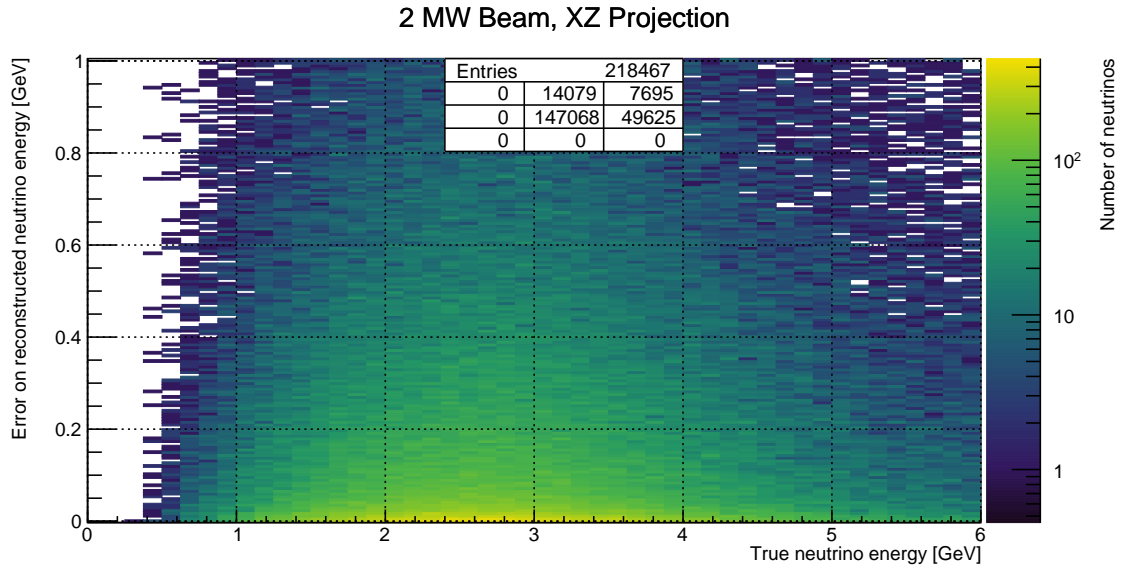


Figure A.22.: Misidentified energy versus true neutrino energy for a simple π^0 -induced EM shower reconstruction algorithm based on a cone-cylinder union. Energy deposited inside the cone-cylinder union by descendants of neutrinos different from the parent of the corresponding π^0 photon is counted as misidentified. Only energy deposited by photons, neutrons, or any of their descendants is included. 2 MW beam of 80 GeV protons. As a primitive simulation of a 2D wire readout, only X- and Z-coordinates are used for the energy reconstruction. Entries: Central cell shows plotted entries, other cells show overflow entries in direction w.r.t. central cell.

A. DUNE ND Event Pile-up Study Data

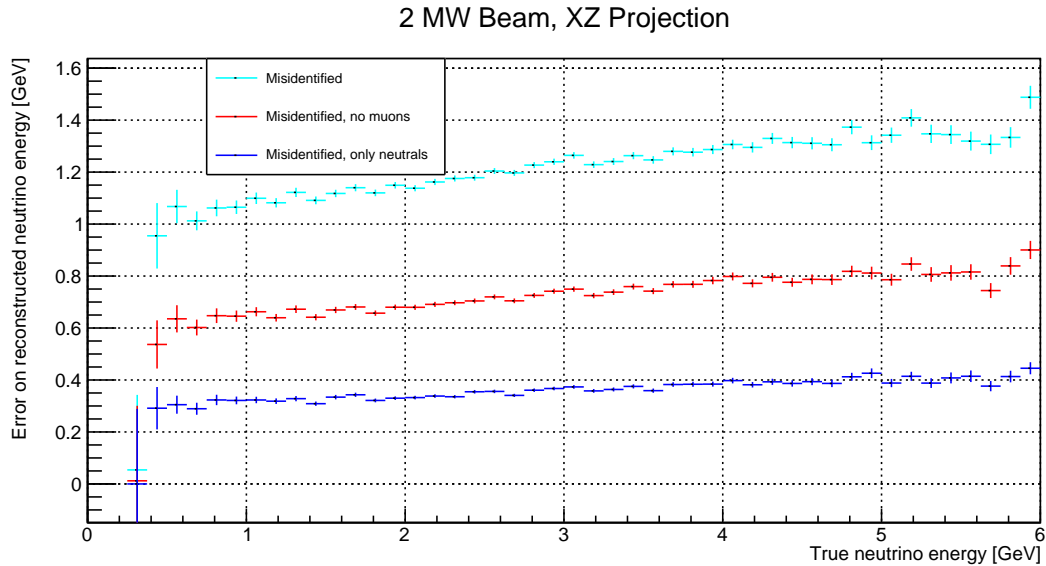


Figure A.23.: Mean misidentified energy versus true neutrino energy for a simple π^0 -induced EM shower reconstruction algorithm based on a cone-cylinder union. All energy deposited inside the cone-cylinder union by descendants of neutrinos different from the parent of the corresponding π^0 photon is counted as misidentified. Colour indicates different selections of misidentified energy: total (cyan); excluding depositions from muons (red); deposition from photons, neutrons, and their descendants only (blue). 2 MW beam of 80 GeV protons. As a primitive simulation of a 2D wire readout, only X- and Z-coordinates are used for the energy reconstruction.

A. DUNE ND Event Pile-up Study Data

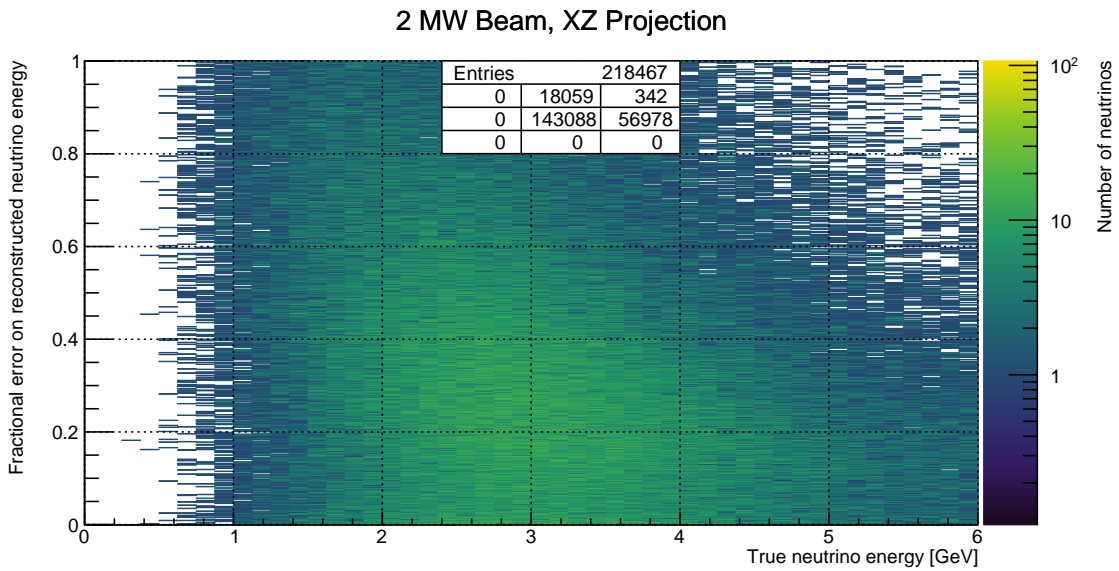


Figure A.24.: Misidentified energy fraction versus true neutrino energy for a simple π^0 -induced EM shower reconstruction algorithm based on a cone-cylinder union. All energy deposited inside the cone-cylinder union by descendants of neutrinos different from the parent of the corresponding π^0 photon is counted as misidentified. 2 MW beam of 80 GeV protons. As a primitive simulation of a 2D wire readout, only X- and Z-coordinates are used for the energy reconstruction. Entries: Central cell shows plotted entries, other cells show overflow entries in direction w.r.t. central cell.

A. DUNE ND Event Pile-up Study Data

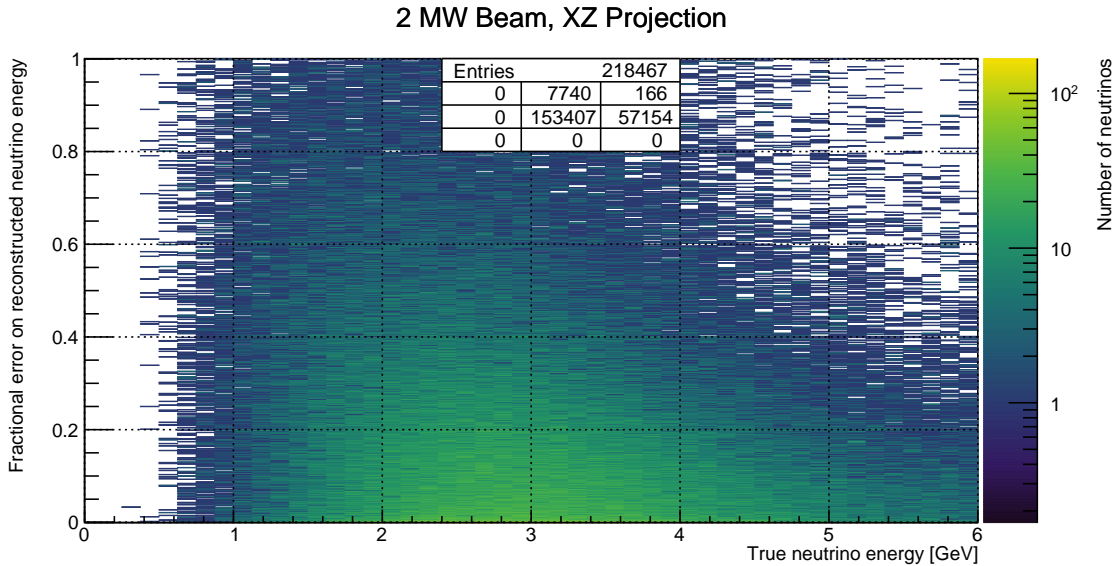


Figure A.25.: Misidentified energy fraction versus true neutrino energy for a simple π^0 -induced EM shower reconstruction algorithm based on a cone-cylinder union. Energy deposited inside the cone-cylinder union by descendants of neutrinos different from the parent of the corresponding π^0 photon is counted as misidentified. Any energy deposited by muons is excluded. 2 MW beam of 80 GeV protons. As a primitive simulation of a 2D wire readout, only X- and Z-coordinates are used for the energy reconstruction. Entries: Central cell shows plotted entries, other cells show overflow entries in direction w.r.t. central cell.

A. DUNE ND Event Pile-up Study Data

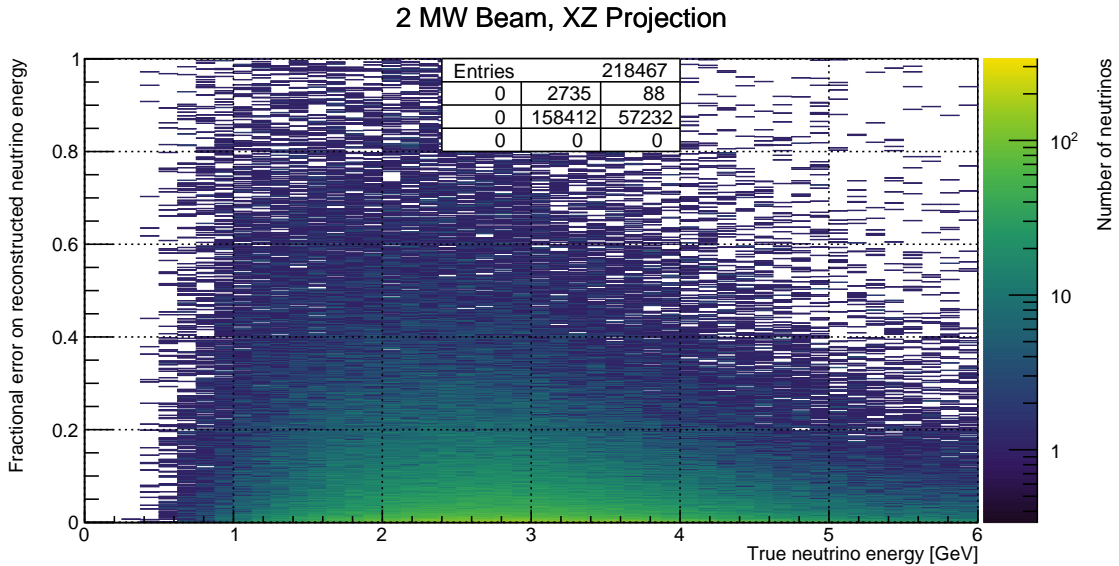


Figure A.26.: Misidentified energy fraction versus true neutrino energy for a simple π^0 -induced EM shower reconstruction algorithm based on a cone-cylinder union. Energy deposited inside the cone-cylinder union by descendants of neutrinos different from the parent of the corresponding π^0 photon is counted as misidentified. Only energy deposited by photons, neutrons, or any of their descendants is included. 2 MW beam of 80 GeV protons. As a primitive simulation of a 2D wire readout, only X- and Z-coordinates are used for the energy reconstruction. Entries: Central cell shows plotted entries, other cells show overflow entries in direction w.r.t. central cell.

A. DUNE ND Event Pile-up Study Data

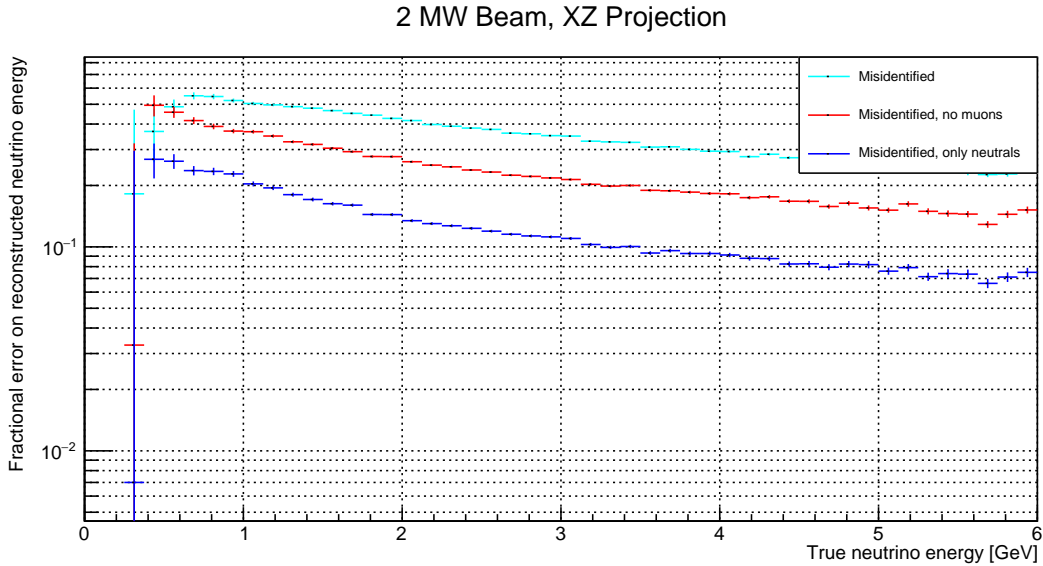


Figure A.27.: Mean misidentified energy fraction versus true neutrino energy for a simple π^0 -induced EM shower reconstruction algorithm based on a cone-cylinder union. All energy deposited inside the cone-cylinder union by descendants of neutrinos different from the parent of the corresponding π^0 photon is counted as misidentified. Colour indicates different selections of misidentified energy: total (cyan); excluding depositions from muons (red); deposition from photons, neutrons, and their descendants only (blue). 2 MW beam of 80 GeV protons. As a primitive simulation of a 2D wire readout, only X- and Z-coordinates are used for the energy reconstruction.

A. DUNE ND Event Pile-up Study Data

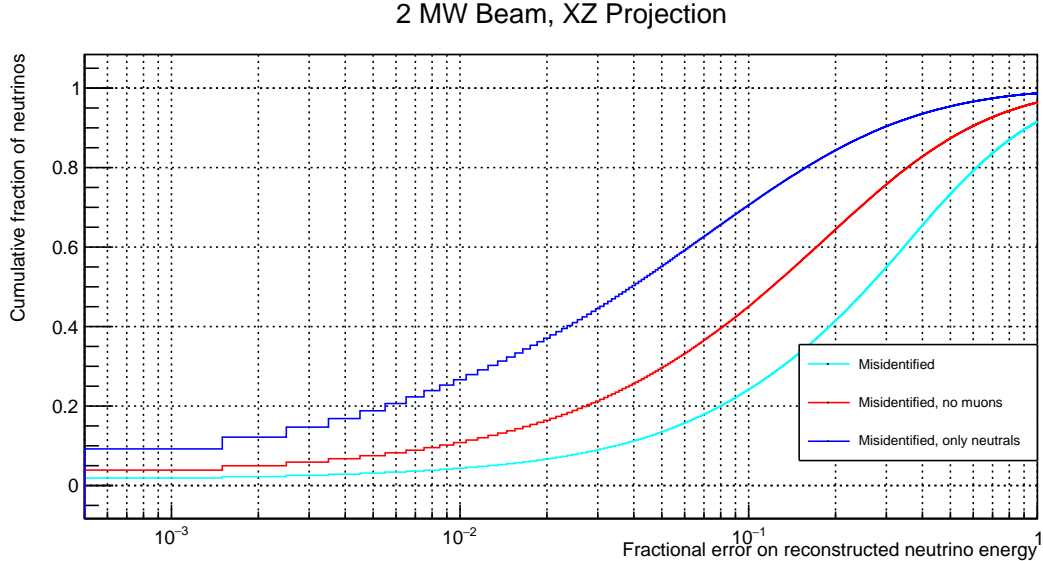


Figure A.28.: Cumulative fraction of neutrinos versus misidentified energy fraction for a simple π^0 -induced EM shower reconstruction algorithm based on a cone-cylinder union. All energy deposited inside the cone-cylinder union by descendants of neutrinos different from the parent of the corresponding π^0 photon is counted as misidentified. Colour indicates different selections of misidentified energy: total (cyan); excluding depositions from muons (red); deposition from photons, neutrons, and their descendants only (blue). The curve depicts the fraction of neutrinos on the y-axis with a misidentified energy fraction equal to or lower than the corresponding value on the x-axis. 2 MW beam of 80 GeV protons. As a primitive simulation of a 2D wire readout, only X- and Z-coordinates are used for the energy reconstruction.

A. DUNE ND Event Pile-up Study Data

A.3. 10 MW Beam at 80 GeV Proton Energy

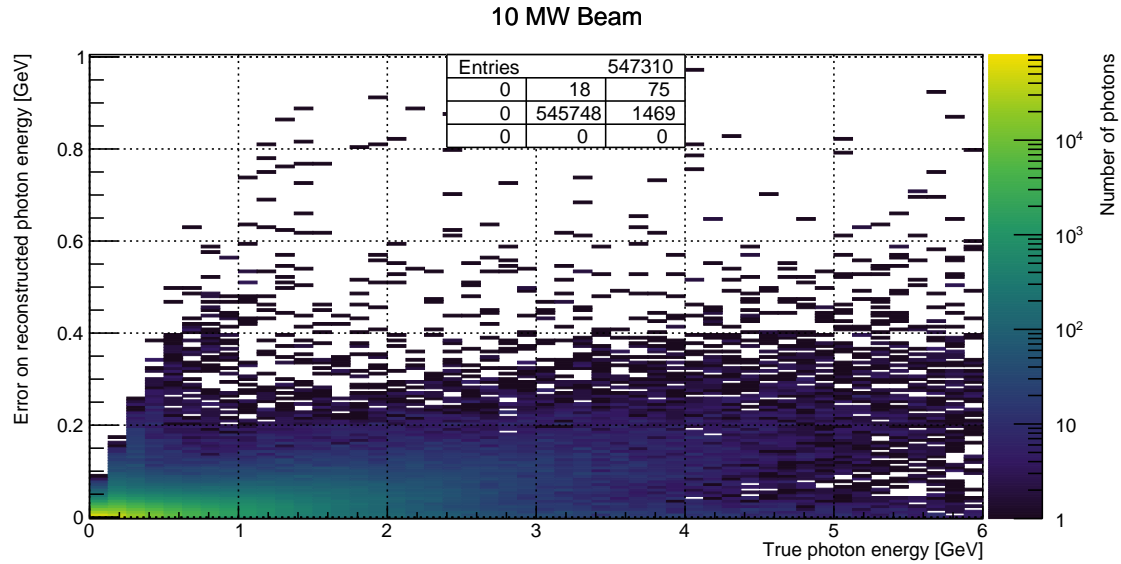


Figure A.29.: Missed energy versus true photon energy for a simple π^0 -induced EM shower reconstruction algorithm based on a cone-cylinder union. All energy deposited outside of the cone-cylinder union is counted as missed. 10 MW beam of 80 GeV protons. Entries: Central cell shows plotted entries, other cells show overflow entries in direction w.r.t. central cell.

A. DUNE ND Event Pile-up Study Data

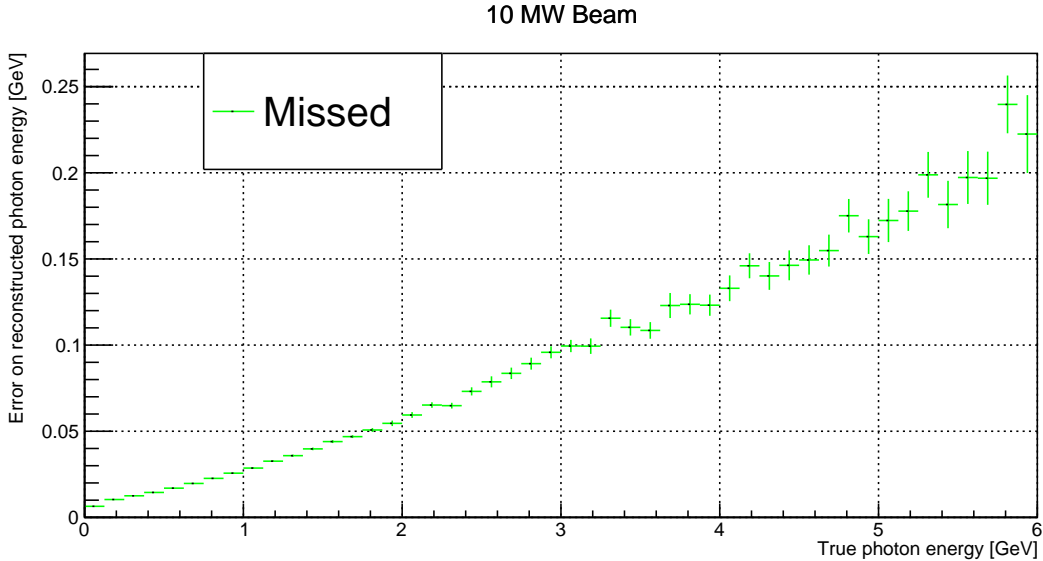


Figure A.30.: Mean missed energy versus true photon energy for a simple π^0 -induced EM shower reconstruction algorithm based on a cone-cylinder union. All energy deposited outside of the cone-cylinder union is counted as missed. 10 MW beam of 80 GeV protons.

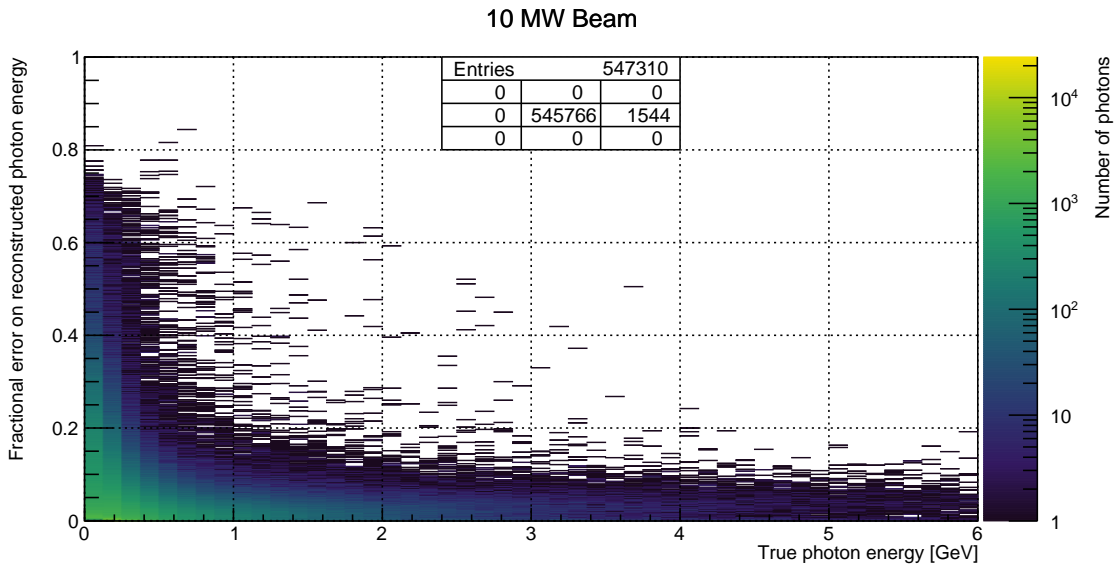


Figure A.31.: Missed energy fraction versus true photon energy for a simple π^0 -induced EM shower reconstruction algorithm based on a cone-cylinder union. All energy deposited outside of the cone-cylinder union is counted as missed. 10 MW beam of 80 GeV protons. Entries: Central cell shows plotted entries, other cells show overflow entries in direction w.r.t. central cell.

A. DUNE ND Event Pile-up Study Data

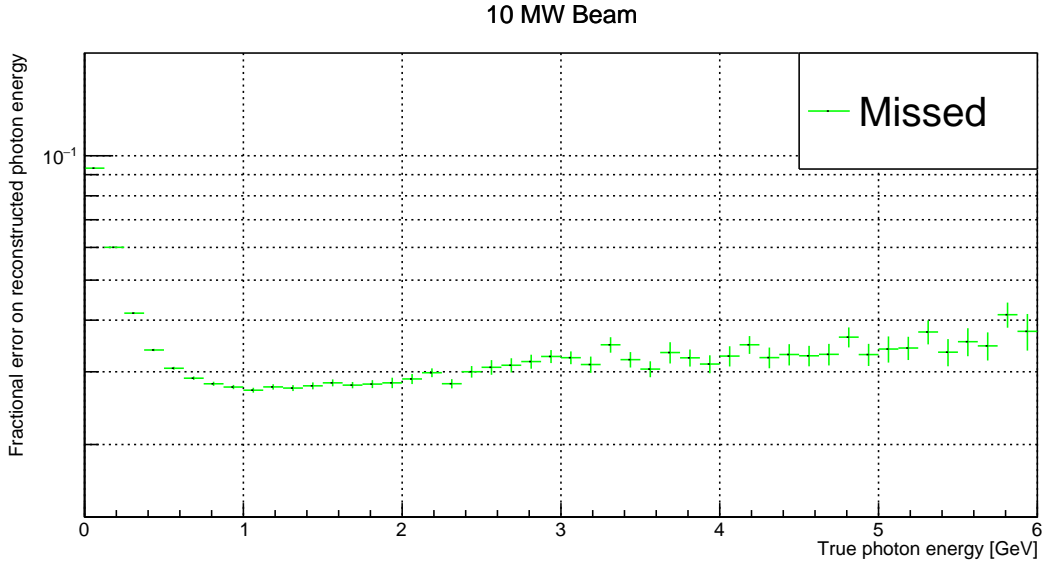


Figure A.32.: Mean missed energy fraction versus true photon energy for a simple π^0 -induced EM shower reconstruction algorithm based on a cone-cylinder union. All energy deposited outside of the cone-cylinder union is counted as missed. 10 MW beam of 80 GeV protons.

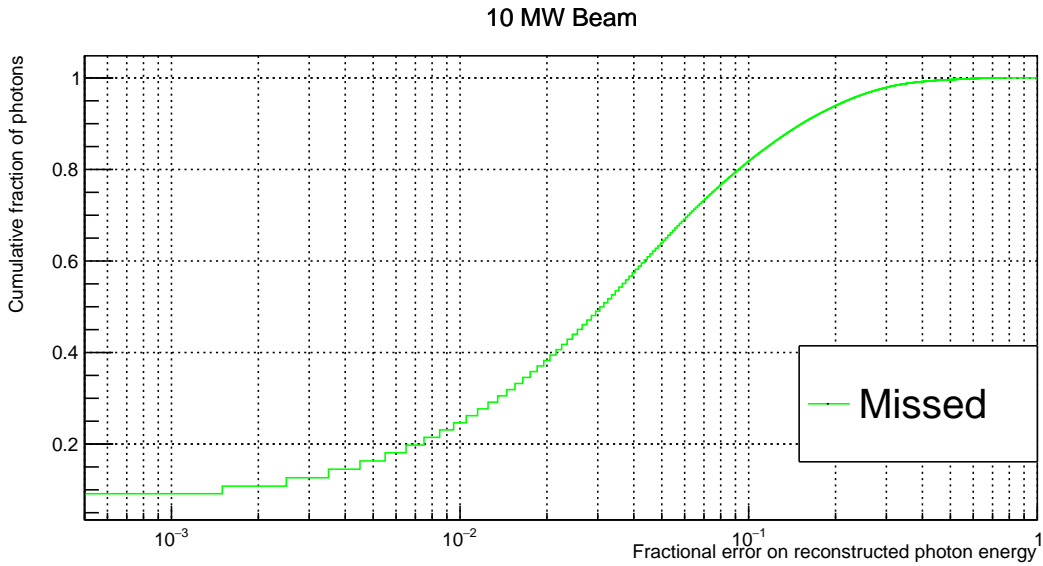


Figure A.33.: Cumulative fraction of photons versus missed energy fraction for a simple π^0 -induced EM shower reconstruction algorithm based on a cone-cylinder union. All energy deposited outside of the cone-cylinder union is counted as missed. The curve depicts the fraction of photons on the y-axis with a missed energy fraction equal to or lower than the corresponding value on the x-axis. 10 MW beam of 80 GeV protons.

A. DUNE ND Event Pile-up Study Data

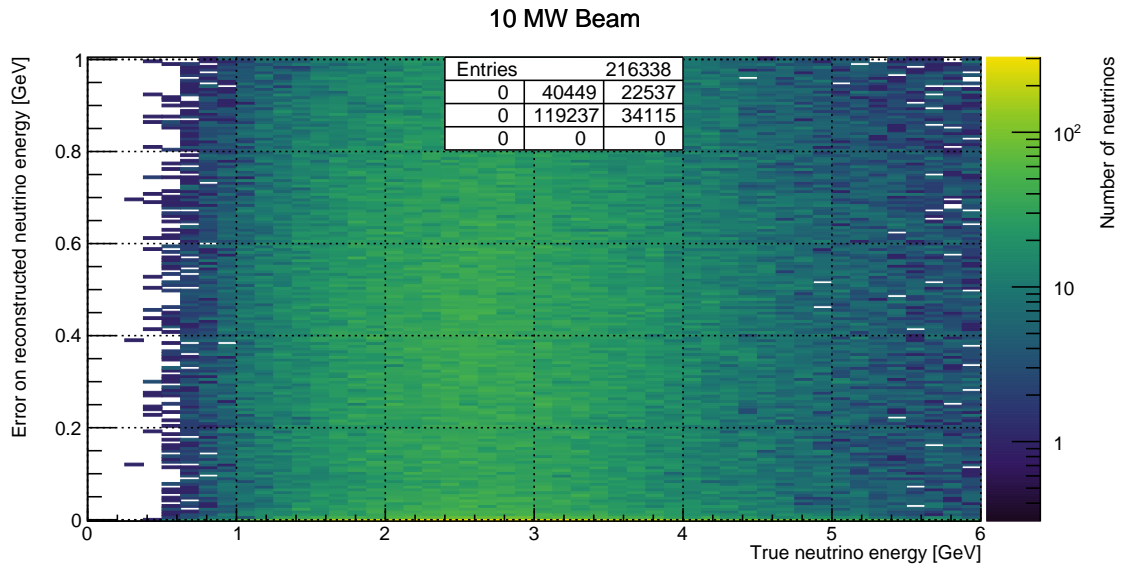


Figure A.34.: Misidentified energy versus true neutrino energy for a simple π^0 -induced EM shower reconstruction algorithm based on a cone-cylinder union. All energy deposited inside the cone-cylinder union by descendants of neutrinos different from the parent of the corresponding π^0 photon is counted as misidentified. 10 MW beam of 80 GeV protons. Entries: Central cell shows plotted entries, other cells show overflow entries in direction w.r.t. central cell.

A. DUNE ND Event Pile-up Study Data

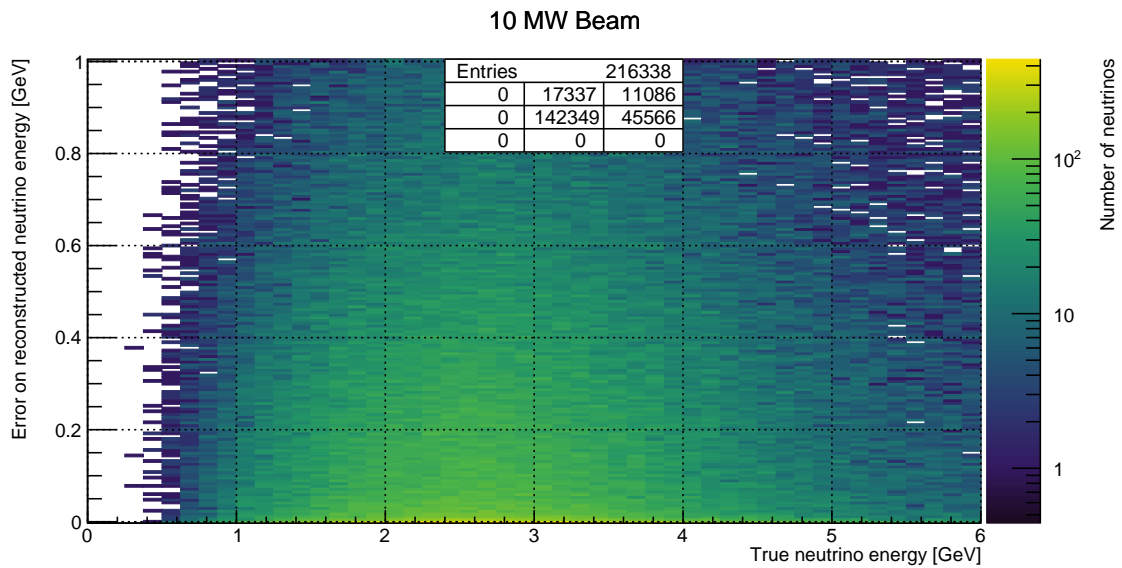


Figure A.35.: Misidentified energy versus true neutrino energy for a simple π^0 -induced EM shower reconstruction algorithm based on a cone-cylinder union. Energy deposited inside the cone-cylinder union by descendants of neutrinos different from the parent of the corresponding π^0 photon is counted as misidentified. Any energy deposited by muons is excluded. 10 MW beam of 80 GeV protons. Entries: Central cell shows plotted entries, other cells show overflow entries in direction w.r.t. central cell.

A. DUNE ND Event Pile-up Study Data

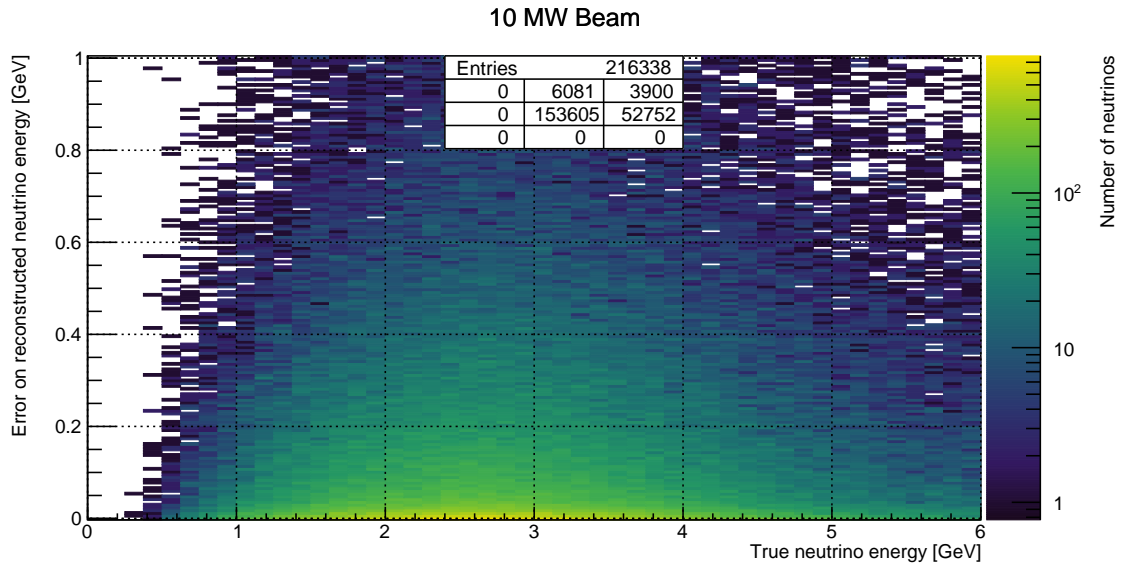


Figure A.36.: Misidentified energy versus true neutrino energy for a simple π^0 -induced EM shower reconstruction algorithm based on a cone-cylinder union. Energy deposited inside the cone-cylinder union by descendants of neutrinos different from the parent of the corresponding π^0 photon is counted as misidentified. Only energy deposited by photons, neutrons, or any of their descendants is included. 10 MW beam of 80 GeV protons. Entries: Central cell shows plotted entries, other cells show overflow entries in direction w.r.t. central cell.

A. DUNE ND Event Pile-up Study Data

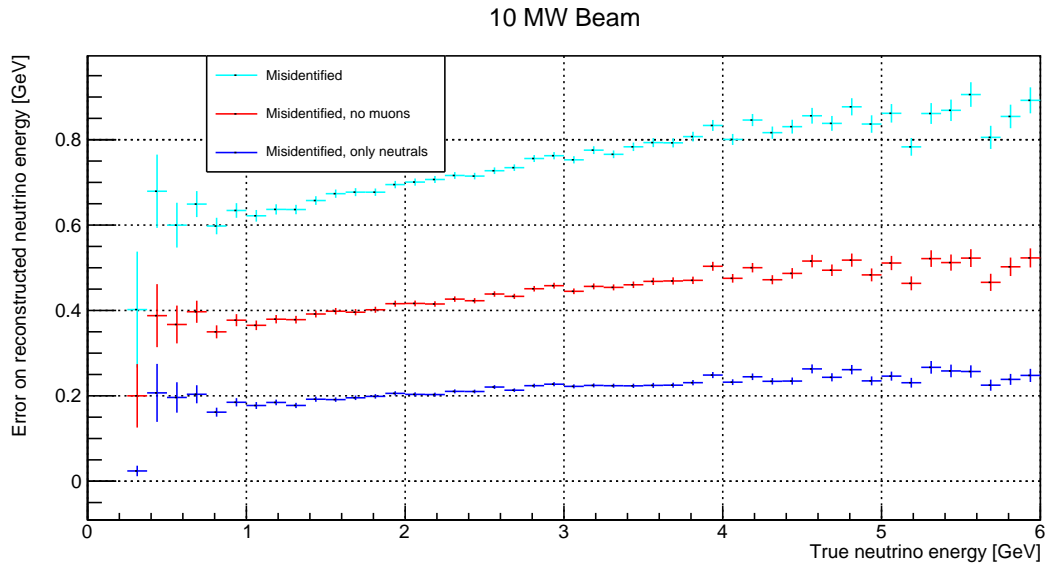


Figure A.37.: Mean misidentified energy versus true neutrino energy for a simple π^0 -induced EM shower reconstruction algorithm based on a cone-cylinder union. All energy deposited inside the cone-cylinder union by descendants of neutrinos different from the parent of the corresponding π^0 photon is counted as misidentified. Colour indicates different selections of misidentified energy: total (cyan); excluding depositions from muons (red); deposition from photons, neutrons, and their descendants only (blue). 10 MW beam of 80 GeV protons.

A. DUNE ND Event Pile-up Study Data

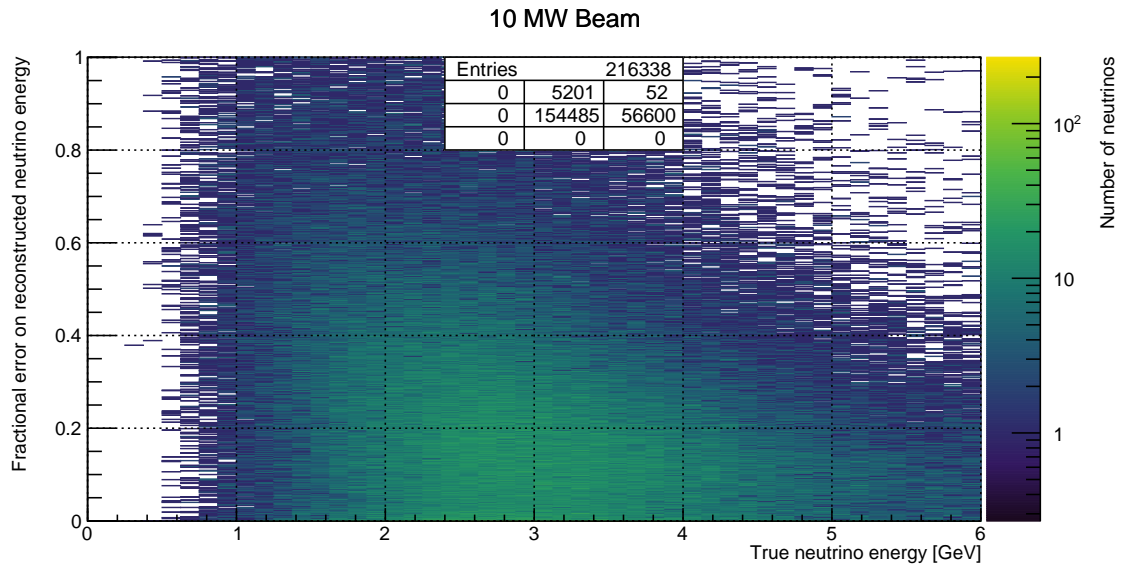


Figure A.38.: Misidentified energy fraction versus true neutrino energy for a simple π^0 -induced EM shower reconstruction algorithm based on a cone-cylinder union. All energy deposited inside the cone-cylinder union by descendants of neutrinos different from the parent of the corresponding π^0 photon is counted as misidentified. 10 MW beam of 80 GeV protons. Entries: Central cell shows plotted entries, other cells show overflow entries in direction w.r.t. central cell.

A. DUNE ND Event Pile-up Study Data

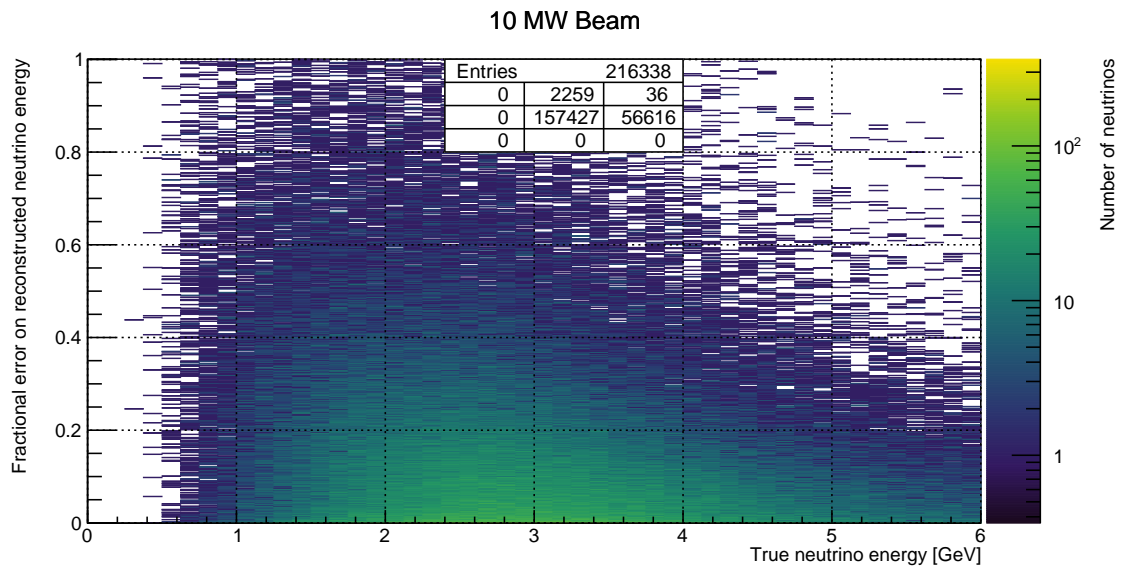


Figure A.39.: Misidentified energy fraction versus true neutrino energy for a simple π^0 -induced EM shower reconstruction algorithm based on a cone-cylinder union. Energy deposited inside the cone-cylinder union by descendants of neutrinos different from the parent of the corresponding π^0 photon is counted as misidentified. Any energy deposited by muons is excluded. 10 MW beam of 80 GeV protons. Entries: Central cell shows plotted entries, other cells show overflow entries in direction w.r.t. central cell.

A. DUNE ND Event Pile-up Study Data

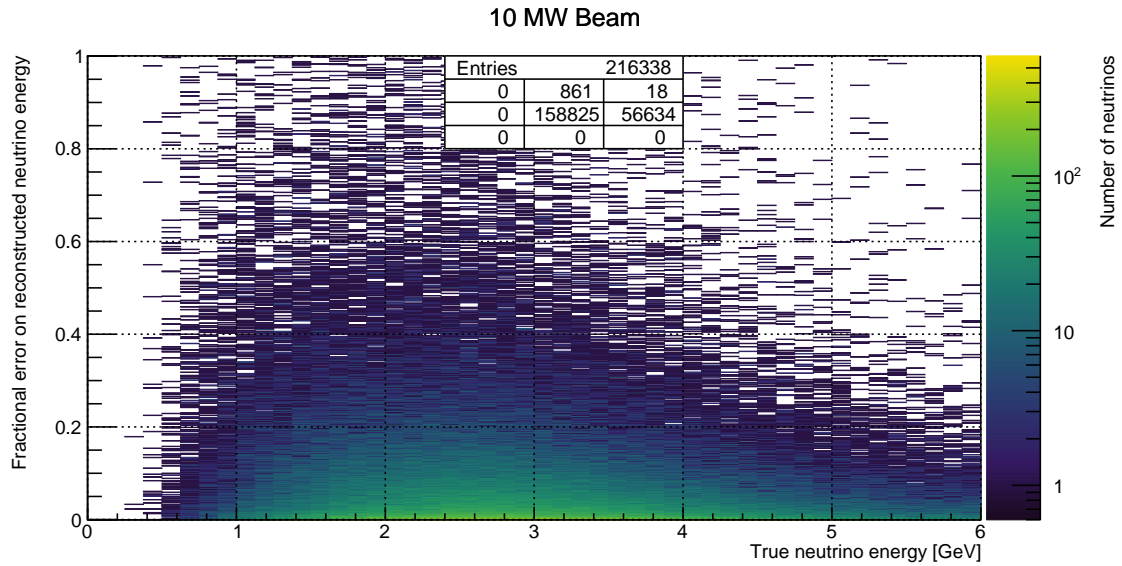


Figure A.40.: Misidentified energy fraction versus true neutrino energy for a simple π^0 -induced EM shower reconstruction algorithm based on a cone-cylinder union. Energy deposited inside the cone-cylinder union by descendants of neutrinos different from the parent of the corresponding π^0 photon is counted as misidentified. Only energy deposited by photons, neutrons, or any of their descendants is included. 10 MW beam of 80 GeV protons. Entries: Central cell shows plotted entries, other cells show overflow entries in direction w.r.t. central cell.

A. DUNE ND Event Pile-up Study Data

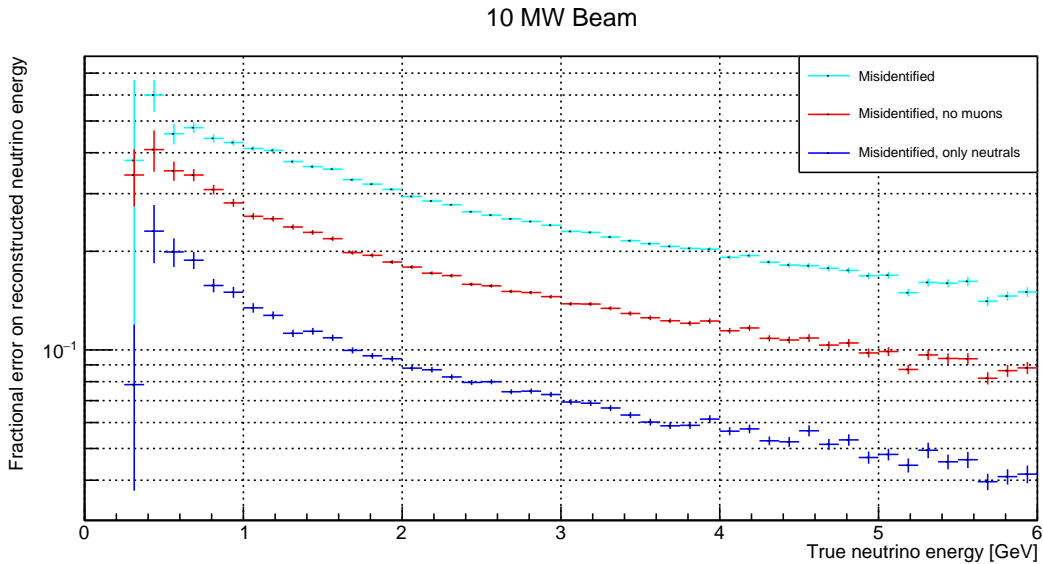


Figure A.41.: Mean misidentified energy fraction versus true neutrino energy for a simple π^0 -induced EM shower reconstruction algorithm based on a cone-cylinder union. All energy deposited inside the cone-cylinder union by descendants of neutrinos different from the parent of the corresponding π^0 photon is counted as misidentified. Colour indicates different selections of misidentified energy: total (cyan); excluding depositions from muons (red); deposition from photons, neutrons, and their descendants only (blue). 10 MW beam of 80 GeV protons.

A. DUNE ND Event Pile-up Study Data

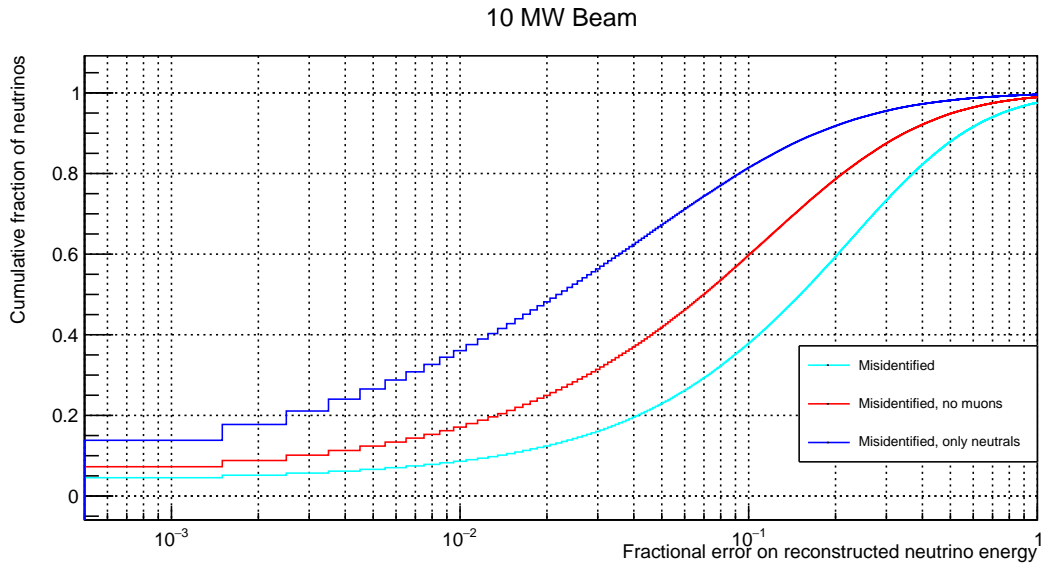


Figure A.42.: Cumulative fraction of neutrinos versus misidentified energy fraction for a simple π^0 -induced EM shower reconstruction algorithm based on a cone-cylinder union. All energy deposited inside the cone-cylinder union by descendants of neutrinos different from the parent of the corresponding π^0 photon is counted as misidentified. Colour indicates different selections of misidentified energy: total (cyan); excluding depositions from muons (red); deposition from photons, neutrons, and their descendants only (blue). The curve depicts the fraction of neutrinos on the y-axis with a misidentified energy fraction equal to or lower than the corresponding value on the x-axis. 10 MW beam of 80 GeV protons.